UNIVERSIDADE DE SANTIAGO DE COMPOSTELA
FACULTAD DE QUÍMICA

Departamento de Química Física

PhD Dissertation

Dynamics study of hydrogen transfer reactions by variational transition state theory

Rubén Meana Pañeda

Santiago de Compostela, Mayo de 2011

ISBN 978-84-9887-767-0 (Edición digital PDF)

D. Antonio Feznández Ramos, Profesor Titular del Departamento de Química Física de la Universidade de Santiago de Compostela,

CERTIFICA:

Que autoriza la presentación de la tesis doctoral titulada “**Dynamics study of hydrogen transfer reactions by variational transition state theory**” realizada bajo su dirección por D. Rubén Meana Pañeda, en el Departamento de Química Física

Y para que conste a todos los efectos, firma el presente certificado en Santiago de Compostela, mayo de 2011,

Dr. Antonio Fernández Ramos

a mis padres, Gonzalo y Ana María,
y a mis hermanas, Silvia y Luján

Contents

Agradecimientos IX

Resumen XI

1. Introduction 1

2. Symmetry numbers and chemical reaction rates 3
- 2.1. Introduction . . . 3
- 2.2. Symmetry numbers and rotation . . . 7
- 2.3. The symmetry number in chemical reactions . . . 10
  - 2.3.1. Some easy examples . . . 10
  - 2.3.2. Symmetric reactions . . . 11
  - 2.3.3. Chiral species . . . 11
  - 2.3.4. Reactions with many conformers . . . 16
  - 2.3.5. Symmetry numbers and internal rotation . . . 17
  - 2.3.6. An example involving an achiral diasteromer . . . 22
- 2.4. Summary . . . 26

3. Least-action tunneling transmission coefficient for polyatomic reactions 27
- 3.1. Introduction . . . 27
- 3.2. Background . . . 28
- 3.3. Method . . . 32
- 3.4. Results and discussion . . . 36
- 3.5. Concluding remarks . . . 44

4. Practical implementation and applications of the least-action tunneling transmission coefficient 45
- 4.1. Introduction . . . 45
- 4.2. Methodology . . . 48
- 4.3. Applications . . . 54
- 4.4. Concluding remarks . . . 59

5. Tunneling transmission coefficients for large systems 61
- 5.1. Introduction . . . 61
- 5.2. Tunneling transmission coefficients . . . 63
- 5.3. Practical implementation of the LCG4 and LAG4 methods . . . 70
- 5.4. Transmission coefficients and KIEs . . . 75

6. The CH_3OH + H hydrogen abstraction reaction 79
6.1. Introduction . . . 79
6.2. Methodology . . . 81
6.2.1. Electronic structure . . . 82
6.2.2. Reaction rates . . . 83
6.3. Results and discussion . . . 84
6.3.1. Stationary points . . . 85
6.3.2. Anharmonicity . . . 86
6.3.3. Theoretical thermal rate constants . . . 88
6.3.4. Arrhenius parameters . . . 92
6.3.5. Branching ratios . . . 97
6.3.6. Kinetic isotope effects . . . 97
6.4. Conclusions . . . 101

7. The [1,7] hydrogen shift in 7-methylocta-1,3(Z),5(Z)-triene 103
7.1. Introduction . . . 103
7.2. Computational details . . . 105
7.3. Results and discussion . . . 108
7.4. Conclusions . . . 116

8. The isomerization reaction of previtamin D_3 117
8.1. Introduction . . . 117
8.2. Calculation method . . . 121
8.3. Results and discussion . . . 122
8.3.1. Conformations of Pre and Vit . . . 123
8.3.2. Thermodynamics equilibrium constants . . . 128
8.3.3. Transition state structures . . . 130
8.3.4. Thermal rate constants . . . 132
8.3.5. Kinetic isotope effects . . . 136
8.4. Concluding remarks . . . 138

9. Conclusions 141

A. Supporting information for Chapter 4 143

B. Supporting information for Chapter 8 145
B.1. Derivation of Equation (8.18) . . . 145
B.2. Tables . . . 146

Bibliography 163

Agradecimientos

Me gustaría expresar mi más sincero agradecimiento a todas las personas e instituciones que han hecho que esta tesis doctoral fuese posible.

En primer lugar, me gustaría darle las gracias a mi director de tesis, el Dr. Antonio Fernández Ramos por haberme dado la oportunidad de trabajar en su grupo de investigación, por toda su inestimable ayuda, así como por todo su esfuerzo, interés y empeño en que este trabajo fuese mejor.

A las Universidades de Oviedo y de Santiago de Compostela por haberme dado la oportunidad de formarme como químico e investigador. En particular al departamento de Química Física y al Centro Singular de Investigación en Química Biológica y Materiales Moleculares (CIQUS) por haber puesto todos los medios humanos y materiales necesarios.

Este trabajo no hubiese sido posible sin la financiación que he recibido del Ministerio de Educación y Ciencia (Proyectos #BQU2003-01639, No. 2003/PX199) y la Xunta de Galicia a través de la Dirección Xeral de Investigación Desenvolvemento e Innovación (Proyectos 2006/XA088, 2006/AX128) y la Axuda para a Consolidación e Estructuración de unidades de investigación competitivas do Sistema Universitario de Galicia, 2007/50, cofinanciada polo FEDER 2007-2013.

Al resto de Drs. del grupo, Saulo A. Vázquez Rodríguez y Emilio Martínez Núñez, con quienes siempre es grato compartir las mismas inquietudes.

También me gustaría darle las gracias a mis colegas de laboratorio, por tantas horas de trabajo compartidas, charlas, congresos... En especial a Juanjo Nogueira, compañero de fatigas durante todo este tiempo, y a nuestro administrador de sistemas, el Dr. Javier López Cacheiro, siempre dispuesto a echar una mano. A toda la gente que ha pasado por el Grupo de Dinámica de las Reacciones Químicas, Teresa Tarrazo Antelo, Nicolás Ramos Berdullas, Marta Pombar Pérez y Alejandro Ramos Tajes. A nuestros nuevos compañeros de despacho en el CIQUS, Ceila Fong Padrón, Daniela Josa y Marcos Rellán Piñeiro. Al Dr. Hosein Mousavipour de quien he recogido el testigo en la investigación de la vitamina D_3, y a todas aquellas personas que han decidido realizar una estancia de investigación en nuestro grupo, la Dra. Teresa Cusati, el Dr. Antonio Sánchez Coronilla, Zahra Homayoon, el Dr. David Glowacki y Javier Aguilar, así como al programa "Partnerships for International Research and Education"(PIRE), que nos ha brindado la oportunidad de conocer y trabajar con estudiantes de grado de Estados Unidos. A los miembros del grupo de Química Cuántica, la Dra. Silvia D. Bouzón Capelo, el Dr. Hubert Cybulski, el Dr. Juan Pablo Senosiain, Stefan Bilan, el Dr. Cristian R. Munteanu y el Dr. José Luis Cagide Fajín, así como a los miembros de otros grupos del departamento de Química Física.

Al CESGA por dejarnos utilizar sus ordenadores, y a todo su personal por habernos dado apoyo técnico durante todo este tiempo.

I would like to thank Prof. D. G. Truhlar for giving me the opportunity to work in his group of research and the Minnesota Supercomputing Institute for computer time and technical support. This acknowledgement is extended to all the members of the Truhlar's group for all the stimulating discussions.

También me gustaría extender mi agradecimiento a todos mis antiguos compañeros y profesores de la Universidad de Oviedo. Recuerdo con especial cariño el entusiasmo que lograba transmitir la gente del departamento de Química Física y Analítica. A los Drs. Pedro Braña Coto, Jose Manuel Montejo Bernardo y Haydeé Valdés por todo el tiempo que invirtieron en mi formación cuando daba mis primeros pasos en la Química Teórica y Computacional.

A toda la gente del grupo de Química Orgánica, por todo lo que me han enseñado durante este tiempo, especialmente a Hugo Lago Santomé y a los Drs. Jose Ramón Suárez y Fernando Cagide Fagín.

A todos mis amigos a los que sería imposible mencionar en su totalidad pero que sin duda han sido de vital importancia en mi desarrollo personal, entre ellos las que constituyen un verdadero irreductible, Beatriz Padilla Vivas y Andrea Naves Arnaldos.

A tí, que todo lo llenas, porque sin duda todo lo que está por venir será aún mejor.

Desde aquí deseo brindar un reconocimiento muy especial a mis padres, y a mis hermanas, por todo su apoyo, cariño y comprensión. Ellos han sido, aliento, en los momentos difíciles, palabras de ánimo, fuerza y afán de superación cuando todo parecía perdido y sin ninguna duda su apoyo económico ha sido vital para la conclusión de esta tesis doctoral.

Resumen

Las reacciones de transferencia de hidrógeno se consideran unas de las más importantes en Química, porque están presentes en multitud de procesos químicos, biológicos e industriales. A modo de ejemplo, estas reacciones son relevantes en química orgánica, química atmosférica, química de la combustión, química interestelar, así como en procesos biológicos importantes tales como las reacciones enzimáticas y la rotura de la cadena de ADN. Además, también juegan un papel crítico en procesos industriales tales como la fabricación de capas de diamante mediante la deposición química de vapor a bajas presiones.

Entender, no sólo cómo tienen lugar, sino cuáles son los factores que influyen en su dinámica es de gran importancia y, por consiguiente, estas reacciones han recibido una amplia atención, tanto desde los puntos de vista experimental, como teórico.

Este tipo de reacciones tienen en común que la partícula que se transfiere, ya bien sea un átomo de hidrógeno, un protón o un hidruro, o bien sus análogos isotópicos, es una partícula ligera, lo que hace esencial en su estudio la consideración de efectos cuánticos tales como el efecto túnel.

El efecto túnel se define como la capacidad de las partículas de atravesar una barrera de energía potencial cuya altura es superior a la energía de la partícula, pasando a través de una región clásicamente prohibida. Su nombre deriva de la analogía con la única manera de atravesar una barrera geográfica sin superarla. En el cálculo de la contribución del efecto túnel a la constante de velocidad es necesario tener en cuenta el carácter multidimensional del mismo, ya que la coordenada de reacción se acopla con el resto de modos normales de vibración perpendiculares a la misma. Experimentalmente este fenómeno se evidencia por la desviación del valor de las constantes de velocidad respecto a la ley de Arrhenius, en especial a bajas temperaturas, y por presentar altos valores del efecto isotópico cinético ("kinetic isotope effect", KIE). El KIE se define como el cociente entre la constante de velocidad del sistema con hidrógeno y la constante de velocidad cuando dicho hidrógeno se sustituye por un isótopo más pesado. Dado que el efecto túnel depende en gran medida de la masa de la partícula que se transfiere, la magnitud de este cociente es de gran importancia en la dilucidación de los mecanismos de reacción.

Para estudiar la constantes de velocidad de estas reacciones químicas existen diversas metodologías. La dinámica cuántica auna todas las ventajas de un tratamiento lo más riguroso posible desde el punto de vista microscópico mediante la resolución de la ecuación de Schrödinger dependiente del tiempo. Por contra tiene como gran desventaja que sólo es aplicable a sistemas con un número de átomos muy pequeño debido a su alto coste computacional. Otras metodologías, como la de los instantones, serían en general adecuadas cuando las temperaturas son muy bajas, pero no tienen una extrapolación obvia a temperaturas intermedias (por encima de 250 K). En este sentido la teoría variacional del estado de transición con un tratamiento

multidimensional del efecto túnel (“variational transition state theory with multidimensional treatment of tunneling”, VTST/MT), encuadrada dentro de las aproximaciones semiclásicas, ha demostrado ser una herramienta muy versátil a la hora de estudiar la dinámica de este tipo de reacciones a temperaturas a partir de aproximadamente 200 K. Esta teoría permite el estudio de sistemas relativamente grandes, puesto que necesita una cantidad de información de la superficie de energía potencial muy reducida, además de ser una metodología susceptible de mejora.

En esta tesis doctoral se han utilizado la teoría convencional del estado de transición (“transition state theory”, TST) y la teoría variacional canónica del estado de transición (“canonical variational transition state theory”, CVT); ambas son variantes de la VTST para un colectivo canónico, esto es, a temperatura constante. La teoría CVT incluye los efectos de recruzamiento localizando la superficie divisoria perpendicular al camino de mínima energía en el punto dónde el valor de la constante de velocidad se minimiza. La constante de velocidad térmica CVT viene dada por la expresión:

$$k^{\mathrm{CVT}}(T) = \sigma \frac{k_{\mathrm{B}}T}{h} \frac{Q^{\mathrm{GT}}(T, s_*^{\mathrm{CVT}}(T))}{\Phi_{\mathrm{R}}(T)} \exp\left[-V_{\mathrm{MEP}}(s_*^{\mathrm{CVT}}(T))/k_{\mathrm{B}}T\right], \tag{1}$$

donde σ es el número de simetría, k_{B} y h son las constantes de Boltzmann y Planck, respectivamente, y $V_{\mathrm{MEP}}(s_*^{\mathrm{CVT}}(T))$ es el valor del potencial en el camino de mínima energía (“minimum energy path”, MEP) en el punto s_*^{CVT}, que es el lugar en el que se coloca la superficie divisoria que minimiza el flujo de trayectorias hacia productos. La función de partición de reactivos por unidad de volumen es $\Phi_{\mathrm{R}}(T)$ y $Q^{\mathrm{GT}}(T, s_*^{\mathrm{CVT}}(T))$ es la función de partición del estado de transición generalizado a $s_*^{\mathrm{CVT}}(T)$. Los efectos cuánticos, a excepción de aquellos sobre la coordenada de reacción se tienen en cuenta considerando funciones de partición vibracionales cuánticas.

Los efectos cuánticos sobre la coordenada de reacción se incorporan en la VTST/MT a través del coeficiente de transmisión, $\kappa(T)$, que multiplica la constante de velocidad

$$k^{\mathrm{CVT/MT}}(T) = \kappa^{\mathrm{CVT/MT}}(T) k^{\mathrm{CVT}}(T) \tag{2}$$

El coeficiente de transmisión se evalúa de manera semiclásica, utilizando la aproximación de Wentzel-Kramers-Brillouin (WKB), como el cociente entre las probabilidades de transmisión semiclásica y clásica ponderadas energéticamente. La probabilidad semiclásica depende inversamente del valor de la integral de acción, que se define como el área bajo la curva de energía potencial. Así, cuando la integral de acción es mínima, el valor del coeficiente de transmisión será máximo. El valor de la integral de acción depende de la forma (la altura y la anchura) de la barrera de energía potencial y de la masa de la partícula que se transfiere. En el contexto de la VTST/MT la barrera de energía sobre la que se evalúa el coeficiente de transmisión viene definida por el potencial vibracional adiabático, que es la suma de la energía potencial del sistema más la energía del punto cero. El camino multidimensional a lo largo del cual se evalúa el efecto túnel constituye la principal diferencia entre los distintos métodos que se han desarrollado para calcular el coeficiente de transmisión. Considerando que el acoplamiento entre el modo normal asociado a la coordenada de reacción y los modos transversales es despreciable, es decir cuando no se considera la curvatura de camino de reacción, el potencial vibracional adiabático se localiza a lo largo del camino de mínima energía. El coeficiente de transmisión calculado de esta forma utiliza la aproximación de curvatura cero (“zero curvature tunneling approximation”, ZCT) y ha demostrado ser un método inadecuado pues subestima seriamente la contribución del efecto túnel a la constante de velocidad.

Entre los métodos que sí tienen en cuenta el acoplamiento entre la coordenada de reacción y los modos transversales, está la aproximación de efecto túnel de pequeña curvatura ("small curvature tunneling approximation", SCT). En esta aproximación, inicialmente propuesta por Marcus y Coltrin y más tarde generalizada por Truhlar y col., la masa de la partícula que se transfiere, es sustituida por una masa efectiva cuyo valor viene dado por una expresión analítica. Esta expresión, tiene en cuenta el acoplamiento de la coordenada de reacción con los modos transversales, lo que hace que el valor de la masa efectiva sea menor que el de la masa de la partícula que se transfiere. Esto conlleva una disminución del valor de la integral de acción, lo que se traduce en un aumento de la probabilidad de túnel.

Aunque la aproximación de pequeña curvatura puede tener en cuenta casos en los que la curvatura es relativamente grande, suele fallar en el caso de reacciones en las que se transfiere una partícula ligera entre dos átomos pesados. Para estos sistemas, en los que el efecto túnel es dominante y el camino de reacción está muy alejado del camino de mínima energía, fue diseñado el método de gran curvatura ("large curvature tunneling", LCT), que evalúa el coeficiente de transmisión a lo largo de caminos rectos entre el valle de reactivos y el valle de productos.

Los métodos de pequeña curvatura y de gran curvatura cubren los dos extremos respecto al valor que puede tomar la curvatura de reacción. Para aquellos sistemas de curvatura intermedia existe un método, denominado método de túnel multidimensional microcanónicamente optimizado ("microcanonical optimized multidimensional tunneling", μOMT), en el que, a cada energía de túnel, se elige como la más grande de entre las probabilidades de túnel de pequeña y de gran curvatura.

Esta tesis doctoral está organizada de forma que cada capítulo se corresponde con un artículo publicado o enviado a publicación y en su conjunto aborda, tanto la mejora de diversos aspectos relacionados principalmente con el desarrollo de nuevos coeficientes de transmisión, como la aplicación de la CVT/SCT a diferentes sistemas en los que la reacción de transferencia de hidrógeno juega un papel importante. Se han estudiado reacciones de interés industrial o tecnológico, como la reacción de abstracción de hidrógeno en metanol por parte de hidrógeno atómico, que resulta de vital importancia en la comprensión de su mecanismo de combustión, así como reacciones de interés biológico, como la transposición sigmatrópica [1,7] de hidrógeno que tiene lugar en la formación de la vitamina D. Esta última supone un reto desde el punto de vista del estudio dinámico cuantitativo de sistemas de gran tamaño con la VTST/MT, y cuyo estudio comparativo con un sistema modelo, como es el 7-metilocta-1,3(Z),5(Z)-trieno, pone de manifiesto la importancia de utilizar sistemas modelo lo más realistas posibles.

La primera parte de la tesis doctoral trata de aspectos metodológicos relacionados con la VTST/MT. En el capítulo 2 se clarifica el concepto y el uso de los números de simetría rotacionales y se dan pautas para su correcta utilización en el contexto de la teoría del estado de transición. Los siguientes tres capítulos incluyen el desarrollo y la puesta a punto de un nuevo método para la evaluación de coeficientes de transmisión.

La segunda parte de la tesis doctoral analiza las aplicaciones de la teoría VTST/MT a diferentes sistemas. En el capítulo 6 se aborda el estudio de la reacción de abstracción de hidrógeno de la molécula de metanol por parte de hidrógeno atómico en fase gas, utilizando para ello métodos de la estructura electrónica de alto nivel. En los dos últimos capítulos se estudian las reacciones [1,7] sigmatrópica de hidrógeno en el 7-metilocta-1,3(Z),5(Z)-trieno y en la vitamina D. Además para estas dos reacciones se ha estudiado el efecto del entorno, es decir, el papel que juega el disolvente en las mismas y su influencia sobre las constantes de velocidad.

El capítulo 2 muestra como evaluar los números de simetría para diferentes configuraciones moleculares y cómo estos se incorporan en la teoría del estado de transición. El concepto de número de simetría rotacional dentro de la TST es de vital importancia pues de él depende la correcta evaluación de las constantes de velocidad térmicas. Como se aprecia en la Ecuación (1), σ aparece como un factor multiplicativo, que surge en el empleo de la función de partición de rotación clásica, que considera las partículas idénticas como físicamente distinguibles, en contra de lo que se establece en mecánica cuántica. En general, el número de simetría viene dado por el cociente entre los números de simetría rotacionales de los reactivos y del estado de transición, aunque hay que tener especial cuidado en su evaluación en los siguientes casos: (i) si la reacción es bimolecular, cuando ambos reactivos son iguales (ii) si la reacción es simétrica (iii) si los reactivos y/o los estados de transición son quirales, (iv) si los reactivos y/o los estados de transición presentan múltiples confórmeros, y (v) si hay una rotación interna en alguna parte del sistema molecular. Todos estos casos son tratados y analizados sistemáticamente en detalle y se incluyen un gran número de ejemplos.

Las aproximaciones ZCT y LCT constituyen dos casos extremos de un método mucho más general. El primer método considera que el camino en el que se evalúa el efecto túnel es el más largo pero el más favorable energéticamente, mientras que el segundo considera el camino más corto, pero el más desfavorable energéticamente. A lo largo de esta tesis doctoral se ha desarrollado e implementado un nuevo método para reacciones poliatómicas, basado en un procedimiento desarrollado por Garrett y Truhlar para reacciones átomo-diátomo, que busca el camino para el que el valor de la integral de acción se minimiza y por lo tanto se maximiza la probabilidad de túnel a lo largo de una familia de caminos que van, desde el camino de mínima energía, hasta el camino recto. Estos caminos de reacción se construyen como una combinación lineal del camino recto y del camino de mínima energía mediante un parámetro que, a cada energía de túnel, los relaciona. Esta nueva aproximación permite obtener coeficientes de transmisión de mínima acción ("least-action tunneling", LAT), y supone la búsqueda del camino que sea el mejor compromiso entre la longitud y la altura de la barrera. En el método de mínima acción es necesario evaluar la energía de las geometrías que quedan muy alejadas del camino de mínima energía en la zona no adiabática. Además, el valor del integral de acción se optimiza variacionalmente, lo que supone llevar a cabo un procedimiento iterativo hasta conseguir la convergencia del valor de la integral de acción. Todo ello, unido a que es necesario repetir dicho proceso para cada energía de túnel, hacen del LAT un método que implica un elevado coste computacional, especialmente cuando se desea utilizar junto con cálculos de dinámica directa. Para ilustrar su funcionamiento se han calculado los coeficientes de transmisión para la reacción de abstracción de hidrógeno $CH_4 + H \longrightarrow CH_3 + H_2$, y para reacciones similares en las que se ha modificado la masa del hidrógeno que está abstrayendo el protón, a fin de ver el efecto de la curvatura en las diferentes aproximaciones.

Los capítulos 4 y 5 describen dos nuevos algoritmos, que permiten llevar a cabo cálculos mediante dinámica directa, para obtener coeficientes de transmisión LAT para reacciones poliatómicas. Estos algoritmos se basan en una interpolación monodimensional ("interpolated LAT one dimension", ILAT1D) y en una doble interpolación ("double interpolated LAT", DILAT). El primero de ellos utiliza un spline monodimensional para interpolar los potenciales efectivos a lo largo de las porciones no adiabáticas de los caminos de túnel, mientras que el segundo además interpola las integrales de acción imaginarias como funciones de las energías de túnel. Este último método fue diseñado para el cálculo de los coeficientes de transmisión multidimensionales LAT en sistemas poliatómicos de elevado tamaño molecular.

El comportamiento de ambos algoritmos se comprobó en las reacciones de abstracción de hidrógeno, $CH_4/CD_3H/CD_4 + CF_3$, obteniéndose resultados muy satisfactorios en términos de fiabilidad y tiempos de cálculo, siendo el método DILAT hasta 30 veces más rápido respecto al cálculo completo y con errores menores al 5 %.

A la luz de estos nuevos métodos y de los ya existentes se realizó un estudio comparativo de los KIEs de la reacción $CH_4 + H \longrightarrow CH_3 + H_2$ con diferentes isotopómeros poniendo de manifiesto las diferencias entre las aproximaciones que evalúan el coeficiente de transmisión explícitamente a lo largo de un camino de reacción como son, la aproximación de curvatura cero, la aproximación de gran curvatura o la aproximación de mínima acción, frente a la aproximación de pequeña curvatura, que recurre a una expresión analítica para tener el cuenta el efecto de la curvatura de reacción.

El excelente acuerdo para la reacción anterior entre las constantes de velocidad térmicas calculadas con métodos de dinámica cuántica y aquellas calculadas mediante CVT/μOMT motivaron, entre otros, el estudio de la reacción de abstracción de hidrógeno del metanol por parte de hidrógeno atómico. Los datos experimentales disponibles hasta la fecha para esta reacción difieren considerablemente unos de otros, tanto en el rango de bajas, como en el de altas temperaturas, independientemente del tipo de técnica experimental utilizada. Utilizando cálculos de estructura electrónica de alto nivel, se evaluaron las constantes de velocidad CVT/μOMT para las dos principales reacciones de abstracción de hidrógeno, $CH_3OH + H \longrightarrow CH_2OH + H_2$ y $CH_3OH + H \longrightarrow CH_3O + H_2$ y se incluyeron los efectos de la anarmonicidad en el modo de torsión respecto al enlace C−O mediante el método de la suma de los valores propios asociados a la torsión (“torsional eigenvalue summation”, TES). Se ha encontrado que esta anarmonicidad es importante a altas temperaturas. En dicho estudio se compararon, los valores obtenidos de las constantes de velocidad, los efectos cinéticos isotópicos y los cocientes de cada una de las constantes de velocidad de las reacciones anteriores respecto a la constante total del proceso, con todos los datos experimentales y teóricos disponibles. Otro hecho destacable es que las constantes de velocidad calculadas muestran un cambio substancial de la energía de activación con la temperatura, lo que invalida un ajuste tipo Arrhenius para analizar la dependencia de las constantes de velocidad con la temperatura.

Respecto al estudio de las reacciones de transferencia de hidrógeno que juegan un papel biológico importante, se ha analizado la reacción de isomerización térmica a través de la que se forma la vitamina D. Es una reacción de transposición sigmatrópica [1,7] de hidrógeno para la que se dispone de numerosos datos experimentales, en diferentes entornos. Este sistema permite examinar la fiabilidad, no sólo de los métodos de estructura electrónica disponibles hasta la fecha, sino también de la VTST/MT para tratar sistemas de tamaño relativamente grande. En este sentido el 7-metilocta-1,3(Z),5(Z)-trieno, ha sido elegido, tanto desde los puntos de vista teórico, como experimental, como sistema modelo para la reacción [1,7] sigmatrópica en la vitamina D.

Las constantes de velocidad teóricas calculadas mediante la CVT/μOMT y los KIEs obtenidos para ambos sistemas concuerdan bastante bien con los datos existentes en la bibliografía. El análisis teórico del efecto isotópico permite la factorización de éste en diferentes contribuciones, poniendo de manifiesto la importancia del efecto túnel en el proceso. En el caso del 7-metilocta-1,3(Z),5(Z)-trieno se estudió la influencia de los diferentes confórmeros sobre la constante de velocidad. Por otra parte la vitamina D posee mucha más flexibilidad conformacional que el 7-metilocta-1,3(Z),5(Z)-trieno, debido a la presencia de dos anillos de seis miembros, lo que diversifica el número de canales de reacción y amplifica la influencia que pueda tener el entorno

sobre cada uno de ellos. Se calcularon las constantes de velocidad de cada uno de los canales independientes con su coeficiente de transmisión correspondiente, lo que ha permitido obtener la constante de velocidad del proceso global y las contribuciones, no sólo de cada canal reactivo, sino de aquellos confórmeros que tienen más importancia en las constantes de velocidad y en los efectos isotópicos. Toda esta información ha posibilitado el análisis sobre el papel jugado por la flexibilidad de la vitamina D en la isomerización y ha permitido establecer las diferencias principales con respecto al sistema modelo, así como la relación estructura-reactividad en ambos sistemas.

Chapter 1

Introduction

Hydrogen transfer reactions are present in many areas of the chemistry and biology. They take place in atmospheric chemistry, [1] combustion chemistry, [2] interstellar chemistry [3] as well as in many important biological processes like enzymatic reactions, [4, 5] DNA strand breaking, [6, 7] catalysis [8] and various facets of organic chemistry. [9] They also play a critical role in industrial processes like the making of diamond films via low-pressure chemical vapor deposition (CVD). [10, 11]

The dynamical study of these kind of reactions is a difficult task due to the need to include quantum mechanical effects. Tunneling is a key issue in the understanding of hydrogen transfer reactions. In general, different methodologies, which take into account the quantum effects, can be used for the calculation of the rate constants. The modern wave packet dynamics calculations, as for instance, the multiconfigurational time-dependent Hartree (MCTDH) approach, [12, 13] or the theory of the instantons, [14, 15] provide very accurate values of the rate constants but are only affordable for reduced-dimensional systems, in the first case, and for reactions that occur at low temperatures, in the second case. Moreover, these dynamical theories are quite complex from a mathematics point of view, so they are difficult to improve.

On the other hand, variational transition state theory with multidimensional treatment of tunneling (VTST/MT) [16, 17] is one of the most accessible and useful theories to study hydrogen transfer reactions, which still needs some improvements. In the framework of VTST theory, quantum effects are included differently for bound modes and for the reaction coordinate. For bound modes, they are included through quantum mechanical vibrational partition functions (normally within the harmonic approximation). Quantum effects on the reaction coordinate are included through a multiplicative transmission coefficient. It is defined as the Boltzmann average between the quantum and classical probabilities. In this context, it is very important to develop new methods to obtain reliable transmission coefficients for reactions where the tunneling contribution is important. There are several approximations to compute transmission coefficients, and one of the major goals of this Dissertation is the development and implementation of a new method which computes them in a more reliable manner.

Probably the most relevant issue in the evaluation of the transmission coefficient is to take into account the multidimensional character of tunneling, by incorporating the effect of the reaction-path curvature. The latter is related to the coupling between the reaction-path coordinate and the transverse modes. Marcus and Coltrin [18] developed the small curvature tunneling (SCT) method for systems with small coupling, and Truhlar and co-workers [19] generalized the method. The SCT approach may break down for heavy-light-heavy systems for which the large curvature tunneling (LCT) [20–23] approach works well. The microcanonical optimized multidimensional tunneling, (μOMT), [24] which is a compromise between SCT and LCT approaches, had been developed for the case of chemical reactions with intermediate curvature values.

Truhlar and Garrett in the 80's proposed a new transmission coefficient for colinear atom-diatom reactions called the least-action tunneling approximation (LAT). [25]. Even for small systems the LAT method is computationally highly demanding when used together with the direct-dynamics approach. We have extended the applicability of the LAT method for polyatomic systems and have reduced the computational cost in order to apply it to very large molecules.

It has also been included a Chapter about the use of the rotational symmetry numbers in the context of the VTST together with a large number of examples to clarify some complicated situations.

The last part of this Dissertation includes VTST applications to several systems involving different active areas of research. Direct-dynamics calculations had been carried out for the hydrogen abstraction reaction from methanol by atomic hydrogen and for reactions of biological interest such as the isomerization reaction of vitamin D. For the latter the effect of the environment has been analyzed and, despite the size of the system, it was possible to report thermal rate constants in good agreement with experiment. There is also a chapter dedicated to the [1,7] sigmatropic shift in the 7-methylocta-1,3(Z),5(Z)-triene, a model system to mimic the isomerization reaction of vitamin D.

It should be noticed that the structure of each chapter of this Dissertation follows the scheme of its corresponding published article, with the exception of the Chapter on vitamin D, which is an unpublished work.

Chapter 2

Symmetry numbers and chemical reaction rates

This Chapter shows how to evaluate rotational symmetry numbers for different molecular configurations and how to apply them to transition state theory. In general, the symmetry number is given by the ratio of the reactant and transition state rotational symmetry numbers. However, special care is advised in the evaluation of symmetry numbers in the following situations: (i) if the reaction is symmetric, (ii) if reactants and/or transition states are chiral, (iii) if the reaction has multiple conformers for reactants and/or transition states and, (iv) if there is an internal rotation of part of the molecular system. All these four situations are treated systematically and analyzed in detail in the present Chapter. We also include a large number of examples to clarify some complicated situations, and in the last section we discuss an example involving an achiral diasteroisomer.

2.1. Introduction

Transition state theory (TST) [17, 26–30] is the most widely used method for calculating rate constants of chemical reactions. The conventional TST rate expression may be written

$$k_{\mathrm{TST}}(T) = \sigma \frac{k_{\mathrm{B}}T}{h} \frac{Q_{\mathrm{TS}}(T)}{\Phi_{\mathrm{R}}(T)} \exp\left[-V^{\ddagger}/k_{\mathrm{B}}T\right] \tag{2.1}$$

where k_{B} is Boltzmann's constant; h is Planck's constant; $V^{\ddagger}$ is the classical barrier height; T is the temperature and σ is the reaction-path symmetry number; $Q_{\mathrm{TS}}(T)$ and $\Phi_{\mathrm{R}}(T)$ are the quantum mechanical transition state quasi-partition function and reactant partition function, respectively, without rotational symmetry numbers, and with the zeroes of energy at the zero-point-exclusive energies of the saddle point and equilibrium reactants, respectively. $Q_{\mathrm{TS}}(T)$ is referred to as a quasi-partition function because it is missing the vibrational degree of freedom corresponding to the reaction coordinate. $\Phi_{\mathrm{R}}(T)$ is the unitless reactant partition function for unimolecular reactions and the reactants partition function per unit volume for bimolecular reactions. Specifically for bimolecular reactions ($\mathrm{A}+\mathrm{B} \longrightarrow \mathrm{P}$), the reactants partition function can be factorized as $\Phi_{\mathrm{R}}(T) = \Phi_{\mathrm{rel}}^{\mathrm{A,B}}(T) Q_{\mathrm{R}}(T) = \Phi_{\mathrm{rel}}^{\mathrm{A,B}}(T) Q_{\mathrm{A}}(T) Q_{\mathrm{B}}(T)$, where $\Phi_{\mathrm{rel}}^{\mathrm{A,B}}$ is the relative translational motion per unit volume and $Q_{\mathrm{R}}(T) = Q_{\mathrm{A}}(T) Q_{\mathrm{B}}(T)$ is the unitless reactants partition function for the internal motions. The present chapter is mainly concerned with σ.

Equation (2.1) can be generalized by variationally optimizing the transition state (so it is no longer located at the saddle point) and by adding a transmission coefficient to account for recrossing and quantum effects (including tunnelling). [17, 28–30] These generalizations do not change the considerations involved in giving a value to σ.

In a classic article, Pollak and Pechukas [31] sorted out conceptual difficulties involving σ and proved that it is always equal to the ratio of the total symmetry number of the reactant divided by the total symmetry of the transition state. Despite the simplicity and clarity of this result, it can sometimes be confusing to apply it to complex reactions, because it may require considering more than the usual rotational symmetry numbers, and it is discouraging to find in some recent applications that the symmetry numbers are ignored, ill-defined, or wrong. In addition, the increased complexity of new applications also raises interesting new questions. For these reasons it is useful to review some of the arguments of Pollak and Pechukas and to add some new comments on the subject. It should be noted that symmetry number arguments similar to those of Pollak and Pechukas were also given by Coulson [32].

In conventional TST, the forward thermal rate constant can be calculated with information about only two configurations, i.e., reactants and the transition state. Leaving the symmetry numbers out of the rotational partition function in Eq. (2.1) means that we are treating the identical particles as distinguishable, and in this case the rotational partition functions would be given by

$$Q^*_{\mathrm{rot}}(T) = \frac{2I}{\hbar^2\beta} \tag{2.2a}$$

for a lineal molecule, where I is the moment of inertia, $\hbar$ is Planck's constant divided by 2π , and β is defined as $1/k_{\mathrm{B}}T$. For nonlinear molecules, the expression for the rotational partition function of distinguishable particles $Q^*_{\mathrm{rot}}(T)$ is

$$Q^*_{\mathrm{rot}}(T) = \left[\left(\frac{2}{\hbar^2\beta}\right)^3 \pi I_{\mathrm{A}} I_{\mathrm{B}} I_{\mathrm{C}}\right]^{1/2} \tag{2.2b}$$

where I_{A}, I_{B} and I_{C} are the principal moments of inertia. The symmetry number in Eq. (2.1) arises from the indistinguishability of identical particles, i.e., the rotational partition is given by

$$Q_{\mathrm{rot}}(T) = \frac{1}{\sigma_{\mathrm{rot}}} Q^*_{\mathrm{rot}}(T) \tag{2.3a}$$

where σ_{rot} is the rotational symmetry number. Therefore the ratio between the rotational partition functions of the transition state, $Q_{\mathrm{rot,TS}}(T)$, and reactants, $Q_{\mathrm{rot,R}}(T)$, leads to:

$$\frac{Q_{\mathrm{rot,TS}}(T)}{Q_{\mathrm{rot,R}}(T)} = \frac{\sigma_{\mathrm{rot,R}}}{\sigma_{\mathrm{rot,TS}}} \frac{Q^*_{\mathrm{rot,TS}}(T)}{Q^*_{\mathrm{rot,R}}(T)} = \sigma \frac{Q^*_{\mathrm{rot,TS}}(T)}{Q^*_{\mathrm{rot,R}}(T)} \tag{2.3b}$$

Therefore, in simple cases, the rotational symmetry numbers in the above partition functions account for all the effects of nuclear indistinguishablility on reaction rates, and the symmetry number in Eq. (2.1) is given by

$$\sigma = \sigma_{\mathrm{rot,R}}/\sigma_{\mathrm{rot,TS}}, \tag{2.4}$$

with $\sigma_{\mathrm{rot,R}}$ and $\sigma_{\mathrm{rot,TS}}$ being the rotational symmetry numbers of the reactants and the transition state, respectively. For a bimolecular reaction, where the reactants are different, $\sigma_{\mathrm{rot,R}}$ is the product of the two σ_{rot} numbers. In some cases, it will not be sufficient to consider just

Table 2.1: Ratios of approximate rotational partition functions for $^{16}O_2$ to the accurate one with only odd J

Temperature(K)	Classical with symmetry factor[a]	Quantal without symmetry[b]
1,000	0.9993	2.0000
600	0.9988	2.0000
300	0.9977	2.0000
200	0.9965	2.0000
100	0.9931	2.0000
50	0.9862	2.0000
25	0.9726	2.0000
10	0.9326	2.0002
5	0.8883	2.0452
1	5.1368	22.3732

For this illustration we use the rigid rotor approximation with a moment of inertia of 75,894 $m_e bohr^2$, where m_e is the mass of an electron.

[a] Ratio of Eq. (2.3a) with $\sigma_{rot} = 2$ to accurate result.

[b] Ratio of partition function with all J to partition function with only odd J.

rotational symmetry numbers, σ_{rot}. We will need to consider rotational translational symmetry numbers $\sigma_{r\text{–}t}$.

It is useful to review the fundamental origin of the symmetry factors. Consider $^{16}O_2$ as an example. Because the ^{16}O nucleus is a boson, the nuclear spin wave function is symmetric under interchange of the nuclei. By Bose–Einstein statistics, the overall wave function must be symmetric under such interchange. Since the nuclear spin wave function is symmetric, and the ground electronic state ($^3\Sigma_g^-$) is odd, the rotational wave function must be antisymmetric (odd). Therefore, half of the rotational quantum numbers J (the even ones) are missing [33]. In the classical limit where sums over rotational levels are replaced by an integral [34], half of the levels being missing decreases the rotational partition function by a factor of two. At low temperature where only a few rotational levels are populated, the factor of two is only approximately correct. In practice, the inclusion of the inaccessible $J = 0$ state would cause a very large error at very low temperature. This is illustrated in Table 2.1, which first shows the ratio of the partition function calculated using Eq. (2.3a) to the accurate one, and then shows the ratio of the hypothetical partition function for all J to the accurate one. The table shows that the symmetry factor is very close to 2 at most temperatures of interest. The classical approximation is so good that one almost always uses it–the main exception being H_2 below room temperature.

When the identical nuclei are fermions, the situation is more complicated. H_2 provide the classic example. Since it is treated in most statistical mechanics texts [34], we just summarize the result. It turns out that one fourth of the nuclear spin states are forbidden for odd J and three fourths are forbidden for even J. Averaging over many states again decreases the partition function by a factor of two.

Polyatomic molecules are more complicated, because there can be more than two identical nuclei, because the vibrational wave functions are not all symmetric, and because the rotational wave functions are more complicated. Consider methane (CH_4) as an example. The total wave function must be antisymmetric with respect to the exchange of both coordinates and spins of the hydrogen nuclei because they are fermions. As discussed in detail elsewhere [35–37], in order to find the correct nuclear degeneracy associated with each rovibrational state, one has to evaluate a direct product between the permutation group symmetries of the rovibrational states and the nuclear spin wave functions. The net result is that, on average, the molecule has only 1/12 as many states as it would have if the nuclear permutation antisymmetry were not enforced.

In the rest of this chapter, except briefly in the discussion of the $H + H_2$ reaction, we shall simply use the classical symmetry factors without considering nuclear spin states or very low temperatures where the classical limit breaks down. Equation (2.4) and the product rule given right below it usually suffice, but exceptions arise when reactants in a bimolecular reaction are indistinguishable, when species are chiral, when a reaction is symmetric (sometimes called a degenerate rearrangement), or when TST is used to account for multiple elementary reactions. Continuing along the line of the article of Pollak and Pechukas, it is the objective of this paper to show by examples how to calculate the reaction-path symmetry number of Eq. (2.1) for any unimolecular or bimolecular reaction.

To evaluate the symmetry number of Eq. (2.1) the first step is to calculate the rotational symmetry number of the reactants and the transition state. This is explained in Section 2.2. Section 2.3 of the present chapter, illustrates by means of examples how to calculate the symmetry numbers for chemical reactions with additional complications such as chiral isomers, symmetric reactions, low-energy conformers, and internal rotation.

a1 **a2**

water

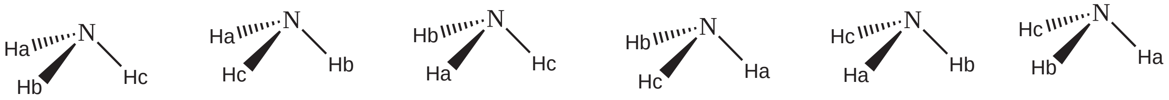

b1 **b2** **b3** **b4** **b5** **b6**

ammonia

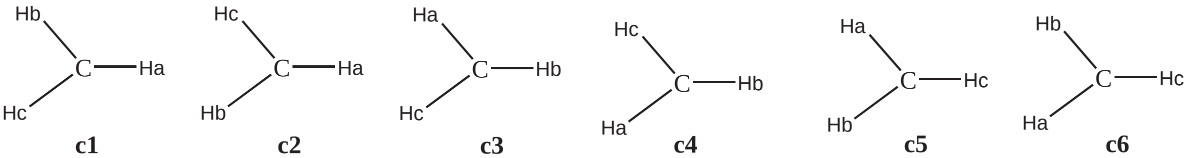

c1 **c2** **c3** **c4** **c5** **c6**

methyl radical

Structure 2.1

2.2. Symmetry numbers and rotation

Consider the molecules depicted in Structure 2.1 in their equilibrium configurations: water, ammonia, and the methyl radical. If all of the indistinguishable atoms are labelled and treated as distinguishable and the molecule is fixed in space, the configurations shown in Structure 2.1 are obtained. That is, there are two possible configurations for water and six each for nonplanar ammonia and planar methyl radical. In general, the total number of possible configurations equals the $m!$ permutations of the m equivalent atoms. Of those, we would like to know which of them cannot be transformed into each other by rotation or translation of the whole molecule. The water molecule, labelled as **a2** in Structure 2.1, can be transformed into **a1** by a rotation of 180° and, therefore, there is only one unique configuration. In the case of ammonia **b5** and **b4** are transformed into **b1** by clockwise rotations of 120° and 240°, respectively, whereas **b3** and **b6** can be transformed into **b2**. However, it is not possible to find any combination of rotation and translation of the ammonia molecule that transforms **b1** into **b2** and, therefore, these two structures are each unique configurations. For the methyl radical **c2**, **c3** and **c6** can be transformed into **c1** by rotations of 180 degrees around the $\mathrm{C{-}H_a}$, $\mathrm{C{-}H_c}$ and $\mathrm{C{-}H_b}$ axes, respectively; additionally **c4** and **c5** are identical to **c1** by rotations of 120° and 240° about an axis that is perpendicular to the molecule and that passes through the central atom. Therefore, there is only one unique configuration of the methyl radical. The rotational symmetry number is given by the number of permutations of m atoms of the same type divided by the number of unique configurations, n_d, that remain different under rotation of the molecule, i.e.,

$$\sigma_\mathrm{rot} = \frac{m!}{n_\mathrm{d}} \tag{2.5}$$

From these examples we find that for water, ammonia, and the methyl radical the symmetry number is two, three and six, respectively. The symmetry number is uniquely determined by the point group symmetry of the molecule. A molecule without any symmetry (denoted as C_1) has a rotational symmetry number of one. The water molecule with C_{2v} point group symmetry in the equilibrium configuration has a rotational symmetry number of two because of the C_2 and E symmetry operations. The methyl radical with D_{3h} point group symmetry has a rotational symmetry number of 6 because of the identity operation, E, three C_2 rotation axes along any of the C−H bonds, and C_3 (rotation of 120°) and C_3^2 (rotation 240°) operations. This makes a total of six rotational symmetry operations. In the same way ammonia, which has C_{3v} symmetry, has a symmetry number of three. Therefore, as a general rule, *the symmetry number of rotation for a given molecule equals the number of rotational symmetry operations.* As a final example let us consider ferrocene, a molecule with D_{5h} point group symmetry. For this molecule the symmetry number of rotation is ten $(E + 2C_5 + 2C_5 + 5C_2)$.

As stated above, the symmetry number of reactants for a bimolecular reaction ($\mathrm{A} + \mathrm{B} \longrightarrow \mathrm{Products}$) is usually given by the product $\sigma_\mathrm{rot,R} = \sigma_\mathrm{rot,A}\sigma_\mathrm{rot,B}$, with $\sigma_\mathrm{rot,A}$ and $\sigma_\mathrm{rot,B}$ being the rotation symmetry numbers of A and B, respectively. However, a bimolecular reaction of the type $\mathrm{A} + \mathrm{A} \longrightarrow \mathrm{Products}$ constitutes a special case. In this case the symmetry number of reactants is given by $\sigma_\mathrm{r-t,R} = 2\sigma_\mathrm{A}^2$. The factor of two appears because of the ability of the reactants to exchange positions between molecules by translation. For instance, let's consider the reaction of a water molecule reacting with another water molecule. The number of possible configurations with labelled hydrogen and oxygen is $2!4! = 48$. Of those, only the 12 depicted

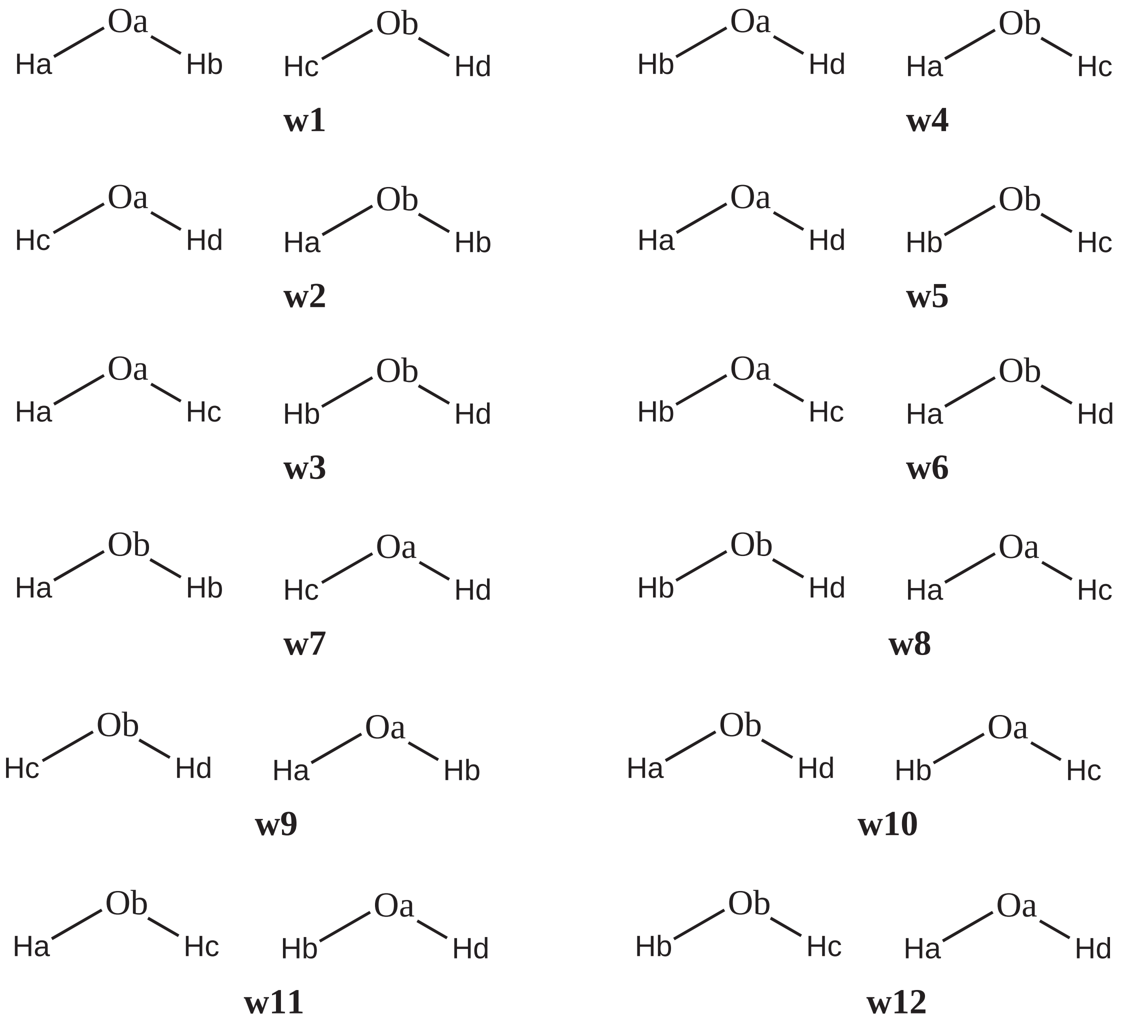

Structure 2.2

in Structure 2.2 cannot be superimposed by rotation, but only six configurations are really distinguishable, because **w1** = **w9**, **w2** = **w7**, **w3** = **w8**, **w4** = **w11**, **w5** = **w12**, and **w6**= **w10** by simply translating the first water molecule to the place of the second and vice versa. Therefore, symmetry number is 48/6 = 8. In this particular case we talk about a symmetry number of rotation-translation $\sigma_{\mathrm{r-t,R}}$ which is given by $\sigma_{\mathrm{r-t,R}} = 2\sigma^2_{\mathrm{rot,A}}$, which in this case is $\sigma_{\mathrm{r-t,R}} = 2(2)^2 = 8$.

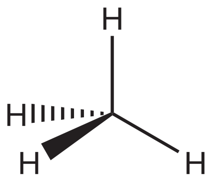

Structure 2.3

Table 2.2: Rotational symmetry, σ_{rot}, of the most common point groups of symmetry

Point group	σ_{rot}
C_1	1
C_s	1
C_2	2
C_{2v}	2
C_{3v}	3
$C_{\infty v}$	1
D_{2h}	4
D_{3h}	6
D_{5h}	10
$D_{\infty h}$	2
D_{3d}	6
T_d	16
O_h	24

In some cases the symmetry number of the molecule has a counterintuitive value. For example, consider the molecule of methane, which is depicted in Structure 2.3. There are four equivalent hydrogen atoms; however, the rotational symmetry number is not four. For methane the number of possible configurations is $4! = 24$ of which only two cannot be superimposed by rotation as indicated below in Structure 2.4. Thus, the symmetry number is $24/2 = 12$. Again this agrees with what is inferred from the point group symmetry of the molecule, which is T_d , because T_d has 12 rotational symmetry operations ($E + 8C_3 + 3C_2$).

d1 **d2**

Structure 2.4

In other cases the symmetry number corresponds to the number of equivalent atoms, such as the symmetry number for ethane (D_{3d} symmetry), which has six equivalent hydrogen atoms and also has a rotational symmetry number of six. Table 2.2 lists the rotation symmetry number for the most common point groups.

2.3. The symmetry number in chemical reactions

Below we illustrate how to calculate the symmetry numbers for a given chemical reaction. This section involves the rotational symmetry numbers of Section 2.2.

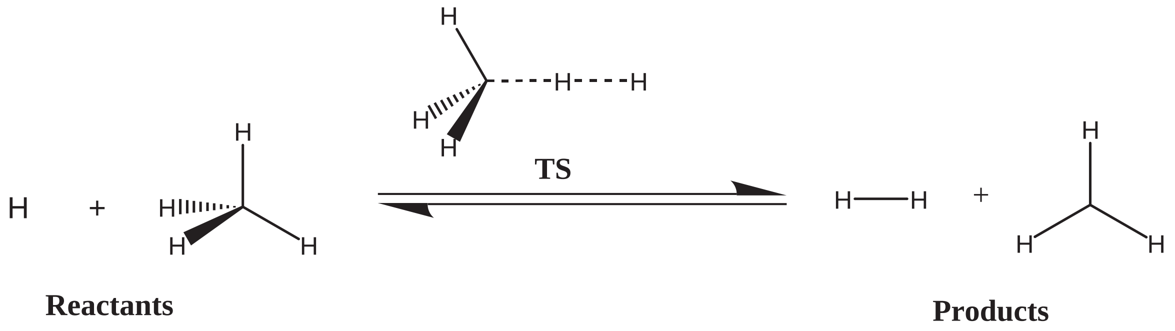

Structure 2.5

2.3.1. Some easy examples

Structure 2.5 illustrates the bimolecular abstraction of hydrogen from methane by a hydrogen atom. The symmetry number for the forward reaction, σ_f, making use of Table 2.2 and Eq. (2.4), is given by

$$\sigma_\mathrm{f} = \frac{\sigma_\mathrm{rot,R}}{\sigma_\mathrm{rot,TS}} = \frac{\sigma_\mathrm{H}\sigma_{\mathrm{rot,CH_4}(T_d)}}{\sigma_{\mathrm{rot,TS}(C_{3v})}} = \frac{1 \times 12}{3} = 4 \tag{2.6}$$

which matches the intuitive answer because there are four equivalent hydrogen atoms to abstract. However, sometimes the symmetry number for a reaction is not intuitive. If the hydrogen is abstracted by the CF_3 radical (which has C_{3v} symmetry in its equilibrium configuration), then the symmetry number is 12 because

$$\sigma_\mathrm{f} = \frac{\sigma_\mathrm{rot,R}}{\sigma_\mathrm{rot,TS}} = \frac{\sigma_{\mathrm{CF_3}(C_{3v})}\sigma_{\mathrm{rot,CH_4}(T_d)}}{\sigma_{\mathrm{rot,TS}(C_{3v})}} = \frac{3 \times 12}{3} = 12 \tag{2.7}$$

This can be difficult to comprehend if the symmetry numbers are visualized in terms of the number of equivalent reactions, because in classical mechanics there are four different hydrogen atoms to abstract. However, when it is recognized that there is only one transition state that is quantum mechanically distinguishable, it becomes clear that the symmetry number of 12 arises entirely from the effect that symmetry has on the rotational partition functions of reactants and the transition state. The reader should keep in mind that the symmetry number results from certain rotational states (that would be present for distinguishable particles) being missing in quantum mechanics. It should be noticed that the difference of a factor of three when comparing Eq. (2.6) with Eq. (2.7) is unrelated to the internal rotation of the CH_3 fragment around the CF_3 as one may be tempted to think. The relation between internal rotation and symmetry numbers is discussed in Section 2.3.5.

2.3.2. Symmetric reactions

An example of a symmetric reaction is $\mathrm{H} + \mathrm{H}_2 \longrightarrow \mathrm{H}_2 + \mathrm{H}$. The rotational symmetry numbers for H, H_2 , and the linear transition state are one, two, and two, respectively. Therefore, the symmetry number for the reaction is naively expected to be one. However, it is important to be more precise, and ask precisely what observable one is calculating. In fact, the reaction of H with H_2 is not observable as a macroscopic reaction rate. It could, however, be observed by measuring the rate of interconversion of ortho and para hydrogen, and this topic is discussed elsewhere [38]. Similar reactions interconverting the two modifications [33, 39] of other molecules, e.g., N_2, may also be imagined, although these are not as well known. The $\mathrm{H} + \mathrm{H}_2$ reaction provides one of the rare examples of a case where calculations of the effect of nuclear identical-particle symmetry have gone beyond the symmetry-number approximation. In particular, Schatz and Kuppermann [40] used the technique of postantisymmetrization [41] to calculate nuclear-motion wave functions with the correct permutation symmetry for $\mathrm{H}+\mathrm{H}_2$ with zero total angular momentum. Para-to-ortho rate constants calculated from distinguishable-atom rate constants with appropriate classical symmetry numbers differ from those calculated with a proper treatment of permutation symmetry by 0.8, 1.6, 3, 5, and 26% at 400, 300, 250, 200, and 100 K, respectively. Just as nonclassical symmetry effects on rotational partition functions are much smaller for all other molecules than for H_2, nonclassical symmetry effects on reaction rates are expected to be much smaller for other reactions than for $\mathrm{H} + \mathrm{H}_2$. In general, any symmetric reaction with just one transition state between reactants and products is unobservable as a macroscopic rate phenomenon, unless one resolves quantum states as in the *ortho-para* conversion of hydrogen.

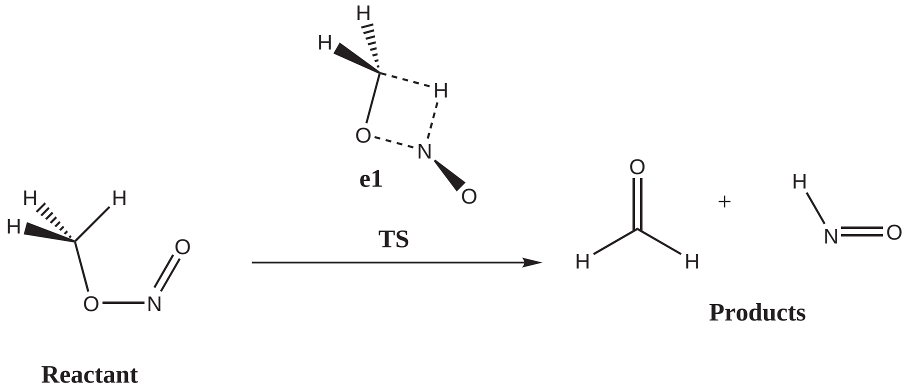

Structure 2.6

2.3.3. Chiral species

In the previous examples none of the species are chiral, so the symmetry number for any nonsymmetric reaction is given by Eq. (2.4). In this section we consider chiral species. We note that some of the species in this section are not considered optically active in the traditional sense because they are short-lived or have low barriers of conversion between the two mirror images. Because of this, we will avoid the words *optically active* and *enantiomer*, and instead use the word chiral, which describes any three-dimensional object that cannot be rotated to coincide with its mirror image. An illustrative example of chiral transition states is the elimination reaction of HNO in the cis-methylnitrite molecule (showed in Structure 2.6). This elimination reaction has a reactant with C_s symmetry in the equilibrium configuration and a four-center transition state with C_1 symmetry as indicated in Structure 2.6.

In the transition state of Structure 2.6 the oxygen atom is not coplanar with the C, O, H, and N atoms. There is another transition state **e1***, with the same energy as **e1**, for which the oxygen is on the opposite side the plane as indicated in Structure 2.7.

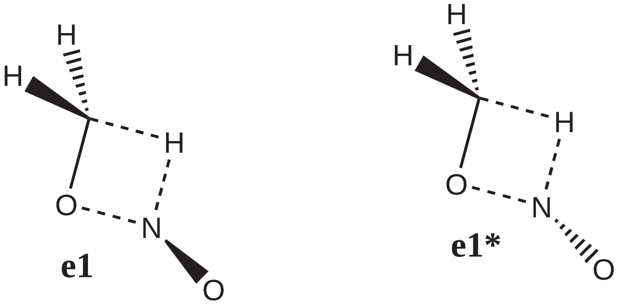

Structure 2.7

The structures **e1** and **e1*** are chiral, i.e., they are mirror images that cannot be superimposed by rotation. (It should be noticed that there is no possibility of having chirality when the molecule has one or more planes of symmetry.) There are two separate elementary reactions leading to products from a common reactant, and therefore the total forward rate constant k_f is

$$k_\mathrm{f} = k_{\mathbf{e1}} + k_{\mathbf{e1}^*} \tag{2.8}$$

where $k_{\mathbf{e1}}$ and $k_{\mathbf{e1}^*}$ are the rate constants for the passage to products from the **e1** and $\mathbf{e1}^*$ transition state structures, respectively. Both rate constants are equal, so the previous equation can be written as

$$k_\mathrm{f} = 2k_{\mathbf{e1}} \tag{2.9}$$

Another example of a chiral transition state is the hydrogen abstraction reaction from methanol by a hydrogen atom. The rotational symmetry number for reactants is one. The transition state has C_1 symmetry and therefore the symmetry number for the elementary

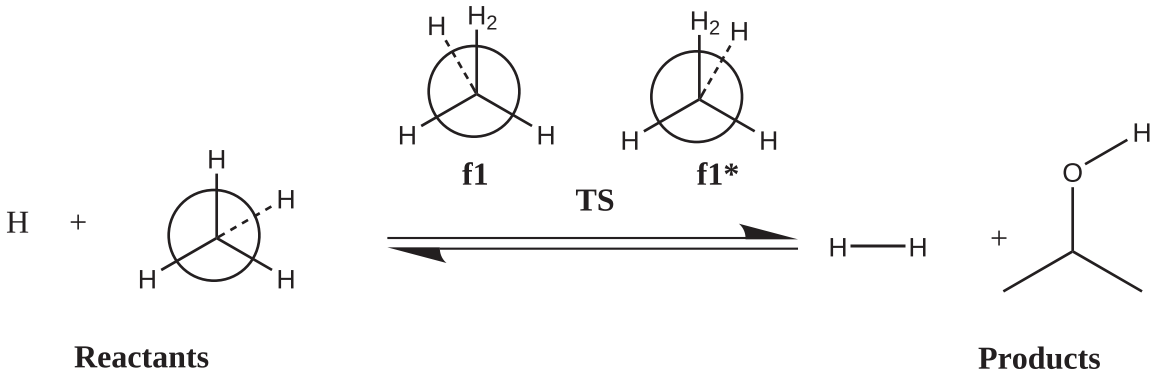

Structure 2.8

reaction is one. However, Chuang *et al.* [42] have calculated two possible transition states, **f1** and **f1***, which are chiral (see Structure 2.8). As in the previous example, there are two elementary reactions with rate constants that are equal, so the total forward rate constant is given by

$$k_{\mathrm{f}} = 2k_{\mathbf{f1}} \tag{2.10}$$

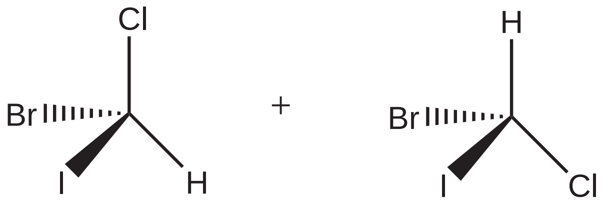

g1 **g1***

Structure 2.9

An example in which the reactants are chiral is the hydrogen abstraction by a hydrogen atom from the C(I)(Br)(Cl)H molecule. This molecule would be present as a racemic mixture of the two possible chiral isomers, as shown in Structure 2.9.

The hydrogen abstraction reaction from **g1** and **g1*** would lead to the two chiral transition states shown in Structure 2.10.

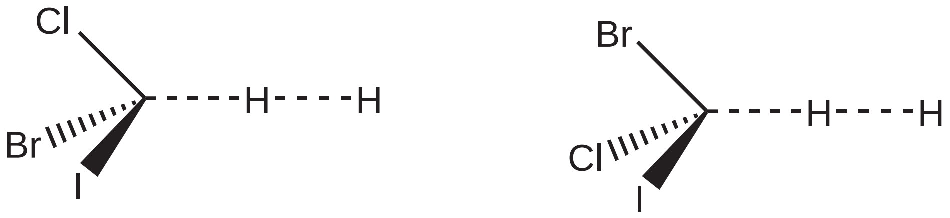

TS1 **TS1***

Structure 2.10

TS1 is only accessible from **g1**, and **TS1*** is only accessible from **g1***. There are two distinct reactions with unique reactants and transition states that lead to the same products.

The rate constant for passage through **TS1**, $k_{\mathbf{TS1}}(T)$ would be

$$k_{\mathbf{TS1}}(T) = \frac{k_{\mathrm{B}}T}{h} \frac{1}{\Phi_{\mathrm{rel}}^{\mathrm{H,CHClBrI}}(T)} \frac{Q_{\mathbf{TS1}}(T)}{Q_{\mathbf{g1}}(T)} \exp\left[-V^{\ddagger}/k_{\mathrm{B}}T\right] \tag{2.11}$$

where $\Phi_{\mathrm{rel}}^{\mathrm{H,CHClBrI}}(T)$ is the relative translational energy per unit of volume and $Q_{\mathbf{g1}}(T)$ is the partition function of **g1** excluding translation. In the same way, the rate constant for passage through **TS1***, which can be reached only from **g1***, would be

$$k_{\mathbf{TS1}^*}(T) = \frac{k_{\mathrm{B}}T}{h} \frac{1}{\Phi_{\mathrm{rel}}^{\mathrm{H,CHClBrI}}(T)} \frac{Q_{\mathbf{TS1}^*}(T)}{Q_{\mathbf{g1}^*}(T)} \exp\left[-V^{\ddagger}/k_{\mathrm{B}}T\right] \tag{2.12}$$

When using the rate constant to calculate a reaction rate, it is important to recognize what the rate constant refers to. In this example, the overall reaction rate for the formation of products is given by $k_{\mathbf{TS1}}(T)[\mathbf{g1}][\mathrm{H}] + k_{\mathbf{TS1^*}}(T)[\mathbf{g1}^*][\mathrm{H}]$, where $[\mathbf{g1}]$, $[\mathbf{g1}^*]$ and [H] are the concentrations of **g1**, **g1*** and H, respectively. Therefore, after one recognizes the unique elementary reactions, the symmetry number is calculated normally using Eq. (2.4).

Another example involving a chiral transition state is the hydrogen abstraction reaction from propane by a hydrogen atom. Propane in the equilibrium configuration has C_{2v} symmetry and has no optical isomers, so the rotational symmetry is two. In Structure 2.11, the non-equivalent hydrogen atoms have been labelled as $\mathrm{H_a}$, $\mathrm{H_b}$ and $\mathrm{H_c}$.

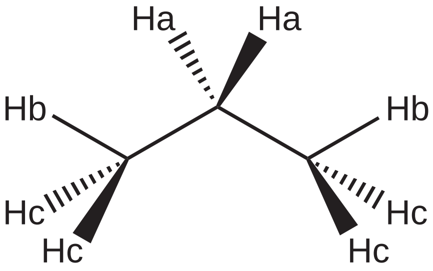

Structure 2.11

There are eight transition state configurations for the formation of H_2 , which are depicted in Structure 2.12. The **h1** and **h2** transition state configurations correspond to the abstraction of a central hydrogen atom. These configurations are superimposable, with the symmetry number for this single transition state equal to one because the symmetry is C_s. The same reasoning can be applied to **h3** and **h4**. For the last four transition state configurations there is no point group symmetry, but **h5** and **h8** are superimposable, and so are **h6** and **h7**. However, **h5** and **h6** cannot be superimposed and therefore are chiral. The thermal rate constant for hydrogen abstraction is the sum of the contributions of all the transition states depicted in Structure 2.13:

$$\begin{aligned} k_{\mathrm{f}}(T) =& \frac{\sigma_{\mathrm{rot,R}} n_{\mathrm{TS}}(\mathbf{h1})}{\sigma_{\mathrm{rot,TS}}(\mathbf{h1}) n_{\mathrm{R}}} k_{\mathbf{h1}}(T) + \frac{\sigma_{\mathrm{rot,R}} n_{\mathrm{TS}}(\mathbf{h3})}{\sigma_{\mathrm{rot,TS}}(\mathbf{h3}) n_{\mathrm{R}}} k_{\mathbf{h3}}(T) + \frac{\sigma_{\mathrm{rot,R}} n_{\mathrm{TS}}(\mathbf{h5})}{\sigma_{\mathrm{rot,TS}}(\mathbf{h5}) n_{\mathrm{R}}} k_{\mathbf{h5}}(T) \\ =& \frac{2\times 1}{1\times 1} k_{\mathbf{h1}}(T) + \frac{2\times 1}{1\times 1} k_{\mathbf{h3}}(T) + \frac{2\times 2}{1\times 1} k_{\mathbf{h5}}(T) \\ =& 2k_{\mathbf{h1}}(T) + 2k_{\mathbf{h3}}(T) + 4k_{\mathbf{h5}}(T) \end{aligned} \tag{2.13}$$

where n_{R} is two for chiral reactants and the unity otherwise, $n_{\mathrm{TS}}(\mathbf{h5})$ is the number of distinct transition state configurations that can be represented by **h5**, which is two because **h5** and **h6** have identical thermodynamic properties, and both $n_{\mathrm{TS}}(h1)$ and $n_{\mathrm{TS}}(h3)$ are equal to one because they do not correspond to a chiral transition state. It should be noted that because the transitions states **h5** and **h6** are non-superimposable, they are part of different elementary reactions. Doubling the rate constant from two to four for the reaction corresponding to **h5** is simply a shortcut that is utilized by recognizing that mirror images have properties that are equivalent. Calculating each of the four elementary reactions separately would yield the same result achieved in Eq. (2.13).

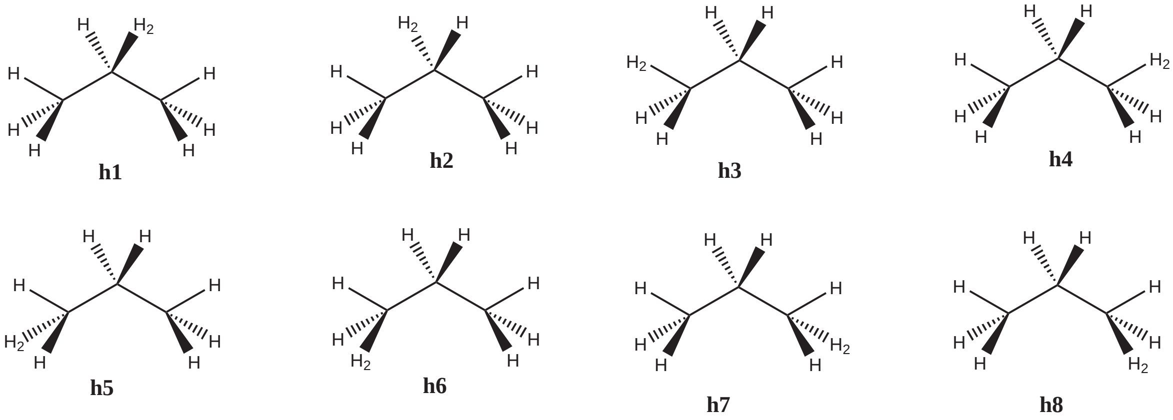

h1 **h2** **h3** **h4**

h5 **h6** **h7** **h8**

Structure 2.12

The hydrogen abstraction reaction of OH with propane [43] is calculated in the same manner. For this reaction, the non-degenerate transition states are in Structure 2.14, and as a first approximation the rate constant is calculated using Eq. (2.13) Structure 2.14. However, abstracting with an OH group rather than an H atom presents a new difficulty because of the ability of the OH group to rotate. To appropriately model this reaction, each of the transition states needs to be modelled by treating the OH group as a hindered rotor. This is discussed in Section 2.3.5.

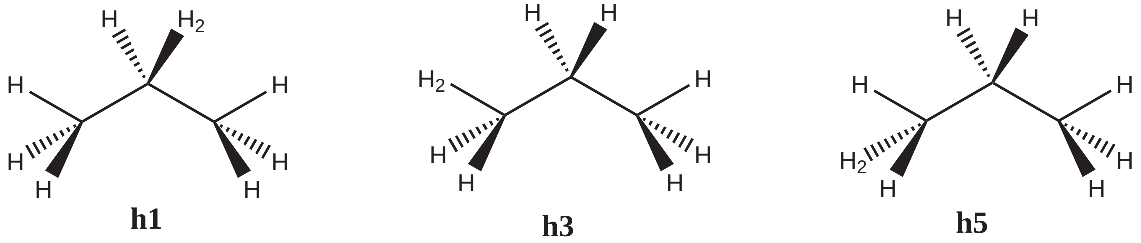

h1 **h3** **h5**

Structure 2.13

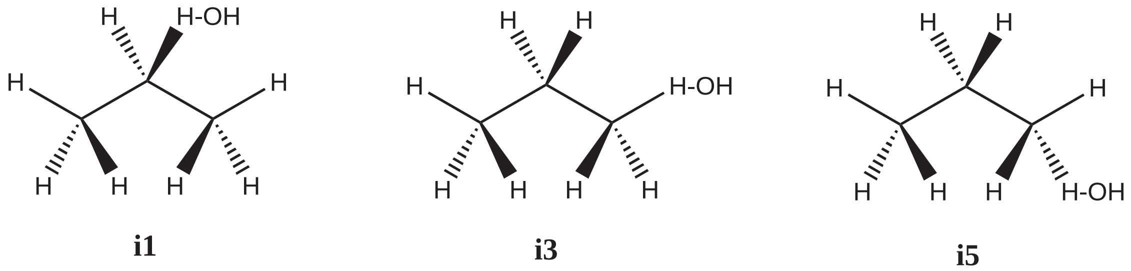

i1 **i3** **i5**

Structure 2.14

2.3.4. Reactions with many conformers

This section demonstrates how to calculate rate constants for reactions in which the reactants have several conformations. An example is considered where the reactants may be present in two energetically different conformations **j1** and **j2** of which only **j2** can lead to products. A model potential for this type of reaction is depicted in Figure 2.1, in which all energies are relative to the most stable conformer of reactants. The reactant conformations are all stable structures that cannot be superimposed by rotation and therefore cannot be taken into account in the rotation symmetry number.

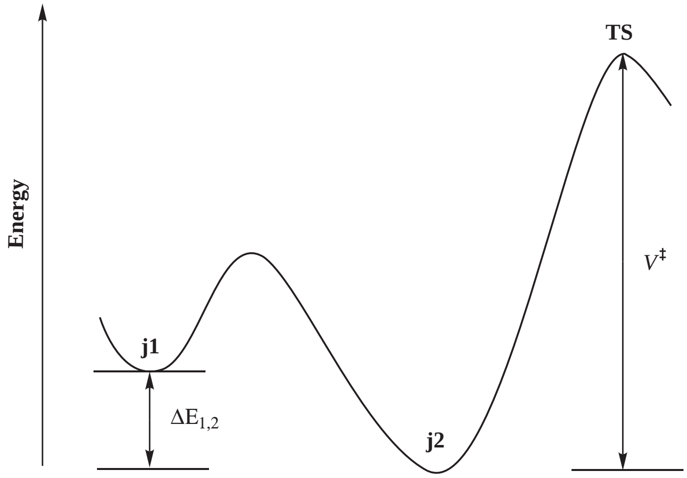

Figure 2.1: Schematic illustration showing a model potential for a reaction with a reactant with two different conformations **j1** and **j2**, of which only **j2** can lead to products through the transition state TS (see text).

The expression for the forward rate constant would be similar to Eq. (2.13), with the difference that there are multiple reactants instead of multiple transition states, and they are not necessarily chiral species with the same energy, i.e.

$$k_{\mathrm{f}}(T) = \frac{k_{\mathrm{B}}T}{h}\frac{Q_{\mathbf{TS}}(T)/\sigma_{\mathrm{rot},\mathbf{TS}}}{\Phi_{\mathbf{j1}}(T)e^{-\Delta E_{1,2}/k_{\mathrm{B}}T}/\sigma_{\mathrm{rot},\mathbf{j1}} + \Phi_{\mathbf{j2}}(T)/\sigma_{\mathrm{rot},\mathbf{j2}}} \times \exp\left[-V^{\ddagger}/k_{\mathrm{B}}T\right] \tag{2.14}$$

where $\sigma_{\mathrm{rot},\mathbf{j1}}$, $\sigma_{\mathrm{rot},\mathbf{j2}}$ and $\sigma_{\mathrm{rot},\mathbf{TS}}$ are the rotation symmetry numbers of **j1**, **j2**, and the transition state, respectively, $\Delta E_{1,2}$ is the energy difference between **j1** and **j2**, i.e., $\Delta E_{1,2} = E(\mathbf{j1}) - E(\mathbf{j2})$ and $V^{\ddagger}$ is the barrier height. For the specific case that **j1** and **j2** are nonsuperimposable mirror images of each other, $\sigma_{\mathrm{rot},\mathbf{j1}} = \sigma_{\mathrm{rot},\mathbf{j2}}$, $\Delta E_{1,2} = 0$, $\Phi_{\mathbf{j1}}(T) = \Phi_{\mathbf{j2}}(T)$ and therefore

$$k_{\mathrm{f}}(T) = \sigma\frac{k_{\mathrm{B}}T}{h}\frac{Q_{\mathbf{TS}}(T)}{\Phi_{\mathbf{j1}}(T)}\exp\left[-V^{\ddagger}/k_{\mathrm{B}}T\right] \tag{2.15}$$

where σ is given by Eq. (2.4), but including the factor of two in the denominator due to the chirality of reactants, i.e.,

$$\sigma = \frac{\sigma_{\mathrm{rot},\mathbf{j1}}}{2\sigma_{\mathrm{rot},\mathbf{TS}}} \tag{2.16}$$

For a general reaction with a set of $\{\mathrm{R_1 ... R_i ... R_N}\}$ conformers of reactants that can lead to a set of $\{\mathrm{T_1 ... T_j ... T_M}\}$ transition states, which lead to products, the forward rate constant is given by

$$k_{\mathrm{f}}(T) = \frac{k_{\mathrm{B}}T}{h} \frac{\sum_{j=1}^{M} \frac{Q_{\mathrm{T_j}}(T) e^{-\Delta E_{\mathrm{T_j}}/k_{\mathrm{B}}T}}{\sigma_{\mathrm{rot,T_j}}}}{\sum_{i=1}^{N} \frac{\Phi_{\mathrm{R}_i}(T) e^{-\Delta E_{\mathrm{R}_i}/k_{\mathrm{B}}T}}{\sigma_{\mathrm{rot,R}_i}}} \exp\left[-V^{\ddagger}/k_{\mathrm{B}}T\right] \tag{2.17}$$

where $\sigma_{\mathrm{rot,R_i}}$, $\sigma_{\mathrm{rot,T_j}}$, $\Phi_{\mathrm{rot,R_i}}(T)$ and $Q_{\mathrm{T_j}}(T)$ are the rotational symmetry numbers and partition functions of conformations $\mathrm{R_i}$ and $\mathrm{T_j}$, respectively. The value of $\Delta E_{\mathrm{R_i}}$ is a positive energy calculated as the difference between the energy of conformation R_i and the energy of the most stable conformation of reactants. In the same manner, $\Delta E_{\mathrm{T_j}}$ is the energy difference between the energy of transition state $\mathrm{T_j}$ and the energy of the most stable transition state that leads to products. The value of $V^{\ddagger}$ is calculated as the difference between the energy of the most stable transition state conformation and the energy of the most stable reactant conformation. It should be noticed that the sum also runs over the different chiral isomers and that all the barriers for interconversions of reactants should be smaller than $V^{\ddagger}$. The above expression is valid when the potentials in the vicinity of the stationary points are well described by the harmonic oscillator approximation. Complications may arise from low barriers of conversion between conformations, which may lead to nearly free internal rotations and the breakdown of the harmonic oscillator approximation, which are discussed in Section 2.3.5.

2.3.5. Symmetry numbers and internal rotation

In this section the implications of internal rotation are considered. It should be noticed that rotational symmetry numbers are based on the rotational symmetry of the molecule, i.e., they are based on the rotation of the molecule as a whole, whereas internal rotation involves the rotation of a given part of the molecule relative to the rest of the molecule, and that it is actually a vibrational mode.

Torsion approximations can properly account for indistinguishable minima corresponding to a nearly free internal rotation. This is demonstrated with the example of the hydrogen abstraction reaction from methane by the fluorine atom. For this reaction, some electronic structure calculations predict a transition state with C_{3v} symmetry (**TS1**), such as the one shown in Structure 2.15.

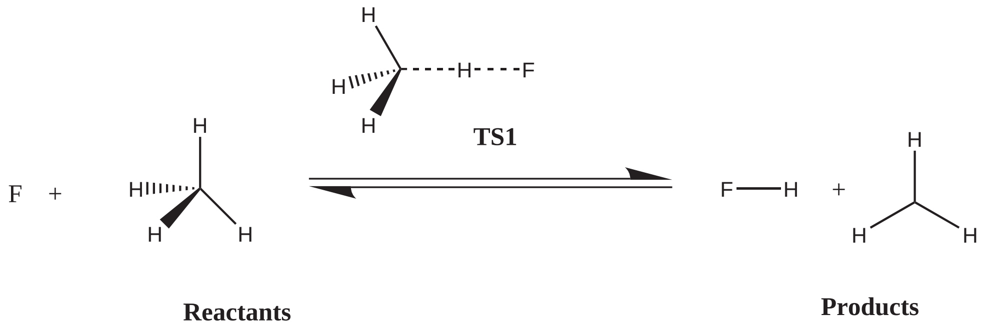

Structure 2.15

Therefore, the symmetry number for this reaction σ_{f1} is:

$$\sigma_{\mathrm{f1}} = \frac{\sigma \mathrm{rot}, \mathrm{R}}{\sigma_{\mathrm{rot},\mathbf{TS1}}} = \frac{\sigma_{\mathrm{F}} \times \sigma_{\mathrm{rot},\mathrm{CH}_4(T_d)}}{\sigma_{\mathrm{rot},\mathbf{TS1}(C_{3v})}} = \frac{1 \times 12}{3} = 4 \tag{2.18}$$

Other electronic structure calculations predict a bent transition state with C_s symmetry (**TS2**) as depicted below

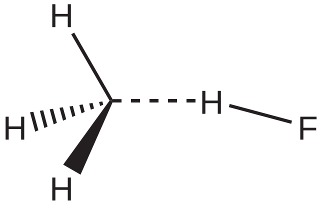

TS2

In this case the symmetry number σ_{f2} is given by

$$\sigma_{\mathrm{f2}} = \frac{\sigma_{\mathrm{rot},\mathrm{R}}}{\sigma_{\mathrm{rot},\mathbf{TS2}}} = \frac{\sigma_{\mathrm{F}} \times \sigma_{\mathrm{rot},\mathrm{CH}_4(\mathrm{T_d})}}{\sigma_{\mathrm{rot},\mathbf{TS2}(C_s)}} = \frac{1 \times 12}{1} = 12 \tag{2.19}$$

The symmetry numbers are correct in both cases. The reaction through **TS1** has C_{3v} symmetry and the reaction through **TS2** has C_s symmetry, which causes the symmetry number for the reaction through **TS2** to be three times larger. However, when the internal rotation for **TS2** is treated correctly, the difference in the partition functions at the transition state will largely reconcile the symmetry number difference. There are three indistinguishable transition state configurations of the type **TS2** for each reactive hydrogen, as shown in Structure 2.16. The three transition state configurations can be obtained from one another through a torsional motion about the C–H bond. This internal rotation leads to a potential with three equivalent minima, which coincide with the above configurations, and to three equivalent maxima, which correspond to the eclipsed configurations. The crucial aspects of the potential of internal rotation are the magnitude of both the vibrational frequency of the torsion, ω_{tor}, and the barrier height between the minima, W_{tor}.

In the regime of a high torsional frequency and low temperature, i.e., when $k_{\mathrm{B}}T \ll \hbar\omega_{\mathrm{tor}}$, the potential is well represented by an inverted parabola and the harmonic oscillator (HO) partition function is a good approximation for this torsional mode. Assuming separable HO partition functions for all the normal modes, the total partition function for **TS2** is given by:

$$Q_{\mathrm{vib,TS2}}(T) = q^{\mathrm{HO}}_{\mathrm{tor},\mathbf{TS2}}(T) \prod_{m=1}^{3N-8} q^{\mathrm{HO}}_{m,\mathrm{vib},\mathbf{TS2}}(T) = \prod_{m=1}^{3N-7} q^{\mathrm{HO}}_{m,\mathrm{vib},\mathbf{TS2}}(T) \tag{2.20}$$

where $q^{\mathrm{HO}}_{\mathrm{tor},\mathbf{TS2}}(T)$ and $q_{m,3N-7,\mathbf{TS2}}(T)$ are two names for the HO vibrational partition function of the torsional mode with frequency ω_{tor}, and $q^{\mathrm{HO}}_{m,\mathrm{vib},\mathbf{TS2}}(T)$ for $m = 1, ..., 3N-8$ are the HO vibrational partition functions of the other modes. In this case the thermal rate constant evaluated by the TST expression is given by:

$$k_{\mathrm{TST}}(T) = 12 \frac{k_{\mathrm{B}}T}{h} \frac{Q^{*}_{\mathrm{rot},\mathbf{TS2}}(T) Q_{\mathrm{vib},\mathbf{TS2}}(T)}{\Phi_{\mathrm{R}}(T)} \exp\left[-V^{\ddagger}/k_{\mathrm{B}}T\right] \tag{2.21}$$

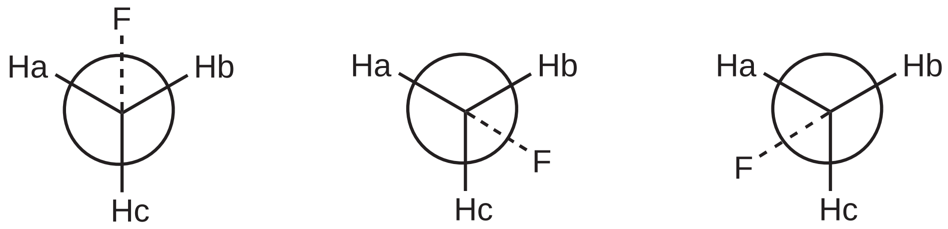

Structure 2.16

where $Q^{*}_{\mathrm{rot},\mathbf{TS2}}(T)$ is the **TS2** rotational partition function for distinguishable particles given by Eq. (2.2b) and $Q_{\mathrm{vib},\mathbf{TS2}}(T)$ is given by Eq. (2.20).

However, when $k_{\mathrm{B}}T \gg W_{\mathrm{tor}}$, the rotation around the C–H bond would be nearly free, therefore the classical free rotor (FR) partition function is a good approximation. The FR partition function is given by:

$$q^{\mathrm{FR}}(T) = \frac{(2\pi I k_{\mathrm{B}} T)^{1/2}}{\hbar \sigma_{\mathrm{int}}} = \frac{1}{\sigma_{\mathrm{int}}} q^{\mathrm{FR}*}(T) \tag{2.22}$$

where I is the effective moment of inertia for internal rotation, $q^{\mathrm{FR}*}(T)$ is the FR partition function without the symmetry number for internal rotation, and σ_{int} is the symmetry number for internal rotation. For the above reaction, σ_{int} is three because the three minima depicted in Structure 2.16 are quantum mechanically indistinguishable. In this case the torsional mode is treated as a free rotation instead of a harmonic vibration, and therefore the TST rate constant is given by:

$$\begin{aligned} k_{\mathrm{TST}}(T) =& 12 \frac{k_{\mathrm{B}}T}{h} \frac{Q^{*}_{\mathrm{rot},\mathrm{TS2}}(T) \frac{q^{\mathrm{FR}*}_{\mathrm{tor},\mathbf{TS2}}(T)}{3} \prod_{m=1}^{3N-8} q^{\mathrm{HO}}_{m,\mathrm{vib},\mathbf{TS2}}(T)}{\Phi_{\mathrm{R}}(T)} \times \exp\left[V^{\ddagger}/k_{\mathrm{B}}T\right] \\ =& 4 \frac{k_{\mathrm{B}}T}{h} \frac{Q^{*}_{\mathrm{rot},\mathbf{TS2}}(T) q^{\mathrm{FR}*}_{\mathrm{tor},\mathbf{TS2}}(T) \prod_{m=1}^{3N-8} q^{\mathrm{HO}}_{m,\mathrm{vib},\mathbf{TS2}}(T)}{\Phi_{\mathrm{R}}(T)} \times \exp\left[V^{\ddagger}/k_{\mathrm{B}}T\right] \end{aligned} \tag{2.23}$$

where the symmetry number of rotation is partially cancelled out by the internal rotation symmetry number. This result indicates that a free rotation for the torsional mode is similar to that for which the transition state is of type **TS1**, since in that case:

$$k_{\mathrm{TST}}(T) = 4 \frac{k_{\mathrm{B}}T}{h} \frac{Q^{*}_{\mathrm{rot},\mathbf{TS1}}(T) q^{\mathrm{HO}}_{m,3N-7,\mathbf{TS1}}(T) \prod_{m=1}^{3N-8} q^{\mathrm{HO}}_{m,vib,\mathbf{TS1}}(T)}{\Phi_{\mathrm{R}}(T)} \times \exp\left[-V^{\ddagger}/k_{\mathrm{B}}T\right] \tag{2.24}$$

The internal rotation for **TS2** is very nearly a free rotation, therefore the factor of three that was lost from the rotational partition function when the C_{3v} symmetry of **TS1** was broken reappears in the vibrational partition function from the internal rotation. However, the rate constants for **TS1** and **TS2** will still be different, as they should be because they are different structures. Most importantly, $q^{\mathrm{FR}*}_{\mathrm{tor},\mathrm{TS2}}(T)$ may not be similar to $q^{\mathrm{HO}}_{m,3N-7,\mathrm{TS1}}(T)$; additionally the other vibrational and rotational partition functions will likely be slightly different. While the factor of three has been recovered, it depends on how the change in geometry has influenced the partition functions as to whether or not the rate constant for **TS1** will be similar to the rate constant for **TS2**.

It should be noticed that Eq. (2.21) and Eq. (2.23) are extreme cases. An important intermediate regime is when $\hbar\omega_{\mathrm{tor}} \ll k_{\mathrm{B}}T \ll W_{\mathrm{tor}}$. The partition function for this intermediate (I) case is given by:

$$Q^{\mathrm{I}}(T) = \frac{k_{\mathrm{B}}T}{\hbar\omega_{\mathrm{tor}}} \tag{2.25}$$

For a reaction in which internal rotations may play a role, it would be desirable to have an expression for the partition function that is accurate for the two extreme cases of FR and HO and displays smooth behaviour for intermediate cases. A function with these characteristics has been given elsewhere [44] and has the form:

$$Q(T) = Q^{\mathrm{HO}}(T)\tanh\left(Q^{\mathrm{FR}}(T)/Q^{\mathrm{I}}(T)\right) \tag{2.26}$$

where $Q^{\mathrm{HO}}(T)$, $Q^{\mathrm{FR}}(T)$ and $Q^{\mathrm{I}}(T)$ are the partition function for the HO, FR and intermediate case of Eq. (2.25), respectively. The example of this section deals with internal rotations in the transition state but the same reasoning can be applied to internal rotations in the reactants or in both reactants and the transition state.

The $H + CH_3OH \longrightarrow H_2 + CH_2OH$ abstraction reaction [42] is a case where an internal rotation approximation is able to account for multiple configurations. If two of the three hydrogens of the methyl group were deuterated, the rate constant for hydrogen abstraction is expected to be approximately three times smaller than that involving the undeuterated methanol because there are one third as many reactive atoms. The rate constant of interest is for the $H + HCD_2OH \longrightarrow H_2 + CD_2OH$ process. The molecule HCD_2OH has the three conformers depicted in Structure 2.17, where **k1** and **k1*** are chiral.

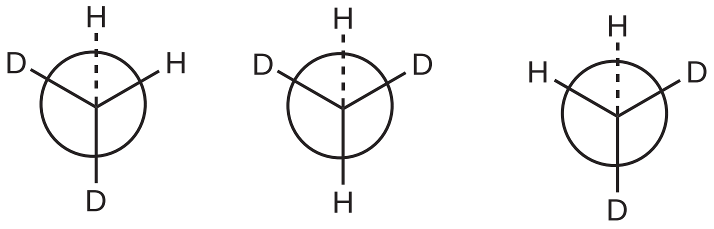

k1 **k2** **k1***

Structure 2.17

Structure 2.18 depicts the two lowest-energy transition states starting from the above reactants

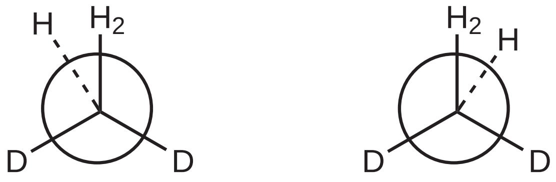

Tk1 **Tk1***

Structure 2.18

For this case Eq. (2.17) leads to the following expression:

$$\begin{aligned}k_{\mathrm{TST}}(T) =& \frac{k_{\mathrm{B}}T}{h}\frac{1}{\Phi_{\mathrm{rel}}^{\mathrm{H,HCD_2OH}}(T)}\exp\left[-V^{\ddagger}/k_{\mathrm{B}}T\right] \\ & \frac{Q^{*}_{\mathrm{rot},\mathbf{Tk1}}(T)Q_{\mathrm{vib},\mathbf{Tk1}}(T)+Q^{*}_{\mathrm{rot},\mathbf{Tk1^*}}(T)Q_{\mathrm{vib},\mathbf{Tk1^*}}(T)}{Q^{*}_{\mathrm{rot},\mathbf{k1}}(T)Q_{\mathrm{vib},\mathbf{k1}}(T)+Q^{*}_{\mathrm{rot},\mathbf{k2}}(T)Q_{\mathrm{vib},\mathbf{k2}}(T)+Q^{*}_{\mathrm{rot},\mathbf{k1^*}}(T)Q_{\mathbf{vib},\mathbf{k1^*}}(T)} \\ =& \frac{k_{\mathrm{B}}T}{h}\frac{1}{\Phi_{\mathrm{rel}}^{\mathrm{H,HCD_2OH}}(T)}\frac{2Q^{*}_{\mathrm{rot},\mathbf{Tk1}}(T)Q_{\mathrm{vib},\mathbf{Tk1}}(T)}{2Q^{*}_{\mathrm{rot},\mathbf{k1}}(T)Q_{\mathrm{vib},\mathbf{k1}}(T)+Q^{*}_{\mathrm{rot},\mathbf{k2}}(T)Q_{\mathrm{vib},\mathbf{k2}}(T)}\exp\left[-V^{\ddagger}/k_{\mathrm{B}}T\right]\end{aligned} \tag{2.27}$$

where $\Phi_{\mathrm{rel}}^{\mathrm{H,HCD_2OH}}$ is the relative translational partition function per unit of volume as mentioned in the Introduction. Notice that this rate constant is about one third the rate constant obtained for the undeuterated reaction as it should be. For distinguishable conformers, as is the case here, it may be desirable to use a torsional method that accounts for the multiple wells of the reactant and/or transition state regions instead of using a simple HO approximation. Specifically, the HO approximation for the torsional mode is replaced by the multiconformer HO (MC–HO) treatment: [45]

$$Q_{\mathrm{tor}}^{\mathrm{MC-HO}} = \sum_{j=1}^{P}\frac{e^{-\beta(U_j+\hbar\omega_{\mathrm{tor},j}/2)}}{1-e^{-\beta\hbar\omega_{\mathrm{tor},j}}} \tag{2.28}$$

where P is the number of distinguishable minima, $\omega_{\mathrm{tor,j}}$, is the harmonic frequency at minimum j of the torsional mode, and U_j is the energy of well j of this mode relative to the lowest well of this mode. In this example we have labeled the torsional mode as $3N-7$ in the transition state and $3N-8$ in reactants In the case of the deuterated methanol, all of the wells have the same energy so $U_j = 0$ in all cases, but **k2** does have a frequency for the torsional mode that is different than **k1** and **k1***. In the same manner, the MC–HO method is used as part of the torsional method to calculate the partition function for the transition state. However, because the multiple transition state configurations are now accounted for using the torsional method, the symmetry number for the transition state is no longer equal to two, rather it is equal to one. This MC–HO partition function for the torsion is then used in the equations given above and the TST rate constant is given by Eq. (2.29),

$$\begin{aligned}k_{\mathrm{TST}}(T) =& \frac{k_{\mathrm{B}}T}{h}\frac{1}{\Phi_{\mathrm{rel}}^{\mathrm{H,HCD_2OH}}(T)}\frac{Q^{\mathrm{MC-HO}}_{3N-7,\mathrm{TS}}(T)Q^{*}_{\mathrm{rot},\mathbf{Tk1}}(T)\prod_{m=1}^{3N-8}q_{m,\mathrm{vib},\mathbf{Tk1}}(T)}{Q^{\mathrm{MC-HO}}_{3N-6,\mathrm{R}}(T)Q^{*}_{\mathrm{rot},\mathbf{k1}}(T)\prod_{m=1}^{3N-7}q_{m,\mathrm{vib},\mathbf{k1}}(T)}\exp\left[-V^{\ddagger}/k_{\mathrm{B}}T\right] \\ =& \frac{k_{\mathrm{B}}T}{h}\frac{1}{\Phi_{\mathrm{rel}}^{\mathrm{H,HCD_2OH}}(T)}\frac{\sum_{j=1}^{2}\left(\frac{e^{-\beta\hbar\omega_{3N-7,j}/2}}{1-e^{-\beta\hbar\omega_{3N-7,j}}}\right)\times Q^{*}_{\mathrm{rot},\mathbf{Tk1}}(T)\prod_{m=1}^{3N-8}q_{m,\mathrm{vib},\mathbf{Tk1}}(T)}{\sum_{j=1}^{3}\left(\frac{e^{-\beta\hbar\omega_{3N-6,j}/2}}{1-e^{-\beta\hbar\omega_{3N-6,j}}}\right)\times Q^{*}_{\mathrm{rot},\mathbf{k1}}(T)\prod_{m=1}^{3N-7}q_{m,\mathrm{vib},\mathbf{k1}}(T)}\exp\left[-V^{\ddagger}/k_{\mathrm{B}}T\right] \\ =& \frac{k_{\mathrm{B}}T}{h}\frac{1}{\Phi_{\mathrm{rel}}^{\mathrm{H,HCD_2OH}}(T)}\exp\left[-V^{\ddagger}/k_{\mathrm{B}}T\right]\times \\ & \frac{2\frac{e^{-\beta\hbar\omega_{3N-7,\mathbf{Tk1}}/2}}{1-e^{-\beta\hbar\omega_{3N-7,\mathbf{Tk1}}}}Q^{*}_{\mathrm{rot},\mathbf{Tk1}}(T)\prod_{m=1}^{3N-8}q_{m,\mathrm{vib},\mathbf{Tk1}}(T)}{\left(2\frac{e^{-\beta\hbar\omega_{3N-6,\mathbf{k1}}/2}}{1-e^{-\beta\hbar\omega_{3N-6,\mathbf{k1}}}}+\frac{e^{-\beta\hbar\omega_{3N-6,\mathbf{k2}}/2}}{1-e^{-\beta\hbar\omega_{3N-6,\mathbf{k2}}}}\right)\times Q^{*}_{\mathrm{rot},\mathbf{k1}}(T)\prod_{m=1}^{3N-7}q_{m,\mathrm{vib},\mathbf{k1}}(T)}\end{aligned} \tag{2.29}$$

Because the summation accounts for three degenerate wells, the torsional treatment causes the reactant partition function to be approximately three times as large as the partition function for undeuterated methanol, which causes the rate constant for the deuterated methanol to be about 1/3 as large, just as expected.

While the rate constant for undeuterated methanol was calculated in an earlier example by accounting for the two nonsuperimposable transition states that were low in energy, a better way to account for the entire range of motion is to use a torsional method for the transition state as well. Note that the strategy used for this example is very similar to the strategy discussed in Section 2.3.4. The difference is that in Section 2.3.4, the vibrations were only calculated using the HO approximation, whereas this example uses the MC-HO partition function in conjunction with Eq. (2.26). Therefore, as the motion becomes more like a free internal rotation, the rotational partition function calculated by Eq. (2.26) remains qualitatively correct. If the multiple conformations of the torsion were calculated using the strategy in Section 2.3.4, there would be substantial error in regions where the HO approximation was not valid. The drawback of Eq. (2.29) is that the rotational and vibrational partition functions, with exception of the torsional mode, are considered to be equal for all conformers.

For further details on the treatment of internal rotation, we refer to references [42, 44–46].

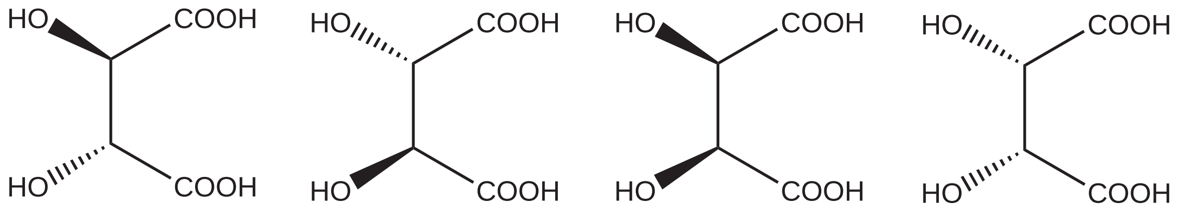

L-tartaric acid D-tartaric acid mesotartaric acid mesotartaric acid

Structure 2.19

2.3.6. An example involving an achiral diasteromer

Tartaric acid is an organic acid that is naturally occurring in the L-(-)-tartaric acid form [47, 48]. Tartaric acid has two carbon stereocenters and which allows it to be synthesized in three distinguishable configurations. There is a set of enantiomers, and there is also a meso complex. These configurations are shown in Structure 2.19.

While L-tartaric acid and D-tartaric acid are distinguishable, the two drawings of mesotartaric acid are superimposable, so there is only a single distinguishable configuration for mesotartaric acid. That is, there are three stereoisomers of tartaric acid; two of them are enantiomers, and the third is an achiral diastereomer.

For a reaction where the acidic proton is abstracted by OH^- to create the conjugate base, we illustrate the transition states (this time explicitly drawing the carboxyl group on the reacting carbon).

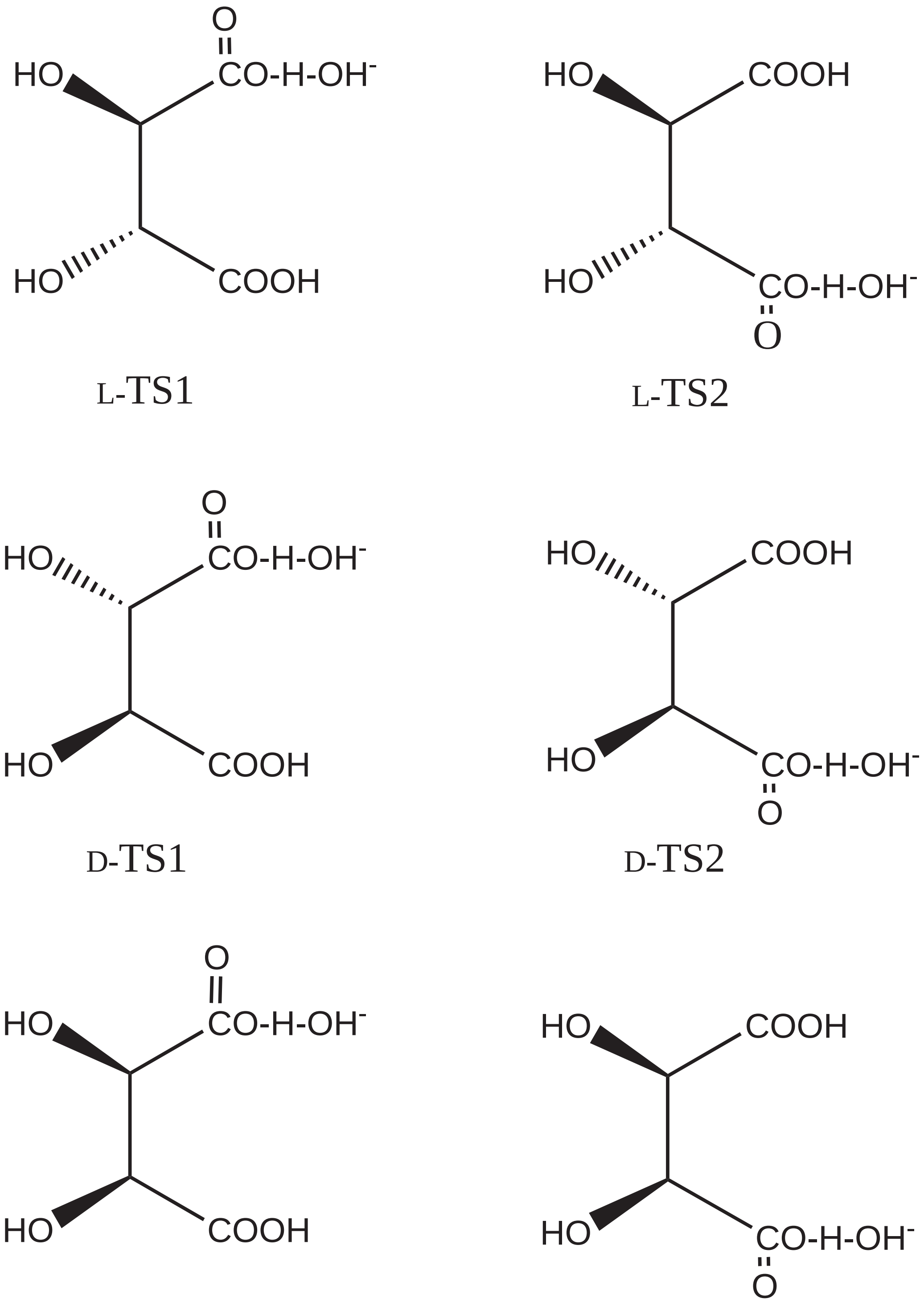

L-TS1 L-TS2

D-TS1 D-TS2

m-TS1 m-TS2

Structure 2.20

The transition states have been labelled according to which reactant they originated from, where L- indicates that it originated from L-tartaric acid, D- indicates that it originated from D-tartaric acid, and m- indicated that is originated from mesotartaric acid. The transition states that originate from the meso reactant are labelled with m-instead of *meso-* because they are not superimposable. L-TS1 and L-TS2 are superimposable by a rotation, so there is only a single indistinguishable transition state for this reaction. This is also true for D-TS1 and D-TS2. For the L- and D-enantiomers, there is a single elementary reaction leading to a single product for each enantiomer, as shown in Structure 2.21.

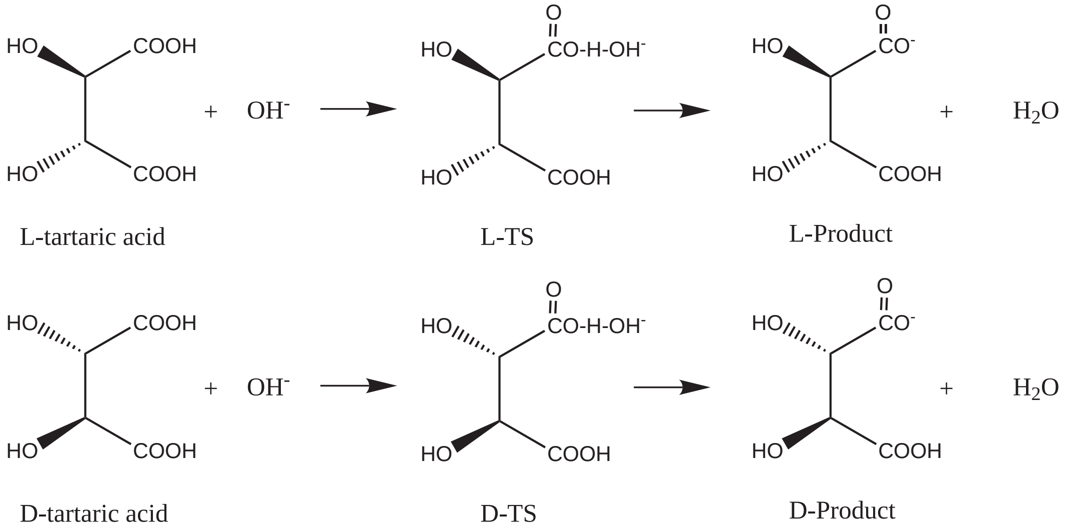

Structure 2.21

The two transition states for mesotartaric acid are not superimposable. There are two elementary reactions with distinct transition states that lead to distinct products. These are shown in Structure 2.22.

Now that the elementary reactions have all been determined, the symmetry numbers for the rate constants can be calculated. For L-tartaric acid, the reactant has C_2 symmetry and the transition state has C_1 symmetry, which yields a symmetry number of 2. Therefore, the forward rate constant for the formation of L-product is

$$k_{\mathrm{L}}(T) = 2\frac{k_{\mathrm{B}}T}{h}\frac{1}{\Phi_{rel}^{\mathrm{L-R,OH^-}}(T)}\frac{Q_{\mathrm{L-TS}}(T)}{Q_{\mathrm{L-R}}(T)Q_{\mathrm{OH^-}}(T)}\exp\left[-V^\ddagger/k_{\mathrm{B}}T\right] \tag{2.30}$$

where $Q_{\mathrm{L-R}}(T)$ is the reactant partition function for L-tartaric acid excluding translation and $\Phi_{\mathrm{rel}}^{\mathrm{L-R,OH^-}}$ is the relative translational partition function per unit volume as stated in Section 2.1. Similarly, the forward rate constant for the formation of D-product is

$$k_{\mathrm{D}}(T) = 2\frac{k_{\mathrm{B}}T}{h}\frac{1}{\Phi_{\mathrm{rel}}^{\mathrm{D-R,OH^-}}(T)}\frac{Q_{\mathrm{D-TS}}(T)}{Q_{\mathrm{D-R}}(T)Q_{\mathrm{OH^-}}(T)}\exp\left[-V^\ddagger/k_{\mathrm{B}}T\right] \tag{2.31}$$

where $Q_{\mathrm{D-R}}(T)$ is the reactant partition function for D-tartaric acid. At this point, we are able to take advantage of mirror images, and we find that $Q_{\mathrm{L-TS}}(T) = Q_{\mathrm{D-TS}}(T)$, $Q_{\mathrm{L-R}}(T) = Q_{\mathrm{D-R}}(T)$, and the barrier heights are the same, therefore $k_{\mathrm{L}}(T) = k_{\mathrm{D}}(T)$.

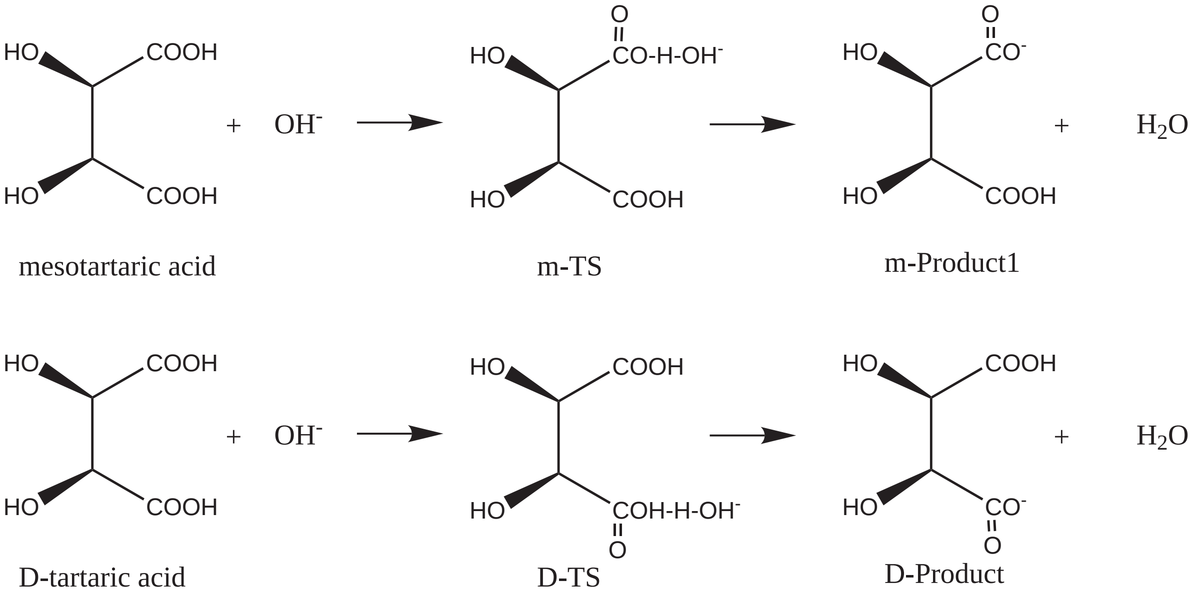

Structure 2.22

For mesotartaric acid, the reactant has C_s symmetry, and both of the transition states have C_1 symmetry, which yield a *rotational* symmetry number of 1. However, the chiral transition states present an additional difficulty, because the single reactant can follow two different elementary reactions, so the symmetry number for the formation of the two products is two. Therefore, each elementary reaction has a symmetry number of one due to the chirality of the transition states [31]. The rate constants for meso-product1 and meso-product2 are

$$k_{\mathrm{m-1}}(T) = \frac{k_{\mathrm{B}}T}{h} \frac{1}{\Phi_{\mathrm{rel}}^{\mathrm{m-R,OH^-}}(T)} \frac{Q_{\mathrm{m-TS1}}(T)}{Q_{\mathrm{m-R}}(T) Q_{\mathrm{OH^-}}(T)} \exp\left[-V^{\ddagger}/k_{\mathrm{B}}T\right] \tag{2.32}$$

$$k_{\mathrm{m-2}}(T) = \frac{k_{\mathrm{B}}T}{h} \frac{1}{\Phi_{\mathrm{rel}}^{\mathrm{m-R,OH^-}}(T)} \frac{Q_{\mathrm{m-TS2}}(T)}{Q_{\mathrm{m-R}}(T) Q_{\mathrm{OH^-}}(T)} \exp\left[-V^{\ddagger}/k_{\mathrm{B}}T\right] \tag{2.33}$$

where $Q_{m-R}(T)$ is the reactant partition function for meso-tartaric acid. Once again, we may take advantage of the mirror images to find that $Q_{\mathrm{m-TS1}}(T) = Q_{\mathrm{m-TS2}}(T)$, and therefore $k_{\mathrm{m-1}}(T) = k_{\mathrm{m-2}}(T)$.

For tartaric acid, there are three possible reactants that can form four possible products. Each product is only accessible from a single reactant. The properties of mirror images can be used to decrease the number of quantities that must be calculated. It is advisable not to employ any additional shortcuts when dealing with a complicated system like this one. We recommend for the rate constants to be used exclusively with their corresponding reactants and products and not to use formulas like Eq. (2.17) in any case where it may be conceptually difficult.

2.4. Summary

The present Chapter shows how to calculate the rotational symmetry numbers for various molecular configurations and how to apply these symmetry numbers to transition state theory. For most reactions, the overall symmetry number is given by the ratio of the reactant and transition state rotational symmetry numbers, as given by Eq. (2.4). For bimolecular reactions where the two reactants are equivalent, the symmetry number is a rotational-translational symmetry number, which gives rise to an additional factor of two.

Section 2.3 contains several examples for calculating the symmetry number for reaction rate constants. Section 2.3.1 gives examples for symmetry numbers that are both intuitive and nonintuitive. Section 2.3.2 illustrates that Eq. (2.4) is technically valid for symmetric reactions, but the number of interest is typically twice as large as predicted by Eq. (2.4) because both the forward and reverse flux contribute equally. Section 2.3.3 illustrates how to account for chiral isomers using the symmetry number. Multiple conformers for reactants and/or transition states are illustrated in Section 2.3.4, and Section 2.3.5 deals with internal rotation, where the treatment used in some previous examples is improved upon. Section 2.3.6 gives an example involving an achiral diasteromer.

Many of the typical problems that arise when using symmetry numbers have been highlighted. Even complicated scenarios are treated systematically by properly calculating rotational symmetry numbers and differentiating between distinguishable and indistinguishable reaction paths.

Chapter 3

Least-action tunneling transmission coefficient for polyatomic reactions

In this Chapter we present a new least-action variational approximation for tunneling in polyatomic reactions based on the procedure developed by Garrett and Truhlar for atom-diatom reactions [J. Chem. Phys. **1983**, *79*, 4931]. The method calculates the semiclassical ground-state tunneling probability at every tunneling energy by minimizing the value of imaginary action integral along a family of paths ranging from the minimum energy path to the straight path. The method is illustrated by applications to two hydrogen-atom abstraction reactions from methane using analytical potential energy surfaces.

3.1. Introduction

Tunneling is a quantum mechanical effect by which a particle can penetrate into classically forbidden regions of coordinate space.[49–51] Less than ten years after the formulation of modern quantum mechanics, Wigner [52] and Bell [53] pointed out the importance of this effect in chemical kinetics. Tunneling is very sensitive to the mass of the particles involved in the tunneling motion and to the shape and height the effective barrier being crossed. Tunneling often competes well with overbarrier processes at low temperatures for processes that involve the transfer of proton or deuteron. It is well established that quantum tunneling effects require a multidimensional treatment and that they are important processes even at room temperature.[54–57] Because the likelihood of tunneling depends on the mass that is being transferred, the analysis of kinetic isotope effects is one of the chief means of getting insight into the reaction mechanisms of many processes of biological and technological importance.[58, 59] Therefore, the treatment of quantum tunneling within a multidimensional framework is very important.

Variational transition state theory with multidimensional tunneling contributions [16, 17] (VTST/MT) has been shown to be capable of accounting for quantum effects on large systems,[60, 61] but the methodology for treating those effects still allows for some improvements. Here we present a new approximation that leads to a more complete treatment of quantum tunneling effects in polyatomic chemical reactions.

In Section 3.2 we present background necessary to understand the new work in the context of VTST/MT. Section 3.3 presents the new LAG4 approximation. Section 3.4 presents the application of the LAG4 method to the $H + CH_4 \longrightarrow H_2 + CH_3$ and $^{15}H + CH_4 \longrightarrow {}^{15}H{-}H + CH_3$ reactions using the Jordan and Gilbert (JG) potential energy surface.[62] Section 3.5 has concluding remarks.

3.2. Background

Variational transition state theory [16, 17, 29, 63–70] is based on transition state theory (TST), also called conventional transition state theory, which was originally formulated by Eyring [26] and Evans and Polanyi [27]. TST calculates the one-way equilibrium flux through the transition state (a surface dividing reactants from products in phase space) and assumes that the transition state is a reaction bottleneck that separates reactants from products such that all trajectories that start in the reactants region and cross the transition state do not recross it before becoming equilibrated as products; this is known as the no-recrosssing assumption. Furthermore, TST assumes that the Born-Oppenheimer approximation is valid and that the reactants are equilibrated canonically (in a fixed-temperature ensemble) or microcanonically (in a fixed-total-energy ensemble).

TST and VTST can be formulated unambiguously in a classical world,[71] and quantum effects on all degrees of freedom except the reaction coordinate can reasonably be included by quantizing their partition functions,[26] as justified to order $\hbar^2$ by Wigner.[52] Quantum effects on the reaction coordinate can be incorporated by the addition of a multiplicative multidimensional factor, called tunneling transmission coefficient,[72–74] but this can only be accomplished consistently in VTST.[75] In fact, VTST/MT incorporates both recrossing (with respect to conventional TST) and quantum tunneling effects, although it needs more information than TST about the potential energy surface of the reaction. TST (without tunneling) needs information only about reactants and the transition state, while VTST/MT needs information at least about the reaction path that joins the transition state with reactants and products and sometimes also about a wider region called the reaction swath which includes additional geometries on the concave side of the reaction path. In the present work, the reaction path is chosen as the minimum energy path (MEP) in isoinertial coordinates,[73, 76] scaled to a reduced mass of μ, and the signed distance along this path is labeled as s. By convention $s = 0$ indicates the location of the transition state, whereas $s < 0$ and $s > 0$ correspond to the reactant and product sides, respectively. The variational method that minimizes the one-way flux from reactants to products through trial dividing surfaces that cross the reaction path at various values of s in a fixed-temperature ensemble is called canonical variational transition state theory or canonical variational theory (CVT).[66, 77] The CVT rate constant for a bimolecular reaction at temperature T is given by

$$k^{\mathrm{CVT}}(T) = \sigma \frac{k_{\mathrm{B}}T}{h} \frac{Q^{\mathrm{GT}}(T, s_*^{\mathrm{CVT}}(T))}{\Phi_{\mathrm{R}}(T)} \exp\left[-V_{\mathrm{MEP}}(s_*^{\mathrm{CVT}}(T))/k_{\mathrm{B}}T\right], \tag{3.1}$$

where σ is the symmetry number,[31, 78] k_{B} and h are the Boltzmann and Planck constants, respectively, and $V_{\mathrm{MEP}}(s_*^{\mathrm{CVT}}(T))$ is the value of the potential on the reaction path at s_*^{CVT}, which is the location along the reaction coordinate of the dividing surface that minimizes the one-way flux rate constant. The quantized reactant partition function per unit volume is $\Phi_{\mathrm{R}}(T)$, and $Q^{\mathrm{GT}}(T, s_*^{\mathrm{CVT}}(T))$ is the quantized generalized transition state partition function at $s_*^{\mathrm{CVT}}(T)$.

In this Chapter we are concerned with quantum effects on the reaction coordinate, which are incorporated by multiplying the CVT rate constant by a transmission coefficient, κ. The resulting rate constant rate constant is given by

$$k^{\mathrm{CVT/SAG}}(T) = \kappa^{\mathrm{CVT/SAG}}(T) k^{\mathrm{CVT}}(T) \tag{3.2}$$

where SAG denotes semiclassical (vibrationally) adiabatic ground-state. Neglecting $\kappa(T)$ is called the quasiclassical approximation.[61] The transmission coefficient, which rigorously is the ratio of the averaged quantum mechanical reaction probabilities to the model underlying TST or VTST without the transmission coefficient, is approximated by the ratio of the averaged SAG and quasiclassical probabilities. The SAG transmission coefficient is evaluated by using an effective potential that (in the first approximation under discussion here) is vibrationally adiabatic with the further approximation [67] that the vibrationally adiabatic potential curves of all the vibrational excited states have the same shape as the ground-state vibrationally adiabatic potential curve, $V_{\mathrm{a}}^{\mathrm{G}}(s)$, so all the tunneling probabilities are evaluated with this potential, which is given in the harmonic approximation by

$$V_{\mathrm{a}}^{\mathrm{G}}(s) = V_{\mathrm{MEP}}(s) + \frac{\hbar}{2} \sum_m \omega_m(s) \tag{3.3}$$

where $\omega_m(s)$ is a frequency of one of the $3N$-7 ($3N$-6 for linear molecules) generalized normal modes at s. In general the harmonic approximation used in the evaluation of the vibrationally adiabatic potential is reasonable for polyatomic systems, the exception being those systems presenting low frequency internal rotations, for which it is important to include anharmonicity on those torsional modes.[79, 80] Because the barrier height, $V_{\mathrm{a}}^{\mathrm{AG}}$, of the ground-state vibrationally adiabatic potential curve may be different from $V_{\mathrm{a}}^{\mathrm{G}}(s_*^{\mathrm{CVT}}(T))$, the CVT/SAG transmission coefficient on the right-hand side of Eq. (3.2) is equal to an intrinsic transmission coefficient $\kappa^{\mathrm{SAG}}(T)$ times the factor $\exp\{\beta[\mathrm{V_a^G}(\mathrm{s_*^{CVT}}(\mathrm{T})) - \mathrm{V_a^{AG}}]\}$ to make the transmission coefficient consistent in spite of the difference in the effective thresholds of the transmission coefficient and of the CVT rate constant. The intrinsic transmission coefficient is given by

$$\kappa^{\mathrm{SAG}}(T) = \frac{\int_0^\infty dE P^{\mathrm{SAG}}(E) \exp(-\beta E)}{\int_{V_{\mathrm{a}}^{\mathrm{AG}}}^\infty dE P^{\mathrm{C}}(E) \exp(-\beta E)}, \tag{3.4}$$

where $P^{\mathrm{C}}(E)$ is the classical probability, which equals zero below $V_{\mathrm{a}}^{\mathrm{AG}}$ and unity otherwise, so the transmission factor can be writen as:

$$\kappa^{\mathrm{SAG}}(T) = \beta \exp(\beta V_{\mathrm{a}}^{\mathrm{AG}}) \int_0^\infty dE P^{\mathrm{SAG}}(E) \exp(-\beta E). \tag{3.5}$$

The semiclassical adiabatic probability of the ground state $P^{\mathrm{SAG}}(E)$ for the whole range of energies is given by

$$P^{\mathrm{SAG}}(E) = \begin{cases} 0, & E < E_0 \\ \{1 + \exp[2\theta(\mathrm{E})]\}^{-1}, & E_0 \leq E \leq V_{\mathrm{a}}^{\mathrm{AG}} \\ 1 - P^{\mathrm{SAG}}(2V_{\mathrm{a}}^{\mathrm{AG}} - E), & V_{\mathrm{a}}^{\mathrm{AG}} \leq E \leq 2V_{\mathrm{a}}^{\mathrm{AG}} - E_0 \\ 1, & 2V_{\mathrm{a}}^{\mathrm{AG}} - E_0 < E \end{cases} \tag{3.6}$$

where E_0 is the lowest energy at which it is possible to have tunneling (this is the energy of the reactant zero-point level when the reaction is written in the exoergic direction) and $\theta(E)$ is the so called action integral, actually the magnitude of the imaginary part of the action integral:

$$\theta(E) = \hbar^{-1} \int_{\tilde{s}_0}^{\tilde{s}_1} ds \{2\mu_{\text{eff}}(s)(V_{\text{a}}^{\text{G}}(s) - E)\}^{1/2} \tag{3.7}$$

where $\mu_{\text{eff}}(s)$ is the effective mass of the tunneling motion, and $\tilde{s}_0$ and $\tilde{s}_1$ are the classical turning points at a given tunneling energy, E, in the reactant and product valleys, respectively. Both turning points have to obey the resonance condition:

$$V_{\text{a}}^{\text{G}}(\tilde{s}_0) = V_{\text{a}}^{\text{G}}(\tilde{s}_1) = E \tag{3.8}$$

The simplest case for the evaluation of the action integral of Eq. (3.7) is when the coupling between the reaction coordinate and the transverse modes is neglected. In that case the effective mass equals that of the isoinertial coordinate system, i.e., $\mu_{\text{eff}}(s) = \mu$. This method is known as the zero-curvature tunneling (ZCT) approximation.[73] The ZCT method is not recommended for general use because it often seriously underestimates the tunneling contribution.[81, 82] Wyatt [83] and Marcus and Coltrin [18, 84] showed that the coupling enters the reaction-path Hamiltonian through the kinetic energy term producing a negative centrifugal effect that shortens the tunneling path by moving it toward the concave side of the reaction path. This is now called corner-cutting tunneling. Marcus and Coltrin derived a corner-cutting approximation to the transmission coefficient for the collinear $\text{H} + \text{H}_2$ reaction (for which the curvature of the MEP in isoinertial coordinates is small) by finding for that case a least-action path, i.e., the tunneling path that minimizes Eq. (3.7), by incorporating the reaction path curvature (the centrifugal effect) into the effective mass. This method was extended to polyatomic systems by making the vibrationally adiabatic approximation for all bound modes of the transition state,[85] by modifying the effective mass to avoid the singularity in the reaction path Hamiltonian due to the breakdown of the natural collision coordinates when the reaction path curvature is large,[19, 86] and by properly including the simultaneous corner cutting in more than one mode of vibration.[87, 88] The resulting method is called the centrifugal-dominant small-curvature semiclassical adiabatic ground-state (CD-SCSAG) approximation or simply the small-curvature tunneling (SCT) approximation.

For systems with large curvature of the isoinertial MEP, such as bimolecular reactions in which the hydrogen atom is transferred between two heavy atoms,[89] tunneling may be dominated by paths that lie very far from the MEP and, therefore, the adiabatic approximation may breakdown. The large-curvature ground-state tunneling (LCT) method [16, 17, 20, 21, 24, 87, 90–92] was designed for such cases. Other straigh-path methods [93–95] have been put forward as well. The latest version of the LCT approximation is called LCG4.[17, 21] At each tunneling energy, LCT includes a set of tunneling paths that are the straight trajectory between the two classical turning points at that energy plus the set of all lower-energy tunneling paths. To evaluate action integrals along these paths requires not only information in the potential valley around the MEP (the regions close to the MEP, which can be treated within the adiabatic approximation), but also information about the broader reaction swath on the concave-side of the MEP; this region is the locus of deep-tunneling paths that are vibrationally nonadiabatic. In the LCT approximation, tunneling into excited vibrational states of the products in the exoergic direction is also included;[24] tunneling into excited states is also included for thermoneutral reactions.[96] The LCG4 approximation is more accurate than the previous LCG3 approximation because it includes a nonquadratic correction in the nonadiabatic region. In general, the evaluation of the LCG4 transmission coefficients is quite demanding from the computational point of view, so two interpolated large curvature tunneling (ILCT) methods, called ILCT1D [22] and ILCT2D,[23] were proposed. The latter evaluates the LCG4 transmission coefficient with an error (with respect to the uninterpolated calculation) smaller than 1%, but it reduces the computer time by more than an order of magnitude.

The SCT and LCT transmission coefficients cover the whole range of reaction-path curvatures, so it seems natural to built a transmission coefficient which, at every tunneling energy, chooses the largest between the SCT and LCT tunneling probabilities, or similarly (essentially equivalently), the smallest between the SCT and LCT imaginary action integrals. This approximation is called microcanonical optimized multidimensional tunneling (μOMT) method.[24] The μOMT tunneling probabilities are, therefore,

$$P^{\mu\mathrm{OMT}}(E) = \max_{E} \left\{ \begin{array}{l} P^{\mathrm{SCT}}(E) \\ P^{\mathrm{LCT}}(E) \end{array} \right. \tag{3.9}$$

where $P^{\mathrm{SCT}}(E)$ and $P^{\mathrm{LCT}}(E)$ are the SCT and LCT probabilities evaluated within the CD-SCSAG and LCG4 approximations, respectively. However, these two approximations are just two particular cases of a more general method in which the tunneling path is variationally optimized by employing a criterion of least imaginary action. This method, which is called least-action ground-state tunneling (LAT) approximation, was developed some years ago for atom-diatom reactions, and it was shown to be superior to the SCT and LCT methods.[25, 97] Other LAT methods using a family of paths similar to that described by Garrett and Truhlar [25] have also been developed for polyatomic reactions, although those methods were only used to compute tunneling splittings. For instance, Taketsugu and Kimihiko [98] used a multidimensional LAT method to obtain the least-action integral at a given tunneling energy. Similarly, Tautermann *et al.* [99–101] obtained the optimal tunneling path to predict ground-state tunneling splittings in symmetric polyatomic systems. So far though the LAT method has not been applied to evaluate thermal rate constants for polyatomic systems. However, it has been extensively applied to atom-diatom reactions,[82] and compared with SCT and LCT approximations. Although all the LCT calculations were performed using the LCG3 approximation, it was concluded that for some cases the μOMT method was as accurate as the LAT method, but on average the latter was superior to the former.

The current μOMT method evaluates the large-curvature probabilities with the LCG4 approximation and it performs well for polyatomic reactions. However, it is interesting to know the effect of full optimization of the tunneling paths in a multidimensional framework in polyatomic reactions even when full optimization may be more expensive computationally than the current methods. In this work we present a new version, which adds the following features to the previous LAT method: (i) it is now developed for polyatomic reactions, and (ii) it uses the same criteria for the specification of the adiabatic and nonadiabatic regions as the LCG4 method. Therefore, we label this version of the least-action tunneling method as LAG4.

3.3. Method

LAG4, like LCG3 and LCG4, is always applied to a reaction in the exoergic or thermoneutral direction with the reactant in its ground vibrational state. The tunneling process may end in the product ground state or in an excited diabatic vibrational mode of the product. In general one sums over the probabilities of producing each final state, but in many cases, one needs to consider only ground-state-to-ground-state tunneling, and this Section will start with the ground-state-to-ground-state process.

The LAG4 approximation involves the minimization of the imaginary action integrals along a given set of paths which are between the MEP and the straight path (which is the reference path for all the LCT methods, including the LCG4 approximation). At a given tunneling energy the end points of any particular tunneling path are given by $\tilde{s}_0$ and $\tilde{s}_1$ with the resonance condition given by Eq. (3.8). The mass-scaled Cartesian geometries of these two classical turning points that are located on the MEP are $\mathbf{x}(\tilde{s}_0)$ and $\mathbf{x}(\tilde{s}_1)$, respectively. The paths to initiate the search for the least-action are built as a function of a single parameter α, such that $\alpha = 0$ yields the MEP and $\alpha = 1$ yields the straight path. Therefore $\alpha = 0$ and $\alpha = 1$ correspond to the ZCT and LCT transmission coefficients, respectively. We introduce a progress variable along the path, called $\xi(\alpha)$, which is in the interval $0 \leq \xi(\alpha) \leq \xi_{\mathrm{P}}(\alpha)$, where $\xi_{\mathrm{P}}(\alpha)$ is the total length of path at a given tunneling energy.

The lengths of the MEP and of the straight path are $\xi_{\mathrm{P}}(0)$ and $\xi_P(1)$, respectively, so all the intermediate paths obey the condition $\xi_{\mathrm{P}}(1) \leq \xi_{\mathrm{P}}(\alpha) \leq \xi_{\mathrm{P}}(0)$. The variable γ is defined by

$$\gamma = \frac{\xi(\alpha)}{\xi_{\mathrm{P}}(\alpha)} \tag{3.10}$$

The γ parameter is in the interval $[0, 1]$, being 0 at the reactants classical turning point and 1 at the products classical turning point. This parameter is useful to unify all the paths with different α values to see how much we have progress along them. We prefer to use $\xi(\alpha)$ instead, because in this case the length of the paths is explicitly used.

The mass-scaled Cartesian geometries for a given value of α, at a point $\xi(\alpha)$ along the path, and, at a given tunneling energy, are $\mathbf{x}\left[\alpha, \xi(\alpha), \tilde{s}_0\right]$. Thus, the mass-scaled Cartesian geometries along the MEP are given by $\mathbf{x}\left[0, \xi(0), \tilde{s}_0\right]$, whereas the ones along the straight path are

$$\mathbf{x}\left[1, \xi(1), \tilde{s}_0\right] = \mathbf{x}(\tilde{s}_0) + \xi(1)\hat{\boldsymbol{\eta}}\left[1, \xi(1), \tilde{s}_0\right] \tag{3.11}$$

where $\mathbf{x}\left[0, 0, \tilde{s}_0\right] = \mathbf{x}(\tilde{s}_0)$. The parameter $\xi(1)$ indicates the progress along the straight path, $\hat{\boldsymbol{\eta}}\left[1, \xi(1), \tilde{s}_0\right]$ is the unit vector along the straight path, i.e.,

$$\hat{\boldsymbol{\eta}}\left[1, \xi(1), \tilde{s}_0\right] = \frac{\mathbf{x}(\tilde{s}_1) - \mathbf{x}(\tilde{s}_0)}{\xi_{\mathrm{P}}(1)} \tag{3.12}$$

where the length of the straight path is $\xi_{\mathrm{P}}(1) = \mid \mathbf{x}(\tilde{s}_1) - \mathbf{x}(\tilde{s}_0) \mid$.

The MEP and the straight path are the extreme cases of a a family of α dependent paths, which are chosen as

$$\mathbf{x}\left[\alpha, \xi(\alpha), \tilde{s}_0\right] = (1 - \alpha)\mathbf{x}\left[0, \xi(0), \tilde{s}_0\right] + \alpha\mathbf{x}\left[1, \xi(1), \tilde{s}_0\right] \tag{3.13}$$

where $\mathbf{x}\left[0, \xi(0), \tilde{s}_0\right]$ and $\mathbf{x}\left[1, \xi(1), \tilde{s}_0\right]$ are the geometries along the MEP and along the straight path, respectively, with the same progress, that is, $\xi(0)/\ \xi_{\mathrm{P}}(0) = \xi(1)/\ \xi_{\mathrm{P}}(1) = \gamma$.

The imaginary action integral for each of these paths is a generalization of the imaginary action integral along the LCT straight path. At every tunneling energy, the paths of Eq. (3.13) are built as a function of the α parameter as showed in Figure 3.1. For small values of α the geometries along the path will be very close to those along the MEP and, therefore, motion along the entire path is treated as vibrationally adiabatic. For intermediate to large values of α the path is divided into three regions. Regions I and III, located on the reactants and products sides, respectively, are treated as vibrationally adiabatic, and region II is vibrationally nonadiabatic.

The vibrationally adiabatic potential is obtained in such a way that the geometry $\mathbf{x}\left[\alpha, \xi(\alpha), \tilde{s}_0\right]$ is perpendicular to the gradient at that s value, that is,

$$\left\{\mathbf{x}\left[\alpha, \xi(\alpha), \tilde{s}_0\right] - \mathbf{x}\left[0, \xi(0), \tilde{s}_0\right]\right\} \frac{\mathrm{d}\mathbf{x}\left[0, \xi(0), \tilde{s}_0\right]}{\mathrm{d}s} = 0 \tag{3.14}$$

The above equation may have multiple solutions, but we are interested in the solution that makes s a continuous function of $\xi(\alpha)$. There is no guarantee that Eq. (3.14) will be met for any geometry along the tunneling path. To find the solution to Eq. (3.14) for a geometry $\mathbf{x}\left[\alpha, \xi(\alpha), \tilde{s}_0\right]$ starting from region I, a root search procedure is set up starting from the reactants side turning point $\tilde{s}_0$, i.e., at $\xi(\alpha) = 0$. The value of s which satisfies Eq. (3.14) is $s_{\mathrm{I}}[\alpha, \xi(\alpha), \tilde{s}_0]$. In the same way can be found a value $s_{\mathrm{III}}[\alpha, \xi(\alpha), \tilde{s}_0]$ starting from products at the classical turning point $\tilde{s}_1$. If it is not possible to find a geometry along the MEP which satisfies Eq. (3.14), it means that there is no projection for that geometry of the tunneling path onto the modes perpendicular to the reaction path in the interval $[\tilde{s}_0, \tilde{s}_1]$. When this happens going from reactants to products, the nonadiabatic region in the reactants side starts at $\xi(\alpha) = \xi_{\mathrm{I}}(\alpha)$, being $\xi_{\mathrm{I}}(\alpha)$ the last value for which $s_{\mathrm{I}}[\alpha, \xi(\alpha), \tilde{s}_0]$ exists. In the same way, the nonadiabatic region in products side starts at $\xi(\alpha) = \xi_{\mathrm{III}}(\alpha)$, being $\xi_{\mathrm{III}}(\alpha)$ the last value for which $s_{\mathrm{III}}[\alpha, \xi(\alpha), \tilde{s}_0]$ exists.

It may occur that $\xi_{\mathrm{III}}(\alpha) < \xi_{\mathrm{I}}(\alpha)$, so there is an overlap between the adiabatic regions and the nonadiabatic region does not exist. In this case the vibrationally adiabatic potential in the interval $[\xi_{\mathrm{III}}(\alpha), \xi_{\mathrm{I}}(\alpha)]$ is evaluated as:

$$\min\left\{V_{\mathrm{a}}^{\mathrm{G}}\left[s_{\mathrm{I}}(0, \xi(0)); \tilde{s_0}\right], V_{\mathrm{a}}^{\mathrm{G}}\left[s_{\mathrm{III}}(0, \xi(0)); \tilde{s_0}\right]\right\} \tag{3.15}$$

Each of the two $s_i(0, \xi(0))$, $i = \mathrm{I}, \mathrm{III}$ values needed for the evaluation of the vibrationally adiabatic potentials $V_{\mathrm{a}}^{\mathrm{G}}\left[s_i(0, \xi(0)); \tilde{s_0})\right]$ is obtained from Eq. (3.14).

In the case that $\xi_{\mathrm{III}}(\alpha) > \xi_{\mathrm{I}}(\alpha)$ the potential is nonadiabatic in the region II, which has boundaries $\xi_{\mathrm{I}}(\alpha)$ and $\xi_{\mathrm{III}}(\alpha)$ with regions I and III, respectively. Therefore, region I corresponds to $0 \leq \xi(\alpha) < \xi_{\mathrm{I}}(\alpha)$, region II to $\xi_{\mathrm{I}}(\alpha) \leq \xi(\alpha) \leq \xi_{\mathrm{III}}(\alpha)$, and region III to $\xi_{\mathrm{III}}(\alpha) < \xi(\alpha) \leq \xi_{\mathrm{P}}(\alpha)$. As shown in Figure 3.1, the path along regions I and III is given by Eq. (3.13) whereas the path along region II is a straight path between the boundaries, where the geometries are given by

$$\mathbf{x}\left[\alpha, \xi(\alpha), \tilde{s}_0\right] = \mathbf{x}\left[\alpha, \xi_{\mathrm{I}}(\alpha), \tilde{s}_0\right] + \frac{\xi(\alpha) - \xi_{\mathrm{I}}(\alpha)}{\xi_{\mathrm{III}}(\alpha) - \xi_{\mathrm{I}}(\alpha)}\Big(\mathbf{x}\left[\alpha, \xi_{\mathrm{III}}(\alpha), \tilde{s}_0\right] - \mathbf{x}\left[\alpha, \xi_{\mathrm{I}}(\alpha), \tilde{s}_0\right]\Big) \tag{3.16}$$

The nonadiabatic region is defined in the same way as for the LCG4 method, i.e., the path is in the adiabatic region when (i) the condition given by Eq. (3.14) is obeyed (ii) all the generalized normal mode coordinates are within their vibrational turning points, (iii) the geometry

$\mathbf{x}\left[\alpha, \xi(\alpha), \tilde{s}_0\right]$ lies within the single-valued region of the reaction path coordinates and (iv) the adiabatic potential should be greater than or equal to the effective potential at the boundary of the nonadiabatic region, in other case the nonadiabatic region is extended until this condition is met. On the other hand, if the adiabatic potential is smaller than the effective potential the difference is due to anharmonicity, so the effective potential is modified with a nonquadratic correction.

The imaginary action integral at every tunneling energy and for each α value along the paths of Eq. (3.13) is:

$$\begin{aligned}
\theta(\alpha, \tilde{s_0}) = & \frac{(2\mu)^{1/2}}{\hbar}\Bigg[\int_0^{\xi_{\mathrm{I}}(\alpha)} d\xi(\alpha)\left\{V_{\mathrm{a}}^{\mathrm{G}}\left[s_{\mathrm{I}}(0,\xi(0));\tilde{s_0}\right] - V_{\mathrm{a}}^{\mathrm{G}}(\tilde{s_0})\right\}^{1/2}\cos\chi_0\left\{\tilde{s_0}, \hat{\boldsymbol{\eta}}\left[\alpha,\xi(\alpha),\tilde{s_0}\right]\right\} \\
& + \int_{\xi_{\mathrm{I}}(\alpha)}^{\xi_{\mathrm{III}}(\alpha)} d\xi(\alpha)\left\{V_{\mathrm{eff}}^{\mathrm{II}}(\alpha,\xi(\alpha),\tilde{s_0}) - V_{\mathrm{a}}^{\mathrm{G}}(\tilde{s_0})\right\}^{1/2} \\
& + \int_{\xi_{\mathrm{III}}(\alpha)}^{\xi_{\mathrm{P}}(\alpha)} d\xi(\alpha)\left\{V_{\mathrm{a}}^{\mathrm{G}}\left[s_{\mathrm{III}}(0,\xi(0));\tilde{s_0}\right] - V_{\mathrm{a}}^{\mathrm{G}}(\tilde{s_0})\right\}^{1/2}\cos\chi_1\left\{\tilde{s_1}, \hat{\boldsymbol{\eta}}\left[\alpha,\xi(\alpha),\tilde{s_1}\right]\right\}\Bigg],
\end{aligned} \tag{3.17}$$

The two cosines of Eq. (3.17), $\cos\chi_i\left\{\tilde{s}_i, \hat{\boldsymbol{\eta}}\left[\alpha,\xi(\alpha),\tilde{s}_i\right]\right\}$ for $i = 0, 1$ are obtained as the dot products between the unit vectors $\hat{\boldsymbol{\eta}}\left[\alpha,\xi(\alpha),\tilde{s}_i\right]$ and the unit vectors tangent to the MEP at s_i, i.e.,

$$\cos\chi_i\left\{\tilde{s}_i, \hat{\boldsymbol{\eta}}\left[\alpha,\xi(\alpha),\tilde{s}_i\right]\right\} = \hat{\boldsymbol{\eta}}\left[\alpha,\xi(\alpha),\tilde{s}_i\right]\frac{\mathrm{d}\mathbf{x}(\tilde{s}_i)}{\mathrm{d}s}, \qquad i = 0, 1 \tag{3.18}$$

The effective potential of Eq. (3.17) of the LAG4 method is the same as that of the LCG4 method, with the difference that now the geometries at which the potential is evaluated are functions of α and of the progress variable ξ, which also depends on α. Therefore the effective potential is given by

$$\begin{aligned}
V_{\mathrm{eff}}^{\mathrm{II}}(\alpha,\xi(\alpha),\tilde{s_0}) = & V\left\{\mathbf{x}\left[\alpha,\xi(\alpha),\tilde{s_0}\right]\right\} + V_{\mathrm{corr}}^{\mathrm{I}}(\alpha,\xi_{\mathrm{I}}(\alpha),\tilde{s_0}) + V_{\mathrm{anh}}^{\mathrm{I}}(\alpha,\tilde{s_0}) \\
& + \frac{\xi(\alpha)-\xi_{\mathrm{I}}(\alpha)}{\xi_{\mathrm{III}}(\alpha)-\xi_{\mathrm{I}}(\alpha)}\left[V_{\mathrm{corr}}^{\mathrm{III}}(\alpha,\xi_{\mathrm{III}}(\alpha),\tilde{s_0}) - V_{\mathrm{corr}}^{\mathrm{I}}(\alpha,\xi_{\mathrm{I}}(\alpha),\tilde{s_0}) + V_{\mathrm{anh}}^{\mathrm{III}}(\alpha,\tilde{s_0}) - V_{\mathrm{anh}}^{\mathrm{I}}(\alpha,\tilde{s_0})\right]
\end{aligned} \tag{3.19}$$

The potentials $V_{\mathrm{corr}}^{i}(\alpha,\xi_i(\alpha),\tilde{s_0}),\ i = \mathrm{I},\mathrm{III}$ correct for the zero-point energy in the modes that are still within their turning points. The potentials $V_{\mathrm{anh}}^{i}(\alpha,\tilde{s_0})$ incorporate anharmonic nonquadratic corrections to the effective potential in the same way as in the LCG4 method.

The optimum tunneling path (i.e., the LAG4 path) of the family of paths given by Eq. (3.13) is the one that minimizes the imaginary action integral of Eq. (3.17). The searching procedure is similar to the one described in Ref. [16], i.e., the smallest value of $\theta(\alpha,\tilde{s_0})$ is found by a quadratic search in α starting with a initial set of 11 equally spaced points. The optimum value of α at every tunneling energy is labeled as $\tilde{\alpha}$.

The tunneling amplitude of the LAG4 path initiated at $\tilde{s_0}$ is approximated using a primitive semiclassical expression

$$T_{\mathrm{tun}}^{\mathrm{LAG4}}(\tilde{\alpha},\tilde{s_0}) = T_{\mathrm{tun}}^{\mathrm{LAG4}}(\tilde{\alpha},\tilde{s_1}) = \exp\left[-\theta(\tilde{\alpha},\tilde{s_0})\right] \tag{3.20}$$

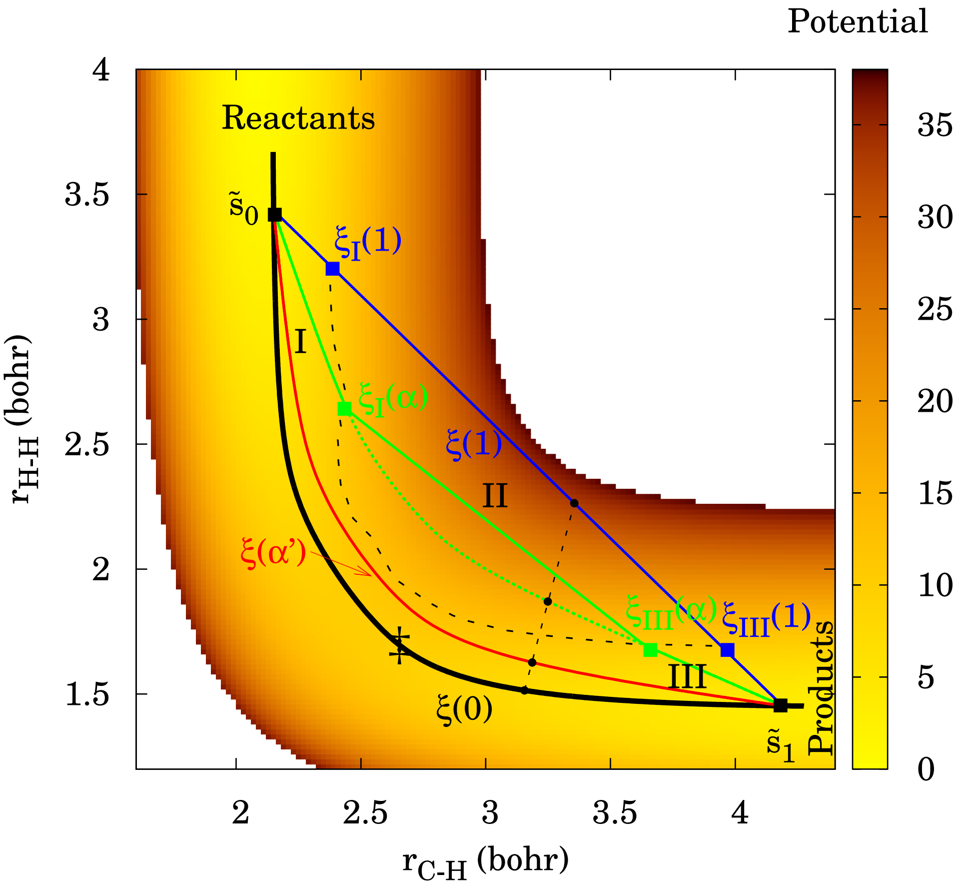

Figure 3.1: Plot of the JG PES (energy in kcal/mol) as a funcion of two distances; $r_{\mathrm{C-H}}$ is the distance between the carbon atom and the abstracted CH_4 hydrogen atom and $r_{\mathrm{H-H}}$ is the distace between the hydrogen atom and the abstracted CH_4 hydrogen atom. The graph also shows some possible reaction paths at a given tunneling energy with classical turning points given by $\tilde{s}_0$ and $\tilde{s}_1$ in the reactant and product sides, respectively. The reaction swath is partitioned into the adiabatic region of reactants (labeled as I), adiabatic region of products (labeled as III) and the nonadiabatic region (labeled as II and with boundaries given by a black dotted-dashed line). The symbol ‡ indicates the position of the saddle point, which is the conventional transition state. Four different paths are plotted as solid curves over the PES using Eq. (3.13). The four different values of α are 0 (black solid line), 0.10 (red line), 0.50 (green line) and 1 (blue line). The path with $\alpha = 0$ corresponds to the MEP and is labelled as $\xi(0)$. The path with $\alpha = 0.10$ (labeled as $\xi(\alpha')$) corresponds to a curved path passing through a region which is completelly vibrationally adiabatic. The path with $\alpha = 0.50$ (labeled as $\xi(\alpha)$) corresponds to a curved path which crosses the nonadiabatic region with boundaries given by $\xi_{\mathrm{I}}(\alpha)$ in the reactants side and by $\xi_{\mathrm{III}}(\alpha)$ in the products side. In the nonadiabatic region this path does not follow the curved path (green dotted line), but the straight path (green solid line). Finally, the path with $\alpha = 1$ (labelled as $\xi(1)$) corresponds to the straight path connecting the geometries of the MEP at the classical turning points. The nonadibatic region starts at $\xi_{\mathrm{I}}(1)$ in the reactants side and ends at $\xi_{\mathrm{III}}(1)$ in the products side. The black dashed line joining the straight path and the MEP indicates the progress along each of the four tunneling paths for a given value of γ (see Eq. (3.10)).

The LAG4 primitive probability, $P^{\mathrm{LAG4}}_{\mathrm{prim}}(E)$, is obtained from the tunneling amplitude of the previous Eq. (3.20) plus the contribution due to the vibrational motion perpendicular to the reaction coordinate along the incoming $T_0(E)$ and outgoing $T_1(E)$ trajectories at tunneling energy E

$$\begin{aligned} P^{\mathrm{LAG4}}_{\mathrm{prim}}(E) =& |T_0(E)+T_1(E)|^2 \\ & + \left(\frac{\cos\chi_0 \left\{\tilde{s}_0, \hat{\boldsymbol{\eta}}\left[\tilde{\alpha}, \xi(\tilde{\alpha}), \tilde{s}_0\right]\right\} + \cos\chi_1 \left\{\tilde{s}_1, \hat{\boldsymbol{\eta}}\left[\tilde{\alpha}, \xi(\tilde{\alpha}), \tilde{s}_1\right]\right\}}{2} \right)^2 \\ & \times \exp\left[-2\theta(\tilde{\alpha}, \tilde{s}_0)\right] \end{aligned} \tag{3.21}$$

The tunneling amplitude of the incoming trajectory along the reaction coordinate is $\exp\left[-\theta(\tilde{\alpha}, \tilde{s}_0)\right] \cos\chi_0 \left\{\tilde{s}_0, \hat{\boldsymbol{\eta}}\left[\tilde{\alpha}, \xi(\tilde{\alpha}), \tilde{s}_0\right]\right\}$ and that of the outgoing trajectory is $\exp\left[-\theta(\tilde{\alpha}, \tilde{s}_0)\right] \cos\chi_1 \left\{\tilde{s}_1, \hat{\boldsymbol{\eta}}\left[\tilde{\alpha}, \xi(\tilde{\alpha}), \tilde{s}_1\right]\right\}$. The expression used in Eq. (3.21) is the average of the two tunneling amplitudes. Similarly the tunneling amplitude due to the all the vibrational degrees of freedom perpendicular to the reaction coordinate is averaged using $T_0(E)$ and $T_1(E)$, instead of using $2T_0(E)$, to inforce macroscopic reversibility. The expression for $T_0(E)$ is similar to the one given in Ref. [17] but evaluated along the LAG4 tunneling path ($\alpha = \tilde{\alpha}$) instead of along the LCG4 tunneling path ($\alpha = 1$).

The primitive probability of Eq. (3.21) can be greater than one because of the integration of the amplitudes over the incoming and outgoing trajectories, so it is enforced to go to 1/2 at the maximum of the vibrational adiabatic potential $V^{\mathrm{AG}}_{\mathrm{a}}$ by the expression

$$P^{\mathrm{LAG4}}(E) = \left\{ 1 + \frac{1}{2} \frac{\left[P^{\mathrm{LAG4}}_{\mathrm{prim}}(V^{\mathrm{AG}}_{\mathrm{a}})\right]^{-1} - 1}{P^{\mathrm{LAG4}}_{\mathrm{prim}}(V^{\mathrm{AG}}_{\mathrm{a}})} P^{\mathrm{LAG4}}_{\mathrm{prim}}(E) \right\} \times \frac{1}{1 + \left[P^{\mathrm{LAG4}}_{\mathrm{prim}}(E)\right]^{-1}} \tag{3.22}$$

It is possible to include tunneling into excited vibrational states of products in the exoergic direction. It can be done easily by using the LAG4 approximation for the ground state and the LCG4 approximation for excited vibrational states. The procedure is described in detail in Ref. [17] and will not be discussed here. The LAT method in its LAG4 version has been implemented in POLYRATE 2008.[102]

3.4. Results and discussion

In this Section we apply VTST/MT, including the LAG4 approximation for the evaluation of the transmission coefficients, for two hydrogen abstraction reactions:

$$\mathrm{H} + \mathrm{CH_4} \longrightarrow \mathrm{H_2} + \mathrm{CH_3} \tag{R1}$$

$$^{15}\mathrm{H} + \mathrm{CH_4} \longrightarrow {}^{15}\mathrm{H{-}H} + \mathrm{CH_3} \tag{R2}$$

Both reactions R1 and R2 were studied using the Jordan and Gilbert (JG) potential energy surface.[62] In the case of reaction R2 we just have changed the mass of the hydrogen, which is abstracting the proton, by that of a methyl group in order to observe the effect of the reaction-path curvature on the transmission coefficients. Both reactions are of the type A + BC →

AB + C, where A, B and C are atoms or groups of atoms. The reaction path curvature is a function of the skew angle, which in isoinertial coordinates is given by

$$\beta = \cos^{-1}\left(\frac{m_\mathrm{A} m_\mathrm{C}}{(m_\mathrm{A}+m_\mathrm{B})(m_\mathrm{B}+m_\mathrm{C})}\right)^{1/2} \tag{3.23}$$

The skew angle is close to 90 degrees when B has a much larger mass than A and C and it is close to zero when the mass of A and C is much larger than the mass of B. For the latter, tunneling effects are more important because a light particle is being transferred between two heavy atoms (heavy–light–heavy system). For reaction R1 the skew angle is $\beta = 47$ degrees, whereas for reaction R2 the skew angle is only $\beta = 20$ degrees. From these values of the skew angle, we expect small values of $\tilde{\alpha}$ at all tunneling energies for reaction R1, because the reaction path curvature is small, whereas large values of $\tilde{\alpha}$ are expected for reaction R2. Indeed, this is the case at low tunneling energies, as showed in Figure 3.2, which plots the variation of θ with α for every tunneling energy for reactions R1 and R2. For any reaction-path curvature the least-action path is always the path with the best compromise between length and energy, i.e, between short paths with high barriers and long paths with low barriers. The two extreme cases are, on one side, the straight path, which is the shortest path between two classical turning points, but the must unfavorable from the energetic point of view and, on the other side, the MEP, which is the longest path but the most favorable energetically. The transmission coefficients obtained using these two prescriptions are the LCT, for the straight path, and the ZCT, for the MEP.

For both reactions, at low tunneling energies and for the paths characterized by the optimum $\tilde{\alpha}$, there is an important area of the reaction swath that is vibrationally nonadiabatic and that involves a significant increase of the potential energy. That increase has to be compensated by shortening the length of the path. That compensation occurs for reaction R2, for which the curvature of the reaction path makes the straight path very short, but not for reaction R1, for which decreasing the length of the path does not compensate the increase in potential energy. This is why the incursion of the least-action path into the vibrationally nonadiabatic region is weaker for reaction R1 than for reaction R2. The sudden increase of the action integral observed in Figure 3.2 for reaction R2 at α values about 0.9 is due to the extension of the nonadiabatic region, because for those paths there are geometries for which Eq. (3.14) is not satisfied. At high tunneling energies the whole reaction swath is vibrationally adiabatic and, therefore, there is no rise in energy even for very short paths, so the least-action path coincides with the straight path.

The transmission coefficients and rate constants for reaction R1 are listed in Table 3.1 and Table 3.2, respectively, whereas the transmission coefficients for reaction R2 are listed in Table 3.3. The LAT results for reactions R1 and R2 show that SCT and LCT underestimate the transmission coefficients for tunneling. As expected SCT is better for small to intermediate curvature and LCT is better for large curvature. The μOMT transmission coefficient also underestimates tunneling but is the best choice when the LAT transmission coefficient is considered to be too expensive.

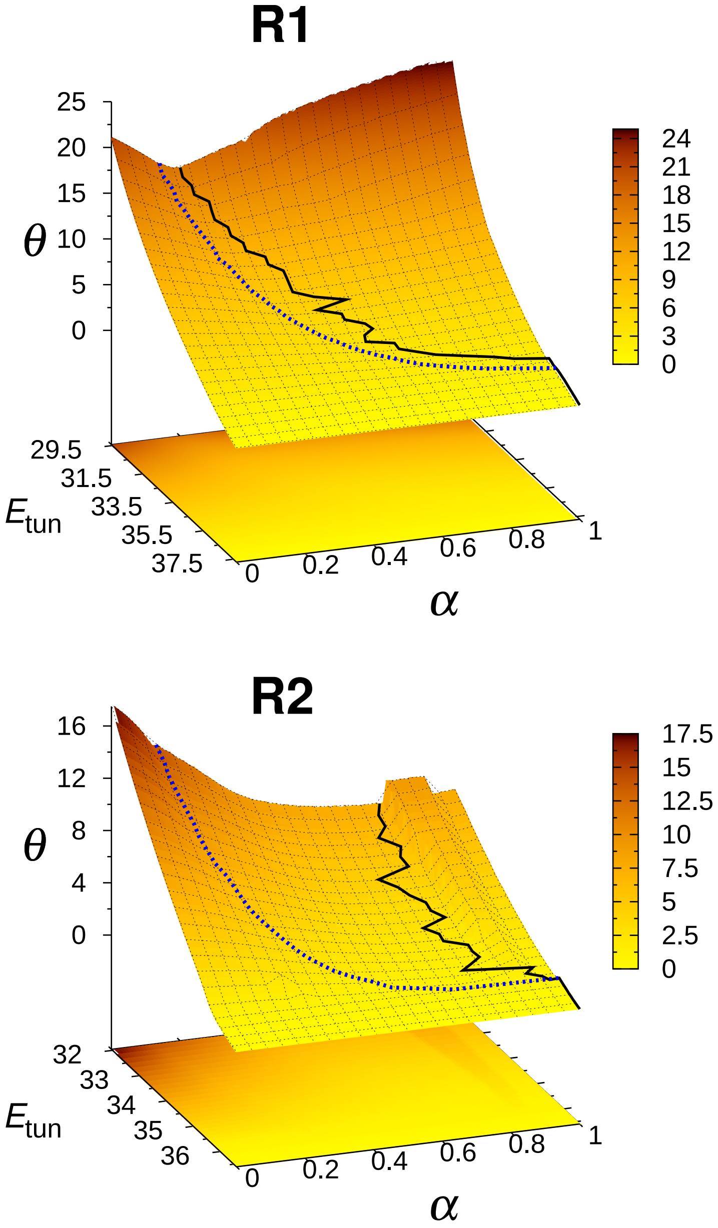

Figure 3.2: Graphs showing the variation of the imaginary-action integral with the α parameter at each of the tunneling energies (in kcal/mol) for reactions R1 and R2. The solid line indicates the locations of $\tilde{\alpha}$ at every tunneling energy. The dashed line indicates the lowest α value for which there is a nonadiabatic region when the paths given by Eq. (3.13) are followed in the direction from reactants to products.

Table 3.1: Transmission coefficients for reaction R1 on the JG surface

T(K)	ZCT	SCT	LCT	μOMT	LAT
200	4.36	18.7	13.7	18.8	27.3
250	2.49	6.27	5.11	6.28	7.30
300	1.87	3.54	3.04	3.54	3.73
400	1.41	2.02	1.84	2.03	2.01
500	1.25	1.57	1.47	1.57	1.54

For reaction R1, we compare the thermal rate constants with accurate multidimensional quantum dynamical calculations [103, 104] in the interval 200–500 K. There are also previous CVT/μOMT calculations [105, 106] for the same interval of temperatures, which showed a very good agreement with the previous quantum calculations. The CVT/LAT rate constants obtained in this work show even a better agreement with the quantum results. The μOMT transmission coefficients are identical to the SCT ones, indicating that the least-action path is quite far from the straight path. Therefore, in this case the LCT transmission coefficients underestimate quantum effects. Sansón *et al.* [107] reached a similar conclusion for the H_2 + Cl reaction, which has similar skew angle than reaction R1. Because the skew angle for R1 is not large (small to intermediate curvature case), it is expected that the SCT transmission coefficient accounts well for tunneling. However, the comparison between SCT and LAT at T=200 K shows that SCT underestimates tunneling at this temperature, although the difference is already small at room temperature. From the comparison of CVT/SCT and CVT/LAT with the accurate rate constants it is difficult to know which of the two transmission coefficients is more accurate, since both approximations lead to very good results; LAT could be more accurate than SCT because it finds the optimum tunneling paths in a set of paths at every tunneling energy and it includes nonadiabaticity; but SCT could also be more accurate because it incorporates a more accurate treatment of systems in the small-curvature limit.

When the curvature of the reaction path is large, as for reaction R2, SCT seriously underestimates tunneling at all temperatures in the range 200–500 K (see Table 3.3) and, therefore, this approximation accounts poorly for quantum effects in this case. The LAT transmission coefficients are also larger than the LCT ones. The straight path used in the LCT method is a particular path in the family of paths generated by Eq. (3.13) and the LCT calculation

Table 3.2: VTST/MT thermal rate constants (in cm^3 molecule^{-1} s^{-1}) compared to accurate quantal ones for reaction R1 on the JG surface

T(K)	CVT/SCT^a	CVT/LCT^a	CVT/μOMT^a	CVT/LAT^b	Accurate^c
200	7.1(-21)^d	5.2(-21)	7.1(-21)	1.0(-20)	9.0(-21)
250	4.3(-19)	3.5(-19)	4.3(-19)	5.0(-19)	5.5(-19)
300	7.8(-18)	6.7(-18)	7.8(-18)	8.2(-18)	9.8(-18)
400	3.6(-16)	3.3(-16)	3.6(-16)	3.6(-16)	4.0(-16)
500	4.1(-15)	3.8(-15)	4.1(-15)	4.0(-15)	3.8(-15)

^{a}From Ref. 106. ^{b}This work. ^{c}From Ref. 104. ^{d}Powers of 10 in parenthesis.

Table 3.3: Transmission coefficients for reaction R2 on the JG surface

T(K)	ZCT	SCT	LCT	μOMT	LAT
200	2.98	4.62	31.3	31.3	36.5
250	2.08	2.83	11.3	11.3	12.5
300	1.69	2.12	6.14	6.14	6.59
400	1.35	1.56	3.10	3.10	3.23
500	1.22	1.34	2.16	2.16	2.22

corresponds, at every energy for which $\tilde{\alpha}$ does not equal 1, to an incompletely optimized LAG calculation (whereas SCT does not). Thus whenever, LCT differs from LAT, it gives less transmission probability. However, the LAT transmission factor is underestimated by LCT by only 14% at T=200 K, and this percentage is reduced by half at room temperature.

To further analyze the tunneling, we examined, at every temperature, the integrand of Eq. (3.5), $P_{\mathrm{W}}(E)$, which is the Boltzmann-weighted transmission probability. The value of P_{W}, with the zero of energy taken here as the maximum of the vibrationally adiabatic ground-state potential curve, is shown at several temperatures for reactions R1 and R2 in Figure 3.3 an Figure 3.4, respectively. The area under the curves gives the tunneling contribution to the transmission coefficients, which it is clearly more important for reaction R2. Figure 3.3 and Figure 3.4 also show how P_{W} evolves with the tunneling energy for different transmission coefficients. Taking the LAT as reference approximation, we observe that for reaction R2 the μOMT curve follows closely the LAT curve, and as a consequence the μOMT transmission coefficients are quite similar to the LAT ones. For reaction R1 the μOMT transmission probabilities coincide with the SCT ones, but that curve is quite far from the LAT curve at T=200 K due to the difference in magnitude of the transmission coefficients. At T=300 K and above the magnitude of SCT and LAT transmission coefficients is similar, so the curves are quite close between them. However, there is a subtlety here, the shape of both curves is different, being the μOMT (or SCT) probabilities smaller, at low tunneling energies, and bigger, at high tunneling energies, when compared with the LAT probabilities. This behaviour is observed even at T=200 K and indicates that the SCT probabilities are too high at tunneling energies close to the top of the barrier. Another argument supporting this conclusion is offerend during the discussion of the graphs depicted in Figure 3.5 and Figure 3.6.

Table 3.4: Representative tunneling energies for reaction R1 (in kcal mol^{-1})^{a}

T(K)	ZCT	SCT	LCT	μOMT	LAT
200	37.03	35.68	36.07	35.68	34.75
250	37.29	36.42	36.14	36.42	36.11
300	37.42	36.81	36.18	36.81	36.16
400	37.61	37.21	37.46	37.21	37.45
500	37.70	37.39	37.59	37.39	37.58

[a] The maximum of the vibrationally adiabatic ground-state potential curve has an energy of 37.70 kcal mol^{-1}.

The Boltzmann-weighted probability also shows the tunneling energy that contributes the most to the different transmission coefficients. This characteristic energy is called representa-

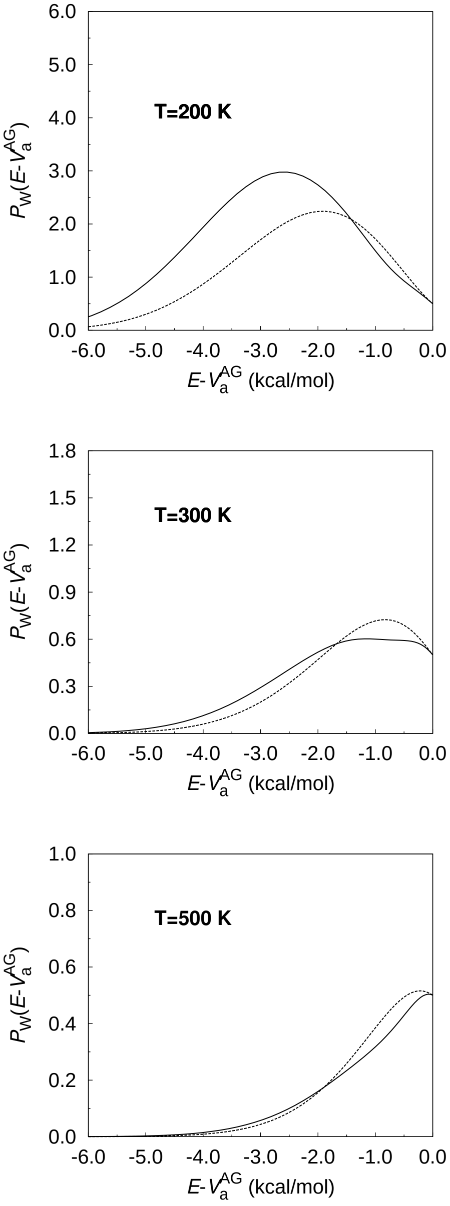

Figure 3.3: Representation of the LAT (solid line) and μOMT (dashed line) Boltzmann-weighted probabilities versus tunneling energy at different temperatures and for reaction R1. The tunneling energies are plotted using the maximum of the vibrationally adiabatic ground-state potential curve, V_a^{AG}, as the temporary zero of energy.

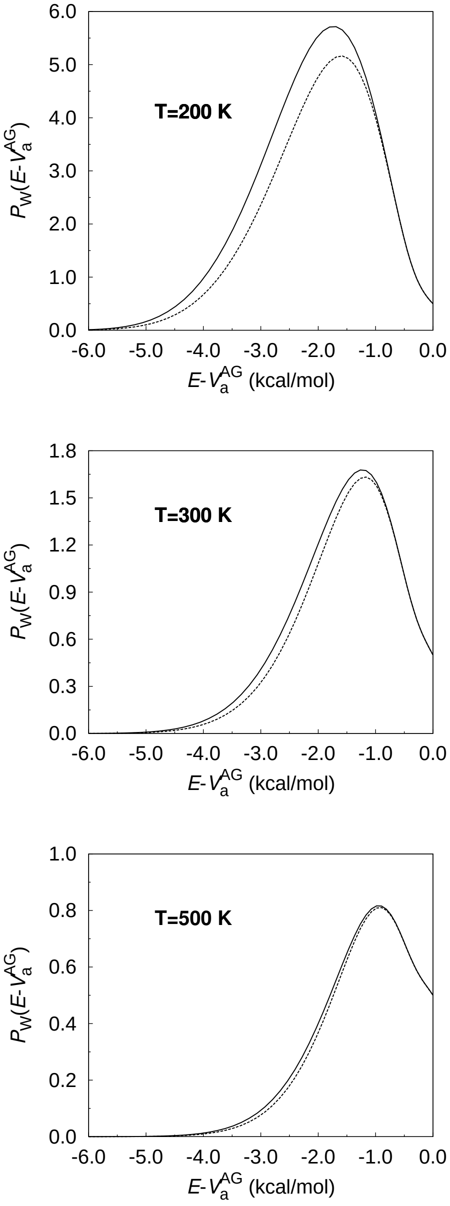

Figure 3.4: Same as Figure 3.3, but for reaction R2.

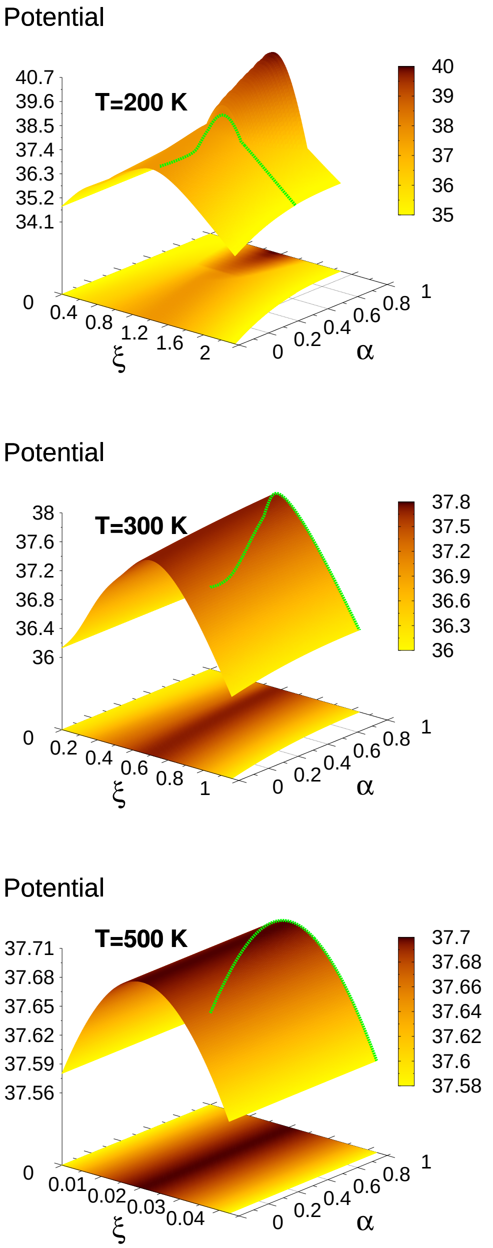

Figure 3.5: Effective potentials (in kcal/mol) at the representative tunneling energy for reaction R1 at different temperatures. The X-axis is the length of the path, ξ (in a_0) and the Y-axis is the α parameter (see Eq. (3.13)) which controls the curvature of the tunneling path. The green lines in each of the graphs are the least-action paths for that particular RTE. See text for details.

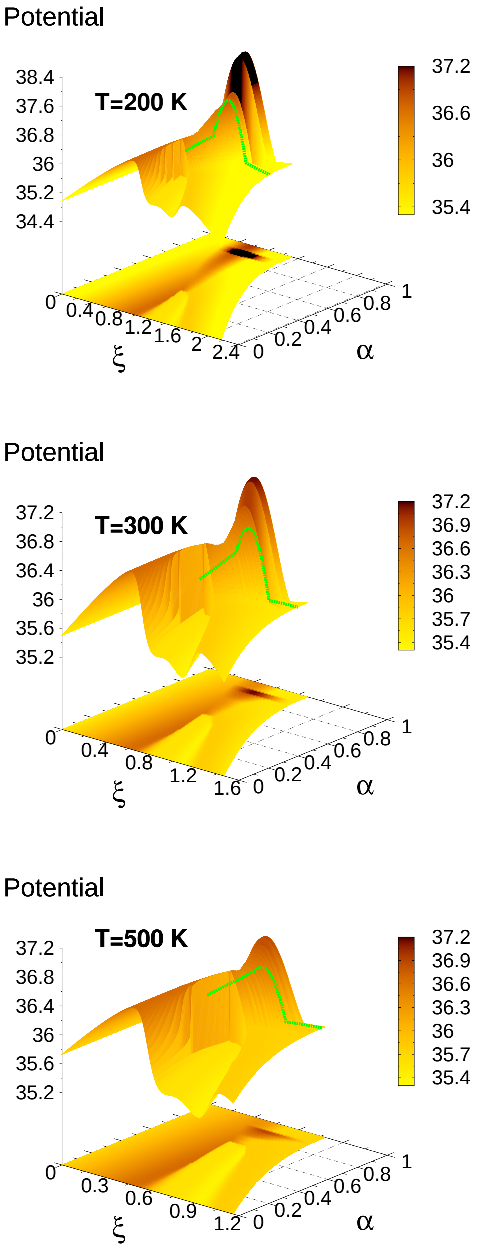

Figure 3.6: Same as Figure 3.5, but for reaction R2.

tive tunneling energy (RTE) and it can be easily identified as the energy for which P_{W} has a maximum. The RTEs for reactions R1 and R2 obtained by different approximations for tunneling are listed in Table 3.4 and Table 3.5, respectively. If the temperature is high the maximum coincides with the top of the barrier, indicating that tunneling is already unimportant. If the LAT imaginary action integral and, therefore, the tunneling probability, is the best compromise between length and energetics for the family of paths of Eq. (3.13), the RTE is the best compromise between the tunneling probability and the Boltzmann factor. It is obvious that at low temperatures the RTE is located at low energies. In the limiting case, at T=0 K the only contribution to the transmission coefficient comes from the tunneling probability at the lowest tunneling energy (i.e., the zero-point energy). As temperature increases more energy levels are populated and tunneling is possible at several energies, and in this case we have to look for the least-action path at every tunneling energy. A quite different approach, known as the *instanton* theory [15, 108–110] seeks, at every temperature (not a every energy) for a unique least-action periodic trajectory, called *instanton*, that comprises all trajectories. Unfortunately, above a given critical temperature (usually for temperatures above 250 K) there is no *instanton* trajectory, although it is still possible to solve the problem approximately using analytical expressions.[111] There is a certain resemblance between RTE and *instanton* in the sense that, at every temperature, both trajectories indicate the most relevant region of the PES for tunneling.

Table 3.5: Representative tunneling energies for reaction R1 (in kcal mol^{-1})^{a}

T(K)	ZCT	SCT	LCT	μOMT	LAT
200	35.90	35.81	35.01	35.01	34.95
250	36.14	35.86	35.34	35.34	35.11
300	36.28	36.00	35.53	35.53	35.52
400	36.57	36.23	35.71	35.71	35.71
500	36.65	36.37	35.74	35.74	35.74

^{a}The maximum of the vibrationally adiabatic ground-state potential curve has an energy of 36.66 kcal mol^{-1}.

Figure 3.5 and Figure 3.6 depict effective potentials, which are given by Eq. (3.19) in the nonadiabatic region and by the vibrationally adiabatic ground-state potential in the adiabatic region, versus the length of the path for several values of α, taking as turning points the representative tunneling energies at T=200, 300 and 500 K for reactions R1 and R1, respectively. Each of the graphs was generated by mapping the PES using Eq. (3.13). The green lines depicted in each of the graphs represent the least-action path. At T=200 K the least action paths for both reactions, R1 and R2, have nonadiabatic regions and the value of $\tilde{\alpha}$ is 0.62 and 0.83, respectively. For reaction R1 the ratio $\xi_{\mathrm{P}}(\tilde{\alpha})/\xi_{\mathrm{P}}(0)$ is 0.78 and the difference $V_{\max}(\tilde{\alpha}) - V_{\mathrm{a}}^{\mathrm{AG}}$ is 0.64 kcal mol^{-1}, whereas for reaction R2 the ratio between lengths is 0.53 and the difference in energy is only 0.05 kcal mol^{-1}. Those numbers show that at T=200 K the shortcut through the nonadiabatic region compensates the rise in energy for both reactions. This behaviour is more noticable for reaction R2, which exhibits a larger reaction-path curvature.

From the previous discussion it seems odd that, at T=300 K, $\tilde{\alpha}$ is 1.00 and 0.93 for reactions R1 and R2, respectively, but it is easily understood taking into account that for the former reaction all the family of curves at that temperature from $\alpha = 0$ to $\alpha = 1$ lie completely on the adiabatic region, so the maximum of the effective potential is always the maximum of the vibrationally adiabatic ground-state potential, as shown in Figure 3.5. The consequence is that there is no energy penalty for shorter paths and, therefore, the least-action path coincides with the straight path. This circumstance does not occur for reaction R2, which has a nonadiabatic region for some values of α. Therefore, when the reaction swath is completely adiabatic the least-action path should be always the straight path and the probabilies obtained with the SCT approximation should not be larger than the LCT ones in that region of the PES. However this occurs for reaction R1, as shown previously in Figure 3.3. On the light of the values of the transmission coefficients obtained by SCT and LAT for R1 this issue seems unimportant, but in a future work it would be interesting to analyze this behaviour in more depth for a large number of reactive systems presenting different reaction-path curvatures.

In this work we have used analytical PES to show how the LAT approximation works for polyatomic systems. However, the method is very expensive in computer time, which is an obstacle for 'on the fly' generation of the PES. The easiest solution to the problem is a 'brute-force' approach consisting in the evaluation of several tunneling energies at the same time by parallelization of the method. A more reasonable approach would be to make use of different interpolation procedures to save computer time. The two graphs of Figure 3.2 give us a hint about a possible solution to the problem. In principle it would be feasible to use a spline under tension similar to the one used in the ILCT2D [23] approximation, with the difference that, instead of interpolating tunneling paths and tunneling energies, we interpolate imaginary-action integrals and tunneling energies. It is possible to make the procedure even cheaper in computer time by interpolating the potential needed for the evaluation of the imaginary-action integral at every α value. A more detailed discussion about how to extend the LAT method to make it practical for its use within the direct dynamics approach will be presented elsewhere.

3.5. Concluding remarks

We have extended the large least-action tunneling (LAT) approximation to polyatomic reactions. The implementation is called least-action ground state version 4 because it is based on the reactant ground state when the reaction is written in the exoergic or thermoneutral direction and because in the limit of large reaction-path curvature it reduces to the large-curvature tunneling (LCT) approximation carried out by the large-curvature ground-state version 4 (LCG4) method. The new method is more complete than the simpler microcanonically optimized multidimensional tunneling (μOMT) approximation, and in the tests presented here it is slightly more accurate. The method has being incorporated in the POLYRATE computer program.

Chapter 4

Practical implementation and applications of the least-action tunneling transmission coefficient

In this Chapter we present two new direct dynamics algorithms for calculating transmission coefficients of polyatomic chemical reactions by the multidimensional least-action tunneling approximation. The new algorithms are called the interpolated least-action tunneling method based on one-dimensional interpolation (ILAT1D) and the double interpolated least-action tunneling (DILAT) method. The DILAT algorithm, which uses a one-dimensional spline under-tension to interpolate both the effective potentials along the nonadiabatic portions of tunneling paths and the imaginary action integrals as functions of tunneling energies, was designed for the calculation of multidimensional LAT transmission coefficients for very large polyatomic systems. The performance of this algorithm has been tested for the $CH_4/CD_3H/CD_4 + CF_3$ hydrogen abstraction reactions with encouraging results, i.e., when the fitting is performed using 13 points, the algorithm is about 30 times faster than the full calculation with deviations that are smaller than 5%. This makes direct dynamics least-action tunneling calculations practical for larger systems, higher levels of electron correlation, and/or larger basis sets.

4.1. Introduction

Hydrogen and proton transfer reactions are among the most prominent reactive processes in chemistry and biology. [58, 59] These reactions are often dominated by quantum mechanical tunneling because the hydrogen atom, due to its small mass, can readily pass through classically forbidden regions of a potential energy surface (PES). Tunneling effects can be taken into account by rigorous quantum mechanical methods, [103, 112–123] which are only applicable to systems with a small number of atoms, or by WKB-like semiclassical methods, [18, 25, 91, 97, 98, 124–131] which can handle a large number of atoms. Among the semiclassical methods, variational transition state theory with multidimensional tunneling corrections (VTST/MT) [16, 17, 29, 63–70, 82, 132, 133] is the best validated practical choice for the study of chemical reactions with several atoms because, on the one hand, it has proved to be very accurate when compared with quantum mechanical dynamics calculations[61, 82] and, on the other hand, it needs only semiglobal information about the PES and in many cases is sensitive to the PES only near to the minimum-energy path.

The simplest case for VTST is when the transition state dividing surface (which is the dynamical bottleneck for reaction) is located at a saddle point and quantum effects on the reaction coordinate are negligible; in such a case all the information required for the evaluation of thermal rate constants can be obtained from the reactants and the conventional transition state. In this case VTST/MT can be safely replaced by conventional transition state theory. [26] Unfortunately, this is hardly ever the case for hydrogen transfer reactions, which, unless they have no barrier, are usually dominated by tunneling even up to temperatures well above room temperature. [54–57, 134]

Even when variational effects (i.e., effects due to the variational transition state not being located at a saddle point) are negligible, the incorporation of quantum effects in the VTST/MT treatment of generalized transition states requires more information about the PES than just reactants and transition state properties. Quantum effects are incorporated differently for the reaction coordinate, which–for overbarrier processes–is the mode with an imaginary frequency at the saddle point, and for the F-1 normal modes of bound motion perpendicular to the reaction coordinate (where F-1 equals $3N$-7 for nonlinear transition states and $3N$-6 for linear transition states, and where N is the number of atoms; the reaction coordinate is labeled as mode F). The thermal rate constant calculated by taking into account only the quantum effects on the coordinates in motion is bound is called quasiclassical, and it is obtained by replacing the classical vibrational partition functions by quantum-mechanical ones. [26, 51] The quantum effects on the reaction coordinate are taken into account through a transmission coefficient [51, 61, 72–74, 128] that multiplies the quasiclassical thermal rate constant. The evaluation of the transmission coefficient requires the selection of a tunneling path or paths.

As a zeroth approximation one may assume that the tunneling path coincides with the minimum energy path (MEP) (the union of the steepest descent paths in isoinertial coordinates down from the saddle point to reactants and that down to products [73, 76, 84]). When zero point effects are taken into account for bound motions transverse to the MEP, this assumption yields the zero-curvature tunneling (ZCT) approximation. [73] The signed distance from the saddle point along the MEP will be called the reaction coordinate, even though the dominant dynamical path may be offset from the MEP; the MEP is tangent to the imaginary-frequency normal mode at the saddle point so this definition coincides with defining the reaction coordinate in the vicinity of the saddle point as distance along that mode.

It has been shown that the ZCT path, i.e., the MEP, is a poor choice as tunneling path, [81, 82] since it does not take account of the MEP's curvature, which couples the reaction coordinate to the other vibrational modes. The curvature has the effect that the dominant tunneling path is on the concave side of the reaction path and, depending on the magnitude of the curvature, tunneling is better treated by the small-curvature tunneling (SCT) approximation [19, 86–88] or by the large curvature tunneling (LCT) approximation [16, 17, 20, 21, 24, 87, 90–92], for the cases of small and large couplings, respectively (for collinear atom-diatom reactions with very small curvature one could also use the Marcus-Coltrin approximation [18]). The path implied by the SCT approximation is not uniquely defined because the calculation is carried out in terms of an effective mass for tunneling along the MEP rather than using the true reduced mass along a tunneling path; the curvature-dependent effective mass is smaller than the true reduced mass to account for shortening of the tunneling path by corner cutting. The large-curvature tunneling approximation, in contrast, involves, for every energy, an explicit sequence of paths chosen as the straight lines that join equipotential points on the reactants and products sides of the vibrationally adiabatic potential curves along the MEP. Neither the SCT nor the LCT is variational; rather they represent limiting cases. However, the tunneling fluxes predicted by the SCT and LCT approximations roughly overlap for intermediate curvature, and so they more or less cover the whole range of curvatures. It is reasonable to define a new tunneling probability that, at every tunneling energy, gives the larger of the SCT and LCT tunneling probabilities. This result is called the (microcanonically) optimized multidimensional tunneling probability (μOMT or, for short, OMT). [24] Note that the ZCT, SCT, LCT, and OMT tunneling approximations are all multidimensional in that they all include the important effect that the vibrational zero-point energy (or –in the LCT and OMT approximations– also excited-state quantized vibrational energies) depends upon the distance along the reaction path or tunneling path; thus the reaction coordinate is not separable in these approximations, and this mimics VTST in removing one of the major approximations of conventional transition state theory. For this reason, it is most appropriate to apply these approximations in the context of VTST rather than conventional transition state theory. The SCT, LCT, and OMT approximations include multidimensional effects not only in the vibrational energy requirements along the tunneling path but also in the choice of the tunneling path.

Very recently [131] we have generalized to polyatomic reactions the least-action tunneling (LAT) path, which was initially developed by Garrett and Truhlar for atom-diatom reactions. [25] In this approximation, one considers, for each tunneling energy and final vibrational state, a sequence of paths parameterized by a unique parameter. These paths are all located at or between the MEP and the LCT path. At every tunneling energy, the path is variationally optimized within this sequence by choosing it as the path with the largest tunneling probability. For this reason, in principle, the LAT transmission coefficients should be more accurate than those obtained by the μOMT approximation.

The current version of the LAT method for ground-state transmission coefficients (which are used to calculate thermally averaged rate constants [17]) may be called the least-action ground-state tunneling method, version 4 (LAG4) because we always base the transmission coefficients for thermal reactions on a ground-state transmission coefficient (computed in the exoergic direction) and because the LCT-like portions of the calculation are based on version 4 of the LCT method. (Note that although the reactant is in the ground state for the prototype tunneling process on which the calculation of the thermally averaged rate is based, a range of vibrational states is populated in the product of the tunneling event, if the energy is high enough to populate dynamically coupled states in the product valley, and tunneling for excited-state reactants is approximated in terms of the ground-state tunneling probabilities and the quantized threshold energies at the variational transition state.) The present Chapter is concerned with the calculation of LAG4 transmission coefficients, and we will simply abbreviate them as LAT. Similarly we use LCT as shorthand for LCG4.

The LCT, μOMT, and LAT transmission coefficients are more computationally intensive than the SCT one because, whereas the SCT transmission coefficient can be obtained from a very limited knowledge of the PES, i.e., from information calculated along the MEP (including its curvature and local force constants for motion transverse to the MEP), the calculation of the other transmission coefficient approximations requires information not only along the MEP but also in the wide region on the concave side the MEP; this region is called the reaction swath [135, 136], and it is the region through which LCT and LAT tunneling paths pass. The LCT, μOMT, and LAT transmission coefficients involve the calculation of a potentially large number of points of the PES in the reaction swath. The development of faster computers and more accurate density functionals has made it possible in many cases to evaluate the energy reasonably accurately at those geometries by direct dynamics, which allows "the calculation of rates or other observables directly from electronic structure information without intermediacy of fitting the electronic energies in the form of a potential energy surface." [137] Direct dynamics together with VTST/MT is a powerful combination that, for instance, is being widely used in the evaluation of thermal rate constants and kinetic isotope effects (KIEs) of many enzymatic reactions.[138]

However, the calculation of LCT and LAT transmission coefficients by direct dynamics is still computationally very demanding if one uses the original algorithms. For that reason we developed an algorithm (called ILCT2D) based on a two-dimensional spline-under-tension, [139] to evaluate LCT tunneling probabilities with a reduction in the computer time by a factor of about 30. [23] The error with respect to the full calculation is less than 1%. It is the objective of the present work to present an analogous efficient algorithm based on spline-under-tension interpolations for calculation of LAT transmission coefficients using direct dynamics, and we will present two such algorithms. To show the performance of the new algorithms, we have chosen the following set of hydrogen abstraction reactions:

$$\mathrm{CH_4 + CF_3 \longrightarrow CH_3 + HCF_3} \tag{R1}$$

$$\mathrm{CD_3H + CF_3 \longrightarrow CD_3 + HCF_3} \tag{R2}$$

$$\mathrm{CD_3H + CF_3 \longrightarrow CD_2H + DCF_3} \tag{R3}$$

$$\mathrm{CD_4 + CF_3 \longrightarrow CD_3 + DCF_3} \tag{R4}$$

which we have previously studied using the SCT, LCT (with the ILCT2D algorithm), and μOMT approximations for tunneling. [23] The calculated thermal rate constants were in good agreement with experimental data. However, the calculated KIEs were too low, particularly those for the ratio R2/R3. In this paper, in addition to developing a more efficient algorithm for LAT calculations, we use it to apply the LAT approximation to these reactions to see if this method improves the previous results.

Section 4.2 presents a general description of the evaluation of tunneling transmission coefficients and presents the new interpolation schemes used for efficient direct dynamics calculations of LAT transmission coefficients. Section 4.3 describes the performance of those interpolation schemes for reactions R1 to R4. Section 4.4 has concluding remarks.

4.2. Methodology

The VTST/MT thermal rate constant [16, 17] can be written as the quasiclassical canonical variational theory (CVT) rate constant $k^{\mathrm{CVT}}(T)$ multiplied by the tunneling transmission coefficient, $\kappa^{\mathrm{CVT/X}}(T)$, i.e.

$$k^{\mathrm{CVT/X}}(T) = \kappa^{\mathrm{CVT/X}}(T) k^{\mathrm{CVT}}(T) \tag{4.1}$$

where X stands for the ZCT, [73] SCT, [88] LCT, [21, 24, 25] μOMT, [24] or LAT [25, 131] approximations for tunneling. In general $\kappa^{\mathrm{CVT/X}}(T)$ is equal to a so called CAG factor (called $\kappa^{\mathrm{CVT/CAG}}(T)$ and almost always very close, within about 15 per cent, to unity) times a more universal transmission coefficient called $\kappa^{\mathrm{X}}(T)$. Since the CAG factor is explained in detail elsewhere, [16, 17, 128] we concentrate here on $\kappa^{\mathrm{X}}(T)$.

The ZCT approximation assumes that the reaction coordinate is adiabatically separated from the F-1 other degrees of freedom and that all the excited-state vibrationally adiabatic potentials that significantly contribute to tunneling have the same shape as the ground-state vibrationally adiabatic potential $V_{\mathrm{a}}^{\mathrm{G}}(s)$, which is given by:

$$V_{\mathrm{a}}^{\mathrm{G}}(s) = V_{\mathrm{MEP}}(s) + \epsilon_{\mathrm{vib}}^{\mathrm{G}}(s) \tag{4.2}$$

where s is the reaction coordinate mentioned in the introduction (it measures progress along the isoinertial MEP, being negative on the reactants side, zero at the saddle point, and positive on the products side, where the isoinertial coordinates are scaled to a reduced mass of μ); $V_{\mathrm{MEP}}(s)$ is the potential along the MEP; and $\epsilon_{\mathrm{vib}}^{\mathrm{G}}(s)$ is the local zero-point vibrational energy. The other tunneling approximations also involve the $V_{\mathrm{a}}^{\mathrm{G}}(s)$, but in more complicated ways.

The lowest energy at which is possible to have tunneling is the energy of the reactant zero-point level when the reaction is written in the exoergic direction; this is called E_0. The transmission coefficient is given by:

$$\kappa^{\mathrm{X}}(T) = \beta \exp(\beta V_{\mathrm{a}}^{\mathrm{AG}}) \int_{E_0}^{\infty} dE P^{\mathrm{X}}(E) \exp(-\beta E) \tag{4.3}$$

where $\beta = (k_{\mathrm{B}}T)^{-1}$, k_{B} is the Boltzmann constant, and T is the temperature; $V_{\mathrm{a}}^{\mathrm{AG}}$ is the maximum of the ground-state vibrationally adiabatic potential; and $P^{\mathrm{X}}(E)$ is the ground-state semiclassical probability at energy E, which is approximated in the ZCT and SCT approximations as

$$P^{\mathrm{X}}(E) = \begin{cases} 0, & E < E_0 \\ \{1 + \exp[2\theta(\mathrm{E})]\}^{-1}, & E_0 \leq E \leq V_{\mathrm{a}}^{\mathrm{AG}} \\ 1 - P^{\mathrm{X}}(2V_{\mathrm{a}}^{\mathrm{AG}} - E), & V_{\mathrm{a}}^{\mathrm{AG}} \leq E \leq 2V_{\mathrm{a}}^{\mathrm{AG}} - E_0 \\ 1, & 2V_{\mathrm{a}}^{\mathrm{AG}} - E_0 < E \end{cases} \tag{4.4}$$

where $\theta(E)$ is the imaginary part of action integral. When $X = \mu$OMT, the tunneling probabilities are obtained as: [24]

$$P^{\mu\mathrm{OMT}}(E) = \max_{E} \begin{cases} P^{\mathrm{SCT}}(E) \\ P^{\mathrm{LCT}}(E) \end{cases} \tag{4.5}$$

where P^{LCT} is obtained from a more complicated expression than P^{SCT}.

In the LCT and LAT approximations, one must sum over tunneling probabilities from the ground state of the reactants to all accessible diabatic vibrational states of the product. In many cases, only the ground-state-to-ground-state process need be considered. Even when the excited states of the product must be considered, it is sufficient to consider the ground-state-to-ground-state case to explain the new algorithms being introduced here, and so we limit our consideration to the ground-state-to-ground-state case. (We previously found [23] that tunneling into excited vibrational states does not make a large contribution for the reactions under consideration here.)

For a given tunneling path, the imaginary part of the action integral is given by:

$$\theta(E) = \hbar^{-1} \int_{\xi_0}^{\xi_1} \mathrm{Im} p(\xi) d\xi \tag{4.6}$$

where ξ is a progress variable along the tunneling path; ξ_0 and ξ_1 mark the beginning and end of the tunneling path, respectively; and $\mathrm{Im}p(\xi)$ is the imaginary part of the momentum in the tunneling direction, which is written as:

$$p(\xi) = \{2\mu_{\mathrm{eff}}(\xi)[E - V_{\mathrm{eff}}(\xi)]\}^{1/2} \tag{4.7}$$

where $\mu_{\mathrm{eff}}(\xi)$ and $V_{\mathrm{eff}}(\xi)$ are respectively the effective reduced mass and the effective potential along the tunneling path. The calculation of the transmission coefficient of Eq. (4.3) requires the evaluation of tunneling probabilities at several energies, and these depend on the tunneling paths. For X = ZCT the tunneling path coincides with the MEP, and therefore the progress variable along the path is s, and the effective potential is given by the ground-state vibrationally adiabatic potential given by Eq. (4.2). The effective mass $\mu_{\mathrm{eff}}(s)$ equals μ. Therefore, in the ZCT approximation the action integral, at every tunneling energy, is given by:

$$\theta(E) = \hbar^{-1} \int_{\tilde{s}_0}^{\tilde{s}_1} ds \{2\mu(V_{\mathrm{a}}^{\mathrm{G}}(s) - E)\}^{1/2} \tag{4.8}$$

where $\tilde{s}_0$ and $\tilde{s}_1$ are the classical turning points in the reactant and product valleys, respectively. Both turning points obey the resonance condition:

$$V_{\mathrm{a}}^{\mathrm{G}}(\tilde{s}_0) = V_{\mathrm{a}}^{\mathrm{G}}(\tilde{s}_1) = E \tag{4.9}$$

and therefore it is equivalent to write $\theta(E)$ or $\theta(\tilde{s}_0)$ in Eq. (4.8).

The coupling between the reaction coordinate and the $F - 1$ other modes produces an internal centrifugal effect that shortens the dominant tunneling path at a given energy by displacing it toward the concave side of the MEP. The SCT approximation incorporates this effect in the effective mass for tunneling without an explicit evaluation of the tunneling path. The SCT action integral is given by:

$$\theta(E) = \hbar^{-1} \int_{\tilde{s}_0}^{\tilde{s}_1} ds \{2\mu_{\mathrm{eff}}(s)(V_{\mathrm{a}}^{\mathrm{G}}(s) - E)\}^{1/2} \tag{4.10}$$

It should be noticed that now the effective mass depends on the progress along the MEP and that $\mu_{\mathrm{eff}} \leq \mu$. For this reason the SCT transmission coefficient is always larger or equal than the ZCT transmission coefficient.

To evaluate the LAT tunneling probability, one must calculate the action integrals of a family tunneling paths that depend on a parameter α; these paths correspond to the MEP when $\alpha = 0$ and to the LCT path, which is a straight path, for $\alpha = 1$. Let $\xi_{\mathrm{P}}(0)$ be the length of the tunneling path along the MEP from $\tilde{s}_0$ to $\tilde{s}_1$ (this is equal to $\tilde{s}_1 - \tilde{s}_0$), and let $\xi_{\mathrm{P}}(1)$ be the length of the straight-line path, which is shorter. Then, the geometry of a point on the path with parameter α is given by

$$\mathbf{x}\left[\alpha, \xi(\alpha), \tilde{s}_0\right] = (1 - \alpha)\mathbf{x}\left[0, \xi(0), \tilde{s}_0\right] + \alpha\mathbf{x}\left[1, \xi(1), \tilde{s}_0\right] \tag{4.11}$$

where $\mathbf{x}\left[0, \xi(0), \tilde{s}_0\right]$ and $\mathbf{x}\left[1, \xi(1), \tilde{s}_0\right]$ are respectively geometries on the MEP and on the straight path; thus $\xi(1)$ is equal to $\xi(0)$ times the ratio of $\xi_{\mathrm{P}}(1)$ to $\xi_{\mathrm{P}}(0)$. Consequently, the progress variable ξ depends on the value of the α parameter, and $\xi(1)$ is less than or equal to $\xi(\alpha)$, which is less than or equal to $\xi(0)$. The probabilities along the series of paths of Eq. (4.11) may involve regions of the PES that are vibrationally nonadiabatic (see Refs. [17, 131] for details), so in general the action integral is split into three terms:

$$\theta(\alpha, E) = \theta_{\mathrm{I}}(\alpha, E) + \theta_{\mathrm{II}}(\alpha, E) + \theta_{\mathrm{III}}(\alpha, E) \tag{4.12}$$

The action integrals $\theta_i(\alpha, E)$, with i equal to I and III correspond to the adiabatic regions on the reactants side ($i = \mathrm{I}$) and on the products side ($i = \mathrm{III}$), respectively, and they are given by the following expressions:

$$\theta_{\mathrm{I}}(\alpha, E) = \hbar^{-1} \int_0^{\xi_{\mathrm{I}}(\alpha)} d\xi(\alpha) \left\{ V_{\mathrm{a}}^{\mathrm{G}} \left[s_{\mathrm{I}}(0, \xi(0)); \tilde{s_0} \right] - V_{\mathrm{a}}^{\mathrm{G}}(\tilde{s_0}) \right\}^{1/2} \cos \chi_0, \tag{4.13}$$

$$\theta_{\mathrm{III}}(\alpha, E) = \hbar^{-1} \int_{\xi_{\mathrm{III}}(\alpha)}^{\xi_{\mathrm{P}}(\alpha)} d\xi(\alpha) \left\{ V_{\mathrm{a}}^{\mathrm{G}} \left[s_{\mathrm{III}}(0, \xi(0)); \tilde{s_0} \right] - V_{\mathrm{a}}^{\mathrm{G}}(\tilde{s_0}) \right\}^{1/2} \cos \chi_1 \tag{4.14}$$

The total length of the path is $\xi_{\mathrm{P}}(\alpha)$; and the values $\xi_{\mathrm{i}}(\alpha)$ $i = \mathrm{I}, \mathrm{III}$ indicate boundaries of the adiabatic region. Each of the $s_i(0, \xi(0))$, $i = \mathrm{I}, \mathrm{III}$ values needed for the evaluation of the vibrationally adiabatic potentials $V_{\mathrm{a}}^{\mathrm{G}} \left[s_i(0, \xi(0)); \tilde{s_0} \right]$ is obtained in such a way that the vector defined by the geometry $\mathbf{x} \left[\alpha, \xi(\alpha), \tilde{s}_0 \right]$ and the reaction path geometry $\mathbf{x} \left[0, \xi(0), \tilde{s}_0 \right]$ is perpendicular to the derivative of $\mathbf{x} \left[0, \xi(0), \tilde{s}_0 \right]$ with respect to s at that s value, i.e.,

$$\left\{ \mathbf{x} \left[\alpha, \xi(\alpha), \tilde{s}_0 \right] - \mathbf{x} \left[0, \xi(0), \tilde{s}_0 \right] \right\} \cdot \frac{\mathrm{d}\mathbf{x} \left[0, \xi(0), \tilde{s}_0 \right]}{\mathrm{d}s} = 0 \tag{4.15}$$

The angles between the gradient and tangent vector to the path at $\tilde{s_0}$ and $\tilde{s_1}$ are χ_0 and χ_1, respectively. If the entire path is adiabatic (i.e., if there is no region II) there will be overlap between regions I and III in the interval $\xi_{\mathrm{III}}(\alpha) \leq \xi(\alpha) \leq \xi_{\mathrm{I}}(\alpha)$ and the vibrationally adiabatic potential in that region is taken to be

$$\min \left\{ V_{\mathrm{a}}^{\mathrm{G}} \left[s_{\mathrm{I}}(0, \xi(0)); \tilde{s_0} \right], V_{\mathrm{a}}^{\mathrm{G}} \left[s_{\mathrm{III}}(0, \xi(0)); \tilde{s_0} \right] \right\} \tag{4.16}$$

The action integral through the nonadiabatic region is given by:

$$\theta_{\mathrm{II}}(\alpha, E) = \hbar^{-1} \int_{\xi_{\mathrm{I}}(\alpha)}^{\xi_{\mathrm{III}}(\alpha)} d\xi(\alpha) \left\{ V_{\mathrm{eff}}^{\mathrm{II}}(\alpha, \xi(\alpha), \tilde{s_0}) - V_{\mathrm{a}}^{\mathrm{G}}(\tilde{s_0}) \right\}^{1/2} \tag{4.17}$$

The effective potential $V_{\mathrm{eff}}^{\mathrm{II}}(\alpha, \xi(\alpha), \tilde{s_0})$ is obtained from

$$\begin{aligned} V_{\mathrm{eff}}^{\mathrm{II}}(\alpha, \xi(\alpha), \tilde{s_0}) &= V \left\{ \mathbf{x} \left[\alpha, \xi(\alpha), \tilde{s_0} \right] \right\} + V_{\mathrm{corr}}^{\mathrm{I}}(\alpha, \xi_{\mathrm{I}}(\alpha), \tilde{s_0}) + V_{\mathrm{anh}}^{\mathrm{I}}(\alpha, \tilde{s_0}) \\ &+ \frac{\xi(\alpha) - \xi_{\mathrm{I}}(\alpha)}{\xi_{\mathrm{III}}(\alpha) - \xi_{\mathrm{I}}(\alpha)} \left[V_{\mathrm{corr}}^{\mathrm{III}}(\alpha, \xi_{\mathrm{III}}(\alpha), \tilde{s_0}) - V_{\mathrm{corr}}^{\mathrm{I}}(\alpha, \xi_{\mathrm{I}}(\alpha), \tilde{s_0}) + V_{\mathrm{anh}}^{\mathrm{III}}(\alpha, \tilde{s_0}) - V_{\mathrm{anh}}^{\mathrm{I}}(\alpha, \tilde{s_0}) \right] \end{aligned} \tag{4.18}$$

In this expression the potentials $V_{\mathrm{corr}}^{i}(\alpha, \xi_i(\alpha), \tilde{s_0})$, $i = \mathrm{I}, \mathrm{III}$ correct for the zero-point energy in the modes that still behave adiabatically. The potentials $V_{\mathrm{anh}}^{i}(\alpha, \tilde{s_0})$ incorporate anharmonic nonquadratic corrections to the effective potential in the same way as in eq 5 of the LCT method. [21] The geometries $\mathbf{x} \left[\alpha, \xi(\alpha), \tilde{s_0} \right]$, needed for the evaluation of the classical potential

$V\left\{\mathbf{x}\left[\alpha,\xi(\alpha),\tilde{s_0}\right]\right\}$, are obtained from the straight path joining the geometries $\mathbf{x}\left[\alpha,\xi_{\mathrm{I}}(\alpha),\tilde{s}_0\right]$ and $\mathbf{x}\left[\alpha,\xi_{\mathrm{III}}(\alpha),\tilde{s}_0\right]$, i.e.,

$$\mathbf{x}\left[\alpha,\xi(\alpha),\tilde{s}_0\right]=\mathbf{x}\left[\alpha,\xi_{\mathrm{I}}(\alpha),\tilde{s}_0\right]+\frac{\xi(\alpha)-\xi_{\mathrm{I}}(\alpha)}{\xi_{\mathrm{III}}(\alpha)-\xi_{\mathrm{I}}(\alpha)}\left(\mathbf{x}\left[\alpha,\xi_{\mathrm{III}}(\alpha),\tilde{s}_0\right]-\mathbf{x}\left[\alpha,\xi_{\mathrm{I}}(\alpha),\tilde{s}_0\right]\right) \tag{4.19}$$

We note that the LCT expressions are obtained for the effective potential of Eq. (4.18) and the action integrals of Eqs. (4.12), (4.13), (4.14), and (4.17) when $\alpha = 1$.

Converged probabilities at every tunneling energy are obtained by the numerical integration of Eqs. (4.13), (4.14), and (4.17) at N points along the path; for the present work we set $N = 180$. If there is a nonadiabatic region, then N_{I} of those N points belong to region I, N_{II} are in region II, and N_{III} are in region III. The potential in regions I or III is obtained from the vibrationally adiabatic potential along the MEP. However, the effective potential at the geometries obtained from Eq. (4.19) requires single-point calculations of the potential energy at points $\xi_i(\alpha),\ i=1,...,N_{\mathrm{II}}$, where $\xi_1(\alpha)=\xi_{\mathrm{I}}(\alpha)$ and $\xi_{\mathrm{N_{II}}}(\alpha)=\xi_{\mathrm{III}}(\alpha)$. We found that the evaluation of the LCT transmission coefficients by the interpolated large-curvature tunneling algorithm based on one-dimensional interpolation (ILCT1D) [22] of these potential energies almost perfectly reproduces the specifically calculated potentials $V\left\{\mathbf{x}\left[1,\xi(1),\tilde{s_0}\right]\right\}$ when the N_{II} points are replaced by $N_{\mathrm{S}} = 9$ equally spaced points which are interpolated by a one-dimensional spline-under-tension. [140, 141] If, at a given tunneling energy, $N_{\mathrm{II}} < 9$ then no interpolation is carried out along the nonadiabatic region of the tunneling path. Similarly, the above procedure can be used to obtain the LAT transmission coefficients; the only difference being that now N_{S} points are used to evaluate the α-dependent effective potential of Eq. (4.18). We call this algorithm the interpolated least-action tunneling method based on one-dimensional interpolation (ILAT1D).

The calculation of transmission coefficients by the full-LAT method (without any interpolation) using direct dynamics requires a large amount of computer time, so we tested the performance of the ILAT1D algorithm by using analytical PESs. We used the same analytical PESs as for the testing of the ILCT1D method and found that the mean unsigned percentage error (MUPE) of the ILAT1D algorithm with respect to a full LAT calculations (as a reference) is smaller than 0.20% in the interval from $T = 200$ to 400 K (see Appendix A for further details of these tests). Therefore, we believe that the transmission coefficients obtained by the ILAT1D algorithm can safely replace full LAT calculations without loss of accuracy. Hereafter, we use the ILAT1D algorithm as a reference in the development of more approximate algorithms, as discussed below.

The ILAT1D algorithm is still very expensive in computer time, since the value, $\tilde{\alpha}$, of α that minimizes the action of Eq. (4.12) is obtained by a golden section search [142] at every tunneling energy. Therefore, we developed another, even more efficient algorithm that further reduces the number of tunneling energies at which the least-action integral, $\theta(\tilde{\alpha}, E)$, has to be explicitly computed. The method is described next.

In the ILAT1D algorithm the least-action integral is evaluated at tunneling energies $E_i,\ i = 1,\ldots,M$, with E_1 being the lowest energy at which it is possible to locate the classical turning points that determine the straight path and M being the number of tunneling energies (all below the maximum of the vibrationally adiabatic potential) at which the tunneling probabilities are calculated. In general one has $40 \leq M \leq 80$. The tunneling energies that are computationally most demanding are those for which there is a nonadiabatic region for some of the possible tunneling paths. It should be noticed that the absence of nonadiabatic region at a given tunneling energy along the LCT path means also the absence of nonadiabatic regions at any of the α-dependent paths at that tunneling energy and that makes the LAT and LCT probabilities to coincide. The potential in the adiabatic region is readily available, because it can be obtained from information along the MEP. Therefore the effort in developing the more efficient algorithm is focused on the E_i, $i = 1, \ldots, M_{\text{II}}$ tunneling energies with nonadiabatic regions along the straight path, where $E_{i=M_{\text{II}}}$ is the highest tunneling energy for which there is a nonadiabatic region along the LCT path. It is possible to reduce computer time by explicitly evaluating the least-action integral at M_{S} tunneling energies instead of at M_{II} tunneling energies. The remaining least-action integrals are obtained implicitly by interpolation with a one-dimensional spline-under-tension. The M_{S} tunneling energies are chosen in such a way that E_1 and $E_{M_{\text{II}}}$ are the first and last energies of the fit, respectively, and the remaining $M_{\text{S}} - 2$ energies are taken as equally spaced between those two values. (We also considered interpolating $\tilde{\alpha}$ instead of $\theta(\tilde{\alpha}, E)$, but we found, as shown in Section 4.3, that the latter is a much better choice because $\theta(\tilde{\alpha}, E)$ changes smoothly with the tunneling energy.) In summary, the new algorithm uses one-dimensional interpolation for both the tunneling paths and the optimized action integrals, and therefore we call the method the double interpolated least-action tunneling (DILAT) method.

The remaining steps are explained fully in previous discussions of the LCT and LAT methods [17, 87, 131, 143] and so are only briefly summarized here. The least-action integrals obtained at every tunneling energy are used to compute tunneling amplitudes defined by

$$T_{\text{tun}}^{\text{LAT}}(\tilde{\alpha}, \tilde{s_0}) = T_{\text{tun}}^{\text{LAT}}(\tilde{\alpha}, \tilde{s_1}) = \exp\left[-\theta(\tilde{\alpha}, \tilde{s_0})\right] \tag{4.20}$$

The LAT primitive probability at every tunneling energy, using either the ILAT1D or the DILAT algorithm, is obtained from the tunneling amplitude of Eq. (4.20) plus the contribution due to the vibrational motion perpendicular to the reaction coordinate along the incoming and outgoing trajectories. The LAT primitive probability is then uniformized such that it goes to 1/2 at the maximum of the ground-state vibrationally adiabatic potential. The resulting LAT tunneling probabilities are also used for the calculation of the nonclassical over-the-barrier tunneling probabilities, as in Eq. (4.4).

Note the the μOMT transmission coefficient is always equal to both the SCT and LCT ones, and the LAT transmission coefficient is always great than or equal to the LCT one. However, the LAT transmission coefficient can be either greater than or smaller than the SCT one, because the LAT paths lie between the MEP and LCT paths, but the LAT method does not incorporate the small-curvature limit explicitly.

A full calculation of the LAT transmission coefficients scales as $M \times N \times L$, since for each of the M tunneling energies, we need to perform L iterations to obtain a converged least-action integral on tunneling paths obtained with N single-point calculations. Typical values for these parameters are $M = 60$, $N = 180$ and $L = 25$, which involves approximately 3×10^5 single-point energy calculations. Many of those points fall in the adiabatic regions, so they can be readily calculated from the information available along the MEP, and only the evaluation of the effective potential of nonadiabatic region II requires additional direct dynamics electronic structure calculations. The number of points in the nonadiabatic region in the full calculation would be $M_{\text{II}} \times \bar{N}_{\text{II}} \times L$, where $\bar{N}_{\text{II}}$ is the average of nonadiabatic points at every tunneling energy. The size of the nonadiabatic region depends on the PES, but reasonable numbers for M_{II} and $\bar{N}_{\text{II}}$ are 40 and 50, respectively, and therefore the number of single point calculations in the nonadiabatic region is approximately 5×10^4. The ILAT1D algorithm reduces the number of single point calculations to $M_{\text{II}} \times N_S \times L$ such that it requires approximately 9000 single point calculations in the nonadiabatic region. The DILAT algorithm reduces further the number of single-point calculations by the ratio M_{II}/M_S.

The ILAT1D and the DILAT algorithms for the calculation of LAT transmission coefficients using direct dynamics have been implemented in a development version of POLYRATE [102], and we plan that they will be made available in an upcoming new version of the program.

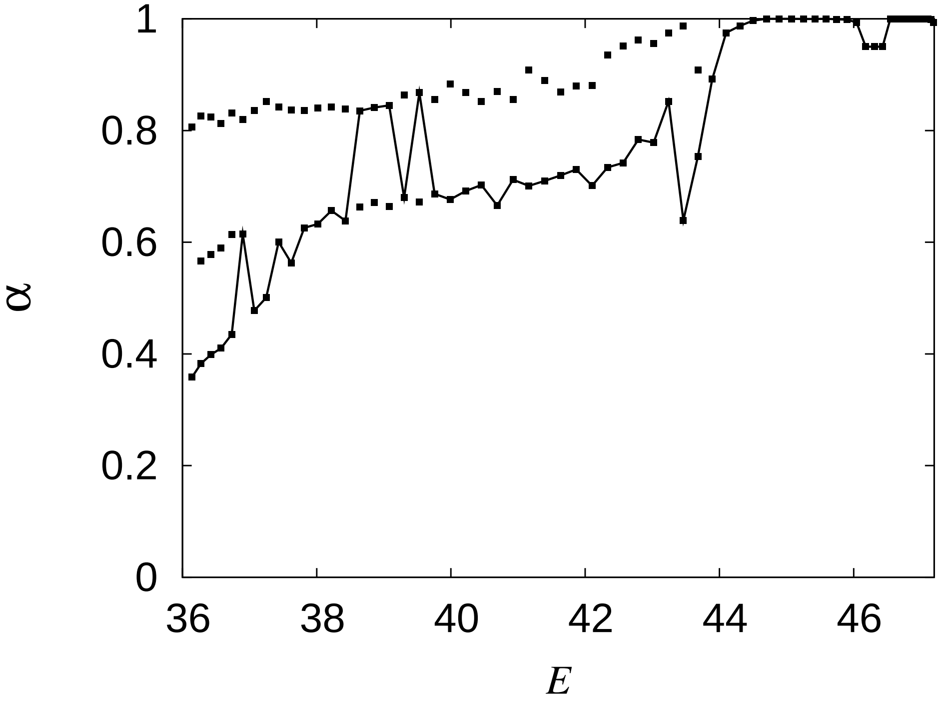

Figure 4.1: Plot of the α parameter versus the tunneling energy (E, in kcal·mol^{-1}) relative to the reactants at their equilibrium separation without zero point energy. The dots correspond to the values of α at which there are local minima of the imaginary action integral at every of the calculated tunneling energies. The solid line joins the global minimum of the α parameter, $\tilde{\alpha}$, at every tunneling energy.

4.3. Applications

The electronic structure calculations needed for the evaluation of LAT transmission coefficients for reactions R1 to R4 using the ILAT1D and DILAT algorithms were performed with the MPWB1K [144] density functional using the 6-31+G(d,p) basis set. [145] The details of the electronic structure calculations can be found in Ref. [23]. The previous calculations showed that the maximum of the vibrationally adiabatic potential occurs at the saddle point, that is, $V_{\mathrm{a}}^{\mathrm{AG}} = V_{\mathrm{a}}^{\ddagger\mathrm{G}}$, and that there are no variational effects in the interval of temperatures between 200 and 700 K, so the variational dividing surface is located at the conventional transition state. Besides, $\kappa^{\mathrm{CVT/X}}(T)$ of Eq. (4.1) equals $\kappa^{\mathrm{X}}(T)$ because $\kappa^{\mathrm{CVT/CAG}}(T) = 1$.

Figure 4.1 shows that the values of $\tilde{\alpha}$ at different tunneling energies may change abruptly, which makes a fit of $\tilde{\alpha}$ as a function of tunneling energy quite difficult and inaccurate, and instead we chose to interpolate the action integrals corresponding to $\tilde{\alpha}$. It is noteworthy that

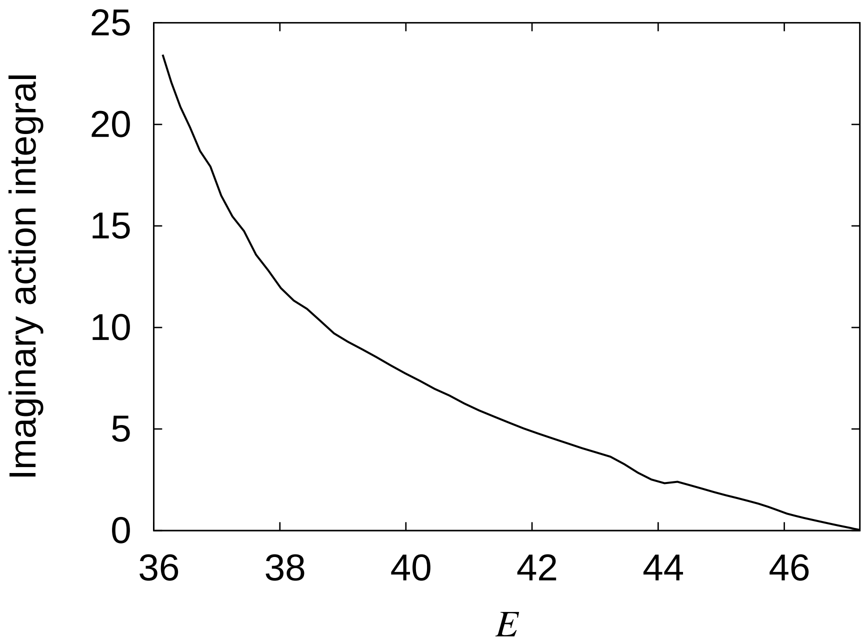

Figure 4.2: The solid line shows the variation of the imaginary action integral, $\theta(\tilde{\alpha}, E)$, of Eq. (4.12) with the tunneling energy (in kcal·mol^{-1}).

there are several tunneling energies with two or even three local minima for the imaginary action integral. However, even in this difficult case, an interpolation of the least-action integral as a function of tunneling energy is easier to perform than an interpolation of $\tilde{\alpha}$ due to the smooth behavior of $\theta(\tilde{\alpha}, E)$, as shown in Figure 4.2.

Table 4.1 lists the number of single-point calculations needed to evaluate the effective potential of Eq. (4.18) for R1 for the calculation of the LAT transmission coefficients with the ILAT1D and DILAT algorithms (the number of points for R2, R3, or R4 is similar than for R1 and is not shown in the table). We use as reference calculations those obtained by the ILAT1D algorithm. The ILAT1D algorithm allows one to obtain LAT transmission coefficients 7.5 times faster than the full LAT calculation. In this case the DILAT algorithm is 50 and 20 times faster than the full calculation for $M_S = 7$ and 17 points, respectively. The next step would be to test the accuracy of the LAT transmission coefficients by the DILAT algorithm by finding the optimum number of M_S points that give the best compromise between accuracy and computational cost. The procedure to obtain the transmission coefficients was the one described in the previous section, i.e., a set of $\theta(\tilde{\alpha}_r, E_r)$ values at energies $E_r,\ r = 1, \ldots, M_S$ is chosen, with $E_{r=1}$ being the lowest tunneling energy at which it is possible to locate the classical turning points on the MEP for defining the straight path and $E_{r=M_S}$ being the last tunneling energy at which there is a nonadiabatic region along the straight path.

The deviation from the ILAT1D values of the DILAT transmission coefficients for different numbers of fitting points is given in Table 4.2 and plotted in Figure 4.3 for reactions R1 to R4. For the present study we have considered temperatures from 250 to 400 K, which for many practical applications is the temperature range for which one needs to evaluate the tunneling. At T = 250 K the smallest value of M_{S} that yields an accuracy better than 5%

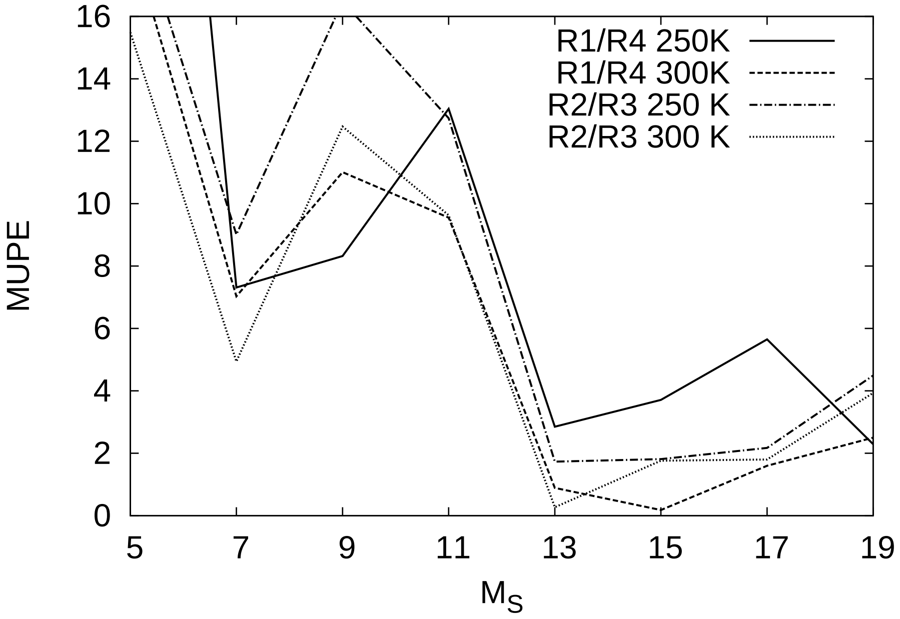

Figure 4.3: MUPEs for $\eta_{1,4}$ and $\eta_{2,3}$ KIEs R1 to R4 obtained by the DILAT algorithm using different fitting points to a spline-under-tension with respect to those LAT values obtained with the ILAT1D algorithm. The solid line plots the MUPE obtained at T = 250 and 300 K.

is M_S = 13 (and an interpolation with this value is hereafter called DILAT(13)). However, the interpolation using M_S = 7 (hereafter DILAT(7)), although it gives MUPES about three times larger than DILAT(13), yields small errors when compared with M_S = 9 or M_S = 11 points and is about two times faster than DILAT(13), so comparisons involving both of them are interesting. At T=300 K all the MUPEs are smaller, with the largest errors for DILAT(7) and DILAT(13) being 6% and 1.7%, respectively. For reactions R1 to R1 Table 4.3 shows the DILAT(7) and DILAT(13) transmission coefficients together with the reference ILAT1D transmission coefficients.

In general Table 4.2 shows convergence to about 5% at 250 K and to about 1% at 300 K.

Table 4.1: Number of single-point calculations (NSP) in the nonadiabatic region needed for the calculation of the LAT transmission coefficients with selected values of M_S for reaction R1

Level	M_S	NSP
Full	43	137895
ILAT1D	43	18564
DILAT	7	2809
	9	3699
	13	5165
	17	7264

Table 4.2: MUPEs for reactions R1 to R4 of the LAT transmission coefficients obtained by DILAT for different numbers of fitting points, M_S, when compared with ILAT1D reference values

	MUPE			
M_S	R1	R2	R3	R4
T = 250 K				
5	16.56	17.76	1.70	18.11
7	7.88	7.12	2.08	0.61
9	9.54	11.32	6.17	1.33
11	9.00	12.12	0.54	3.58
13	0.51	1.28	3.06	2.27
15	1.74	2.59	0.77	5.25
17	0.51	2.15	0.02	4.86
19	3.68	5.10	0.63	5.83
T = 300 K				
5	13.06	14.12	1.19	4.62
7	6.06	5.20	0.27	1.04
9	9.85	9.90	2.93	1.31
11	8.79	9.31	0.29	0.69
13	1.30	1.67	1.39	0.40
15	1.39	2.13	0.36	1.21
17	0.61	1.79	0.01	0.97
19	4.02	4.28	0.36	1.56

The transmission coefficients are compared in Table 4.3. To compute the KIEs $\eta_{1,4}(T) \equiv k_{R1}(T)/k_{R4}(T)$ and $\eta_{2,3}(T) \equiv k_{R2}(T)/k_{R3}(T)$ using several tunneling approximations we have factored them into two contributions,

$$\eta^{\mathrm{TST/X}}(T) = \eta^{\mathrm{X}}_{\mathrm{tun}}(T)\eta^{\mathrm{TST}}(T) \tag{4.21}$$

In Eq. (4.21) $\eta^{X}_{\mathrm{tun}}(T)$ includes quantum effects (tunneling plus nonclassical reflection) on the reaction coordinate using the approximation X, where X = SCT, LCT, μOMT, or LAT, and $\eta^{\mathrm{TST}}(T)$ includes the symmetry numbers, the classical translational and rotational contributions, and the quasiclassical quantized vibrational contribution. (There is no potential energy contribution in the cases considered here because the variational transition state is the conventional transition state for these reactions.)

Table 4.4 lists the KIEs obtained by the different tunneling approximations together with the experimental [146, 147] data. In general, all the methods underestimate the observed KIEs although the ones obtained with the LAT approximation for tunneling are in better agreement with experimental values. The LCT transmission coefficients may underestimate the tunneling contribution in same cases, as was pointed out by Sansón *et al.*[107], however the KIEs obtained by this approximation are quite similar to the LAT ones. The μOMT approximation gives similar results to those obtained with the LAT approximation for the hydrogen abstraction processes, but it gives larger values for the deuterium transfer. Therefore, this discrepancy is due to the magnitude of the SCT transmission coefficients for deuterium transfer, which has the effect of decreasing the calculated KIEs. In any case the $\eta_{2,3}(T)$ KIEs calculated using the LAT

Table 4.3: Transmission coefficients for reactions R1 to R4

Reaction	T(K)	SCT	LCT[a]	μOMT[a]	LAT[b]		
			ILCT2D		DILAT(7)	DILAT(13)	ILAT1D
R1	250	21.9	28.1	31.4	39.4	36.1	36.3
	300	9.18	9.26	10.7	11.6	10.7	10.9
	350	5.32	4.97	5.78	5.75	5.43	5.52
	400	3.69	3.37	3.88	3.73	3.57	3.62
	500	2.37	2.16	2.42	2.28	2.22	2.25
R2	250	16.1	15.8	18.2	19.6	18.0	18.2
	300	7.40	6.83	7.91	7.79	7.27	7.39
	350	4.54	4.13	4.74	4.50	4.27	4.33
	400	3.27	2.98	3.36	3.16	3.03	3.07
	500	2.18	2.02	2.22	2.09	2.03	2.06
R3	250	15.2	10.7	16.0	11.8	11.7	12.1
	300	6.52	4.60	6.68	4.84	4.76	4.83
	350	3.94	2.92	3.98	3.00	2.98	2.99
	400	2.85	2.22	2.86	2.26	2.24	2.25
	500	1.95	1.64	1.95	1.66	1.65	1.65
R4	250	14.3	10.3	15.3	11.7	11.9	11.6
	300	6.29	4.49	6.47	4.65	4.68	4.70
	350	3.85	2.87	3.90	2.92	2.92	2.83
	400	2.80	2.20	2.82	2.22	2.22	2.22
	500	1.93	1.63	1.93	1.64	1.64	1.64

[a] From Ref. [23]. There are errors in Table 7 of Ref. [23]; the correct values of the LCT and μOMT transmission coefficients are listed here.

[b] LAT transmission coefficients.

approximation for tunneling are still too small when compared to the available experimental data. From these values we arrive to the same conclusions as in Ref [23], i.e., at the moment we cannot explain this discrepancy, and we encourage further experiments on these systems.

Finally, it is interesting to analyze the errors (with respect to a ILAT1D calculation) of the DILAT method, not just in the case of the transmission coefficients, but also in the context of the KIEs. In the worst scenario the largest error in the evaluation of the KIEs would be the sum of the MUPEs, i.e., assuming no error cancellation. Using this worst-case possibility, we establish a maximum error of the DILAT(7) algorithm at T = 250 K of 9% for $\eta_{1,4}(T)$ and $\eta_{2,3}(T)$. For DILAT(13), these errors go down to 3% and 4% for $\eta_{1,4}(T)$ and $\eta_{2,3}(T)$, respectively. In round numbers, the errors of the DILAT(7) and DILAT(13) algorithms, at T = 250 K, are smaller than 10% and 5%, respectively. In fact the errors, as shown in Figure 4.3, due to error cancellation are 7% and 4% for $\eta_{1,4}(T)$ and 9% and 2% for $\eta_{2,3}(T)$ using DILAT(7) and DILAT(13), respectively.

At $T = 300$ K, if we assume no error cancellation, the MUPEs for $\eta_{1,4}(T)$ and $\eta_{2,3}(T)$ would be about 7% and 3% for DILAT(7) and DILAT(13), respectively. Similar calculated errors are obtained for DILAT(7), but when using DILAT(13) the calculated MUPEs are less than 1% for both of the two evaluated KIEs. These results are very encouraging, especially when we

Table 4.4: Calculated KIEs using various approximations for tunneling. The last column lists the experimental KIEs

T(K)	$\eta^{\mathrm{TST}}(T)$	$\eta^{\mathrm{TST/SCT}}(T)$	$\eta^{\mathrm{TST/LCT}}(T)$	$\eta^{\mathrm{TST/\mu OMT}}(T)$	$\eta^{\mathrm{TST/LAT}\ a}(T)$			$\eta_{\mathrm{exp(T)}}{}^{b}$
				R1/R4				
250	7.8	11.9	21.3	16.0	26.3	23.7	24.4	–
300	5.8	8.4	11.9	9.6	14.5	13.3	13.5	–
350	4.6	6.4	8.0	6.8	9.1	8.6	9.0	–
400	3.9	5.1	6.0	5.4	6.5	6.3	6.4	6.5^{c}
500	3.0	3.7	4.0	3.8	4.2	4.1	4.1	4.8^{c}
				R2 / R3				
250	5.7	6.0	8.4	6.5	9.4	8.8	8.6	–
300	4.4	5.0	6.5	5.2	7.1	6.7	6.7	–
350	3.7	4.3	5.3	4.4	5.7	5.3	5.4	13.0
400	3.2	3.6	4.3	3.2	4.5	4.3	4.4	8.5
500	2.6	2.9	3.2	3.0	3.3	3.2	3.2	5.0

[a] LAT transmission factors obtained with DILAT(7), DILAT(13) and ILAT1D algorithms are listed in columns 6, 7 and 8, respectively.

[b] From Refs. [146] and [147].

[c] Erratum in Table 8 of Ref. [23]; the correct values of the experimental KIEs are listed here.

take into account that the DILAT(7) and DILAT(13) methods are, respectively, 6.6 and 3.6 times faster than ILAT1D and about 50 and 30 times faster than the full (uninterpolated) calculation. It should also be noticed that this is a difficult case with two or three minima in the action integral at every tunneling energy, so for reactions with a less abrupt PES, the errors are expected to be smaller. The present results show that the DILAT(13) algorithm is reliable above $T = 250$ K to within 5% for the cases studied, although more testing would be needed to make broadly applicable statements of this nature.

4.4. Concluding remarks

We have presented two algorithms for efficient direct dynamics evaluation of the LAT transmission coefficients for polyatomic reactions. The interpolated least-action tunneling method based on one-dimensional interpolation (ILAT1D) uses the same philosophy as the previous ILCT1D algorithm; in particular, both make use of spline-under-tension interpolations for the effective potentials in the nonadiabatic regions of the tunneling paths. This algorithm, depending on the system, is about 5 to 10 times faster than the full calculation without loss of accuracy. However, the ILAT1D procedure is still quite expensive for polyatomic systems, so we have developed a much less expensive algorithm called double interpolated least-action tunneling, DILAT, which employs one-dimensional interpolations of not only the effective potential along nonadiabatic portions of the tunneling paths but also of the values of the action integrals as functions of energy; this even simpler method still provides quite accurate results. The performance of the DILAT algorithm was tested for four hydrogen/deuterium abstraction reactions and we found that the optimum number of effective potential energies to be calculated in the nonadiabatic region is $M_S = 13$. The DILAT method based on 13 tunneling energies can be from 3 to 5 times faster than the ILAT1D algorithm, depending on the characteristics of the nonadiabatic region, but with an error of less than 5%. The method is being incorporated into the POLYRATE computer program.

The LAT calculations do not account for the discrepancy from experimental $\eta_{2,3}(T)$ KIEs of the previously computed KIEs that were based on the less accurate LCT approximation. This discrepancy remains unexplained.

Chapter 5

Tunneling transmission coefficients for large systems

The accurate evaluation of quantum effects is of great importance in many reaction processes. Variational transition state theory with multidimensional tunneling is the natural choice for the study of these reactions, because it incorporates quantum effects through a multiplicative transmission coefficient and it can deal with large systems. Currently, the main approximation used for taking into account tunneling is the small-curvature approximation, mainly because the large curvature and the least-action approximations are computationally very demanding and their use it is usually associated to small systems. Here we describe two algorithms based on splines under tension, which allow the evaluation of these two transmission coefficients for large systems. The analysis of kinetic isotope effects on a model reaction show that the least-action transmission coefficient should be used instead of the more inexpensive, but probably less accurate small curvature transmission coefficient.

5.1. Introduction

The contribution of the theoretical methods to the understanding of complex reaction mechanisms relies on both, the accuracy of the electronic structure calculations and the reliability of the dynamics models. The electronic structure calculations provide us with the potential energy surface and the thermochemistry of the reaction, whereas the dynamics models provide us with the kinetic parameters (for instance, thermal rate constants). There are reactions for which the thermochemical calculations are sufficient to disregard a given proposed mechanism, without proceeding further, i.e., it is enough to know the relative stability of all the stationary points (reactants, intermediates and transition states) to decide the reaction path. This is usually the case for reactions in which classical dynamics effects (recrossing) and/or quantum dynamics effects (tunneling) are not significant. Besides, if we need to evaluate the thermal rate constants, conventional transition state theory (CTST), [26, 27] which only requires information at reactants and the transition state, would be adequate. On the other hand, there are systems with a small number of atoms (about 6 or 7) for which it is now possible to evaluate accurately the thermal rate constants by quantum dynamical methods. However, there is a large number of chemical reactions which do not fall in any of these categories, i.e., they are too big to be treated by quantum dynamics and they present dynamical effects which cannot be handled by CTST. For instance, this is the case for most of the proton transfer reactions.

Proton transfer reactions are probably the most important group of processes that take place in Chemistry and Biology. [58, 59] Protons, because of their light weight, can undergo tunneling, i.e. they can penetrate quite easily through classically forbidden potential energy barriers. [49–53] Therefore, tunneling is a quantum mechanical effect that can not be taken into account by classical methods (like for instance, classical trajectories). On the other hand, the applicability of quantum dynamics is reduced to small systems, so we have to find alternative methodologies able to deal with tunneling in large systems. Methods based on semiclassical methods, such as the Wentzel-Kramers-Brillouin (WKB) approximation, [127] meet those requirements, they can be used for large systems and include quantum mechanical tunneling using classical concepts. In the WKB approximation tunneling is considered as the penetration through a barrier with negative kinetic energy so the momentum and the action are imaginary. Usually the error introduced by semiclassics regarding to quantum calculations is about 15%.

Variational transition state theory [16, 17, 29, 63–70] with multidimensional corrections for tunneling (VTST/MT) is a semiclassical (WKB like) theory based on CTST, which incorporates both classical dynamics effects (recrossing) and quantum mechanical tunneling. It has been tested against quantum mechanical calculations for several atom–diatom reactions and for the polyatomic $\mathrm{H} + \mathrm{CH}_4 \rightarrow \mathrm{H}_2 + \mathrm{CH}_3$ hydrogen abstraction reaction.[103] In general, the comparison showed a very good agreement, so it makes VTST/MT one of the most suitable candidates to study proton transfer reactions. It is not our intention to explain all the aspects related to VTST, which can be looked up in a recent review [17], so hereafter we focus mainly our attention onto the tunneling effect, since for most of the proton transfer reactions is a crucial phenomena.

The most common version of VTST is canonical variational transition state theory (CVT) [66, 77], in which the rate constants are calculated considering a fixed-temperature ensemble. The CVT/MT thermal rate constant, $k^{\mathrm{CVT/X}}$, is given by

$$k^{\mathrm{CVT/X}}(T) = \kappa^{\mathrm{CVT/X}}(T) k^{\mathrm{CVT}}(T) \tag{5.1}$$

where $k^{\mathrm{CVT}}(T)$ is the CVT thermal rate constant that minimizes the one-way flux from reactants to products through trial dividing surfaces that cross the reaction path at several points. The reaction path is chosen as the minimum energy path (MEP) in isoinertial coordinates,[73, 76] scaled to a reduced mass of μ, and the signed distance along this path is labeled as s. By convention $s = 0$ indicates the location of the transition state, whereas $s < 0$ and $s > 0$ correspond to the reactant and product sides, respectively. The $k^{\mathrm{CVT}}(T)$ rate constant is 'quasiclassical' because involves quantized vibrational partition functions in its evaluation. $\kappa^{\mathrm{CVT/X}}(T)$ is the transmission coefficient, which gives the tunneling contribution in the approximation X to the final rate constant. All the $3N$-7 normal modes perpendicular to the reaction coordinate ($3N$-6 in linear molecules), being N the number of atoms, are quantized (through the vibrational partition functions) and, therefore, the transmission coefficient takes into account the quantum effects associated to the reaction-coordinate motion. The transmission coefficients accompanying Eq. (8.1) are typically evaluated by any of the following approximations: zero-curvature tunneling (ZCT)[73], which neglects the coupling between the reaction coordinate and the transverse modes; small curvature tunneling (SCT), [18, 19, 84, 86–88] which incorporates such coupling, but considering that tunneling effect is not too large; large-curvature tunneling (LCT), [16, 17, 20, 21, 24, 87, 90–92] which considers straight trajectories as the tunneling paths and it was specially designed for reactions with important quantum effects; the microcanonically optimized multidimensional tunneling (μOMT), [24] which is the best compromise, at every tunneling energy between SCT and LCT and; the least-action tunneling (LAT), [25, 97, 131] which samples a given family of paths between the ZCT and LCT paths with the objective of seeking the path that minimizes the imaginary action. Very recently we have extended the range of application of the LAT method to polyatomic reactions. [131] A more detailed description of these methods is presented in Section 5.2.

The LCT and LAT transmission coefficients are computationally quite demanding, which makes SCT the most practical choice for large systems. This technical problem has led to a misuse of the SCT approximation in some cases. An important group of proton transfer processes, which certainly would benefit from a greater availability of the LCT and LAT transmission coefficients, are the enzymatic reactions, because there are many enzymes for which the rate-determining step for reaction is the proton transfer between the enzyme and the substrate. One of the main experimentally determined kinetic parameters to get insight into the mechanism of the enzymatic catalysis is the analysis of intrinsic isotope effects (KIEs). In general, the isotopic substitution is carried out on the transferred atom, so the KIE is the ratio between the thermal rate constant for transfer of the root species (hydrogen) and that for transfer of the heavier isotope (deuterium or tritium). Nowadays it is quite established that quantum effects are of great importance in enzymatic proton transfer, [5, 57, 61, 148, 149] due mainly to the observation of abnormally large KIEs. This is usually considered one of the signatures of tunneling, since protons are lighter and pass through the barrier easier than the heavier isotopes. In general, although not always, [150–153] we expect tunneling to be more important for hydrogen than for deuterium. [154] We also expect LCT to be a better approximation for the hydrogen transfer than SCT, at least in some cases. Pang *et al.* found that tunneling dominates the proton transfer reaction from nicotinamide adenine dinucleotide (NADH) to enzyme-bound flavin mononucleotide (FMN) in the flavoprotein morphinose reductase. They also found that LCT described tunneling more adequately than SCT for the proton transfer, whereas SCT was more adequate for the deuteron transfer. This example shows the importance of making LCT and LAT computationally more accessible. This issue will be discussed in Section 5.3.

Finally in Section 5.4 we discuss briefly with an example the influence of the choice of the tunneling transmission coefficient over the computed KIEs.

5.2. Tunneling transmission coefficients

In VTST, the tunneling transmission coefficient [72–74] is evaluated as the ratio between the semiclassical adiabatic ground state (SAG) probability and the quasiclassical probability:

$$\kappa^{\mathrm{SAG}}(T) = \frac{\int_0^\infty dE P^{\mathrm{SAG}}(E)\exp(-\beta E)}{\int_{V_{\mathrm{a}}^{\mathrm{AG}}}^\infty dE P^{\mathrm{C}}(E)\exp(-\beta E)}, \tag{5.2}$$

where $P^{\mathrm{C}}(E)$ is the classical probability, which equals zero below $V_{\mathrm{a}}^{\mathrm{AG}}$ (the maximum of the vibrationally adiabatic potential) and unity otherwise, so the transmission coefficient can be written as:

$$\kappa^{\mathrm{SAG}}(T) = \beta\exp(\beta V_{\mathrm{a}}^{\mathrm{AG}})\int_0^\infty dE P^{\mathrm{SAG}}(E)\exp(-\beta E). \tag{5.3}$$

As shown in Eq. (5.2) and Eq. (5.3), the tunneling transmission coefficient is evaluated by using an effective potential that in the first approximation, is vibrationally adiabatic and harmonic with the further approximation [67] that the vibrationally adiabatic potential curves of all the vibrational excited states have the same shape as the ground-state vibrationally adiabatic potential curve, $V_{\mathrm{a}}^{\mathrm{G}}(s)$, so all the tunneling probabilities are evaluated with this potential, which is given by

$$V_{\mathrm{a}}^{\mathrm{G}}(s) = V_{\mathrm{MEP}}(s) + \frac{\hbar}{2}\sum_{m}\omega_m(s) \tag{5.4}$$

where $\omega_m(s)$ is the frequency of one of the $3N$-7 generalized normal modes at s. The semiclassical adiabatic probability of the ground state for tunneling $P^{\mathrm{SAG}}(E)$ is given by the semiclassical-WKB relation

$$P^{\mathrm{SAG}}(E) = \frac{1}{1+\exp\left[2\theta(E)\right]} \tag{5.5}$$

where $\theta(E)$ is the imaginary action integral:

$$\theta(E) = \hbar^{-1}\int_{\tilde{s}_0}^{\tilde{s}_1} ds\{2\mu_{\mathrm{eff}}(s)(V_{\mathrm{a}}^{\mathrm{G}}(s)-E)\}^{1/2} \tag{5.6}$$

where $\mu_{\mathrm{eff}}(s)$ is the effective mass of the tunneling motion, and $\tilde{s}_0$ and $\tilde{s}_1$ are the classical turning points at a given tunneling energy, E, in the reactant and product valleys, respectively. Both turning points obey the resonance condition:

$$V_{\mathrm{a}}^{\mathrm{G}}(\tilde{s}_0) = V_{\mathrm{a}}^{\mathrm{G}}(\tilde{s}_1) = E \tag{5.7}$$

The transmission coefficient does not include only tunneling but also the non-classical reflection above the barrier. Thus, the semiclassical probability for the whole range of energies is given by

$$P^{\mathrm{SAG}}(E) = \begin{cases} 0, & E < E_0 \\ \{1+\exp[2\theta(\mathrm{E})]\}^{-1}, & E_0 \leq E \leq V_{\mathrm{a}}^{\mathrm{AG}} \\ 1 - P^{\mathrm{SAG}}(2V_{\mathrm{a}}^{\mathrm{AG}} - E), & V_{\mathrm{a}}^{\mathrm{AG}} \leq E \leq 2V_{\mathrm{a}}^{\mathrm{AG}} - E_0 \\ 1, & 2V_{\mathrm{a}}^{\mathrm{AG}} - E_0 < E \end{cases} \tag{5.8}$$

where E_0 is the lowest energy at which it is possible to have tunneling.

When Eq. (5.6) is evaluated within the ZCT [73] approximation, there is no coupling between the reaction coordinate and the transverse modes and therefore the tunneling path follows the MEP. From the classical point of view the MEP is the most favorable path but the longest, because usually it involves a substantial motion of the heavy atoms which readjust their positions. However, the best tunneling path is the one that minimizes the imaginary action (maximizes the tunneling probability), i.e., the one with the best compromise between energy and length of the path. Currently, this transmission coefficient is calculated only for comparative purposes, because it has been shown that seriously underestimates the tunneling contribution[81, 82]. Marcus and Coltrin[18, 84] showed that the coupling between the reaction coordinate and the transverse modes shortens the tunneling path increasing the tunneling probability. They showed, that for the collinear $\mathrm{H} + \mathrm{H}_2$ reaction, the coupling curves the reaction path in such a way that the least-action path is obtained. The coupling can be incorporated as an effective mass into Eq. (5.6). Unfortunately the method could only handle cases in which the reaction path curvature was small, because when the reaction path curvature is large there is a singularity in the reaction path Hamiltonian due to the breakdown of the natural collision coordinates. Truhlar and coworkers [19, 86–88] modified the method (i.e. the effective mass) developing an analytical expression that avoids the singularity and extends its range of application to polyatomic reactions. This method is called the centrifugal-dominant small-curvature semiclassical adiabatic ground-state (CD-SCSAG) approximation or in abbreviated form the small-curvature tunneling (SCT) approximation. It should be noticed that the effective mass obtained by SCT is always smaller than (considers coupling) or equal to (neglects coupling) the mass of the transferred particle.

For a reaction of the type A + BC → AB + C, where A, B and C are atoms or groups of atoms, the reaction path curvature is a function of the skew angle, which in isoinertial coordinates (coordinates in which the kinetic energy consists of diagonal square terms) is given by

$$\beta = \cos^{-1}\left(\frac{m_{\mathrm{A}} m_{\mathrm{C}}}{(m_{\mathrm{A}} + m_{\mathrm{B}})(m_{\mathrm{B}} + m_{\mathrm{C}})}\right)^{1/2} \tag{5.9}$$

The skew angle is close to zero when the masses of A and C are much larger than the mass of B and it is close to 90 degrees when B has a much larger mass than A and C. Tunneling effects are more important for small skew angles because a light particle is being transferred between two atoms (i.e. heavy–light–heavy system)[89]. In those cases tunneling may be dominated by paths that lie very far from the MEP and the adiabatic approximation may breakdown. The large-curvature ground-state tunneling (LCT) method [16, 17, 20, 21, 24, 87, 90–92] considers the extreme case in which tunneling is dominated at every tunneling energy by paths that are straight trajectories between the two classical turning points. The geometries along a given straight path are given by

$$\mathbf{x}\left[\xi, \tilde{s}_0\right] = \mathbf{x}(\tilde{s}_0) + \frac{\xi}{\xi_{\mathrm{P}}}\left[\mathbf{x}(\tilde{s}_1) - \mathbf{x}(\tilde{s}_0)\right] \tag{5.10}$$

where $\mathbf{x}(\tilde{s}_0)$ and $\mathbf{x}(\tilde{s}_1)$ are the MEP geometries at the classical turning points. The parameter ξ indicates the progress along the straight path. The length of the path is given by

$$\xi_{\mathrm{P}} = \mid \mathbf{x}(\tilde{s}_1) - \mathbf{x}(\tilde{s}_0) \mid . \tag{5.11}$$

The evaluation of the action integrals along these paths requires not only information of the potential valley around the MEP, which can be treated within the adiabatic approximation, but also information about the reaction swath on the concave-side of the MEP, which is vibrationally nonadiabatic. The vibrationally adiabatic region in the reactants and products sides is labeled as I and III, respectively, whereas the nonadiabatic region is labeled as II (see Figure 5.1). The vibrationally adiabatic potential is obtained in such a way that the geometry $\mathbf{x}\left[\xi, \tilde{s}_0\right]$ is perpendicular to the gradient at that s value, i.e.,

$$\left\{\mathbf{x}\left[\xi, \tilde{s}_0\right] - \mathbf{x}(\tilde{s}_0)\right\} \frac{\mathrm{d}\mathbf{x}(\tilde{s}_0)}{\mathrm{d}s} = 0 \tag{5.12}$$

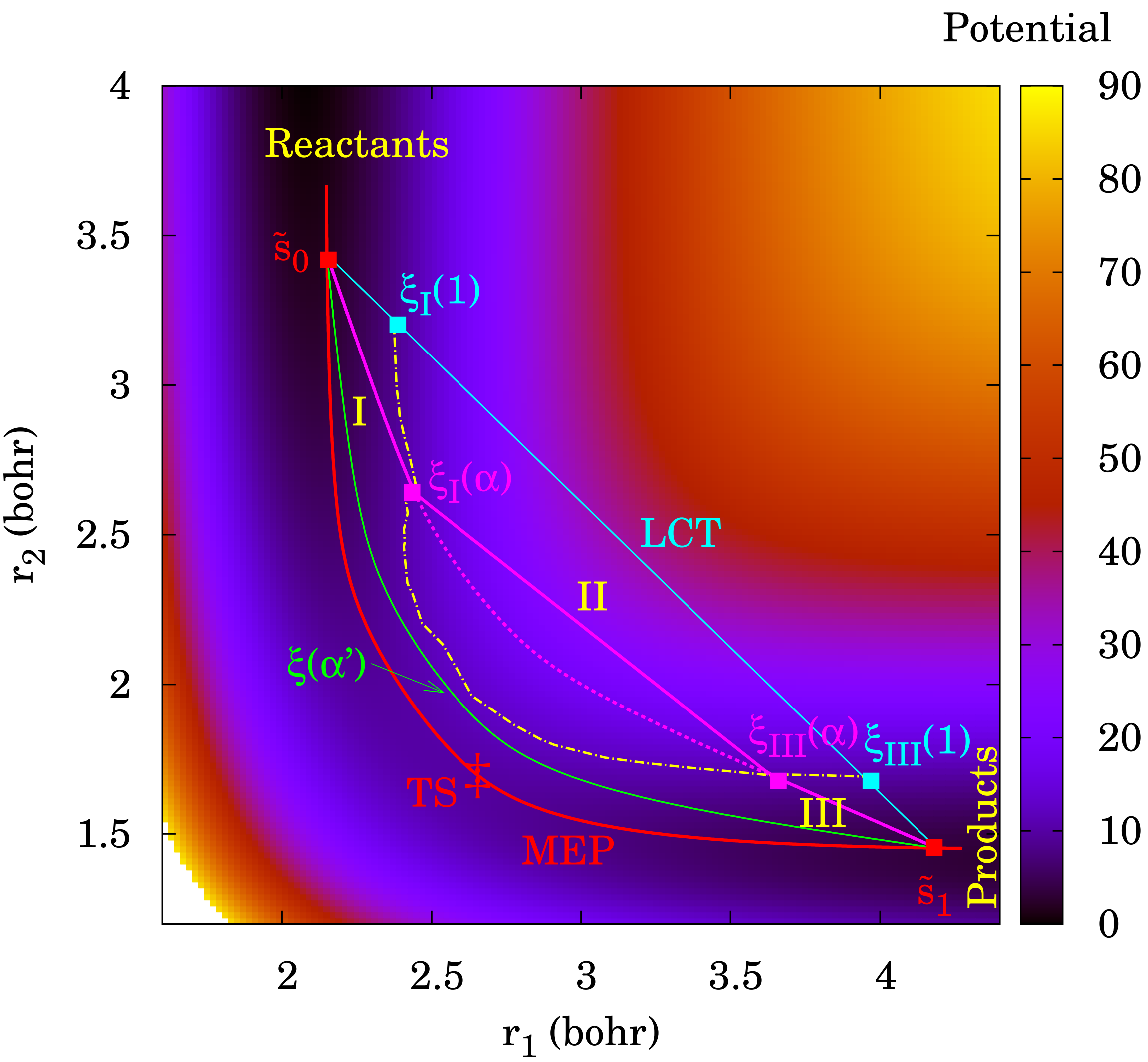

Figure 5.1: Generic contour plot of the PES of a bimolecular reaction as a function of to distances r_1 and r_2. The dashed-dotted yellow line divides the adiabatic region (labeled as I for reactants and III for products) from the non-adiabatic region (labeled as II). Four different tunneling paths are plotted: (i) The path with α=0, (red solid line) corresponds to the MEP. (ii) The path with α=0.12 (green solid line, labeled as $\xi(\alpha')$) corresponds to a curved path passing through a region, which is completely vibrationally adiabatic. (iii) The path with α=0.50 (magenta solid line, labeled as $\xi(\alpha)$) corresponds to a curved path which crosses the nonadiabatic region with boundaries given by $\xi_{\mathrm{I}}(\alpha)$ in the reactants side and by $\xi_{\mathrm{III}}(\alpha)$ in the products side. This path does not follow the curved path (magenta dotted line) but the straight path (magenta solid line) through the nonadiabatic region. (iv) The path with α=1, (cyan solid line) corresponds to the LCT. The boundaries of the nonadiabatic region are given by $\xi_{\mathrm{I}}(1)$ in the reactants side and by $\xi_{\mathrm{III}}(1)$ in the products side.

If it is not possible to find a geometry along the MEP which satisfies Eq. (5.12), it means that there is no projection for that geometry of the tunneling path onto the modes perpendicular to the reaction path in the interval $[\tilde{s}_0, \tilde{s}_1]$. When this happens going from reactants to products, the nonadiabatic region in the reactants side starts at $\xi = \xi_{\mathrm{I}}$, being ξ_{I} the last value for which there is projection onto the MEP. That point on the MEP is labeled as $s_{\mathrm{I}}[\xi, \tilde{s}_0]$. In the same way, the nonadiabatic region in products side starts at $\xi = \xi_{\mathrm{III}}$, being ξ_{III} the last value for which $s_{\mathrm{III}}[\xi, \tilde{s}_0]$ exists. If there is an overlap between the adiabatic regions and the nonadiabatic region does not exists, i.e., $\xi_{\mathrm{III}} < \xi_{\mathrm{I}}$, the vibrationally adiabatic potential in the interval $[\xi_{\mathrm{III}}, \xi_{\mathrm{I}}]$ is evaluated as:

$$\min\left\{V_{\mathrm{a}}^{\mathrm{G}}\left[s_{\mathrm{I}}(\xi); \tilde{s_0}\right], V_{\mathrm{a}}^{\mathrm{G}}\left[s_{\mathrm{III}}(\xi); \tilde{s_0})\right]\right\} \tag{5.13}$$

Each of the two $s_i,\ i = \mathrm{I}, \mathrm{III}$ values needed for the evaluation of the vibrationally adiabatic potentials $V_{\mathrm{a}}^{\mathrm{G}}\left[s_i(\xi); \tilde{s_0})\right]$ is obtained from Eq. (5.12).

The nonadiabatic region has boundaries ξ_{I} and ξ_{III} with regions I and III, respectively. Therefore, region I is located in the interval $0 \leq \xi < \xi_{\mathrm{I}}$, region II in the interval $\xi_{\mathrm{I}} \leq \xi \leq \xi_{\mathrm{III}}$, and region III in the interval $\xi_{\mathrm{III}} < \xi \leq \xi_{\mathrm{P}}$. Besides of the condition (i), given by Eq. (5.12), we consider that a given geometry is in the adiabatic region when (ii) all the generalized normal mode coordinates are within their vibrational turning points, (iii) the geometry $\mathbf{x}\left[\xi, \tilde{s}_0\right]$ lies within the single-valued region of the reaction path coordinates and (iv) the adiabatic potential should be greater than or equal to the effective potential at the boundary of the nonadiabatic region, in other case the nonadiabatic region is extended until this condition is met. On the other hand, if the adiabatic potential is smaller than the effective potential the difference is due to anharmonicity, so the effective potential is modified with a nonquadratic correction. Condition (iv) entails the difference between the large curvature ground-state version 3 (LCG3) and large curvature ground-state version 4 (LCG4) [17, 21] methods. The previous LCG3 method usually involved abrupt changes in the effective potential at the boundaries between the adiabatic and nonadiabatic regions, leading to spuriously large transmission coefficients at low temperatures [155–157]. The effective potential in the LCG4 approximation is given by

$$\begin{aligned} V_{\mathrm{eff}}^{\mathrm{II}}(\xi, \tilde{s_0}) = {} & V\left\{\mathbf{x}\left[\xi, \tilde{s_0}\right]\right\} + V_{\mathrm{corr}}^{\mathrm{I}}(\xi_{\mathrm{I}}, \tilde{s_0}) + V_{\mathrm{anh}}^{\mathrm{I}}(\xi_{\mathrm{I}}, \tilde{s_0}) \\ & + \frac{\xi - \xi_{\mathrm{I}}}{\xi_{\mathrm{III}} - \xi_{\mathrm{I}}}\left[V_{\mathrm{corr}}^{\mathrm{III}}(\xi_{\mathrm{III}}, \tilde{s_0}) - V_{\mathrm{corr}}^{\mathrm{I}}(\xi_{\mathrm{I}}, \tilde{s_0}) + V_{\mathrm{anh}}^{\mathrm{III}}(\xi_{\mathrm{III}}, \tilde{s_0}) - V_{\mathrm{anh}}^{\mathrm{I}}(\xi_{\mathrm{I}}, \tilde{s_0})\right] \end{aligned} \tag{5.14}$$

The potentials $V_{\mathrm{corr}}^{i}(\xi_i, \tilde{s_0}),\ i = \mathrm{I}, \mathrm{III}$ correct for the zero-point energy in the modes that are still within their turning points. The potentials $V_{\mathrm{anh}}^{i}(\xi_i, \tilde{s_0})$ incorporate anharmonic nonquadratic corrections to the effective potential, i.e.,

$$V_{\mathrm{anh}}^{i}(\xi_i, \tilde{s_0}) = V_{\mathrm{a}}^{\mathrm{G}}\left[s_i(\xi); \tilde{s_0})\right] - V_{\mathrm{eff}}^{\mathrm{II}}(\xi_i, \tilde{s_0}), \qquad i = \mathrm{I}, \mathrm{III} \tag{5.15}$$

The LCG4 imaginary action integral at every tunneling energy along the straight paths given by Eq. (5.10) is:

$$\begin{aligned} \theta(\tilde{s_0}) = {} & \frac{(2\mu)^{1/2}}{\hbar}\left[\int_0^{\xi_{\mathrm{I}}} d\xi \left\{V_{\mathrm{a}}^{\mathrm{G}}\left[(s_{\mathrm{I}}; \tilde{s_0})\right] - V_{\mathrm{a}}^{\mathrm{G}}(\tilde{s_0})\right\}^{1/2} \cos\chi_0\left\{\tilde{s_0}, \hat{\boldsymbol{\eta}}\left[\xi, \tilde{s_0}\right]\right\}\right. \\ & + \int_{\xi_{\mathrm{I}}}^{\xi_{\mathrm{III}}} d\xi \left\{V_{\mathrm{eff}}^{\mathrm{II}}(\xi, \tilde{s_0}) - V_{\mathrm{a}}^{\mathrm{G}}(\tilde{s_0})\right\}^{1/2} \\ & \left. + \int_{\xi_{\mathrm{III}}}^{\xi_{\mathrm{P}}} d\xi \left\{V_{\mathrm{a}}^{\mathrm{G}}\left[(s_{\mathrm{III}}; \tilde{s_0})\right] - V_{\mathrm{a}}^{\mathrm{G}}(\tilde{s_0})\right\}^{1/2} \cos\chi_1\left\{\tilde{s_1}, \hat{\boldsymbol{\eta}}\left[\xi, \tilde{s_1}\right]\right\}\right], \end{aligned} \tag{5.16}$$

The two cosines of Eq. (5.16), $\cos\chi_i\left\{\tilde{s}_i, \hat{\boldsymbol{\eta}}\left[\xi, \tilde{s}_i\right]\right\}$ for $i=0,1$ are obtained as the dot products between the unit vectors $\hat{\boldsymbol{\eta}}\left[\xi, \tilde{s}_i\right]=\frac{\mathbf{x}(\tilde{s}_1)-\mathbf{x}(\tilde{s}_0)}{\xi_{\mathrm{P}}}$ and the unit vectors tangent to the MEP at s_i, i.e.,

$$\cos\chi_i\left\{\tilde{s}_i, \hat{\boldsymbol{\eta}}\left[\xi, \tilde{s}_i\right]\right\}=\hat{\boldsymbol{\eta}}\left[\xi, \tilde{s}_i\right] \frac{\mathrm{d}\mathbf{x}(\tilde{s}_i)}{\mathrm{d}s}, \qquad i=0,1 \tag{5.17}$$

The tunneling amplitude of the LCG4 path initiated at the reactants turning point $\tilde{s_0}$ is approximated using a primitive semiclassical expression

$$T_{\text{tun}}^{\text{LCG4}}(\tilde{s_0})=T_{\text{tun}}^{\text{LCG4}}(\tilde{s_1})=\exp\left[-\theta(\tilde{s_0})\right] \tag{5.18}$$

The LCG4 primitive probability, $P_{\text{prim}}^{\text{LCG4}}(E)$, is obtained from the tunneling amplitude of the previous Eq. (5.18) plus the contribution due to the vibrational motion perpendicular to the reaction coordinate along the incoming $T_0(E)$ and outgoing $T_1(E)$ trajectories at tunneling energy E

$$\begin{aligned} P_{\text{prim}}^{\text{LCG4}}(E)= & \left|T_0(E)+T_1(E)\right|^2 \\ & +\left(\frac{\cos\chi_0\left\{\tilde{s_0}, \hat{\boldsymbol{\eta}}\left[\xi, \tilde{s_0}\right]\right\}+\cos\chi_1\left\{\tilde{s_1}, \hat{\boldsymbol{\eta}}\left[\xi, \tilde{s_1}\right]\right\}}{2}\right)^2 \\ & \times \exp\left[-2\theta(\tilde{s_0})\right] \end{aligned} \tag{5.19}$$

The tunneling amplitude of the incoming trajectory along the reaction coordinate is $\exp\left[-\theta(\tilde{s_0})\right]\cos\chi_0\left\{\tilde{s_0}, \hat{\boldsymbol{\eta}}\left[\xi, \tilde{s_0}\right]\right\}$ and that of the outgoing trajectory is $\exp\left[-\theta(\tilde{s_0})\right]\cos\chi_1\left\{\tilde{s_1}, \hat{\boldsymbol{\eta}}\left[\xi, \tilde{s_1}\right]\right\}$. To enforce macroscopic reversibility, the expression used in Eq. (5.19) is the average of the two tunneling amplitudes and the amplitude due to the all the vibrational degrees of freedom perpendicular to the reaction coordinate is averaged using $T_0(E)$ and $T_1(E)$. The expressions for $T_0(E)$ and $T_0(E)$ are given in Ref. [17].

The primitive probability of Eq. (5.19) has to be uniformized prior to its use in Eq. (5.8) because it can be greater than one, so it is enforced to go to 1/2 at the maximum of the vibrational adiabatic potential V_{a}^{AG} by the expression:

$$P^{\text{LCG4}}(E)=\left\{1+\frac{1}{2}\frac{\left[P_{\text{prim}}^{\text{LCG4}}(V_{\text{a}}^{\text{AG}})\right]^{-1}-1}{P_{\text{prim}}^{\text{LCG4}}(V_{\text{a}}^{\text{AG}})} P_{\text{prim}}^{\text{LCG4}}(E)\right\} \times \frac{1}{1+\left[P_{\text{prim}}^{\text{LCG4}}(E)\right]^{-1}} \tag{5.20}$$

In the LCG4 method the tunneling path starts and ends as vibrationally adiabatic but during the tunneling process the potential can be nonadiabatic and tunneling may end up in vibrationally excited states. The contribution of those final vibrationally excited states (considering always the reaction in the exoergic direction) is included by finding all accessible vibrational states of a projected mode defined as linear combination of all the generalized normal modes coupled to the tunneling path [24, 87, 91, 92, 96].

The LCG4 approximation is a particular case of a more general method that minimizes the action integral for a family of α dependent paths for which the MEP is located at $\alpha=0$ and the LCT path at $\alpha=1$ (hereafter we indicate explicitly the dependence with α of the progress variable along the straight path and use $\xi(1)$ instead of ξ). This method is called least-action tunneling (LAT) and since it is based on the LCG4 approximation is called least-action tunneling ground-state version 4 (LAG4) approximation. The family of paths used for the search of the least-action at every tunneling energy is given by

$$\mathbf{x}\left[\alpha,\xi(\alpha),\tilde{s}_0\right]=(1-\alpha)\mathbf{x}\left[0,\xi(0),\tilde{s}_0\right]+\alpha\mathbf{x}\left[1,\xi(1),\tilde{s}_0\right] \tag{5.21}$$

where $\mathbf{x}\left[0,\xi(0),\tilde{s}_0\right]$ and $\mathbf{x}\left[1,\xi(1),\tilde{s}_0\right]$ are the geometries along the MEP and along the straight path, respectively. It should be noticed that the progression variable ξ depends on the value of the α parameter.

The LAG4 imaginary action integral at every tunneling energy and for each α value along the paths of Eq (5.21) is:

$$\begin{aligned}\theta(\alpha,\tilde{s_0})=&\frac{(2\mu)^{1/2}}{\hbar}\left[\int_0^{\xi_{\mathrm{I}}(\alpha)}d\xi(\alpha)\left\{V_{\mathrm{a}}^{\mathrm{G}}\left[s_{\mathrm{I}}(0,\xi(0));\tilde{s_0}\right]-V_{\mathrm{a}}^{\mathrm{G}}(\tilde{s_0})\right\}^{1/2}\cos\chi_0\left\{\tilde{s_0},\hat{\boldsymbol{\eta}}\left[\alpha,\xi(\alpha),\tilde{s}_0\right]\right\}\right.\\&+\int_{\xi_{\mathrm{I}}(\alpha)}^{\xi_{\mathrm{III}}(\alpha)}d\xi(\alpha)\left\{V_{\mathrm{eff}}^{\mathrm{II}}(\alpha,\xi(\alpha),\tilde{s_0})-V_{\mathrm{a}}^{\mathrm{G}}(\tilde{s_0})\right\}^{1/2}\\&\left.+\int_{\xi_{\mathrm{III}}(\alpha)}^{\xi_{\mathrm{P}}(\alpha)}d\xi(\alpha)\left\{V_{\mathrm{a}}^{\mathrm{G}}\left[s_{\mathrm{III}}(0,\xi(0));\tilde{s_0}\right]-V_{\mathrm{a}}^{\mathrm{G}}(\tilde{s_0})\right\}^{1/2}\cos\chi_1\left\{\tilde{s_1},\hat{\boldsymbol{\eta}}\left[\alpha,\xi(\alpha),\tilde{s}_1\right]\right\}\right],\end{aligned} \tag{5.22}$$

Eq. (5.22) is similar to Eq. (5.16) with the difference that the action integral is not restricted to the straight paths.

The effective potential of Eq. (5.22) of the LAG4 method is the same as that of the LCG4 method, with the difference that now the geometries at which the potential is evaluated are functions of α and of the progress variable ξ, which also depends on α. Therefore the effective potential is given by

$$\begin{aligned}V_{\mathrm{eff}}^{\mathrm{II}}(\alpha,\xi(\alpha),\tilde{s_0})=&V\left\{\mathbf{x}\left[\alpha,\xi(\alpha),\tilde{s_0}\right]\right\}+V_{\mathrm{corr}}^{\mathrm{I}}(\alpha,\xi_{\mathrm{I}}(\alpha),\tilde{s_0})+V_{\mathrm{anh}}^{\mathrm{I}}(\alpha,\tilde{s_0})\\&+\frac{\xi(\alpha)-\xi_{\mathrm{I}}(\alpha)}{\xi_{\mathrm{III}}(\alpha)-\xi_{\mathrm{I}}(\alpha)}\left[V_{\mathrm{corr}}^{\mathrm{III}}(\alpha,\xi_{\mathrm{III}}(\alpha),\tilde{s_0})-V_{\mathrm{corr}}^{\mathrm{I}}(\alpha,\xi_{\mathrm{I}}(\alpha),\tilde{s_0})+V_{\mathrm{anh}}^{\mathrm{III}}(\alpha,\tilde{s_0})-V_{\mathrm{anh}}^{\mathrm{I}}(\alpha,\tilde{s_0})\right]\end{aligned} \tag{5.23}$$

The potentials $V_{\mathrm{corr}}^{i}(\alpha,\xi_i(\alpha),\tilde{s_0}),\ i=\mathrm{I},\mathrm{III}$ correct for the zero-point energy in the modes that are still within their turning points. and the potentials $V_{\mathrm{anh}}^{i}(\alpha,\tilde{s_0})$ incorporate anharmonic nonquadratic corrections to the effective potential in the same way as in the LCG4 method.

As shown in Figure 5.1, in the case that the whole path is adiabatic, which it may happen for small values of α, the path given by Eq. (5.21) is the reference path between the two classical turning points. However, if there is a nonadiabatic region (region II), the path along regions I $(0\le\xi(\alpha)<\xi_{\mathrm{I}}(\alpha))$ and III $(\xi_{\mathrm{III}}(\alpha)<\xi(\alpha)\le\xi_{\mathrm{P}}(\alpha))$ is evaluated along the reference path given by Eq. (5.21), whereas the path along region II $(\xi_{\mathrm{I}}(\alpha)\le\xi(\alpha)\le\xi_{\mathrm{III}}(\alpha))$ is built as a straight path between the boundaries, where the geometries are given by

$$\mathbf{x}\left[\alpha,\xi(\alpha),\tilde{s}_0\right]=\mathbf{x}\left[\alpha,\xi_{\mathrm{I}}(\alpha),\tilde{s}_0\right]+\frac{\xi(\alpha)-\xi_{\mathrm{I}}(\alpha)}{\xi_{\mathrm{III}}(\alpha)-\xi_{\mathrm{I}}(\alpha)}\left(\mathbf{x}\left[\alpha,\xi_{\mathrm{III}}(\alpha),\tilde{s}_0\right]-\mathbf{x}\left[\alpha,\xi_{\mathrm{I}}(\alpha),\tilde{s}_0\right]\right) \tag{5.24}$$

The LAG4 path is the optimum path from the family of paths given by Eq. (5.21), i.e., it is the one that minimizes the imaginary action integral of Eq (5.22). The optimum value of α at every tunneling energy, which we label as $\tilde{\alpha}$, is found through a search in which different initial $\theta(\alpha_i, \tilde{s_0})$ values are calculated for a given number K of equally spaced points ($i = 1, \ldots, K$). We have found out that $K = 11$ is a good starting guess. In the grid of K points we search for the values of the imaginary action which are minima, i.e., the values $\theta(\alpha_j, \tilde{s_0})$ with $j = 1, \ldots, K_m$, being K_m the number of minima. If there is only one minimum ($K_m = 1$), we limit the search to the interval $[\alpha_{i-1}, \alpha_{i+1}]$, where $\alpha_j = \alpha_i$ is inside the interval. From the three initial values $\{\alpha_{i-1}, \alpha_j, \alpha_{i+1}\}$, two new values are obtained as $\alpha_L = \frac{1}{2}[\alpha_i - \alpha_{i-1}]$ and $\alpha_R = \frac{1}{2}[\alpha_{i+1} - \alpha_i]$ and two new values of the imaginary action are calculated $\theta(\alpha_L, \tilde{s_0})$ and $\theta(\alpha_R, \tilde{s_0})$. Of the set of 5 resulting α values $\{\alpha_{i-1}, \alpha_L, \alpha_j, \alpha_R, \alpha_{i+1}\}$, we take the three new values of α based on the values of the imaginary actions $\{\theta(\alpha_{i-1}, \tilde{s_0}), \theta(\alpha_L, \tilde{s_0}), \theta(\alpha_j, \tilde{s_0}), \theta(\alpha_R, \tilde{s_0}), \theta(\alpha_{i+1}, \tilde{s_0})\}$. There are the following possibilities: a) if $\theta(\alpha_L, \tilde{s_0}) < \theta(\alpha_R, \tilde{s_0})$ there are two possibilities: a1) if $\theta(\alpha_L, \tilde{s_0}) < \theta(\alpha_j, \tilde{s_0})$ then the new set of three values of α is $\{\alpha_{i-1}, \alpha_L, \alpha_j\}$; a2) if $\theta(\alpha_L, \tilde{s_0}) > \theta(\alpha_j, \tilde{s_0})$ then $\{\alpha_L, \alpha_j, \alpha_R\}$; b) if $\theta(\alpha_L, \tilde{s_0}) > \theta(\alpha_R, \tilde{s_0})$ there are also two possibilities: b1) if $\theta(\alpha_R, \tilde{s_0}) < \theta(\alpha_j, \tilde{s_0})$ then $\{\alpha_j, \alpha_R, \alpha_{i+1}\}$; b2) if $\theta(\alpha_R, \tilde{s_0}) > \theta(\alpha_j, \tilde{s_0})$ then $\{\alpha_L, \alpha_j, \alpha_R\}$. The new 3 values of α substitute the initial values and the process is repeated. Convergence is achieved when two successive loops give differences in α smaller than 10^{-6} or differences in the imaginary action smaller than 5×10^{-5}. Usually the number of iterations is smaller than 15. If there is more than one minima, ($K_m > 1$), the above iterative process is repeated for each of them. Of all the obtained local minima, we choose the absolute minimum, i.e. the lowest value of the imaginary action, which is labeled as $\theta(\tilde{\alpha}, \tilde{s_0})$.

The next step is to calculate the LAG4 primitive probabilities, which are obtained in the same way than the LCG4 ones, but in this case considering the optimized path with $\alpha = \tilde{\alpha}$ instead of the path with $\alpha = 1$. The evaluation of the LAG4 transmission coefficients involve an extra computational cost when compared with the evaluation of the LCG4 ones, because, at every tunneling energy, we have to search for the best tunneling path.

In principle, an approximate way of obtaining better transmission coefficients than the SCT and LCT ones, but avoiding the explicit evaluation of the LAT transmission coefficients, is to built a transmission coefficient which, at every tunneling energy, chooses the largest between the SCT and LCT tunneling probabilities (the smallest between the SCT and LCT imaginary action integrals). This approximation is called microcanonical optimized multidimensional tunneling (μOMT) method. [24] The μOMT tunneling probabilities are, therefore,

$$P^{\mu\mathrm{OMT}}(E) = \max_{E} \left\{ \begin{array}{l} P^{\mathrm{SCT}}(E) \\ P^{\mathrm{LCT}}(E) \end{array} \right. \tag{5.25}$$

where $P^{\mathrm{SCT}}(E)$ and $P^{\mathrm{LCT}}(E)$ are the SCT and LCT probabilities evaluated within the CD-SCSAG and LCG4 approximations, respectively.

5.3. Practical implementation of the LCG4 and LAG4 methods

One of the main problems for the applicability of LCG4 and LAG4 methods to large systems is their computational cost. Both methods use the harmonic approximation to build the potential along the tunneling path in the adiabatic region from the information along the MEP. In the nonadiabatic region, extrapolation from the MEP is not possible, so we have to compute the values of the effective potential given by Eq. (5.14) in LCG4 and by Eq. (5.23) in LAG4, respectively. The procedure for reducing the computer time is different for LCG4 than for LAG4, so we discuss them separately.

The LCG4 transmission coefficients are calculated by numerical integration of Eq. (5.2), which involves the evaluation of about 80 tunneling energies; at every of these tunneling energies the calculation, also by numerical integration, of the imaginary action integral (and therefore of the tunneling probability), requires about 180 single-point energy calculations of the potential along the straight path, involving a total of 14400 points (hereafter we use 'point' as an abbreviated form of 'single-point-energy'). Of that large amount of points, a number of them, which in general may oscillate between 1000 and 5000 (depending on the system), are in the nonadiabatic region. At every tunneling energy the nonadiabatic region along the straight path has boundaries $\xi_{\mathrm{I}}(1) < \xi(1) < \xi_{\mathrm{III}}(1)$ as shown in Figure 5.1. One way of reducing the computational cost is to evaluate the energies at selected values of $\xi(1)$ along the nonadiabatic region of the straight path and to interpolate the remaining energies. We have found that the fitting of the calculated points to a spline-under-tension function [140, 141] gives very good results, i.e., the calculation of 9 or 11 points at every tunneling energy leads to errors, when compared to the full-LCG4 calculations, of about 3%. This algorithm is called interpolated large curvature tunneling in one dimension (ILCT1D)[22] and it reduces the computer time about 5 times compared to the full calculation.

A much cheaper and accurate way of evaluating LCG4 transmission coefficients is by interpolation, of not only the energies along the straight paths, but also of the tunneling energies, i.e., all the energies are evaluated within a two-dimensional grid. As for the ILCT1D algorithm, we perform interpolation in the progress variable $\xi(1)$ at every tunneling energy, but we also perform interpolation in the tunneling energies. We called this algorithm interpolated large curvature tunneling in two dimensions (ILCT2D)[23]. The ILCT2D algorithm works as follows: (i) Generation of a $M \times N$ two-dimensional grid at M tunneling energies E_i, with $i = 1, \ldots, M$, in such a way that $E_{i=1}$ is the lowest energy at which tunneling is possible, i.e., E_0 and $E_{i=M}$ is the maximum of the vibrationally adiabatic potential, i.e., $E_M = V_{\mathrm{a}}^{\mathrm{AG}}$. For every of the E_i tunneling energies we select $\xi_j(1)$ points along the tunneling path, $(j = 1, \ldots, N)$, taking into account that $\xi_1(1) = 0$ and that $\xi_N(1) = \xi_P(1)$, being $\xi_{\mathrm{P}}(1)$ the length of the straight path. (ii) Calculation of each of the $(E_i, \xi_j(1))$ points of the grid. (iii) Transformation of the previous grid with points $(E_i, \xi_j(1))$ in a unit-square grid $(\overline{E}_i, \overline{\xi}_j(1))$ by performing the scaling:

$$\overline{E}_i = \frac{E_i - E_0}{V_{\mathrm{a}}^{\mathrm{AG}} - E_0} \qquad \text{and} \qquad \overline{\xi}_j(1) = \frac{\xi_j(1)}{\xi_P(1)} \tag{5.26}$$

(iv) The grid of points is fitted to a two-dimensional spline under tension following the procedure described by Renka and Cline [139]. (v) The effective potential of Eq. (5.14) is obtained from the fit.

To illustrate how the ILCT2D method performs, we have apply it to the $\mathrm{H}+\mathrm{CH}_4 \rightarrow \mathrm{H}_2+\mathrm{CH}_3$ hydrogen abstraction reaction using the Jordan and Gilbert analytical potential energy surface (JG-PES). [62] Figure 5.2 shows how the effective potential, which is delimited by the MEP and the straight path at the lowest tunneling energy, is transformed into a unit-square grid. The grid was built with $M = 9$ tunneling energies and $N = 11$ points along each tunneling path; of these 99 points many of them fall in the adiabatic region, so additional calculations are needed only for those points which are inside the nonadiabatic region. In general the ILCT2D algorithm is about 30 times faster than the full LCG4 calculation. It should be noticed that the top side of the square grid is the maximum of the vibrationally adiabatic potential, whereas the left and right sides correspond to the MEP in the reactants and products sides, respectively. The bottom side of the square corresponds to the lowest tunneling energy.

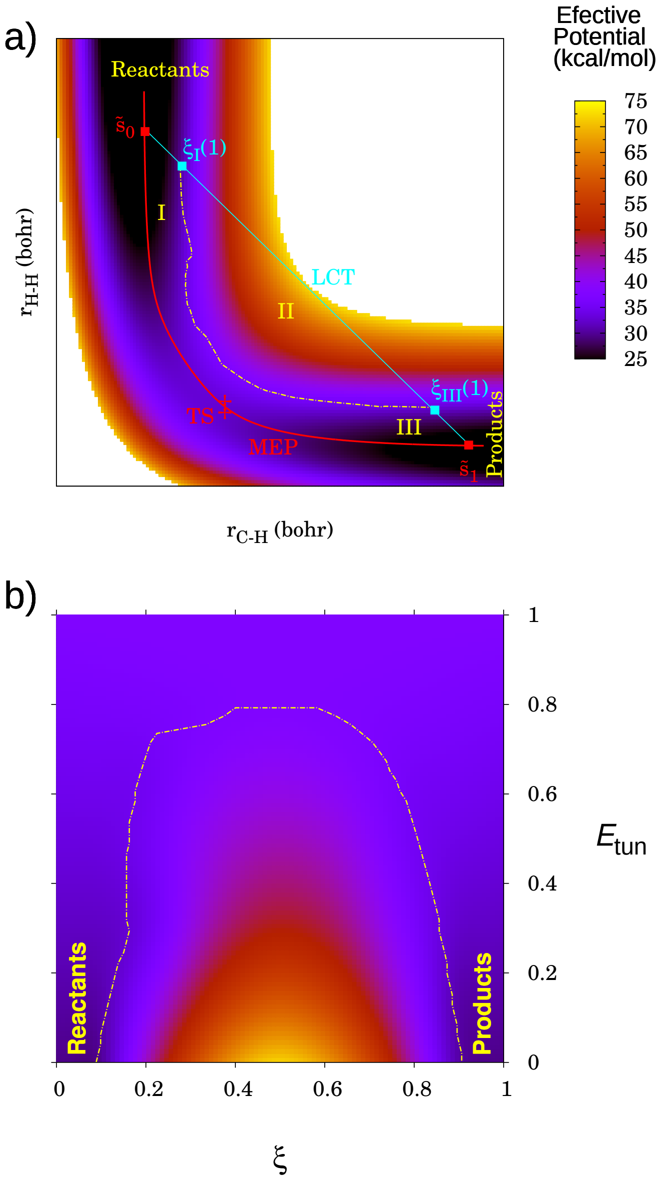

Figure 5.2: (a) Plot of the effective potential for the H + $CH_4 \rightarrow H_2 + CH_3$ hydrogen abstraction reaction; r_{C-H} is the distance between the carbon atom and the abstracted CH_4 hydrogen atom and r_{H-H} is the distance between the hydrogen atom and the abstracted CH_4 hydrogen atom. The solid yellow dotted-dashed line indicates the boundaries between the adiabatic and the non-adiabatic regions. The cyan solid line represents the straight path at a given tunneling energy with classical turning points given by $\tilde{s_0}$ and $\tilde{s_1}$ in the reactants and the products side, respectively. The reaction swath is partitioned into the adiabatic region of reactants (labeled as I), adiabatic region of products (labeled as III), and the nonadiabatic region (labeled as II and with boundaries given by a yellow dotted-dashed line). (b) Unit-square effective potential surface obtained from the (a) PES. The bottom side of the square is the unitary line given in (a) by the LCT path. The sides of the square represent the vibrationally adiabatic potential along the MEP. The top side of the square is the maximum of the vibrationally adiabatic potential.

Table 5.1 lists both, the full-LCT and the ILCT2D transmission coefficients, at temperatures in the interval 200–400 K. Comparison between both transmission coefficients shows, that even at the lowest temperature the error is smaller than 1%. Taking into account that the grid was built with $M = 9$ tunneling energies and $N = 11$ points along each tunneling path and that some of these 99 points fall in the adiabatic region, the ILCT2D algorithm is about 30 times faster than the full LCG4 calculation. This huge reduction in computer time shows that LCG4 calculations could became feasible for large systems.

Table 5.1: Several transmission coefficients obtained for the JG-PES

T(K)	SCT	LCG4	ILCT2D	μOMT	LAG4	ILAT1D
200.0	18.74	13.66	13.75	18.76	27.59	27.37
250.0	6.27	5.11	5.13	6.28	7.34	7.31
300.0	3.54	3.04	3.05	3.54	3.74	3.74
400.0	2.02	1.84	1.84	2.03	2.01	2.01

The evaluation of LAG4 transmission coefficients is much more expensive than that of LCG4 transmission coefficients, since at each tunneling energy, the imaginary action has to be evaluated until the optimum value is found. If the LCG4 calculations take about 80(tunneling energies)×180(points along $\xi(1)$) = 14400, the LAG4 calculation needs that number of computations for each cycle of optimization of α (a close number is 3×10^5). It is possible to apply modified versions of the previous algorithms to the LAG4 method, although the construction of a two dimensional grid in this case involves to choose N_A values α_k, $(k = 1, \ldots, N_A)$, with the condition that $\alpha_1 = 0$ is the MEP and $\alpha_{N_A} = 1$ is the straight path. For each of those α_k paths, we have to select $\xi_j(\alpha_k)$ points along the tunneling path, $(j = 1, \ldots, N)$, where $\xi_1(\alpha_k) = 0$ and $\xi_N(\alpha_k) = \xi_P(\alpha_k)$ (the total length of the tunneling path). Therefore a point inside the grid has coordinates $(\alpha_k, \xi_j(\alpha_k))$. The next step would be to transform this grid into a unit square and search for the value of α which minimizes the action at this tunneling energy. The construction of the two-dimensional grid and the search for $\tilde{\alpha}$ has to be repeated for every of the tunneling energies.

We find the above procedure very complicated, so instead we present here a different algorithm. Initially a number M of tunneling energies E_i $i = 1, \ldots, M$ is chosen with the boundary conditions that $E_{i=1}$ corresponds to the lowest tunneling energy E_0, whereas $E_{i=M}$ corresponds to the latest tunneling energy for which there is a nonadiabatic region (here it is different than for the ILCT2D method, for which $E_M = V_{\mathrm{a}}^{\mathrm{AG}}$). At every of these tunneling energies a search of $\tilde{\alpha}$ is carried out as indicated in Section 5.2. The difference with the full calculation is that, in this case, the progress variable is evaluated only at some selected $\xi_j(\alpha)$ points $(j = 1, \ldots, N_B)$ within the nonadiabatic region of the tunneling path, i.e., the boundaries are $\xi_1(\alpha) = \xi_{\mathrm{I}}(\alpha)$ and $\xi_{N_B}(\alpha) = \xi_{\mathrm{III}}(\alpha)$. The effective potential at every value of α is obtained by a one-dimensional fit to a spline under tension. This process is repeated for each of the E_i tunneling energies, so we end up with a set of M values of $\tilde{\alpha}_i$ and $\theta(\tilde{\alpha}_i)$. Now there is the possibility of fitting the $\tilde{\alpha}_i$ parameters or the imaginary actions $\theta(\tilde{\alpha}_i)$ to a one-dimensional spline under tension. We have found out that the fitting of the imaginary actions to $N = 7$ number of tunneling energies gives very good results. Figure 5.3 shows the very good agreement between the least imaginary actions obtained by the full-LAG4 calculation (depicted as a black line) and those obtained by the interpolated algorithm (depicted as a green line). The algorithm uses a one-dimensional interpolation, so we call the method interpolated least-action tunneling in one-dimension (ILAT1D). In general the number of points that have to be evaluated is about 2000, which means a reduction of about 150 times regarding to the full-LAG4 calculation. A comparison between the full calculation and the ILAT1D algorithm is carried out in Table 5.1. Although the ILAG1D algorithm may need further testing, the difference between both methods is smaller than 1%, which is a very encouraging result.

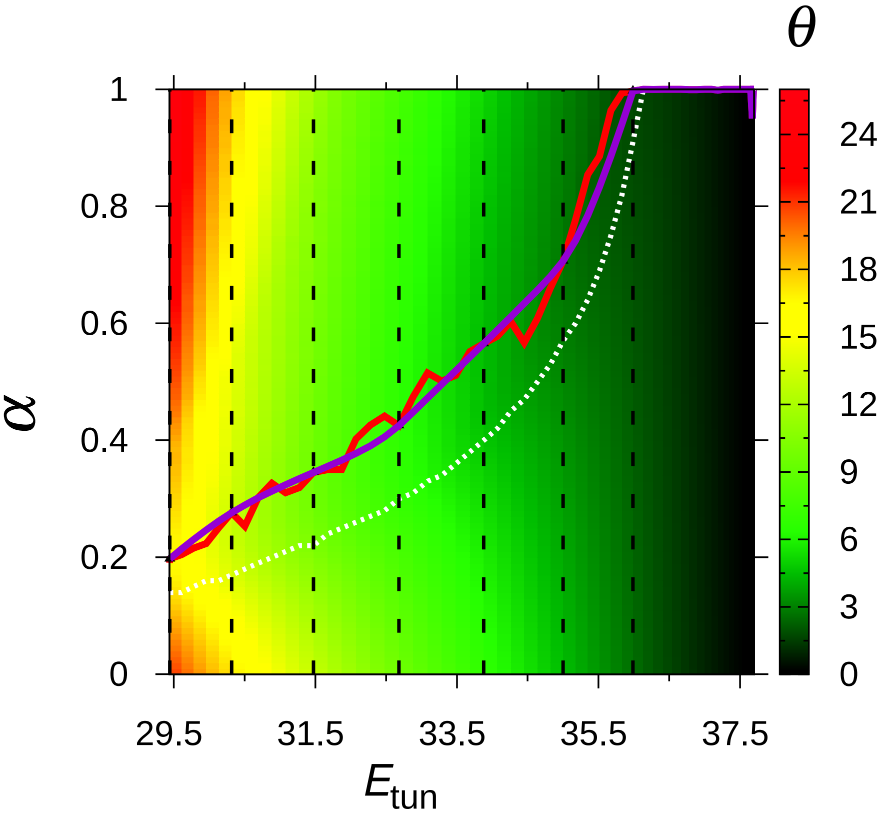

Figure 5.3: Two-dimensional projection showing the variation of the imaginary action integral with the α parameter at every of the tunneling energies. The red solid line indicates the values of $\tilde{\alpha}$ at every tunneling energy obtained by the full-LAG4 calculation, whereas the violet solid line corresponds to the values of $\tilde{\alpha}$ obtained by ILAT1D method. The vertical black dashed lines indicate the tunneling energies at which the ILAT1D method computes the imaginary action prior to the interpolation procedure. The white dotted line indicates the boundaries between the adiabatic and nonadibatic regions.

5.4. Transmission coefficients and KIEs

In this Section we analyze the effect that the approximations used for computing tunneling contributions have on the KIEs. As mentioned in the Introduction, this issue is of great relevance because the KIEs are one of the most important parameters for the elucidation of the reaction mechanisms in enzymes. Here we discuss a number of abstraction reactions with several isotopic substitutions of the type $\mathrm{CH_3X + Y \rightarrow CH_3 + XY}$, where $\mathrm{X = H}$ or D and $\mathrm{Y = H, D}$ or T, i.e.,

$$\mathrm{CH_4 + H \longrightarrow CH_3 + H_2} \tag{R1}$$

$$\mathrm{CH_3D + H \longrightarrow CH_3 + DH} \tag{R2}$$

$$\mathrm{CH_4 + D \longrightarrow CH_3 + HD} \tag{R3}$$

$$\mathrm{CH_3D + D \longrightarrow CH_3 + D_2} \tag{R4}$$

$$\mathrm{CH_4 + T \longrightarrow CH_3 + HT} \tag{R5}$$

$$\mathrm{CH_3D + T \longrightarrow CH_3 + DT} \tag{R6}$$

All the calculations are based on the JG-PES. Table 5.2 shows that the LAG4 transmission coefficients are always the largest for the hydrogen transfer reaction independent of which is the acceptor atom, whereas the SCT transmission coefficients are always the largest for the deuterium transfer. In principle one would expect the LAG4 transmission coefficients to be the largest for any isotope, although is difficult to decide which of the two methods (SCT or LAG4) is more accurate if the curvature is not too large.

Table 5.2: Transmission coefficients computed with the SCT, LCG4 and LAG4 approximations for reactions R1 to R6 using the JG-PES

T(K)	$\kappa_\mathrm{H}(T)$				$\kappa_\mathrm{D}(T)$			
	SCT	LCG4	μOMT	LAG4	SCT	LCG4	μOMT	LAG4
	$\mathrm{CH_4 + H}$				$\mathrm{CH_3D + H}$			
200.00	18.74	13.66	18.76	27.59	8.19	4.75	8.19	5.40
250.00	6.27	5.11	6.28	7.34	3.54	2.47	3.54	2.55
300.00	3.54	3.04	3.54	3.74	2.34	1.81	2.34	1.83
400.00	2.02	1.84	2.03	2.01	1.59	1.37	1.59	1.38
	$\mathrm{CH_4 + D}$				$\mathrm{CH_3D + D}$			
200.00	6.71	9.82	9.82	16.06	6.23	4.03	6.23	5.14
250.00	3.36	4.25	4.25	5.70	3.12	2.29	3.12	2.51
300.00	2.33	2.74	2.74	3.32	2.18	1.73	2.18	1.80
400.00	1.61	1.77	1.77	1.96	1.54	1.34	1.54	1.36
	$\mathrm{CH_4 + T}$				$\mathrm{CH_3D + T}$			
200.00	3.64	8.24	8.24	12.49	4.65	3.70	4.65	4.56
250.00	2.25	3.73	3.73	4.82	2.63	2.22	2.63	2.42
300.00	1.74	2.47	2.47	2.93	1.95	1.71	1.95	1.79
400.00	1.36	1.66	1.66	1.82	1.45	1.34	1.45	1.36

The skew angles given by Eq. (5.9) range and listed in Table 5.3 from small curvature for reaction R2 to large curvature for reaction R5. However, the LCG4 transmission coefficients always underestimate tunneling with respect to the LAG4 transmission coefficients independently of the reaction path curvature, although the LCG4 values are larger than the SCT values for the hydrogen abstractions. The μOMT transmission coefficient takes into account that LCG4 is larger for the hydrogen abstraction and that SCT is larger for the deuterium abstraction, so it seems to solve the problem. However, the KIEs calculated by the different tunneling approximations, and listed in Table 5.4, show that the μOMT transmission coefficients seriously underestimate tunneling when compared with the LAG4 ones, because SCT gives values which are too large for the deuterium transfer and LCG4 gives values which are small for hydrogen transfer. Thus, the μOMT KIEs give values which are between the calculated SCT and the LCG4 KIEs. The SCT and μOMT KIEs only coincide when the acceptor is a hydrogen atom, as the mass of the acceptor increases both KIEs get more different, i.e., the SCT KIEs become to small. The LAG4 KIEs are always larger than KIEs obtained by the other approximations. Although this example is not conclusive, from the LCG4, μOMT and SCT approximations, it seems that the latter is the approximation which underestimates the quantum KIEs by the largest amount. This result is disappointing taking into account that the SCT is the most applied approximation for the study of enzymatic reactions.

Table 5.3: Reactions studied with the JG-PES. The skew angle given by Eq. (5.9) is given in the second column. The largest transmission coefficients for each of the reactions at T=300 K is indicated in the third column

Reaction	β	κ
CH_4+H →CH_3+H_2	46.8	LAG4
CH_3D+H →CH_3+DH	57.2	μOMT(SCT)[a]
CH_4+D →CH_3+HD	37.8	LAG4
CH_3D+D →CH_3+D_2	48.4	μOMT(SCT)
CH_4+T →CH_3+HT	33.1	LAG4
CH_3D+T →CH_3+DT	43.4	μOMT(SCT)

[a] The μOMT and the SCT transmission coefficients are equivalent.

In summary, the results obtained for this series of reactions show that SCT should be used with care. A small transmission coefficient does not guarantee that tunneling is well handle by the SCT approximation (see for instance reaction R5 in Table 5.2) Of course, there are reactions for which SCT should work very well as it is the case for heavy atom reorganization reactions at low temperatures [158, 159] or for hydrogen transfer reactions with very wide barriers. [160] However, there are hydrogen transfer reactions presenting very large KIEs [161–164], for which the results obtained with SCT are doubtful. We recommend the use of the ILAT1D algorithm as alternative for the study of large systems.

Table 5.4: KIEs due to tunneling ($\kappa_\mathrm{H}/\kappa_\mathrm{D}$) computed with different tunneling approximations using the JG-PES

	$\kappa_\mathrm{H}(T)/\kappa_\mathrm{D}(T)$			
T(K)	SCT	LCG4	μOMT	LAG4
	CH_4 + H / CH_3D + H			
200.00	2.29	2.88	2.29	5.11
250.00	1.77	2.07	1.77	2.88
300.00	1.51	1.68	1.51	2.04
400.00	1.27	1.34	1.27	1.46
	CH_4 + D / CH_3D + D			
200.00	1.08	2.44	1.58	3.12
250.00	1.08	1.86	1.36	2.27
300.00	1.07	1.58	1.26	1.84
400.00	1.05	1.33	1.15	1.45
	CH_4 + T / CH_3D + T			
200.00	0.78	2.23	1.77	2.74
250.00	0.85	1.68	1.42	1.99
300.00	0.90	1.45	1.27	1.64
400.00	0.94	1.24	1.14	1.33

Chapter 6

The CH_3OH + H hydrogen abstraction reaction

We report a detailed theoretical study of the hydrogen abstraction reaction from methanol by atomic hydrogen. The study includes the analysis of thermal rate constants, branching ratios and kinetic isotope effects. Specifically, we have performed high-level computations at the MC3BB level together with direct dynamics calculations by canonical variational transition state theory (CVT) with the microcanonically optimized multidimensional tunneling (μOMT) transmission coefficient (CVT/μOMT) to study both the $CH_3OH + H \longrightarrow CH_2OH + H_2$ (R1) reaction and the $CH_3OH+H \longrightarrow CH_3O+H_2$ (R2) reaction. The CVT/μOMT calculations show that reaction R1 dominates in the whole range $298 \leq T(\mathrm{K}) \leq 2500$, and that anharmonic effects on the torsional mode about the C–O bond are important, mainly at high temperatures. The activation energy for the total reaction sum of R1 and R2 reactions changes substantially with temperature and therefore the use of straight-line Arrhenius plots is not valid. We recommend the use of new expressions for the total R1 + R2 reaction and for the R1 and R2 individual reactions.

6.1. Introduction

The combustion of methanol is a complex process which is not completely understood, [165–177] although the importance of the H and OH radicals in the early stages of the combustion is well established; these radicals are formed mainly from unimolecular decomposition of methanol. [175, 178–180] For instance, the hydrogen abstraction reaction by atomic hydrogen consumes a significant fraction of the methanol, particularly under fuel-rich conditions, [169] through the reactions:

$$CH_3OH + H \longrightarrow CH_2OH + H_2 \tag{R1}$$

$$CH_3OH + H \longrightarrow CH_3O + H_2 \tag{R2}$$

There is a third possible reaction, which could compete with the R1 and R2 hydrogen abstraction reactions, that leads to the formation of methyl radicals:

$$CH_3OH + H \longrightarrow CH_3 + H_2O \tag{R3}$$

However, the experiments on the pyrolysis of methanol carried out by Aronowitz et al. [181] in the temperature range 1070-1225 K and the discharge flow reactor experiments carried out by Hoyermann *et al.* [182] between 500 and 680 K, indicate that the disappearance of methanol through this channel is only minor. This aspect has been also confirmed by theoretical calculations. [183]

Reactions R1 and R2 involve the formation of the hydroxymethyl CH_2OH and methoxy CH_3O radicals, respectively. The formation of these two radicals and the ratio between their concentrations is of great importance in the of combustion of methanol, because the two species are isomers that have different reactivities. Direct measurements of the total hydrogen abstraction (R1 + R2) thermal rate constants were carried out by Aders and Wagner, [184] Meagher *et al.*, [185] and by Hoyermann *et al.* [182] These experiments were performed in the temperature range T = 295-680 K. At higher temperatures (between T = 1000 and 2740 K), the total abstraction rate constants were obtained from lean methanol flames [178] and from the pyrolysis of methanol [180] –in both cases the measurement of the thermal rate constants is complicated by side reactions. There is a significant discrepancy between the low-temperature experiments, which yield activation energies about 5.4 kcal/mol, and the high-temperature activation energies reported by Vandooren and Tiggelen [178] and by Cribb *et al.* [180] with values of 2.6 and 14.1 kcal/mol, respectively.Tsang [186] gave a recommended expression in the temperature range of T = 600 to 2000 K using bond-order bond-energy (BEBO) transition state calculations to fit the low-temperature experiments and those of Vandooren and Tiggelen [178]. To our knowledge the latest review on the R1 + R2 hydrogen abstraction reactions was carried out by Baulch *et al.* [187], who disregarded the low-temperature data of Meagher *et al.* [185] obtained by electron spin resonance (ESR) and used the mean value of the results of Vandooren and Tiggelen [178] and Cribb *et al.*[180] at T = 2000 K. The recommended expressions reported by Tsang [186] and by Baulch *et al.* [187] give similar results at about T = 600 K, but they disagree by more than a factor of 4 at T = 2000 K, as a consequence of including different experimental results in their fits at high temperatures.

Another aspect about which there is very little information is the branching ratio between R1 and R2, because the above experiments do not distinguish between the two reactions. For instance, Held and Dryer [171] indicated that reaction R1 dominates at low temperatures and that the ratio of the two reaction rate constants does not change with temperature. Tsang, [186] using experimental data on methyl attack on methanol recommended a $k_{\mathrm{R1}}/k_{\mathrm{R2}}$ value of 4 with an uncertainty factor of 3, where k_{R1} and k_{R2} are the thermal rate constants of reactions R1 and R1, respectively. Li and Williams [174] gave a temperature-dependent expression for the ratio $k_{\mathrm{R1}}/k_{\mathrm{R2}}$ constants, but the accuracy of their result is difficult to assess, since it is based on a methanol combustion mechanism that involves 92 elementary reactions.

As indicated above, both the values of the thermal rate constants for the hydrogen abstraction reactions from methanol and the branching ratios are uncertain mainly due to the large number of side reactions that must be considered. In cases like this theoretical calculations can be useful. Several authors have carried out electronic structure calculations at various levels of theory [42, 183, 188–195] and have computed thermal rate constants. [42, 183, 190–192, 195] We are concerned here only with gas-phase studies. The thermal rate constant obtained by Lendvay et al. [183] and by Jodkowski et al. [190] were calculated by combining conventional transition state theory [26] with one-dimensional tunneling corrections (Wigner correction [52] in Ref. [183] and Eckart barrier correction [50] in Ref. [190]). Carvalho et al. [195] performed zero-order interpolated variational transition state [196] with zero-curvature tunneling (ZCT) [73] corrections for tunneling. Kerkeni and Clary [191] applied a two-dimensional reduced dimensionality quantum dynamics model to reactions R1 and R2 and pointed out the importance of including quantum effects for both reactions. In this context, it should be noticed that both the one-dimensional and the ZCT models for tunneling seriously underestimate those quantum effects, [70, 81, 82, 133, 197] so an approach based on multidimensional tunneling paths is needed.

Variational transition state theory [63–67] with multidimensional corrections for tunneling (VTST/MT) [16, 17, 29, 67–70, 132, 133] can yield accurate thermal rate constants [61, 82] for reactions with important quantum effects. It can also account for recrossing effects, so, the accuracy of the VTST/MT results depends largely on the accuracy of the potential energy surface. For the hydrogen abstraction reaction R1, VTST/MT calculations have been carried previously by Chuang *et al.* [42], but the results were handicapped by the low accuracy of the electronic structure calculations, which yield a gas-phase classical barrier height of 7.8 kcal/mol, which differs considerably from benchmark calculations performed at the W1RO level [198] that lead to a classical barrier height of 9.6 kcal/mol [199] and from a later estimate of 9.7 kcal/mol. [193]

Nowadays, it is possible to use VTST/MT together with electronic structure calculations that are very close to chemical accuracy. In this context, it is the main goal of this work to provide reliable thermal rate constants for reactions R1 and R2, so in first place we perform electronic structure calculations at one of the most accurate levels for reaction R1, as suggested in a comprehensive examination [193] of R1, and in second place, we apply VTST/MT.

Another aspect of interest, which may help to identify the main channel for hydrogen abstraction, is the evaluation of the kinetic isotope effects (KIEs).Meagher *et al* [185] have reported experimental thermal rate constants for the reaction

$$CH_3OH + D \longrightarrow CH_2OH + HD \tag{R4}$$

in the temperature range $298 \leq T(\mathrm{K}) \leq 575$.

Hoyerman *et al* [182], in the temperature range $500 \leq T(\mathrm{K}) \leq 680$, prepared deuterated methanol and reported values of the thermal rate constants for the reactions:

$$CD_3OD + H \longrightarrow CD_2OD + HD \tag{R5}$$

$$CD_3OH + H \longrightarrow CD_2OH + HD \tag{R6}$$

In the analysis of the products of reactions R5 and R6 those authors detected the presence of CD_2O, CDOH, and CD_2HOH radicals, which can be obtained by fast reactions of the radicals CD_2OD, and CD_2OH with atomic hydrogen. The products CDOH, and CD_2HOH can only be obtained from hydrogen abstraction reactions from the methyl group, whereas the CD_2O radical can also be obtained from the methoxy radical. Therefore, they could not unambiguously conclude that reaction R1 dominates at those tempereratures.

From the theoretical point of view, the detailed analysis of KIEs can bring additional information about the role played by quantum effects on these systems, so we include reactions R4 and R5 in the present VTST/MT study.

6.2. Methodology

In this section, we first describe the method used to carry out the electronic structure calculations to build the potential energy surface, and after that, we briefly describe canonical variational transition state theory with multidimensional tunneling corrections.

6.2.1. Electronic structure

Benchmark calculations of reaction energies, barrier heights, and transition state geometries for reaction R1 were reported by Pu and Truhlar. [193] Those authors classified the methods by their asymptotic computational scaling behaviors N^{α} (where N is the number of atoms, and α is a parameter in the range 3–7), obtaining, for reaction R1, a consensus value from the N^7 methods for the forward barrier and reaction energy of 9.7 kcal/mol and −6.3 kcal/mol, respectively. These values are very close to those obtained at the W1RO and W1BD levels which lead to values of 9.6 kcal/mol for the barrier height and −6.1 and −6.0 kcal/mol, respectively, for the reaction energy, as shown in Table 6.1. In this work we use one of the methods that Pu and Truhlar [193] recommend for high-level dynamics calculations, i.e., the multicoefficient three-parameters Becke88-Becke95 (MC3BB) method, [200] which yields a barrier height of 9.8 kcal/mol. This method also gives a very similar reaction energetics to the W1R0 and W1BD methods for reaction R2. The experimental enthalpies of reaction [201] show that reaction R1 is exothermic whereas reaction R2 is almost thermoneutral (although most of the theoretical methods listed in Table 6.1 predict a slight endothermicity). The CCSD(T,full)//MP2(full)/cc-pVTZ and CCSD(T,full)/cc-pVTZ give similar results to the MC3BB methods, but the latter is more suitable for dynamical calculations because it scales as N^5, whereas CCSD(T, full) methods scale as N^7. On the other hand the G2 calculations carried out by Lendvay *et al.* [183] and by Jodkowski *et al.* [190], which also scale as N^7, yield to reaction barrier heights that are probably too high by more than 0.5 kcal/mol.

Table 6.1: Energetic parameters (in kcal/mol) of reactions R1 and R2 obtained at different levels of theory. $V^{\ddagger}$ is the barrier height, ΔE is the classical energy of reaction, $\Delta H_0^{\ddagger,o}$ is the enthalpy of activation at 0 K, and ΔH_0^o is the enthalpy of reaction at 0 K. Experimental values are also listed for comparison

Method	$V^{\ddagger}$	ΔE	$\Delta H_0^{\ddagger,o}$	ΔH_0^o	Reference
				R1	
Estimate	9.7	-6.3	–	–	[193]
W1RO	9.6	-6.1	8.2	-8.5	[198]
W1BD	9.6	-6.0	8.2	-8.4	This work
MC3BB	9.8	-4.7	8.4	-7.2	[193]
G2	10.6	-5.6	9.0	-8.2	[183, 190]
CCSD(T,full)//MP2(full)/cc-pVTZ	9.9	-5.5	8.6	-7.9	[191]
CCSD(T,full)/cc-pVTZ	9.8	-6.1	7.8	-8.5	[195]
Exp.	–	–	–	-8.8 ± 0.4	[201]
				R2	
W1RO	15.3	3.7	13.3	0.7	This work
W1BD	15.2	3.7	13.3	0.6	This work
MC3BB	15.6	3.8	13.7	0.8	This work
G2	16.3	3.1	14.2	0.6	[183, 190]
CCSD(T)//MP2(full)/cc-pVTZ	14.9	2.8	13.3	0.2	[191]
CCSD(T,full)/cc-pVTZ	14.8	2.3	12.7	-0.7	[195]
Exp.	–	–	–	-0.3 ± 1.0	[201]

The MC3BB method merges scaling-all-correlation (SAC) theory [202] with a modification of the Becke88-Becke95 [203, 204] 1-parameter model for kinetics (BB1K) [205] with empirical parameters to make the method more accurate than other methods scaling as N^5. The MC3BB energy is obtained by the expression:

$$E(\text{MC3BB}) = c_2[E(\text{HF/DIDZ}) + c_1\Delta E(\text{MP2}|\text{HF/DIDZ})] + (1-c_2)E(\text{BB}X/\text{MG3S}) \quad (6.1)$$

where the empirical coefficients c_1 and c_2 are equal to 1.332 and 0.205 respectively; BBX is the same as BB1K except that the percentage of Hartree-Fock exchange is 39% instead of 42%; DIDZ refers to the 6-31+G(d,p) basis set, [145] and MG3S [206] is a minimally augmented polarized triple-ζ basis set.

6.2.2. Reaction rates

The thermal rate constants for the hydrogen abstraction reactions from methanol were calculated by means of canonical variational transition-state theory with a multidimensional treatment of tunneling (CVT/MT). [66, 77] All the electronic structure calculations were performed at the MC3BB level using a direct dynamics approach, [137] i.e., the points to build the potential energy surface needed for the dynamics were calculated "on the fly". The canonical variational version of transition state theory implies that the reactants are equilibrated canonically (in a fixed-temperature ensemble) and that the transition state dividing surface (the bottleneck for reaction) minimizes the one-way flux toward products by passing through the point on the minimum energy path (MEP) [73, 76, 207] that presents a maximum in the generalized free energy of activation. [66, 208, 209]

The MEP is the union of the paths of steepest descent in isoinertial coordinates from the saddle point to the reactants and to the products, and the signed distance along this path is labeled as s. The MEP was followed in mass-scaled Cartesian coordinates (mass-weighted Cartesian coordinates divided by the square root of an arbitrary scaling mass μ) by the Page-McIver method [210] using a stepsize of 0.005 a_0 and a scaling mass $\mu = 1$, and Hessians were calculated each 9 steps. All the harmonic vibrational frequencies along the MEP were obtained using redundant internal coordinates [211] and scaled by a factor of 0.9669. [200] The CVT/MT expression to evaluate thermal rate constants, $k^{\text{CVT/X}}$, at a given temperature, T, is given by:

$$k^{\text{CVT/X}}(T) = \kappa^{\text{CVT/X}}(T)k^{\text{CVT}}(T), \quad (6.2)$$

where $\kappa^{\text{CVT/X}}(T)$ is the ground-state transmission coefficient computed with the multidimensional method X, and $k^{\text{CVT}}(T)$ is the quasiclassical canonical thermal rate constant:

$$k^{\text{CVT}}(T) = \min_s k^{\text{GT}}(T,s) = \sigma\frac{1}{\beta h}\frac{Q^{\text{GT}}(T,s_*^{\text{CVT}})}{\Phi_{\text{R}}(T)}\exp\left[-\beta V_{\text{MEP}}\left(s_*^{\text{CVT}}\right)\right] \quad (6.3)$$

where k_{B} is the Boltzmann constant; h is the Planck constant; σ is the symmetry number; [31, 78] $V_{\text{MEP}}\left(s_*^{\text{CVT}}\right)$ is the classical potential at point s_*^{CVT} of the MEP. The value s_*^{CVT} is chosen as the point of the MEP in which the free energy of activation has a maximum, or similarly, as the generalized transition (GT) at which is located the bottleneck for reaction. $Q^{\text{GT}}(T,s_*^{\text{CVT}})$ is the product of the rotational, vibrational and electronic partition functions of the generalized transition state. $\Phi_{\text{R}}(T)$ is the partition function of reactants per unit volume and is given as the product of the partition functions for the two reactants species and their relative translational motion. Note that we omit symmetry numbers from rotational partition functions and instead accumulate these in an overall symmetry number σ, as discussed further below.

The term 'quasiclassical' means that, except for the reaction coordinate, which corresponds to the mode with imaginary frequency at the transition state, all the remaining $3N-7$ vibrational modes ($3N-6$ modes for linear molecules; N being the number of atoms) are treated quantally by using quantum vibrational partition functions in the rate constant expression of Eq. (6.3). Quantum mechanical effects on the reaction-coordinate motion are incorporated by the ground-state transmission coefficient [67, 128] which multiplies the rate constant of Eq. (6.2) and is given by:

$$\kappa^{\mathrm{CVT/X}}(T) = \kappa^{\mathrm{CVT/CAG}}(T)\kappa^{\mathrm{X}}(T) \tag{6.4}$$

where $\kappa^{\mathrm{CVT/CAG}}(T)$ corrects for the different thresholds which may have the CVT thermal rate constant and the tunneling transmission coefficient $\kappa^{\mathrm{X}}(T)$. [128] For reactions with tight transition states, such as reactions R1 and R2, $\kappa^{\mathrm{CVT/CAG}}(T)$ is usually very close, within 5%, to unity. The tunneling transmission coefficient $\kappa^{\mathrm{X}}(T)$ is given by:

$$\kappa^{\mathrm{X}}(T) = \beta \exp(\beta V_{\mathrm{a}}^{\mathrm{AG}}) \int_{E_0}^{\infty} dE P^{\mathrm{X}}(E) \exp(-\beta E) \tag{6.5}$$

where $P^{\mathrm{X}}(E)$ is the semiclassical ground-state reaction probability computed by approximation X. The lower limit of the integral is the lowest energy at which it is possible to have tunneling, i.e., it is the energy of the reactant zero-point level when the reaction is written in the exoergic direction; $V_{\mathrm{a}}^{\mathrm{AG}}$ is the maximum of the vibrationally adiabatic potential which is given by:

$$V_{\mathrm{a}}^{\mathrm{G}}(s) = V_{\mathrm{MEP}}(s) + \epsilon_{\mathrm{int}}^{G}(s), \tag{6.6}$$

where $\epsilon_{\mathrm{int}}^{\mathrm{G}}(s)$ denotes the zero-point energy of the vibrational modes transverse to the MEP.

In the present work, the semiclassical probability $P^{\mathrm{X}}(E)$ at every tunneling energy E has been calculated by the microcanonically optimized multidimensional tunneling (μOMT) approximation [24], which chooses the largest value between the small-curvature tunneling [19, 86–88] (SCT) probability, $P^{\mathrm{SCT}}(E)$, and the large-curvature tunneling [16, 17, 20, 21, 24, 87, 90–92] (LCT) probability $P^{\mathrm{LCT}}(E)$; the latter being evaluated with the version 4 of the LCT method: [21]

$$P^{\mu\mathrm{OMT}}(E) = \max_{E} \left\{ \begin{array}{l} P^{\mathrm{SCT}}(E) \\ P^{\mathrm{LCT}}(E) \end{array} \right. \tag{6.7}$$

The LCT tunneling probabilities were evaluated using the interpolated large-curvature tunneling in two dimensions (ILCT2D) [23] algorithm. The electronic structure calculations were performed with *Gaussian03*, [212] the thermal rate constants CVT/μOMT were calculated with version 9.7 of the POLYRATE program. [213] A modified version of the GAUSSRATE9.7 [214] program made the linkage between the two packages. Some data used in the next Section were extracted from graphs made by the *WinDig* program [215], i.e., from: Figure 4 of Ref. [182], Figure 13 of Ref. [191], and Figure 3 of Ref. [192].

6.3. Results and discussion

In this section, we first describe some important issues related to the stationary points of the hydrogen abstraction reaction, which includes the anharmonic treatment of the torsional mode about the C–O bond, then we discuss the CVT/μOMT calculations carried out in this work, initially in the context of previous theoretical calculations and secondly in the context of the experiment. Finally, we discuss the results obtained in this work for the branching ratios and KIEs.

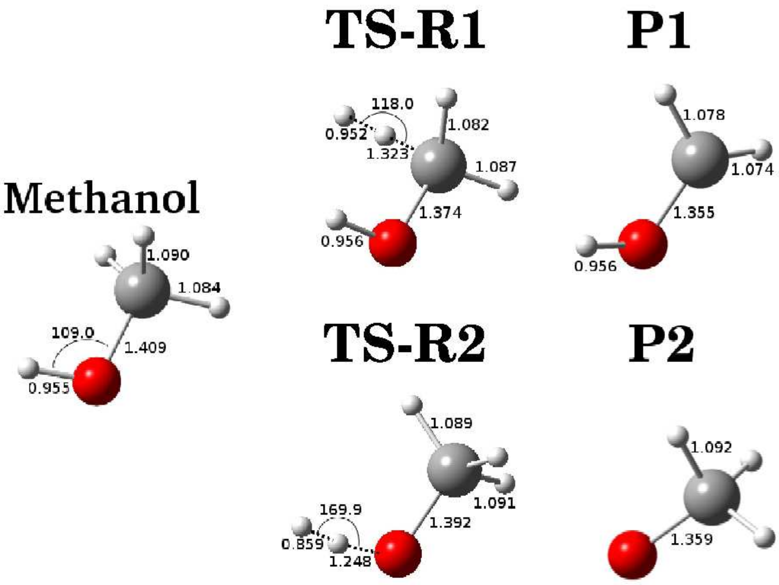

Figure 6.1: Geometries of the stationary points for reactions R1 and R2. TS-R1 and TS-R2 are the transition state geometries for reactions R1 and R2, respectively. Distances are in Å; bond and dihedral angles are in degrees.

6.3.1. Stationary points

All electronic structure calculations needed for the dynamics calculations were carried out at MC3BB level. [200] The optimized geometries of the stationary points are shown in Figure 6.1. The equilibrium configuration of methanol has C_s point-group symmetry. The hydrogen atom can be abstracted from the CH_3 group or from the OH group, forming the hydroxymethyl radical (reaction R1) or the methoxy radical (reaction R2) from the transition states TS-R1 and TS-R2, respectively. For reaction R1 the hydrogen atom from the methyl group is abstracted in a *gauche* conformation, forming a dihedral angle with the hydrogen atom of the hydroxyl of 74°. This transition state is chiral and therefore it has one enantiomer. The interconversion between enantiomers is possible by rotation about the C−O bond. The top of the rotational barrier is a second-order saddle point and corresponds to the eclipsed conformation. The calculated barrier height at the MC3BB has a value of 2.9 kcal/mol with respect to the saddle point energy. The interconversion is also possible through a second-order saddle point corresponding to an *anti* conformation, but in this case the barrier is higher, i.e., 4.0 kcal/mol. Chuang et al. [42] using a semiempirical method obtained similar barriers of 3.3 kcal/mol and 4.2 kcal/mol for the eclipsed and *anti* conformations. Those authors pointed out that the barriers between transition states (which are the minima along the torsion coordinate) are high enough, so they can be treated as two independent reactive channels.

Several theoretical works [190, 191, 195] ignored the chiral nature of the transition state and pointed out that for reaction R1, because methanol has three reactive hydrogens, the symmetry number entering the transition state theory expression (same as Eq. (6.3) but with the dividing surface located at the transition state) should be three. It should be noticed that the symmetry number is given by [31, 78]:

$$\sigma = \frac{\sigma_{\mathrm{R}} n_{\mathrm{TS}}}{\sigma_{\mathrm{TS}} n_{\mathrm{R}}} \tag{6.8}$$

where n_{TS} and n_{R} are the number of enantiomers of the transition state and the reactants, respectively; σ_{R} and σ_{TS} are the symmetry numbers of the rotational partition function of the reactants and the transition state, respectively. Taking into account that the minimum-energy configuration of methanol belongs to the C_s point-group symmetry (so $\sigma_{\mathrm{R}} = 1$) and that the transition state has two enantiomers, the symmetry number for reaction R1 is two. To our knowledge, this issue was only correctly addressed by Chuang et al. [42]. Hereafter, all the theoretical rate constants that included a factor of three [190, 191, 195] were multiplied by 2/3 to correct the symmetry number.

For reaction R2 the symmetry number is the unity.

6.3.2. Anharmonicity

The previous theoretical works [42, 190, 191, 195] have treated the torsional motion of the methyl group of methanol as a harmonic-oscillator (HO) vibration, i.e., the partition function, $Q_{\mathrm{tor}}^{\mathrm{HO,CH_3OH}}$, of this normal mode is given by:

$$Q_{\mathrm{tor}}^{\mathrm{HO,CH_3OH}}(T) = \frac{e^{-\beta\hbar\omega_{\mathrm{tor}}^{\mathrm{CH_3OH}}/2}}{1 - e^{-\beta\hbar\omega_{\mathrm{tor}}^{\mathrm{CH_3OH}}}} \tag{6.9}$$

This may not be a good approximation at high temperatures, so we have calculated the torsional potential about the C–O bond by performing MC3BB calculations every 5 degrees, in which all geometric parameters were optimized with the exception of the dihedral angle. The calculations were carried out on methanol and on both transition states, TS-R1 and TS-R2. The results are plotted in Figure 6.2. It should be noticed that the two chiral transition states of reaction R1 are now connected by the torsional potential, so instead of using the HO partition function and include the symmetry number of Eq. (6.8), which accounts for the two enantiomers, it is better to consider a multiconformer harmonic-oscillator (MC-HO) partition function, which, in general, is given by: [79]

$$Q_{\mathrm{tor}}^{\mathrm{MC-HO}}(T) = \sum_{j=1}^{P} \frac{e^{-\beta(U_j + \hbar\omega_{\mathrm{tor},j}/2)}}{1 - e^{-\beta\hbar\omega_{\mathrm{tor},j}}} \tag{6.10}$$

where U_j is the energy of well j relative to the lowest well of the torsional potential, $\omega_{\mathrm{tor},j}$ is the harmonic frequency of well j, and the sum runs over the P distinguishable conformers. If there is only one conformer then Eq. (6.10) reduces to Eq. (6.9). For transtion state TS-R1, $P = 2$, whereas for both TS-R2 and methanol $P = 1$ (so in this case e use either the HO or the MC-OH expression).

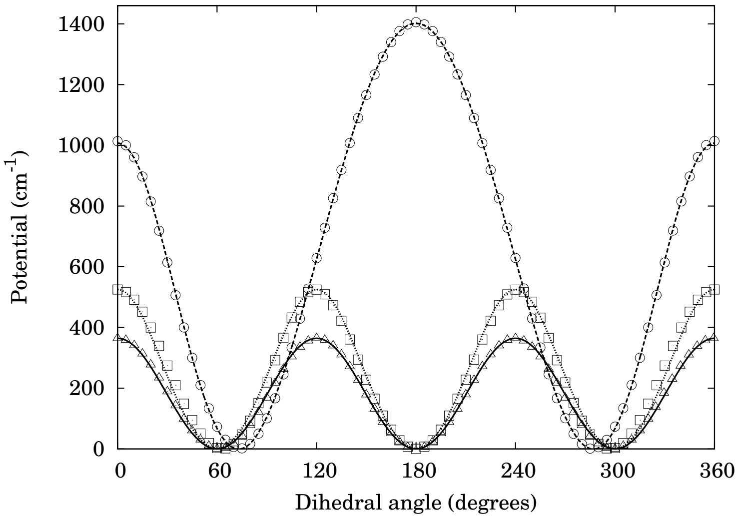

Figure 6.2: Torsional potentials (in cm^{-1}) calculated at the MC3BB level about the C–O bond for methanol (triangles), TS-R1 (circles), and TS-R2 (squares). The potentials were fitted to cosine Fourier series given by Eqs. (6.12), (6.13), and (6.14) and shown in the plot as solid line, dashed line, and dotted line for methanol, TS-R1 and TS-R2, respectively.

The one-dimensional hindered-rotor partition function can be calculated conveniently by the torsional eigenvalue summation (TES) method, [79] and we simplify the calculations by assuming that: (i) the reduced moment of inertia, I, is independent of the reaction coordinate, and (ii) the potentials can be accurately fitted to a cosine Fourier series of the type:

$$V(\phi) = b_0 + \sum_{n=1}^{n_{\max}} b_n \cos(n\phi) \tag{6.11}$$

where b_0, $b_n, n = 1 \ldots n_{\max}$, are parameters.

We have calculated the reduced moments of inertia of methanol, TS-R1, and TS-R2 at the equilibrium configurations using the scheme developed by Pitzer, [216] which allows the calculation of a single asymmetric top attached to a rigid frame. The calculated reduced moments of inertia (in atomic units) for methanol, TS-R1 and TS-R2 have values of 3956.3, 4439.8 and 12191, respectively. For the relaxed scans starting at each of the three stationary points the largest variation of the reduced moment of inertia along the torsion coordinate with respect to the equilibrium value was smaller than 3%, so approximation (i) is very good in this case.

As shown in Figure 6.2, the cosine Fourier series potentials for methanol:

$$V(\phi)_{\mathrm{CH_3OH}}/\mathrm{cm}^{-1} = 180.401 + 182.1\cos(3\phi) + 1.8\cos(6\phi), \tag{6.12}$$

TS-R1:

$$V(\phi)_{\mathrm{TS-R1}}/\mathrm{cm}^{-1} = 632.053 - 317.0\cos(\phi) + 548.3\cos(2\phi) + 119.9\cos(3\phi) + 23.0\cos(4\phi), \tag{6.13}$$

and TS-R2:

$$V(\phi)_{\mathrm{TS-R2}}/\mathrm{cm}^{-1} = 251.859 + 260.4\cos(3\phi) + 11.5\cos(6\phi) + 1.1\cos(9\phi), \tag{6.14}$$

fit the MC3BB torsion potential accurately.

The TES partition function is simply obtained from eigenvalue summation of the torsional coordinate, i.e.,

$$Q_{\rm tor}^{\rm TES}(T) = \frac{1}{\sigma_{\rm tor}} \sum_{j=0}^{j_{max}} e^{-\beta E_j} \tag{6.15}$$

where E_j are the energies (eigenvalues) obtained from solving the Schrödinger equation (see Ref. [79] for details), and $j_{\rm max}$ is the total number of eigenvalues, which should be large enough that the calculated partition function is converged (usually $j_{\rm max} = 200$ suffices); $\sigma_{\rm tor}$ is the symmetry number due to torsion (number of indistinguishable minima due to internal rotation), which is the unity for TS-R1 and 3 for both methanol and TS-R2. The lowest eigenvalue of the TES method gives the zero-point energy of the torsional potential, and therefore the frequency associated to it. The harmonic frequencies associated to the C–O bond torsion in methanol, TS-R1 and TS-R2 are 290, 359, and 190 cm^{-1}, respectively, whereas the anharmonic frequencies obtained by the TES method are 250, 342, and 186 cm^{-1}, respectively.

We denote as $Q_{\rm tor}^{\rm MC-HO-Z}(T)$ the zero-point energy (ZPE) corrected MC-HO partition function with the TES calculated frequencies. The total anharmonicity on the torsional mode is the product of two effects: (1) that due to corrections in the ZPE, which is given by the quotient $Q_{\rm tor}^{\rm MC-HO-Z}(T)/Q_{\rm tor}^{\rm MC-HO}(T)$, and (2) that due to the deviations from the HO approximation, which is given by the quotient $Q_{\rm tor}^{\rm TES}(T)/Q_{\rm tor}^{\rm MC-HO-Z}(T)$. As shown in Table 6.2, in general the anharmonicity is more important for the equilibrum configuration of methanol, when compared with the transition states TS-R1 and TS-R2, because the former has the lowest torsional barrier of the three of them. At low temperatures the ZPE effect is quite important, and at $T =$ 300 K there is an important ZPE effect in methanol that makes the MC-HO-Z partition function 16% higher than the MC-HO partition function. As the temperature increases more levels are populated, and the leading effect is the level separation, which remains constant in the harmonic oscillator whereas it may decrease in the anharmonic treatment. As a consequence the harmonic partition function increases faster than the TES partition function and at $T =$ 2500 K it is a 41% higher for the equilibrium configuration of methanol. This effect is also important for TS-R2 and at $T =$ 2500 K the MC-HO partition fuction is 28% higher than the TES partition function. For TS-R1, which has the largest torsional barriers of the three configurations considered here, the TES partition function is less than 10% higher than the MC-HO partition function at 300 K and 2500 K (the discrepancy is larger at some intermediate temperatures, i.e., about 20% at $T =$ 1000 K), so in general the harmonic approximation is better than for TS-R2 and for methanol.

6.3.3. Theoretical thermal rate constants

The thermal rate constants obtained by TST, CVT, CVT/ZCT and CVT/μOMT methods for the hydrogen abstraction are listed in Table 6.3. Note that here we use the acronym TST, or the superscript ‡, to denote conventional transition state theory results without tunneling but with anharmonic treatment of the C–O bond torsion. In fact all the thermal rate constants listed in Table 6.3 were obtained by multiplying the thermal rate constants obtained using the harmonic approximation for all the degrees of freedom by the coefficient, $\alpha_{\rm tor}^{\ddagger}(T)$, which includes the anharmonic effects on the torsional modes, i.e., for the TST thermal rate constant:

$$k_{\rm tor,TES}^{\rm TST}(T) = \alpha_{\rm tor}^{\ddagger}(T) k_{\rm tor,MC-HO}^{\rm TST}(T) \tag{6.16}$$

Table 6.2: Multiconformer harmonic-oscillator (MC-HO), and torsional eigenvalue summation (TES) partition functions of methanol, TS-R1 and TS-R2, respectively

	CH_3OH			TS-R1			TS-R2		
T(K)	MC-HO	MC-HO-Z	TES	MC-HO	MC-HO-Z	TES	MC-HO	MC-HO-Z	TES
300.00	0.664	0.788	0.793	1.031	1.092	1.134	1.061	1.082	1.183
400.00	0.916	1.078	1.070	1.448	1.527	1.623	1.436	1.463	1.615
500.00	1.164	1.363	1.322	1.855	1.952	2.121	1.808	1.841	2.024
700.00	1.652	1.929	1.763	2.653	2.787	3.128	2.546	2.593	2.771
1000.00	2.378	2.770	2.318	3.834	4.023	4.607	3.649	3.716	3.739
1500.00	3.582	4.168	3.069	5.786	6.068	6.876	5.483	5.583	5.071
2000.00	4.782	5.563	3.689	7.732	8.106	8.887	7.315	7.448	6.179
2500.00	5.982	6.957	4.226	9.674	10.142	10.683	9.146	9.312	7.141

where $k^{\mathrm{TST}}_{\mathrm{tor,TES}}(T)$ and $k^{\mathrm{TST}}_{\mathrm{tor,MC-HO}}(T)$ are the calculated TST thermal rate constants using the TES and MC-HO partition functions for the torsion, respectively. The coefficient between them is given by the following quotient between partition functions:

$$\alpha^{\ddagger}_{\mathrm{tor}}(T) = \frac{Q^{\mathrm{TES},\ddagger}_{\mathrm{tor}}(T)\,Q^{\mathrm{MC-HO,CH_3OH}}_{\mathrm{tor}}(T)}{Q^{\mathrm{TES,CH_3OH}}_{\mathrm{tor}}(T)\,Q^{\mathrm{MC-HO},\ddagger}_{\mathrm{tor}}(T)} \tag{6.17}$$

In Eq. (6.17) the symbol ‡ refers to TS-R1 or to TS-R2 depending whether we are discussing reaction R1 or reaction R2, and CH_3OH refers to methanol in its equilibrium configuration.

At $T = 300$ K the coefficients $\alpha^{\mathrm{TS-R1}}_{\mathrm{tor}}$ and $\alpha^{\mathrm{TS-R2}}_{\mathrm{tor}}$ are 0.93, because in both cases the anharmonicity is mainly due to the ZPE effect in methanol. At high temperatures both methanol and TS-R1 show important deviations from the MC-HO partition functions. This is not the case for TS-R1, so the quotient between partition functions deviates more from the harmonic oscillator approximation for R1 than for R2. For instance, at $T = 2500$ K $\alpha^{\mathrm{TS-R1}}_{\mathrm{tor}}$ and $\alpha^{\mathrm{TS-R2}}_{\mathrm{tor}}$ are 1.56 and 1.11, respectively. Since R1 is the dominant channel for the hydrogen abstraction reaction, the anharmonic treatment of the torsional mode slightly lowers the total thermal rate constants at room temperature and moderately rises them at high temperatures, when compared to the harmonic oscillator values.

The ZCT and μOMT transmission coefficients are given in Table 6.4. The LCT transmission coefficients are not listed because they were always smaller than the SCT ones; the latter coincided at all temperatures in the interval of temperatures 300–2500 K with the μOMT transmission coefficients. The barrier height for reaction R1 is much lower than that for reaction R2, and the dynamics calculations confirm that reaction R1 is faster than reaction R2 between 300 and 2500 K and only at high temperatures does the contribution of R2 start to be important. Tunneling is more important for reaction R2, with the μOMT transmission coefficient at $T =$ 300 K being 29.8 (2.45 times larger than for reaction R1.) However, the variational effects decrease the rate constants at $T = 300$ K by a factor of 0.67, and the CVT/μOMT rate constant is just 19.9 times larger than the TST one. For reaction R1 tunneling is less important, but variational effects are very small, and therefore at $T = 300$ K the CVT/μOMT rate constant is 11.2 times larger than the TST result, with a μOMT transmission coefficient of 12.2. It is important to include the coupling between the reaction coordinate and the normal

Table 6.3: Thermal rate constants (in cm^{3}molecule^{-1}s^{-1}) obtained with TST, CVT and with CVT with the ZCT and μOMT approximations for tunneling for reactions R1 an R2. All rate constants include the anharmonicity parameter of Eq. (6.17)

	R1				R2			
T(K)	TST	CVT	CVT/ZCT	CVT/μOMT	TST	CVT	CVT/ZCT	CVT/μOMT
298	1.67(-17)[a]	1.53(-17)	4.71(-17)	1.93(-16)	2.47(-21)	1.64(-21)	1.72(-20)	5.16(-20)
300	1.84(-17)	1.68(-17)	5.11(-17)	2.05(-16)	2.89(-21)	1.92(-21)	1.95(-20)	5.74(-20)
400	7.17(-16)	6.73(-16)	1.23(-15)	2.79(-15)	1.04(-18)	7.83(-19)	2.48(-18)	4.50(-18)
500	7.09(-15)	6.74(-15)	9.88(-15)	1.68(-14)	3.82(-17)	3.08(-17)	6.20(-17)	8.99(-17)
600	3.51(-14)	3.36(-14)	4.37(-14)	6.36(-14)	4.44(-16)	3.74(-16)	6.00(-16)	7.74(-16)
700	1.16(-13)	1.12(-13)	1.35(-13)	1.79(-13)	2.66(-15)	2.31(-15)	3.25(-15)	3.92(-15)
1000	1.20(-12)	1.16(-12)	1.27(-12)	1.46(-12)	7.76(-14)	7.06(-14)	8.32(-14)	9.10(-14)
1500	9.80(-12)	9.50(-12)	9.90(-12)	1.05(-11)	1.37(-12)	1.28(-12)	1.38(-12)	1.43(-12)
2000	3.32(-11)	3.21(-11)	3.29(-11)	3.41(-11)	6.76(-12)	6.41(-12)	6.67(-12)	6.82(-12)
2500	7.59(-11)	7.31(-11)	7.43(-11)	7.59(-11)	1.93(-11)	1.84(-11)	1.89(-11)	1.92(-11)

[a] Powers of ten in parenthesis.

modes orthogonal to it, because the ZCT transmission coefficients seriously underestimate the tunneling contribution for both reactions. It should be noticed that the ZCT transmission coefficient is multidimensional, because it includes the variation of $\epsilon^{G}_{\mathrm{int}}(s)$ with s, which is a multidimensional effect, but it treats the MEP as if it were one-dimensional by neglecting its curvature, although it is a multidimensional path.

The Wigner [52] and Eckart [50] tunneling contributions used by Lendvay *et al* [183] and by Jodkowski *et al.* [190], respectively, are obtained from the second derivative of $V_{\mathrm{MEP}}(s)$ at the top of the potential, i.e., those are completely one-dimensional models based on the normal mode with imaginary frequency at the transition state. The imaginary frequencies at the MC3BB level for reactions R1 and R2 are, respectively, 1466i cm^{-1} and 1718i cm^{-1}, and with values of the Wigner transmission coefficients at $T = 300$ K of 3.06 and 3.83. (The failure of the Wigner model is not surprising when one considers that the value of 3.83 results from retaining only the first two terms of a series that begins $1 + 2.83 + \cdots$.) The transmission coefficients predicted by the Wigner expression are too small. However, the transmission coefficients reported by Jodkowski *et al.* [190], which were based on the Eckart potential are unusually large with values of 7.5 and 27.2 at $T = 400$ K for reactions R1 and R2, respectively, as compared to the μOMT transmission coefficients of 4.1 and 5.7. Those authors obtained such a large values because their calculations used imaginary frequencies with values of 1827i cm^{-1} and 2246i cm^{-1} for reactions R1 and R2, respectively. In one-dimensional models larger imaginary frequencies lead always to narrower potentials and therefore to larger transmission coefficients (see Figure 6.3). In multidimensional models, such as μOMT, this is not so straightforward, because although very close to the transition state the reactive motion can be regarded as one-dimensional (at that stage the reaction coordinate involves essentially the motion of the atoms of the mode with imaginary frequency), as the reaction progresses toward reactants and toward products more normal mode motions get involved and coupling between the reaction coordinate and the other modes becomes important. As a consequence, the magnitude of the

Table 6.4: Transmission coefficients computed with the ZCT and μOMT approximations for R1 and R2 reactions

	R1		R2	
T(K)	CVT/ZCT	CVT/μOMT	CVT/ZCT	CVT/μOMT
300	3.03	12.2	10.1	29.8
400	1.83	4.14	3.17	5.74
500	1.47	2.50	2.01	2.92
700	1.21	1.60	1.41	1.69
1000	1.10	1.26	1.18	1.29
1500	1.04	1.11	1.07	1.12
2000	1.02	1.06	1.04	1.06
2500	1.02	1.04	1.03	1.04

tunneling effect does not depend exclusively on the magnitude of the imaginary frequency at the transition state, although is still a useful but rough indication of the amount of tunneling.

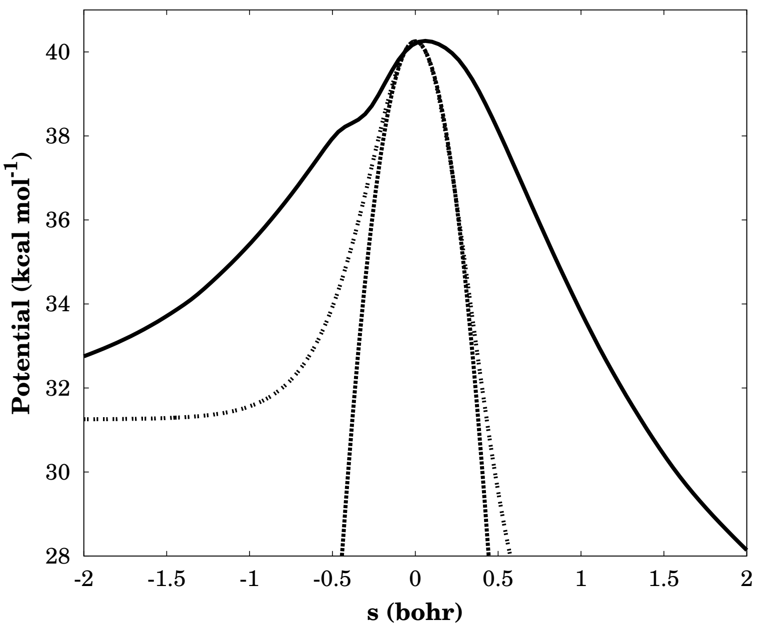

Figure 6.3: Vibrationally adiabatic potential for reaction R1 (solid line) compared to Wigner (inverse parabola) and Eckart potentials that were obtained with the imaginary frequency reported in Ref. [190] for reaction R1, i.e. 1827i cm^{-1}. The three potentials are normalized to the same value at the saddle point ($s = 0$).

Kerkeni and Clary [191] reported values for the imaginary frequencies calculated at the MP2(full)/cc-pVTZ level which are 1802i cm^{-1} and 2158i cm^{-1} for reactions R1 and R2, respectively. These large values are obtained because the MP2(full)/cc-pVTZ level yields barrier heights which are too high in this case (i.e., 14.4 and 24.4 kcal/mol for reactions R1 and R2, respectively), making the potential near to the top of the barrier too narrow. For this reason their tunneling calculations are a 42% larger than our μOMT transmission coefficients at $T = 300$ K. (For reactions R1 and R2 the μOMT transmission coefficients are about 12 and 30, whereas those obtained by Kerkeni and Clary [191] are about 17 and 38.) At $T = 700$ K the agreement is very good for reaction R1, but less satisfactory for reaction R2, with the transmission coefficients reported by them being about 1.7 and 4.3, for reactions R1 and R2, respectively. As we have mentioned previously, at high temperatures most of the tunneling (if any) occurs near the top of the barrier and the magnitude of the transmission coefficient is more sensitive to the value of the imaginary frequency, which in this case is too high.

The issues raised in this discussion point out the importance of choosing electronic structure methods consistent not just with the energetics of the reaction (which can often be achieved by performing very accurate single-point calculations on optimized geometries obtained at a lower level), but also with other aspects of the potential energy surface, such as geometries and vibrational frequencies, which may have an important impact on the dynamics. On the other hand, the multidimensional methods for tunneling show the limited reliability of one-dimensional methods, since the latter do not account for many of the features of the chemical reaction.

6.3.4. Arrhenius parameters

Table 6.5 lists the Arrhenius parameters obtained by different experimental techniques or by different theoretical methods for the R1 + R2 hydrogen abstraction process. The discharge flow reactor experiments are available at temperatures ranging from 295 to 680 K, which is a temperature region in which quantum effects are very relevant. To establish some difference between these data and those obtained from high-temperature experiments (as for instance pyrolysis and unimolecular decomposition), all data were divided into two sets, one 'low-temperature' (low T) set for data between 295 and 700 K and one 'high-temperature' (high T) set for data which are roughly between 700 and 2000 K. Although we do not recommend two-parameter Arrhenius fits in general, we made such fits in Table 6.5 simply as a convenient way to make comparisons.

Whereas the activation energies in Table 6.5 represent averages over given temperature intervals, it is also interesting to consider the temperature-dependent activation energy given by the local slope of an Arrhenius plot as

$$E_\mathrm{a} = -R\frac{d\mathrm{ln}k}{d(1/T)} \tag{6.18}$$

Figure 6.4 plots E_a as a function of temperature and shows that the anharmonicity in the torsional mode increases the energy of activation regarding to the harmonic treatment. Besides, E_a increases substantially with temperature, i.e., from 5.73 kcal/mol (5.67 kcal/mol with the harmonic approximation) at $T = 300$ K to 17.7 kcal/mol (17.3 kcal/mol using the harmonic approximation) at $T = 2500$ K. This behavior is not just due to the quantum effects, which decrease both the preexponential factor and the activation energy at low T with respect to the classical rate constant, because the TST activation energy also increases when going from low T to high T in values averaged over intervals (see Table 6.5); using Eq. (6.18) with TST gives 8.6 kcal/mol at $T = 300$ K and 18.3 kcal/mol at $T = 2500$ K. The change of the activation energy with temperature is typical of many bimolecular gas-phase reaction rate constants [217–220], and it leads to curved Arrhenius plots. Figure 6.5 shows a concave Arrhenius plot even at high T which is an indication of the rise of the activation energy with temperature.

Table 6.5: Arrhenius parameters (activation energies E_a, in kcal/mol, and logarithm (to the base 10) of the preexponencial factor, $log(A/\text{cm}^3\text{s}^{-1}\text{molecule}^{-1})$ for the overall CH_3OH + H reaction

Reference	T(K)	$logA$	E_a	Experimental technique/Theoretical method
Aders and Wagner [184]	295−653	-10.42	5.30	Discharge flow reactor
Meagher *et al.* [185]	298−575	-10.96	5.44	ESR
Warnatz [167]	300−700	-10.18	6.10	Combustion
Hoyermann *et al.* [182]	500−680	-10.66	5.29	Discharge flow reactor
Li and Williams [174]	300−700	-9.95	6.75	Laminar counterflow flame
Baulch *et al.* [187]	300−700	-10.40	5.60	Fit to values of Refs. [178, 180, 182, 184]
Chuang *et al.* [42]	300−700	-10.93	4.11	CVT/μOMT
Lendvay *et al.* [183]	300−700	-9.53	6.96	TST/Wigner
Jodkowski *et al.* [190]	300−700	-11.00	6.13	TST/Eckart
Carvalho *et al.* [195]	300−600	-10.66	6.59	IVTST-0/ZCT
Kerkeni and Clary [191]	320−680	-10.76	6.59	Reduced dimensionality QD
This work	300−700	-10.11	-9.17	TST
This work	300−700	-10.59	7.18	CVT/μOMT
Westbrook and Dryer [165]	1000−2180	-10.28	7.01	Pyrolysis
Vandooren and Tiggelen [178]	1000−2000	-10.25	2.61	Beam molecular sampling
Spindler and Wagner [179]	1600−2100	-10.28	5.25	Thermal unimolecular decomposition
Warnatz [167]	700−2000	-10.18	6.10	Combustion
Cribb *et al.* [180]	1800−2740	-9.32	14.06	Pyrolysis
Li and Williams [174]	700−2000	-9.02	9.90	Laminar counterflow flame
Held and Dryer [171]	633−2050	-10.52	6.10	Several experimental techniques
Tsang [186]	600−2000	-9.08	9.37	Fit to BEBO calculations
Baulch *et al.* [187]	700−2000	-9.88	7.36	Fit to values of Refs. [178, 180, 182, 184]
Chuang *et al.* [42]	700−2000	-9.75	7.34	CVT/μOMT
Lendvay *et al.* [183]	700−2000	-8.82	9.37	TST/Wigner
Jodkowski *et al.* [190]	700−2000	-9.38	11.19	TST/Eckart
Carvalho *et al.* [195]	800−2000	-9.31	11.18	IVTST-0/ZCT
Kerkeni and Clary [191]	680−2000	-9.97	9.11	Reduced dimensionality QD
This work	700−2000	-9.09	12.67	TST
This work	700−2000	-9.18	11.84	CVT/μOMT

On the basis of the rigorous definition given by Tolman [221, 222] in which the activation energy is interpreted as the average energy over all reacting molecules minus the average energy over all reactant molecules (independently of whether they react or not), it is possible to interpret the change of the activation energy with temperature. [218, 223, 224] Basically, an activation energy that increases with temperature means that at higher temperatures the average energy of reacting systems is increasing more rapidly than the average energy of all possible reactants. From the point of view of TST, the variation of the activation energy with temperature depends strongly on the magnitude of the transitional modes (the normal modes at the transition state structure coming from the rotational and translational motions of reactants), [225] an issue that was already pointed out byMeagher *et al.* [185] for the overall CH_3OH + H reaction.

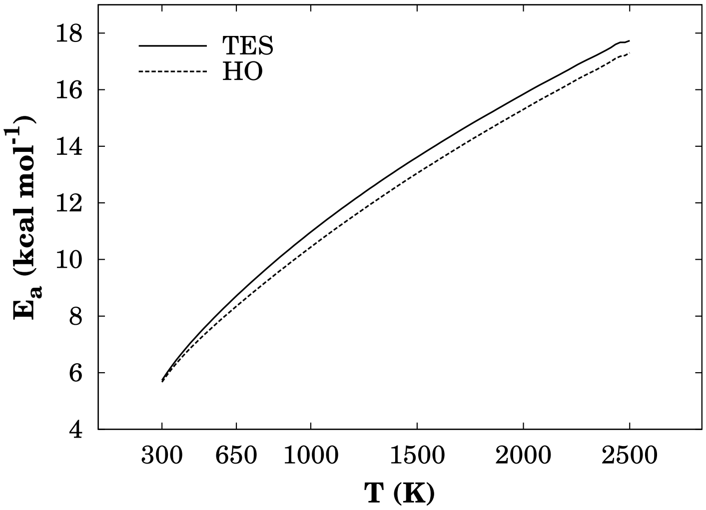

Figure 6.4: Variation of the activation energy (in kcal/mol) with temperature for the total CH_3OH + H reaction (R1 + R2). HO and TES refer, respectively, to the harmonic oscillator and the torsional eigenvalue summation treatments given to the torsional mode.

From the experimental point of view only the measurements of Li and Williams [174] are available at low T and high T and in this case a clear increase of the activation energy with temperature is observed. With the exception of this work and that of Cribb *et al.* [180] the high T experiments do not show a clear increase of the activation energy with respect to the low T experiments, so we believe that those high T experiments deserve further checking. It should be also noticed that most of the experimental data reported (listed in Table 6.5) were fitted to Arrhenius expressions (the work of Li and Williams [174] is an exception). Some of these Arrhenius parameters were later on used in the modeling of the mechanism of combustion and oxidation of methanol; [172, 175] the approximation of uncurved Arrhenius plots could affect the conclusions of those studies.

Figure 6.5 shows that the our CVT/μOMT results are very similar to the reduced dimensionality quantum dynamics results of Kerkeni and Clary [191] till about $T = 1000$ K, and at higher temperatures they are closer to the thermal rate constants calculated by Jodkowski *et al.* [190]. In the interval of temperatures at which the discharge flow reactor experiments by Aders and Wagner [184] were carried out and the ESR experiments by Meagher *et al.* [185] were performed, the calculated CVT/μOMT thermal rate constants lay below those values because the theoretical calculations lead to a much higher activation energy. The experimental data of Hoyermann *et al.* [182] are about 6 and 3 times larger than the CVT/μOMT results at $T = 500$ K and $T = 680$ K, respectively, indicating also that their results have a more nearly constant slope. Actually, their results have the same slope as the values reported by Aders and Wagner [184], which is surprising because the measurements by Hoyermann *et al.* [182] start at temperatures about 200 K higher; therefore, a larger activation energy would be expected. Meagher *et al.* [185] pointed out that, since that their ESR experiments measure the disappearance of the H atom radical (the discharge flow reactor experiments also measure that concentration) part of the hydrogen radical could be consumed by the side reaction $CH_2OH + H \longrightarrow CH_3 + OH$. However, both, the preexponential factor obtained, which is typical of that for a hydrogen abstraction reaction, and the high linearity in the decay of the hydrogen radical concentration, suggest that that side reaction is unimportant. This is still a controversial issue, because some of the modeling involved in the study of the mechanism of combustion of methanol [169, 171, 172] indicate its importance in the consumption of hydrogen radical and in the generation of OH radicals.

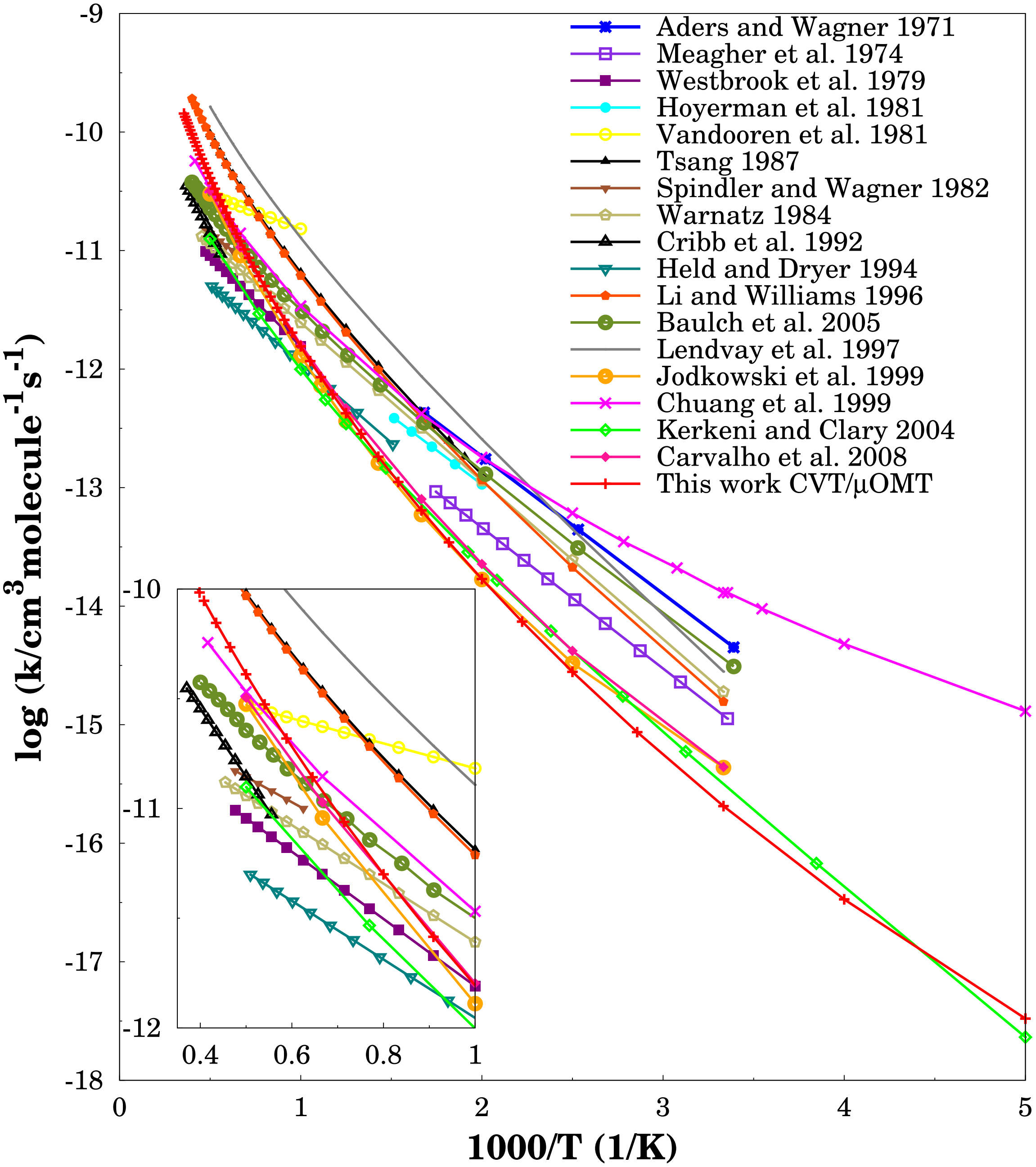

Figure 6.5: Arrhenius plot that compares the CVTμOMT total (R1 + R2) thermal rate constants computed at the MC3BB level with experimental and theoretical works available in the literature. The left-bottom corner of the figure is a zoom with the data at high temperatures.

At high T reliable values of the thermal rate constants for reactions R1 and R2 are very important because most of the modeling of the combustion of methanol is carried out at these temperatures. The diversity of the values of the rate constants (see Table 6.5 and left corner of Figure 6.5) indicate a great uncertainty in the experimental data. Because the energy of activation changes with temperature the data are only comparable at the same interval of temperatures; nevertheless most of the data are incongruent with the low T experiments. Thus, the experiments of Westbrook and Dryer [165], Warnatz [167], Vandooren and Tiggelen [178], Spindler and Wagner [179] and Held and Dryer [171] lead to activation energies which are too low as compared to theory. Cribb *et al.* [180] reported a value for the activation energy of 14.1 kcal/mol for the interval between T = 1800 and 2740 K that is in relatively good agreement with the value of 16.7 kcal/mol obtained by CVT/μOMT for the same interval.

As mentioned above the large dependence of the activation energy on temperature discourages the use of Arrhenius expression for the overall R1 + R2 reaction even in small temperature ranges. One alternative to the equation of Arrhenius which is widely used in practice is:

$$k(T) = A \left(\frac{T}{300}\right)^n e^{-E/T} \tag{6.19}$$

where A, n and E are parameters and T is temperature. As shown in Refs. [225] and [226], Eq. (6.19) fits perfectly the curved Arrhenius plot only if the activation energy increases linearly with temperature, which is not the case here. However, at temperatures of combustion, as shown in Figure 6.4, the dependence of E_a with temperature is almost linear, so in Table 6.6 we report values of the A, n and E fitting parameters for the total thermal rate constants above T = 700 K. To reproduce well the whole interval between T = 300 K and 2500 K it is necessary to use a more elaborate expression that reproduces the asymptotic behavior at low temperatures, i.e., [226]

$$k(T) = A \left(\frac{T}{300}\right)^n \exp\left[\frac{-E(T+T_0)}{T^2+T_0^2}\right] \tag{6.20}$$

This equation has four fitting parameters A, n, E and T_0. The errors are calculated as the value of the root mean square residual (RMSR), which is given by:

$$\mathrm{RMSR} = \left\{\frac{1}{N}\left[\sum_{i=1}^{N} \ln\left(\frac{k(T_i)}{k_M(p_1,...,p_K,T_i)}\right)\right]^2\right\}^{1/2} \tag{6.21}$$

where N is the number of temperatures, which in this case were taken every 10 K; $k(T_i)$ is the CVT/μOMT thermal rate constant at T_i, and $k_M(p_1,...,p_K,T_i)$ are the fitted thermal rate constants involving the K parameters given by Eq (6.19) ($K = 3$) or by Eq. (6.20) ($K = 4$). All parameters are listed in Table 6.6. Since Eq. (6.19) is only used at high temperatures, the RMSR values are vey small for both fits. We recommend Eq. (6.20) at low and mid-range T, and either fit may be used at temperatures above T = 700 K.

Table 6.6: Fitting parameters to the CVT/μOMT thermal rate constants for the total reaction R1 + R2 and for R1 and R2 using Eqs. (6.19) and (6.20). The RMSR values are also given

	Reaction		
Parameter	R1 + R2	R1	R2
Eq. (6.19) ($700 \leq T(\mathrm{K}) \leq 2500$)			
$A(\mathrm{cm^3 s^{-1} molecule^{-1}})$	1.170×10^{-12}	1.713×10^{-12}	1.898×10^{-12}
n	2.612	2.351	2.147
E(K)	2850	2975	5603
RMSR	0.017	0.014	0.010
Eq. (6.20) ($300 \leq T(\mathrm{K}) \leq 2500$)			
$A(\mathrm{cm^3 s^{-1} molecule^{-1}})$	4.738×10^{-13}	7.334×10^{-13}	3.504×10^{-13}
n	2.922	2.632	2.707
E(K)	2005	2128	4008
T_0(K)	204.5	208.7	188.8
RMSR	0.017	0.016	0.011

6.3.5. Branching ratios

Reactions R1 and R2 obtained by CVT/μOMT were also fitted to Eqs. (6.19) and (6.20). The results are given in Table 6.6. With the exception of the experiments of Li *et al.* [175], all the theoretical and experimental data plotted in Fig. 6.6 show that reaction R1 dominates over the whole range of temperatures 300–2500 K. All the theoretical works show some temperature dependence of the branching ratio with temperature. The CVT/μOMT calculations with the torsional mode treated within the harmonic approximation and the work of Lendvay *et al.* [183] predict similar branching ratios, with percentages that never reach 30% even at $T = 2000$ K, whereas the works of Kerkeni and Clary [191] and Jodkowski *et al.* [190] predict even smaller percentages for reaction R2. When anharmonicity is included the branching ratio increases, and at $T = 2000$ K R1 contributes about 80% to the total abstraction reaction. In this context, the assumption of Held and Dryer [171] seems quite unrealistic, because they consider that the branching ratio is independent of temperature, which is equivalent to assuming that both reactions have the same activation energy. On the other hand, the results reported by Li *et al.* [175] indicate that at $T = 500$ K, R2 contributes by more than 30% to the total abstraction reaction, and at about $T = 800$ K reaction R2 starts to dominate. However, at temperatures between 500 and 680 K, Hoyermann *et al.* [182] by doing deuterium isotopic susbstitution of methanol with the further analysis of the products showed, although not conclusively, that reaction R1 is the main channel for hydrogen abstraction from methanol. The theoretical calculations also support that conclusion. The comparison of theory and experiment for the branching ratio between reactions R1 and R2 brings into question the accuracy of the experimental results, so we recommend the use of Eqs. (6.19) and (6.20) with the parameters of Table 6.6 for the study of mechanisms related to the combustion of methanol.

6.3.6. Kinetic isotope effects

The KIE is an important tool to study reaction mechanisms and analyze tunneling effects. We have calculated two KIEs at low temperatures (at which only R1 contributes significantly

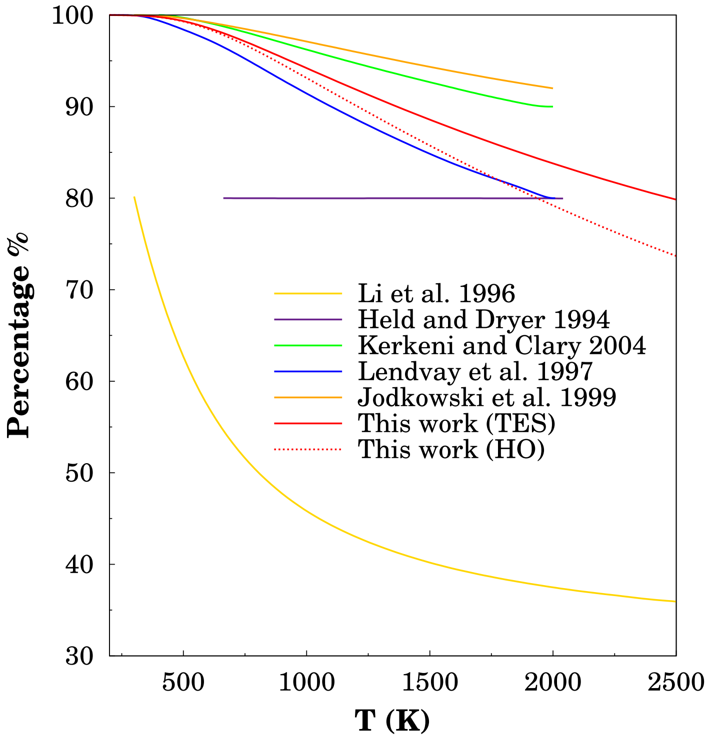

Figure 6.6: Branching ratio expressed as a percentage: $\frac{k_{\mathrm{R1}}(T)}{k_{\mathrm{R1}}(T)+k_{\mathrm{R2}}(T)} \times 100$. Several theoretical and experimental data are plotted. HO and TES have the same meaning as in Figure. 6.4

to the total abstraction rate constant), i.e., the secondary KIE defined as the reaction rate ratio between reactions R1 and R4, $\eta_{1,4}(T)$, and the primary KIE given by the ratio between reactions R1 and R5, $\eta_{1,5}(T)$. We use the notation

$$\eta(T) = \frac{k_{\mathrm{H}}(T)}{k_{\mathrm{D}}(T)} \tag{6.22}$$

where $k_{\mathrm{H}}(T)$ is the rate constant for reaction R1, and $k_{\mathrm{D}}(T)$ is that for R4 or R5 reactions.

The KIEs are factorized into their quasiclassical, $\eta_{\mathrm{QC}}(T)$, and tunneling, $\eta_{\mathrm{tun}}(T)$ contributions, i.e.,

$$\eta(T) = \eta_{\mathrm{tun}}(T)\eta_{\mathrm{QC}}(T) \tag{6.23}$$

where

$$\eta_{\mathrm{tun}}(T) = \frac{\kappa_{\mathrm{H}}^{\mathrm{CVT}/\mu\mathrm{OMT}}(T)}{\kappa_{\mathrm{D}}^{\mathrm{CVT}/\mu\mathrm{OMT}}(T)} \tag{6.24}$$

and $\eta_{\mathrm{QC}}(T)$ is given by

$$\eta_{\mathrm{QC}}(T) = \eta_{\mathrm{var}}(T)\eta^{\mathrm{TST}}(T) \tag{6.25}$$

where $\eta_{\mathrm{var}}(T)$ is the variational contribution to the KIE, and $\eta^{\mathrm{TST}}(T)$ is the TST contribution to the KIE and is given by

$$\eta^{\mathrm{TST}}(T) = \eta_{\mathrm{trans}}\eta_{\mathrm{rot}}^{\mathrm{TST}}\eta_{\mathrm{vib,tor}}^{\mathrm{TST}}(T) \tag{6.26}$$

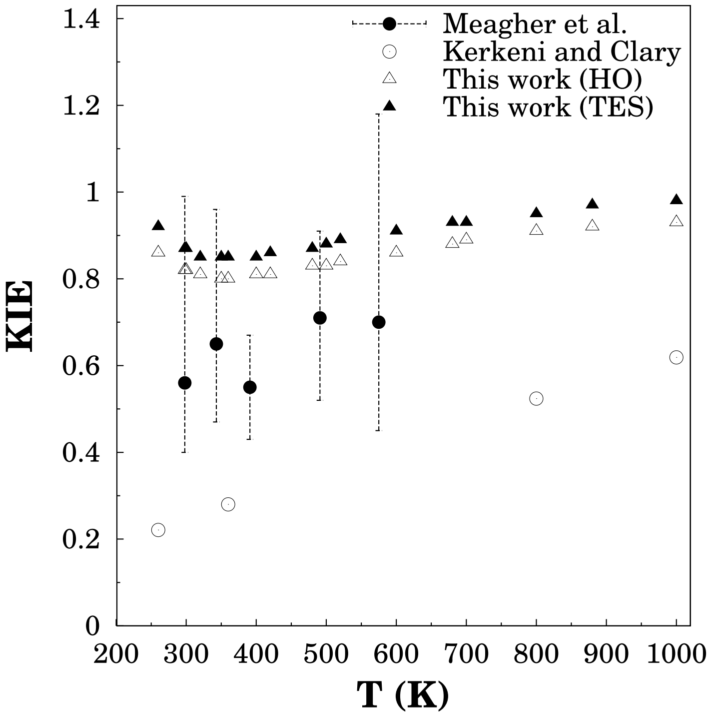

Figure 6.7: Values of $\eta_{1,4}$ between $T = 250$ and 1000 K. The experimental data of Ref. [185] are indicated with error bars. HO and TES have the same meaning as in Figure. 6.4

where η_{trans} and $\eta_{\text{rot}}^{\text{TST}}$ are the translational and rotational temperature-independent contributions and $\eta_{\text{vib,tor}}^{\text{TST}}(T)$ is the temperature-dependent vibrational contribution in which the torsional mode was treated using the TES method.

The experimental data of Meagher*et al.* [185] (see Figure 6.7) show that the secondary KIE $\eta_{1,4}$ is inverse (smaller than the unity). Both sets of theoretical results shown in Figure 6.7 also exhibit this tendency, although our CVT/μOMT results are in better agreement with the experimental data. The contributions to the KIE are listed in Table 6.7. The product of translational and rotational contributions does not change with temperature and equals 2.00. The anharmonic contribution of the torsional mode to the KIE is quite modest and the largest difference with respect to the harmonic oscillator treatment occurs at low-T and is about 7%. The vibrational and variational contributions are smaller than unity, and at $T = 300$ K their product is 0.24, which gives a quasiclasical KIE of 0.47. The experimental KIEs have significant error bars and are roughly between 0.4 and 1.2, with the data clustered between 0.5 and 0.7. The CVT/μOMT results show that tunneling increases the total KIE because a multidimensional effect that greatly favors tunneling in reaction R1 over reaction R4 is that the vibrationally adiabatic barrier height is larger for the former reaction, i.e., 8.48 kcal/mol, whereas for reaction R4 is 7.72 kcal/mol. At $T = 300$ K this leads to μOMT transmission coefficients which are 12.2 and 6.63 for reactions R1 and R4, respectively, increasing the KIE by a factor of 1.84 and leading to a final predicted value for the KIE in good agreement with experiment.

Table 6.7: Contributions to the KIE $\eta_{1,4}$ (see text) obtained at the MC3BB level and using the CVT/μOMT thermal rate constants.[a] Both $\eta^{\mathrm{TST}}_{\mathrm{vib,HO}}$ and $\eta^{\mathrm{TST}}_{\mathrm{vib,tor}}$ are the vibrational contributions to the KIE using, respectively, the harmonic oscillator and TES approximations to the torsional mode

T(K)	$\eta^{\mathrm{TST}}_{\mathrm{vib,HO}}(T)$	$\eta^{\mathrm{TST}}_{\mathrm{vib,tor}}(T)$	$\eta^{\mathrm{TST}}(T)$	$\eta_{\mathrm{var}}(T)$	$\eta_{\mathrm{QC}}(T)$	$\eta_{\mathrm{tun}}(T)$	$\eta_{1,4}(T)$
300	0.24	0.26	0.47[a]	0.91	0.43	1.84	0.87
400	0.32	0.33	0.62	0.93	0.58	1.36	0.85
500	0.37	0.38	0.72	0.95	0.69	1.20	0.88
700	0.42	0.44	0.83	0.96	0.82	1.09	0.93
1000	0.46	0.48	0.90	0.96	0.91	1.04	0.98
1500	0.49	0.51	0.95	0.96	0.95	1.02	1.01

[a] $\eta_{\mathrm{trans}} = 2.70$; $\eta^{\mathrm{TST}}_{\mathrm{rot}} = 0.74$.

Table 6.8: Same as Table 6.7 but for $\eta_{1,5}$

T(K)	$\eta^{\mathrm{TST}}_{\mathrm{vib,HO}}(T)$	$\eta^{\mathrm{TST}}_{\mathrm{vib,tor}}(T)$	$\eta^{\mathrm{TST}}(T)$	$\eta_{\mathrm{var}}(T)$	$\eta_{\mathrm{QC}}(T)$	$\eta_{\mathrm{tun}}(T)$	$\eta_{1,5}(T)$
300	6.50	7.30	8.65[a]	0.78	7.29	2.24	20.99
400	3.95	4.45	5.27	0.83	4.64	1.70	9.45
500	2.92	3.29	3.89	0.87	3.52	1.44	5.83
700	2.08	2.33	2.77	0.90	2.56	1.22	3.46
1000	1.63	1.84	2.18	0.92	2.04	1.11	2.45
1500	1.40	1.57	1.86	0.93	1.75	1.05	1.97

[a] $\eta_{\mathrm{trans}} = 1.01$; $\eta^{\mathrm{TST}}_{\mathrm{rot}} = 1.18$.

The contributions to the calculated CVT/μOMT primary KIE $\eta_{1,5}$ are listed in Table 6.8. The final predicted KIE agrees quite well with the experimental data obtained by Hoyermann *et al.* [182] (see Figure 6.8), although the KIEs obtained from their raw data may be unreliable because the thermal rate constants reported by them have large error bars. They also fitted the thermal rate constants for R5 and for R6 to the same Arrhenius expression. This looks like a good approximation since our CVT/μOMT calculations for R6 deviate less than 2% from those obtained for R5 in the temperature range 300-2500 K, so we do not report those values here. The translational, rotational, and variational contributions are very close to unity, and their product leads to a value of only 1.29 at $T = 300$ K, so the main contribution to the quasiclassical KIE is due to vibration. For the factorization employed in Table 6.8, the vibrational contribution to the KIE is given by:

$$\eta^{\mathrm{TST}}_{\mathrm{vib,tor}}(T) = \frac{Q^{\mathrm{TS-R1}}_{\mathrm{vib,tor}}(T)\,Q^{\mathrm{CD_3OH}}_{\mathrm{vib,tor}}(T)}{Q^{\mathrm{TS-R5}}_{\mathrm{vib,tor}}(T)\,Q^{\mathrm{CH_3OH}}_{\mathrm{vib,tor}}(T)} \tag{6.27}$$

where $Q^{\mathrm{TS-R1}}_{\mathrm{vib,tor}}(T)$ and $Q^{\mathrm{TS-R5}}_{\mathrm{vib,tor}}(T)$ are the vibrational partition functions of the conventional transition states (saddle points) of the R1 and R5 reactions, respectively, and $Q^{\mathrm{CD_3OH}}_{\mathrm{vib,tor}}(T)$ and $Q^{\mathrm{CH_3OH}}_{\mathrm{vib,tor}}(T)$ are the reactant vibrational partition functions of CD_3OH and CH_3OH, respectively. All of them include the calculation of the torsional mode partition function by the TES

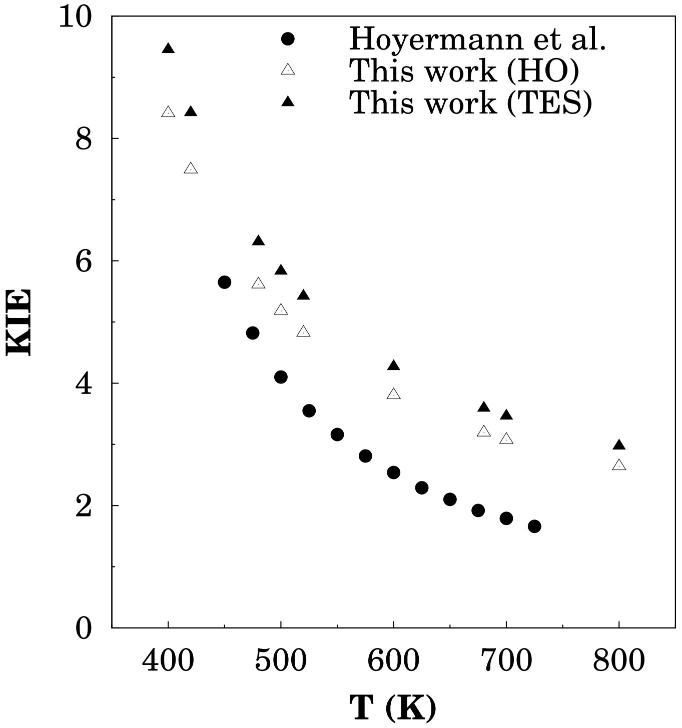

Figure 6.8: Values of $\eta_{1,5}(T)$ between $T = 250$ and 1000 K. HO and TES have the same meaning as in Figure. 6.4

method. The vibrational KIE is larger than the unity because the quotient between reactants partition functions is quite big due mainly to the difference in the value of the frequencies of the C-D and C-H stretches. This mass effect largely compensates the quotient between the vibrational partition function of the transition states, which is smaller than the unity. In the case of the $\eta_{1,4}(T)$ KIE, the latter is the only contribution to the vibrational KIE, because the vibrational frequencies of reactants are the same. Moreover, the anharmonic treatment of the torsional mode increases the vibrational contribution to the KIE by about 10%.

In this case it is also easy to understand that the tunneling contribution increases the KIE, since the hydrogen atom is lighter than deuterium, and therefore it has a larger probability of penetrating the barrier, if the barriers are the same. In the SCT and μOMT approximations, the effective barriers are not the same, but still the expected trend holds.

This last section shows that, although most of the theoretical models discussed in this paper predict similar thermal rate constants for the hydrogen abstraction reactions, a multidimensional tunneling method is needed in order to obtain good agreement with some of the KIEs.

6.4. Conclusions

In the present work we have performed high-level MC3BB direct-dynamics CVT/μOMT calculations in the temperatures interval 300-2500 K for the two competing hydrogen abstraction reactions R1 and R2 from methanol by atomic hydrogen. We have pointed out the importance of using multidimensional models for treating tunneling, which, with other factors being equal, provide both more reliable absolute thermal rate constants and kinetic isotope effects. It turned out that at high temperatures the anharmonicity of the torsional mode about the C–O bond plays an important role, because it leads to thermal rate constants that deviate substantially from those obtained by the harmonic oscillator approximation. On the other hand, our calculations and previous theoretical works clearly indicate that the activation energy for the overall R1 + R2 process increases substantially with temperature; a conclusion not supported by the high T experimental data (above $T = 700$ K), which do not show a clear trend. For this reason for reactions R1 + R2, R1 and R2 we recommend the use of Eq. (6.20) in the whole range of temperatures, although Eq. (6.19) can also be used at high T. We propose these equations (in detriment of the Arrhenius equation) for further studies involving these reactions (as for instance, combustion reactions). Reaction R1 dominates at all temperatures in the interval 300-2500 K, contributing 100% at room temperature and about 75% at $T = 2500$ K, so the branching ratio R1/R2 changes with temperature. Our calculated KIEs are in quite good agreement with experiment.

Chapter 7

The [1,7] hydrogen shift in 7-methylocta-1,3(Z),5(Z)-triene

Direct-dynamics canonical variational transition-state theory calculations with microcanonically optimized multidimensional transmission coefficient (CVT/μOMT) for tunneling were carried out at the MPWB1K/6-31+G(d,p) level to study the [1,7] sigmatropic hydrogen rearrangement in 7-methylocta-1,3(Z),5(Z)-triene. This compound has twenty four conformers, of which only one leads to products, although all of them have to be included in the theoretical treatment. The calculated CVT/μOMT rate constants are in good agreement with the available experimental data. To try to understand the role of tunneling in the hydrogen shift reaction, we have also calculated the thermal rate constants for the monodeuterated compound in the interval T = 333.2−388.2 K. This allowed us to evaluate primary kinetic isotope effects (KIEs) and make a direct comparison with experiment. Our calculations show that both the large measured KIE and the large measured difference in the activation energies between the deuterated and root compounds are due to the quantum tunneling. The tunneling contribution to the KIE becomes noticeable only when the coupling between the reaction coordinate and the transverse modes is taken into account. Our results confirm previous experimental and theoretical works, which guessed that the obtained kinetic parameters pointed to a reaction with an important contribution due to tunneling. The above conclusion would be essentially valid for the case of the [1,7] hydrogen shift in previtamin D_3 because of the similarity to the studied model system.

7.1. Introduction

Sigmatropic hydrogen shifts are hydrogen transfer reactions that play an important role in some biologically relevant processes. A clear example is the [1,7] hydrogen shift in previtamin D_3. [227] The vitamin is formed from 7-dehydrocholesterol in two well-defined steps. [228–230] The first step is a photochemical process in which cholesterol is transformed into previtamin D_3 when irradiated with ultraviolet light. In the second step, this previtamin leads to vitamin D_3 by thermal isomerization, i.e., by antarafacial [1,7] hydrogen shift between carbons C_9 and C_{19}, as indicated in Scheme 7.1.

The [1,7] hydrogen shift involves the transfer of a light particle between two heavy atoms; tunneling through the barrier may be of importance. In this context, the measurement of kinetic isotope effects (KIEs) is a very useful tool in the understanding of the significance of tunneling in hydrogen transfer reactions. [58] Usually, a large KIE indicates the presence of tunneling because hydrogen tunnels through a classical barrier better than deuterium, so the rate constant of the process for the former atom increases more than for the latter. This would be always the case if tunneling were a one-dimensional effect. However, because of its multidimensional nature, there are cases for which tunneling may be important even with low KIEs. [150] One of the advantages of performing theoretical reaction dynamics studies is the possibility of calculating separately the effect of different contributions to the KIE, i.e., the classical (rotational, vibrational, and electronic) and the quantum (tunneling) contributions. In particular, variational transition-state theory with multidimensional tunneling corrections (VTST/MT) has proven to be a powerful and useful tool. [231]

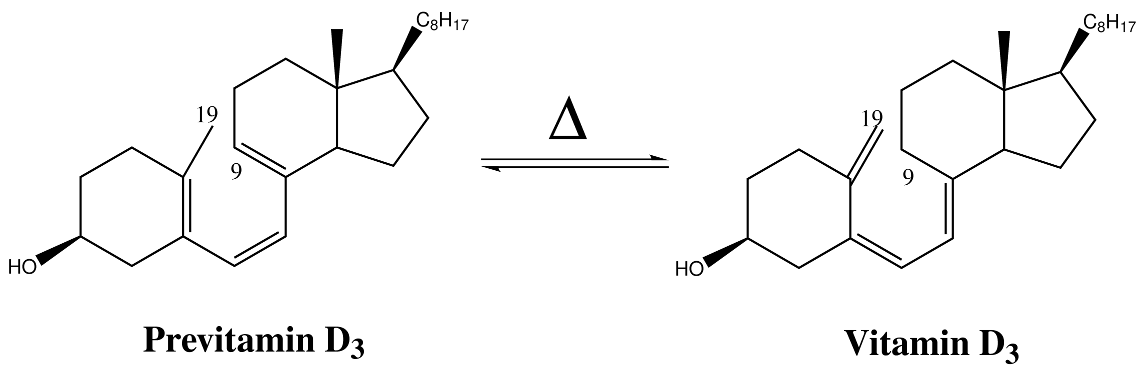

Scheme 7.1: Thermal Isomerization of Previtamin D_3 to Vitamin D_3

Vitamin D_3 is a big molecule to be treated with semiclassical direct-dynamics models, and even if we use density functional theory (DFT) methods for the electronic structure calculations, these would be very expensive in computer time. Of course, one can use semiempirical methods with specific reaction parameters (SRPs), [137] but in this case, we preferred to use straight high-level direct dynamics, because it is easy to find good models to describe the main features of the [1,7] hydrogen shift in the previtamin D_3. One model system with these characteristics is 1,3(Z),5(Z)-octatriene, because it contains the essence of the hydrogen transfer active site. Kinetic isotope effects on the hydrogen shift of this system were measured by Baldwin and Reddy [232] in the range of temperatures 333.2-388.2 K, although these authors could not draw firm conclusions about the thermal dependence of the KIEs because of the complexity of the kinetics and the difficulty to distinguish between primary and secondary KIEs. In this aspect, an easier system to study, although slightly larger, is the hydrogen shift in 7-methylocta-1,3(Z),5(Z)-triene, because the reaction leads to a single conformer called 2-methylocta-2,4(Z),6(Z)-triene. In this case, it is possible to deuterate only the transferred hydrogen, so there are no contributions from secondary KIEs in the measurement. These measurements of the primary KIEs in 7-methylocta-1,3-(Z),5(Z)-triene were also carried out by Baldwin and Reddy [233] in the range of temperatures 333.2−388.2 K, and in this case, it was possible to easily measure the temperature dependence of the rate constants. Those authors obtained KIEs of 7.0 at $T = 333.2$ K and 4.6 at $T = 388$ K, respectively, and concluded that tunneling effects for this reaction are substantial because the difference between the activation energies for the root and deuterated compounds is large. Jensen [234] and Hess [235] independently corroborated this conclusion by carrying out electronic structure calculations.

The former applied the conventional transition-state theory to the reaction after performing B3LYP/6-31+G* calculations on the stationary points. Hess calculated a KIE of 3.89 at 333.2 K, which is about half the experimental value obtained by Baldwin and Reddy, [233] concluding that the difference is due to the neglect of tunneling in his calculation.

The above KIEs are very similar to those measured by Okamura *et al.* [236] for the [1,7]-sigmatropic hydrogen shift of previtamin D_3 to vitamin D_3, which range from 7.4 at $T = 333.2$ K to 6.1 at $T = 358.7$ K. They used a pentadeuterio derivative of previtamin D_3, but in this case, a negligible secondary KIE is expected. The similarity between the KIEs indicates that tunneling may also play an important role in this case and that 7-methylocta-1,3(Z),5(Z)-triene is a good system to model the hydrogen shift process in previtamin D_3. Therefore, the aim of this paper is to use VTST/MT to get insight into the role played by tunneling in the [1,7] hydrogen shift of 7-methylocta-1,3(Z),5(Z)-triene by analyzing the calculated KIEs. Because of the similarities between this molecule and previtamin D_3, the conclusions obtained would be common to both systems.

7.2. Computational details

All the electronic structure calculations have been performed at the MPWB1K level [237] with the 6-31+G(d,p) basis set, [145] also called DIDZ. MPWB1K is a DFT method based on the Perdew and Wang 1991 exchange functional [238] (MPW) and Becke's 1995 meta correlation functional (B95), [204] which has been optimized for kinetics calculations, so we also expect a good performance of the method in this case. The geometry optimizations and frequency calculations at the stationary points were performed with *Gaussian03*. [212]

All dynamics calculations were carried out by VTST/MT using the MPWB1K/DIDZ level to build the potential energy surface. VTST/MT improves conventional transition-state theory in two aspects: [16, 17] (a) it minimizes the recrossing by variationally locating the transition-state dividing surface at an optimized position orthogonal to the minimum energy path (MEP); and (b) it incorporates multidimensional tunneling effects into the reaction coordinate by a multiplicative transmission coefficient. The MEP was followed in redundant curvilinear (internal) coordinates [211] by using the Page-McIver algorithm. [210] The advantage of using internal coordinates along the MEP is that it provides more reliable normal-mode frequencies along the MEP than rectilinear (Cartesian) coordinates. [239, 240] A converged MEP was obtained with a step size of $0.01a_o$, scale mass $\mu = 1$ amu, and Hessian calculations every nine steps. All frequencies were scaled by the recommended factor of 0.9537. [241]

Variational effects were incorporated by the canonical variational transition-state theory (CVT), [66, 242, 243] in which the flux is minimized for a canonical ensemble. The CVT rate constant, $k^{\mathrm{CVT}}(T)$, at temperature T, can be obtained as the minimum of the generalized transition-state theory rate constant, $k^{\mathrm{GT}}(T,s)$, as a function of s, that is,

$$k^{\mathrm{CVT}}(TT) = \min_s k^{\mathrm{GT}}(T,s) = \sigma \frac{1}{\beta h} \frac{Q^{\mathrm{GT}}(T, s_*^{\mathrm{CVT}})}{Q^{\mathrm{R}}(T)} \exp\left[-\beta V_{\mathrm{MEP}}\left(s_*^{\mathrm{CVT}}\right)\right] \tag{7.1}$$

where s is the arc length along the MEP measured from the saddle point; s_*^{CVT} is the value of s at which $k^{\mathrm{GT}}(T,s)$ has a minimum; σ is the symmetry number; $\beta = (k_{\mathrm{B}}T)^{-1}$, where k_{B} is the Boltzmann's constant; $V_{\mathrm{MEP}}(s_*^{\mathrm{CVT}})$ is the classical MEP potential at $s = s_*^{\mathrm{CVT}}$; and

$Q^{\mathrm{GT}}(T, s_*^{\mathrm{CVT}})$ and $Q^{\mathrm{R}}(T)$ are the internal (rotational, vibrational, and electronic) partition functions of the generalized transition state at $s = s_*^{\mathrm{CVT}}$ and reactants, respectively.

Tunneling effects were incorporated into the thermal CVT rate constants by a multiplicative ground-state (G) transmission coefficient, $\kappa^{\mathrm{CVT/G}}(T)$, so the final rate constant is given by

$$k^{\mathrm{CVT/G}}(T) = \kappa^{\mathrm{CVT/G}}(T) k^{\mathrm{CVT}}(T), \tag{7.2}$$

where

$$\kappa^{\mathrm{CVT/G}}(T) = \beta \exp\left[\beta V_{\mathrm{a}}^{\mathrm{AG}}(s_*^{\mathrm{CVT}})\right] \int_{E_0}^{\infty} dE P^{\mathrm{G}}(E) \exp(-\beta E) \tag{7.3}$$

where $V_{\mathrm{a}}^{\mathrm{G}}$ is the vibrationally adiabatic potential, which is given by

$$V_{\mathrm{a}}^{\mathrm{G}}(s) = V_{\mathrm{MEP}}(s) + \epsilon_{\mathrm{int}}^{G}(s), \tag{7.4}$$

where $\epsilon_{\mathrm{int}}^{\mathrm{G}}(s)$ is the internal energy (rotational and vibrational) at s, which in the ground-state approximation equals the zero-point energy (ZPE) at s. The semiclassical ground-state probability $P^{\mathrm{G}}(E)$ was calculated over the vibrational adiabatic potential by optimizing microcanonically (at every energy) the largest probability between the small curvature tunneling (SCT) probability, [244] $P^{\mathrm{SCT}}(E)$, and the large curvature tunneling (LCT) probability, [16, 17, 20, 21, 245] $P^{\mathrm{LCT}}(E)$, evaluated with the LCG4 version. [21] The resulting probability is, therefore, given by

$$P^{\mu\mathrm{OMT}}(E) = \max_{E} \left\{ \begin{array}{l} P^{\mathrm{SCT}}(E) \\ P^{\mathrm{LCT}}(E) \end{array} \right. \tag{7.5}$$

where μOMT stands for microcanonically optimized multidimensional tunneling. [24] The semiclasical probability in the whole range of energies is given by

$$P^{\mathrm{SAG}}(E) = \begin{cases} 0, & E < E_0 \\ \{1 + \exp[2\theta(\mathrm{E})]\}^{-1}, & E_0 \le E \le V_{\mathrm{a}}^{\mathrm{AG}} \\ 1 - P^{\mathrm{SAG}}(2V_{\mathrm{a}}^{\mathrm{AG}} - E), & V_{\mathrm{a}}^{\mathrm{AG}} \le E \le 2V_{\mathrm{a}}^{\mathrm{AG}} - E_0 \\ 1, & 2V_{\mathrm{a}}^{\mathrm{AG}} - E_0 < E \end{cases} \tag{7.6}$$

where E_0 is the lowest energy at which it is possible to have tunneling, V^{AG} is the top of the vibrationally adiabatic potential, and $\theta(E)$ is the imaginary action integral. This integral in the SCT approximation is given by

$$\theta(E) = \frac{1}{\hbar} \int_{s_0}^{s_1} ds 2\mu_{\mathrm{eff}}^{\mathrm{SC}}(s) \{(V_{\mathrm{a}}^{\mathrm{G}}(s) - E)\}^{1/2} \tag{7.7}$$

where s_0 and s_1 are the classical turning points and $\mu_{\mathrm{eff}}^{\mathrm{SC}}(s)$ is the effective mass, which is a function of the couplings between the reaction coordinate and the transverse modes at a given value of s. If this coupling is neglected, $\mu_{\mathrm{eff}}^{\mathrm{SC}}(s)$ equals the scaling mass and the approximation is called zero-curvature tunneling (ZCT). The probabilities evaluated under the ZCT approximation always underestimate the tunneling contribution, because the coupling curves the tunneling trajectory toward the inside of the MEP (centrifugal effect), shortening the tunneling distance. [18] In fact, the SCT trajectory is not calculated explicitly, but it has been shown that its effect can be incorporated in the effective mass, which decreases its value (decreasing the value of the imaginary integral and, therefore, increasing the tunneling probability) in regards to the constant scaling mass.

On the other hand, the evaluation of the μOMT transmission coefficients also requires the calculation of the LCT probabilities. In this case, we need more information of the potential energy surface and not just the MEP; in fact, the evaluation of $P^{\mathrm{LCT}}(E)$ can be quite expensive from the computational point of view. Recently one of us, together with Truhlar, developed an algorithm, called ILCT2D (interpolated large-curvature tunneling with a two-dimensional spline under tension), that allows the calculation of such probabilities with similar results to the full LCT calculation but about 30 times faster. [23] We have used the ILCT2D algorithm in this case.

It should be noticed that the μOMT transmission coefficient is an approximation to the least-action path, which is the one that minimizes the action integral at each tunneling energy. [25] The least-action path is the best compromise between long but energetically favorable tunneling paths (like the MEP) and short but energetically unfavorable tunneling (like the linear paths). Because the explicit evaluation of the least-action path, and therefore of the least-action probability, is very difficult in systems with many degrees of freedom, the μOMT probability represents a good compromise between longer paths closer to the MEP, which are well-described by the SCT approximation, and shorter paths, which are well-described by the LCT approximation. Actually, the μOMT tranmission coefficient was as accurate as the least-action path transmission coefficient for triatomic systems when compared with quantum dynamics calculations. [246]

With these prescriptions, the calculated rate constant obtained using the transmission coefficient from the μOMT probability, $\kappa^{\mathrm{CVT}/\mu\mathrm{OMT}}(T)$, is given by

$$\kappa^{\mathrm{CVT}/\mu\mathrm{OMT}}(T) = \kappa^{\mathrm{CVT}/\mu\mathrm{OMT}}(T) k^{\mathrm{CVT}}(T) \tag{7.8}$$

On the other hand, the primary total KIEs, $\eta^{\mathrm{H/D}}(T)$, were factorized by their classical, $\eta_{\mathrm{cl}}(T)$, and tunneling, $\eta_{\mathrm{tun}}(T)$, contributions, that is,

$$\eta^{\mathrm{H/D}}(T) = \frac{k_{\mathrm{H}}^{\mathrm{CVT}/\mu\mathrm{OMT}}(T)}{k_{\mathrm{D}}^{\mathrm{CVT}/\mu\mathrm{OMT}}(T)} = \eta_{\mathrm{tun}}(T)\eta_{\mathrm{cl}}(T) \tag{7.9}$$

where

$$\eta_{\mathrm{tun}}(T) = \frac{\kappa_{\mathrm{H}}^{\mathrm{CVT}/\mu\mathrm{OMT}}(T)}{\kappa_{\mathrm{D}}^{\mathrm{CVT}/\mu\mathrm{OMT}}(T)} \tag{7.10}$$

and η_{cl} is given by

$$\eta_{\mathrm{cl}}(T) = \eta_{\mathrm{var}}(T)\eta_{\mathrm{int}}(T) \tag{7.11}$$

where $\eta_{\mathrm{var}}(T)$ and $\eta_{\mathrm{int}}(T)$ are the variational and internal (rotational and vibrational) KIEs, respectively. The variational KIE is given by the ratio

$$\eta_{\mathrm{var}}(T) = \frac{k_{\mathrm{H}}^{\mathrm{CVT}}(T) k_{\mathrm{D}}^{\mathrm{TST}}(T)}{k_{\mathrm{D}}^{\mathrm{CVT}}(T) k_{\mathrm{H}}^{\mathrm{TST}}(T)} \tag{7.12}$$

where k^{TST} indicates conventional TST rate constant (i.e., with the dividing surface located at the TS), whereas the KIE due to internal motions is given by

$$\eta_{\text{int}}(T) = \frac{\eta_{\text{int,H}}(T)}{\eta_{\text{int,D}}(T)} = \frac{Q^{\text{TS}}_{\text{rot,H}}(T)Q^{\text{TS}}_{\text{rot,D}}(T)}{Q^{\text{TS}}_{\text{rot,D}}(T)Q^{\text{TS}}_{\text{rot,H}}(T)} \frac{Q^{\text{TS}}_{\text{vib,H}}(T)Q^{\text{TS}}_{\text{vib,D}}(T)}{Q^{\text{TS}}_{\text{vib,D}}(T)Q^{\text{TS}}_{\text{vib,H}}(T)} \tag{7.13}$$

where Q_{rot} and Q_{vib} are the rotational and vibrational partition functions, respectively. The subscripts R and TS stand for reactants and transition state, respectively.

All the rate constant calculations were performed with the program GAUSSRATE9.1, [214] which is an interface between POLYRATE9.3 [213] and Gaussian03. [212]

7.3. Results and discussion

Figure 7.1 shows the thirteen possible conformers of the 7-methylocta-1,3(Z),5(Z)-triene and their corresponding enantiomers (denoted with an asterisk). All the structures can be characterized by specifying the value of the three different dihedral angles, ϕ_1, ϕ_2 and ϕ_3, defined as the torsions about the C_2-C_3, C_4-C_5, and C_6-C_7 atoms, respectively (see Figure 7.1 and Table 7.1). According to the value of the first two dihedral angles, all equilibrium structures can be divided in four groups, and in each of those the rotation about the C_6-C_7 bond defines the different conformers. The first group includes all the s-trans, s-trans structures, i.e. **R1**, **R10/R10*** and **R4**. In this group the two dihedral angles (ϕ_1 and ϕ_2) are about 180°. The second group involves rotation about the first dihedral angle leading to the s-cis, s-trans structures, **R5/R5***, **R11/R11***, **R12/R12*** and **R3/R3***. In this group ϕ_2 is about 170°. The third group of geometries arises when ϕ_1 is kept constant and ϕ_2 takes values from 56° to 98° (conformers **R6/R6***, **R9/R9***, and **R2/R2***). The fourth group includes the **R8/R8***, **R13/R13***, and **R7/R7*** conformations. They are obtained by rotation of both ϕ_1 and ϕ_2 with respect to the s-trans, s-trans group (the first group). According to the MPWB1K/DIDZ calculations, the **R1** conformer is the most stable, and has s-trans, s-trans configuration. This is in agreement with the B3LYP/6-31G* calculations of Hess. [235]

Table 7.1 lists some of the key distances and angles of all the equilibrium conformations. Some of the transition states for interconversion between equilibrium structures are also listed. Conformer **R7** has the most suitable configuration for the [1,7] hydrogen shift with a C_1-H_17 distance of 3.253 Å, although the transfer is also possible from conformer **R2**. The direct product of reaction from conformer **R7** through **TS7** is 2-methylocta-2,4(Z),6(Z)-triene (shown as **P1** in Figure 7.2), whereas the direct product od reaction of conformer **R2** through **TS2** is 2-methylocta-2,4(Z),6(E)-triene (shown as **P2** in Figure 7.2). The energetically most probable route for the hydrogen transfer is through conformer **R7**. This conformer has to surmount a classical barrier of 18.98 kcal·mol^{-1} to lead to products. In the case of conformer **R2**, the classical barrier is 42.59 kcal·mol^{-1}, and although **R2** is *about* 5 kcal·mol^{-1} more stable than **R7**, the difference in the barrier heights shows that the hydrogen shift would take place only through transition state **TS7**.

Figure 7.1: The thirteen conformers of the 7-methylocta-1,3(Z),5(Z)-triene and their corresponding enantiomers (denoted by an asterisk). Details about the geometries and relative energies of the stationary points are given in Table. 7.1

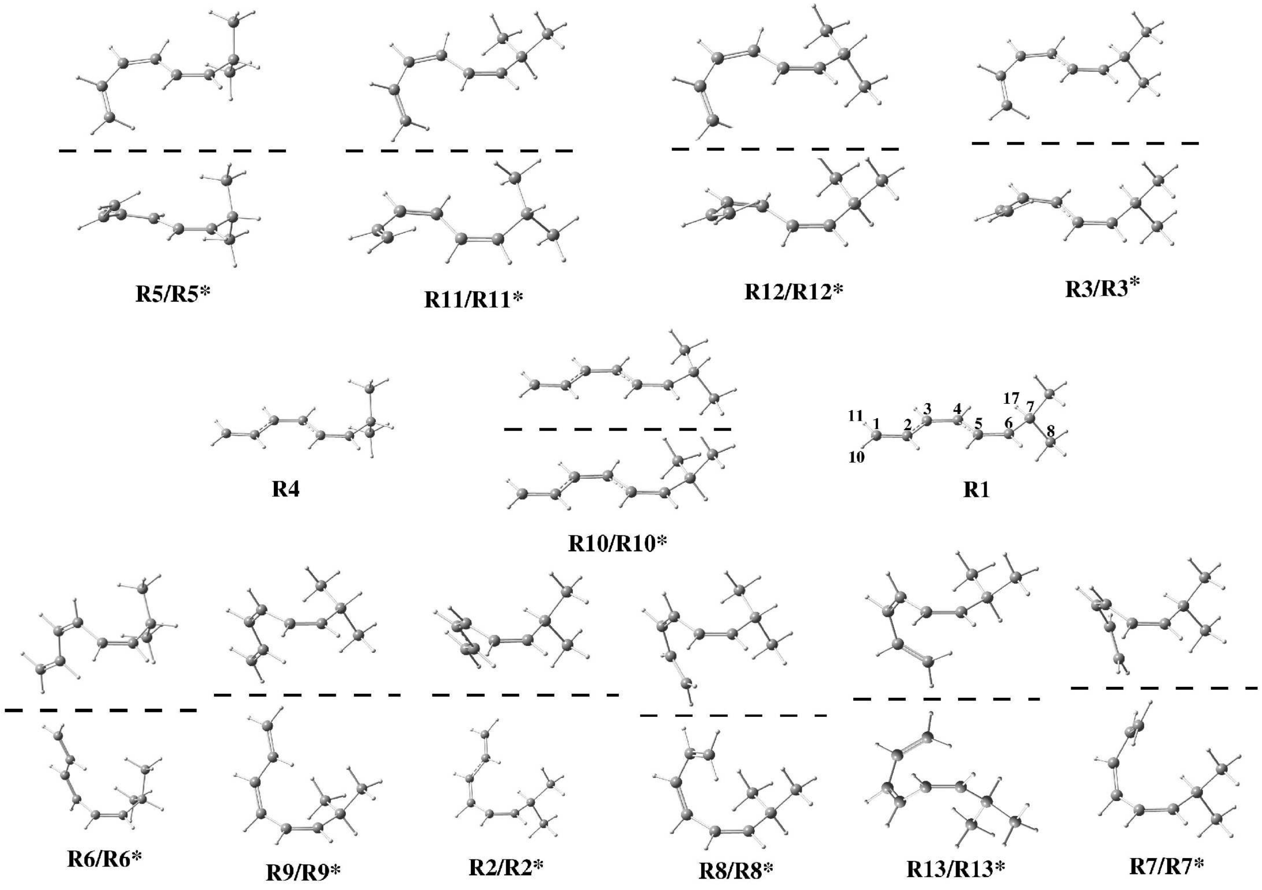

Table 7.1: Relative classical potential energies (in kcal/mol) and main geometric (distances in Å and angles in degrees) of the stationary points involved in the [1,7] hydrogen shift in 7-methylocta-1,3(Z),5(Z)-triene calculated at the MPWB1K/6-31+G(d,p) level; numbering as for structure **R1** in Figure 7.1

Structure	Energy(gas)	ϕ_1^a	ϕ_2^a	ϕ_3^a	α_1^a	α_2^a	α_3^a	$d(C_7 - H_{17})$	$d(C_1 - C_7)$	$d(C_1 - H_{17})$
R1	0.00	180.0	180.0	0.0	109.7	117.1	110.5	1.089	6.745	6.400
R2/R2*	2.78	-175.3	55.6	-8.0	109.1	117.1	110.2	1.088	4.302	3.519
R3/R3*	3.18	-39.9	171.3	0.0	109.6	117.3	110.5	1.089	5.612	5.530
R4	3.30	180.0	180.0	180.0	105.9	117.1	111.6	1.090	6.793	7.727
R5/R5*	6.41	-39.8	170.2	-173.3	106.0	117.3	111.6	1.090	5.616	6.374
R6/R6*	7.44	179.3	97.7	164.1	106.3	117.1	110.8	1.091	5.431	6.424
R7/R7*	7.70	36.9	58.8	-8.5	108.6	117.4	110.4	1.088	3.685	3.265
R8/R8*	11.58	29.9	74.0	128.0	105.1	117.3	110.8	1.094	4.017	5.089
R9/R9*	6.79	-176.5	67.7	126.6	104.2	117.0	110.9	1.094	4.805	5.891
R10/R10*	3.80	-179.9	-179.3	126.5	105.1	117.1	110.3	1.094	6.888	7.533
R11/R11*	6.79	-37.6	166.4	-124.5	105.0	117.3	110.5	1.094	5.586	5.912
R12/R12*	6.85	-37.8	166.5	127.4	105.7	117.3	110.2	1.094	5.588	6.393
R13/R13*	11.28	-24.5	82.9	-111.4	106.5	117.1	110.4	1.096	3.717	3.382
TS7/TS7*	26.68	10.3	22.0	-64.5	100.0	114.8	114.0	1.330	2.641	1.368
TS2/TS2*	45.38	-127.1	27.7	-80.8	103.0	114.8	114.3	1.434	2.756	1.382
P1/P1*	0.60	-0.1	4.1	-96.7	76.7	109.1	115.1	3.016	3.514	1.091
P2/P2*	0.67	176.8	4.7	-65.1	101.0	108.2	115.5	4.524	4.598	1.090
TS-1-2/TS-1*-2*	4.82	179.8	98.5	5.1	108.2	117.0	110.7	1.090	5.376	4.940
TS-1-3/TS-1*-3*	6.08	-98.1	-178.7	-0.2	109.7	117.3	110.5	1.089	6.191	6.019
TS-1-10/TS-1*-10*	4.55	179.7	177.6	89.1	107.3	117.1	109.5	1.095	6.857	7.211
TS-2-7/TS-2*-7*	10.37	104.2	59.6	-3.7	108.7	117.2	110.3	1.089	4.493	4.023
TS-2-10*/TS-2*-10	7.77	-179.1	96.8	-122.2	105.9	117.1	110.6	1.094	5.510	5.540
TS-3-7/TS-3*-7*	8.81	18.7	93.5	6.2	108.2	117.1	110.8	1.090	4.350	4.260
TS-3-11/TS-3*-11*	7.82	-38.9	167.1	-81.6	107.2	117.3	109.5	1.094	5.614	5.651
TS-3-12/TS-3*-12*	7.35	-36.7	166.5	94.7	107.3	117.3	109.6	1.095	5.557	6.247
TS-4-5/TS-4*-5*	9.36	-98.2	-179.0	179.7	106.0	177.3	111.6	1.090	6.219	7.063
TS-4-9/TS-4*-9*	7.64	-179.6	97.9	133.2	105.6	117.0	110.8	1.094	5.503	6.585
TS-4-10/TS-4*-10*	4.19	-179.7	-177.5	153.9	105.1	117.1	110.8	1.091	6.830	7.666
TS-5-11/TS-5*-11*	7.09	-37.1	166.9	-149.0	105.2	117.3	110.9	1.092	5.563	6.120
TS-5-12/TS-5*-12*	7.47	-39.2	168.2	160.5	105.4	117.3	110.6	1.091	5.618	6.435
TS-6-10/TS-6*-10*	7.47	179.2	105.4	164.9	106.5	117.1	110.7	1.091	5.605	6.602
TS-8-7/TS-8*-7*	11.65	9.0	83.6	125.1	105.6	117.4	110.6	1.094	4.011	5.088
TS-8-9/TS-8*-9*	11.65	7.2	88.9	122.2	105.8	117.3	110.4	1.094	4.115	5.186
TS-8-12/TS-8*-12*	11.65	8.2	91.8	125.8	105.8	117.2	110.4	1.094	4.199	5.262
TS-10-11*/TS-10*-11	9.75	97.9	178.7	125.4	105.3	117.3	110.3	1.094	6.280	6.752
TS-10-12/TS-10*-12*	9.76	-97.5	-178.0	125.2	105.3	117.3	110.3	1.094	6.283	6.992
TS-11-13/TS-11*-13*	11.36	-27.0	95.9	-119.3	105.9	117.3	110.7	1.096	3.976	3.812

[a] $\phi_1 = \phi(C_1 - C_2 - C_3 - C_4), \phi_2 = \phi(C_3 - C_4 - C_5 - C_6), \phi_3 = \phi(C_5 - C_6 - C_7 - C_{17}), \alpha_1 = \alpha(C_6 - C_7 - H_{17}), \alpha_2 = \alpha(H_{10} - C_1 - H_{11}), \alpha_3 = \alpha(C_8 - C_7 - C_9)$.

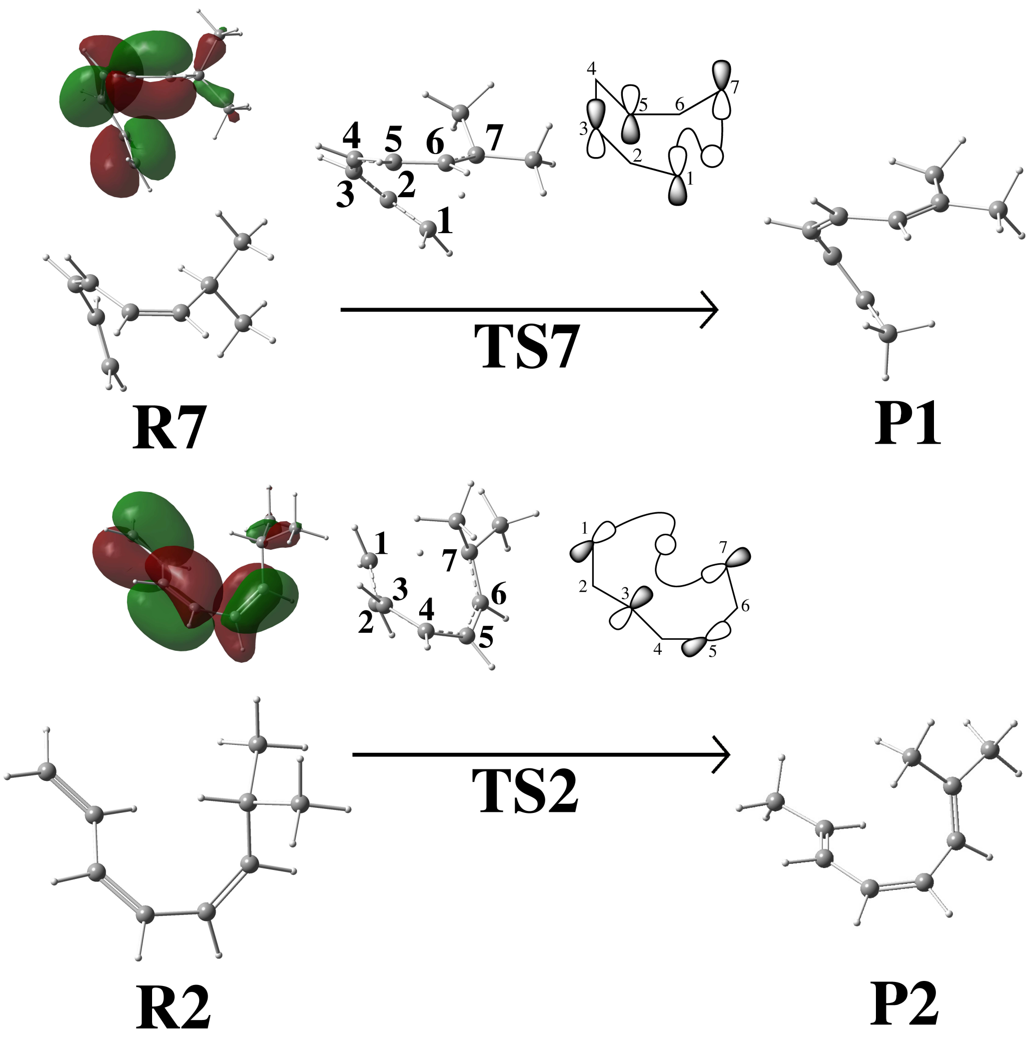

Figure 7.2: Structures of the two reactive conformers leading to products by [1,7] hydrogen shift. The HOMO orbitals of the reactants are also displayed, showing that both reactions occurs via antafacial attack. Details about the geometries and relative energies are given in Table. 7.1

Despite the fact that there is only one relevant channel for reaction, all conformers are important for the dynamics calculations because the barriers of internal rotation around the single bonds among the different conformers are much smaller than the barrier for reaction. As a consequence, all the conformers can be easily reached and all the regions in phase space related to reactants should be included. [247]

The CVT thermal rate constant in a case like this is given by [248]

$$k^{\mathrm{CVT}}(T) = \frac{1}{\beta h} \frac{\left(n^{\mathbf{TS}}/\sigma^{\mathbf{TS}}\right) Q^{\mathrm{GT}}\left(T, s_*^{\mathrm{CVT}}\right)}{\sum_{i=1}^{13}\left(n^{\mathbf{R}_i}/\sigma^{\mathbf{R}_i}\right) Q^{\mathbf{R}_i}(T) \exp^{-\beta \Delta E_{\mathbf{R}_i}}} \exp\left[-\beta V_{\mathrm{MEP}}\left(s_*^{\mathrm{CVT}}\right)\right] \tag{7.14}$$

where the sum runs over the thirteen conformers ($i = 1, \ \dots \ , \ 13$), $n^{\mathbf{R}_i}$ takes into account if conformer $\mathbf{R}_i$ has enantiomers; $Q^{\mathbf{R}_i}(T)$ and $\Delta E_{\mathbf{R}_i}$ are the partition function and the relative energy of conformer $\mathbf{R}_i$, respectively, calculated with respect to the most stable conformer. The rotational symmetry numbers, ($\sigma^{\mathbf{R}_i}$ and $\sigma^{\mathbf{TS}}$) are all unit. The number of the enantiomers for the structures with C_1 symmetry is two, that is $n^{\mathbf{R}_i} = 2$ for $i = 2-3, 5-10$, just like in the case of the transition state **TS7** ($n^{\mathbf{TS}} = 2$); whereas for the structures **R1** and **R4**, which belong to the C_s point group of symmetry, $n^{\mathbf{R}_i} = 1$.

The value of the MEP at s = s_*^{CVT} is also referred to the most stable conformer, which in this case is **R1**. On the other hand, the aspects related to tunneling are unaltered by the number of conformers because the [1,7] hydrogen shift involves the participation of only one of the conformers. Therefore, we still make use of Eq. (7.8), but using Eq. (7.14) instead of Eq. (7.1) for the evaluation of the CVT thermal rate constants. This equation takes into account the number of enantiomers of reactant and transition state which multiplies the number of symmetry of each specie. The quotient between the number of enantiomers of the transition state **TS7** and of the most stable conformer of 7-methylocta-1,3(Z),5(Z)-triene, **R1** (which contribution to the denominator of Eq. (7.14) is the largest), is a factor of two.

The calculated thermal rate constants are listed in Table 7.2 and plotted in Figure 7.3. The CVT/μOMT values are in good agrement with the experimental ones for both the hydrogen and deuterium transfers. Variational effects are not very important; this is usually the case for hydrogen transfer reactions with relatively large barriers, because these reactions present tight transition states. As shown in Table 7.3, the calculated activation energies for the hydrogen shift are a little bit larger than the experimental ones, whereas those for the deuterium shift are slightly lower. These differences in the activation energies would affect the KIEs, although the overall agreement between theory and experiment is good, considering the size of the model system. Hess [235] calculated at the B3LYP/6-31+G* level a difference in activation energies $E_{\mathrm{a}}^{\mathrm{D}} - E_{\mathrm{a}}^{\mathrm{H}} = 0.9$ kcal·mol^{-1}. This value coincides with our calculated "classical" CVT value. When tunneling through the reaction coordinate barrier is taken into account, the difference $E_{\mathrm{a}}^{\mathrm{D}} - E_{\mathrm{a}}^{\mathrm{H}}$ increases. When the contribution of the ZCT transmission coefficients is included, the effect is almost negligible (0.06 kcal·mol^{-1}), but when we use the μOMT transmission coefficients, the difference increases to 0.41 kcal·mol^{-1}. In any case, the difference $E_{\mathrm{a}}^{\mathrm{D}} - E_{\mathrm{a}}^{\mathrm{H}}$ (1.29 kcal·mol^{-1}) is still small when compared with 2.0 kcal·mol^{-1} obtained by Baldwin and Reddy, [233] but still within the 95% confidence interval proposed by those authors, which is ±0.9 kcal·mol^{-1}. From the above numbers, although the ZCT transmission coefficients are larger than 2 at 333.2 K (see Table 7.4), there is no increase in the difference $E_{\mathrm{a}}^{\mathrm{D}} - E_{\mathrm{a}}^{\mathrm{H}}$, and only when the coupling between the reaction coordinate and the transverse modes is included, the difference is noticeable with respect to the classical value. Another effect of the coupling

Table 7.2: Calculated (columns 2, 3 and 4) and experimental (column 5) thermal rate constants (in s^{-1}) for the [1,7] hydrogen (and deuterium) shift in 7-methylocta-1,3(Z),5(Z)-triene

T(K)	TST	CVT	CVT/μOMT	Exp^a
		$k_H(T)$		
298.2	1.48×10^{-7}	1.45×10^{-7}	1.09×10^{-6}	
333.2	1.02×10^{-5}	1.00×10^{-5}	4.80×10^{-5}	$5.6\ \times10^{-5}$
348.2	4.82×10^{-5}	4.72×10^{-5}	1.96×10^{-4}	2.14×10^{-4}
368.2	3.12×10^{-4}	3.06×10^{-4}	1.08×10^{-3}	1.16×10^{-3}
388.2	1.67×10^{-3}	1.63×10^{-3}	5.03×10^{-3}	5.51×10^{-2}
400.0	4.13×10^{-3}	4.05×10^{-3}	1.16×10^{-2}	
		$k_D(T)$		
298.2	3.23×10^{-8}	3.20×10^{-8}	1.55×10^{-7}	
333.2	2.60×10^{-6}	2.60×10^{-6}	8.72×10^{-6}	$8.0\ \times10^{-6}$
348.2	1.30×10^{-5}	1.29×10^{-5}	3.84×10^{-5}	$3.3\ \times10^{-5}$
368.2	9.03×10^{-5}	8.94×10^{-5}	2.33×10^{-4}	2.21×10^{-4}
388.2	5.13×10^{-4}	5.08×10^{-4}	1.19×10^{-3}	1.21×10^{-3}
400.0	1.31×10^{-3}	1.30×10^{-3}	2.89×10^{-3}	

[a] From Ref. [233]

is that the μOMT transmission coefficients are larger than the ZCT transmission coefficients, although the former are essentially well-reproduced by the SCT values, as shown in Table 7.4.

As we mentioned in the previous section, the SCT transmission coefficients work better than the LCT ones when the coupling is weak or intermediate, although in this case, the main reason for the similarity between the SCT and the μOMT transmission coefficients is that, for the range of temperatures studied, the energies that contribute mostly to tunneling are very close to the top of the vibrationally adiabatic potential. Actually, at a given temperature, there is an energy at which the integral of Eq. (7.3) has a maximum. This energy is called the representative tunneling energy [249] (RTE) and at $T = 333.2$ K is 140.54 kcal·mol^{-1} and 140.00 kcal·mol^{-1} for the hydrogen and deuterium shifts, respectively. Taking into account that the maximum of the vibrational adiabatic potential is 141.94 and 140.70 kcal·mol^{-1} for the root and

Table 7.3: Arrhenius parameters (activation energy, E_a, in kcal·mol^{-1}, and logarithm of the preexponential factor, $\log(A/s^{-1})$), for [1,7] sigmatropic hydrogen (and deuterium) shift reactions^a

	[1,7] H shift		[1,7] D shift	
	E_a	$logA$	E_a	$logA$
CVT	23.83	10.63	24.71	10.62
CVT/ZCT	22.64	10.24	23.58	10.23
CVT/μOMT	21.60	9.86	22.89	9.96
Baldwin and Reddy[8]	21.5	9.8	23.5	1.3

[a] The fit to the calculated values included only temperatures in the interval 333.2-388.2 K to get a more reliable comparison with the experimental data.

Figure 7.3: Thermal rate constants calculated in this work by the CVT/μOMT method for the hydrogen (solid line) and deuterium (dashed line) shift reactions of 7-methylocta-1,3(Z),5(Z)-triene. The experimental values (squares) are also plotted for comparison.

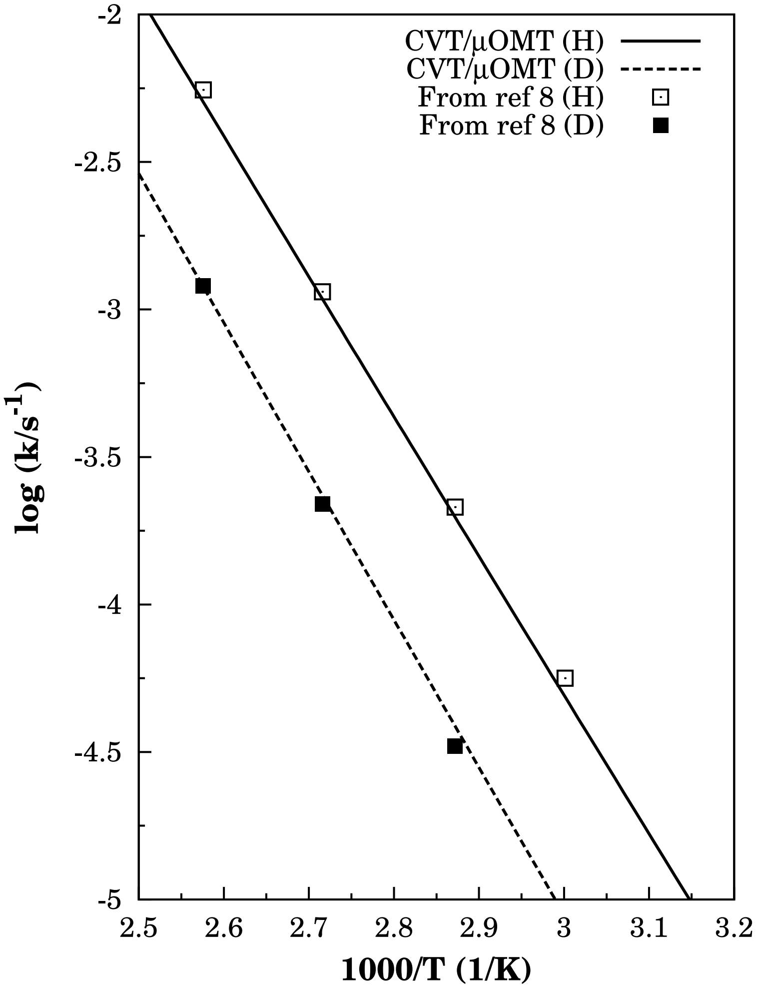

Table 7.4: Transmission coefficients, κ, evaluated by different approximations for [1,7] hydrogen (and deuterium) shift in the 7-methylocta-1,3(Z),5(Z)-triene

	κH(T)				κD(T)			
T (K)	ZCT	SCT	LCT	μOMT	ZCT	SCT	LCT	μOMT
298.2	3.06	7.40	3.89	7.50	2.80	4.85	3.10	4.85
333.2	2.42	4.78	2.78	4.80	2.24	3.35	2.30	3.35
348.2	2.24	4.14	2.50	4.16	2.08	2.98	2.20	2.98
368.2	2.05	3.52	2.24	3.53	1.91	2.61	2.00	2.61
388.2	1.91	3.08	2.04	3.08	1.79	2.34	1.85	2.34
400.0	1.83	2.87	1.95	2.87	1.72	2.22	1.78	2.22

Table 7.5: Factors in the KIEs^{a}

T(K)	$\eta_{\text{var}}(T)$	$\eta_{\text{int}}(T)$	$\eta_{\text{cl}}(T)$	$\eta_{\text{tun}}^{\text{ZCT}}(T)$	$\eta_{\text{tun}}^{\mu\text{OMT}}(T)$	$\eta_{\text{calc}}(T)$	$\eta_{\text{exp}}(T)$
298.2	0.99	4.59	4.54	1.09	1.55	7.02	
333.2	0.98	3.92	3.84	1.08	1.43	5.50	$7.0^{+1.3}_{-0.8}$
348.2	0.99	3.70	3.67	1.08	1.40	5.11	$6.5^{+0.7}_{-1.1}$
368.2	0.99	3.46	3.42	1.07	1.35	4.62	$5.2^{+0.9}_{-0.6}$
388.2	0.99	3.25	3.22	1.07	1.32	4.23	4.6 ± 0.6
400.0	0.99	3.14	3.11	1.06	1.29	4.02	

[a] The classical, $\eta_{\text{cl}}(T)$, and total, $\eta_{\text{calc}}(T)$, KIEs are given by Eq. (7.11) and Eq. (7.9), respectively. The experimental KIEs, $\eta_{\text{exp}}(T)$, are taken from Baldwin and Reddy [233] considering a deviation of $E_{\text{a}}^{\text{D}} - E_{\text{a}}^{\text{H}} = 0.1$ kcal·mol^{-1}. The factors $\eta_{\text{tun}}^{\text{ZCT}}(T)$ and $\eta_{\text{tun}}^{\mu\text{OMT}}(T)$ are also listed for comparison.

deuterated species, respectively, the RTE is roughly only 1.40 and 0.70 kcal·mol^{-1} below the top of the barrier for hydrogen and deuterium transfer, respectively, as shown in Figure 7.4. At these energies, because of the proximity of the top of the barrier, the curvature of the reaction path due to the coupling has to be small. However its influence is still important, and the SCT transmission coefficients are substantially larger than the ZCT ones. In this context, this study on the [1,7] hydrogen shift emphasizes the importance of treating tunneling phenomena as multidimensional events.

We can obtain a similar conclusion from the analysis of the KIEs, which are listed in Table 7.5. At T = 333.2, the classical KIE is only 3.84, which is quite close to the value of 3.89 calculated by Hess. Variational effects have a small impact in the calculated TST classical KIEs. The ZCT transmission coefficients practically keep the classical KIE unaltered, and therefore, the tunneling contribution to the reaction remains masked. This result may seem awkward because, in the ZCT case, the RTE is also close to the top of the barrier and we expect tunneling to be controlled by the curvature at the top of the barrier, which is given by the imaginary frequency. Its value is $\omega_{\text{H}}^{\ddagger} = 1315i$ cm^{-1} for hydrogen transfer and $\omega_{\text{D}}^{\ddagger} = 1080i$ cm^{-1} for deuterium transfer. The ratio between both frequencies is only 1.21, which is far from the expected value of $\sqrt{2}$, if we assume a pure hydrogen (deuterium) motion for this normal mode. This result indicates that the imaginary frequency normal mode also involves the motion of heavy atoms, so the ratio $\omega_{\text{H}}^{\ddagger}/\omega_{\text{D}}^{\ddagger}$ is far from the ratio of the masses, $m_{\text{D}}/m_{\text{H}}$. At the same time it should be noticed that the ZCT transmission coefficients are calculated along the MEP, and that this path includes the displacement of all the internal degrees of freedom and not only the hydrogen (deuterium) coordinate. The KIE due to tunneling increases when the curvature along the reaction coordinate is included. The calculated KIEs are somewhat smaller than the experimental values but clearly show the tendency that, in this case, the large primary KIE is due to quantum tunneling.

The above conclusions can be extrapolated to the [1,7] hydrogen shift in previtamin D$_3$, because this molecule has similar characteristics to the model system studied here. The KIEs measured by Okamura *et al.* [236] are similar to those obtained by Baldwin and Reddy for the hydrogen shift in 7-methylocta-1,3(Z),5(Z)-triene. The former author also measured an $E_{\text{a}}^{\text{D}} - E_{\text{a}}^{\text{H}}$ difference of 1.2 kcal·mol^{-1}, which is in very good agreement with our μOMT results for the model system.

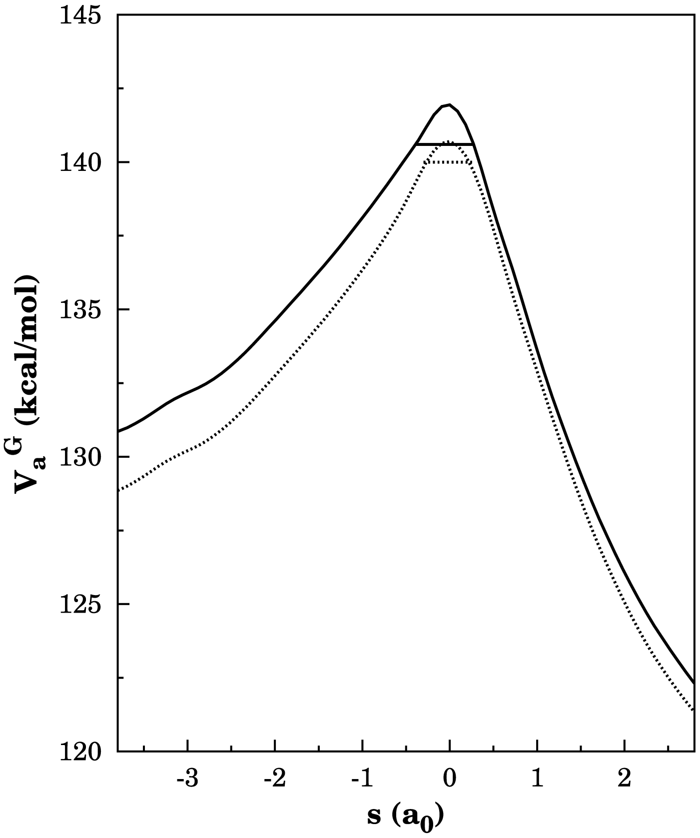

Figure 7.4: Ground-state vibrationally adiabatic potential for the hydrogen (solid line) and deuterium (dotted line) shift reactions of 7-methylocta-1,3(Z),5(Z)-triene. The straight lines indicate the representative tunneling energy at a temperature of $T = 333.2$ K.

7.4. Conclusions

The evaluation of thermal rate constants by high-level direct-dynamics CVT/μOMT calculations at the MPWB1K/DIDZ level has shown to be adequate to study the [1,7] sigmatropic hydrogen shift in 7-methylocta-1,3(Z),5(Z)-triene, which can be considered a model system for previtamin D_3. The calculated activation energies and primary KIEs are in reasonable agreement with the experimental data when quantum tunneling is taken into account. The CVT/μOMT calculations also indicate that it is important to consider the coupling between the reaction coordinate and the transverse modes to obtain KIEs comparable to the experimental values.

Chapter 8

The isomerization reaction of previtamin D_3

The thermal isomerization reaction that converts previtamin D into vitamin D consists in a intramolecular [1,7]-sigmatropic hydrogen shift with antarafacial stereochemistry. We have studied the dynamics of this reaction by means of the variational transition state theory with multidimensional corrections for tunneling in both gas phase and n-hexane environments. Two issues that may have an important effect on the dynamics were analyzed in depth, i.e., the conformational analysis of previtamin D and the quantum effects associated to the hydrogen transfer reaction. The characterization of the conformers of both previtamin D and vitamin D allowed us to calculate the thermal equilibrium constants of the process. Of the large number conformers of previtamin D that were located, there are sixteen that have the right disposition to react. The transition state structures associated to these reaction paths are very close in energy, so an accurate study of both the thermal rate constants and the kinetic isotope effects of the isomerization process should take them all into account. This issue is particularly important because the contribution of each of the reaction paths to the total thermal rate constant is quite sensitive to the environment. The dynamics results confirm that tunneling plays an important role and that model systems that were considered previously to study the hydrogen shift reaction cannot mimic the complexity introduced by the rings flexibility of previtamin D.

8.1. Introduction

Vitamin D is found in phytoplankton, which is one of the oldest forms of life. These organisms convert ergosterol (also called provitamin D_2) to previtamin D_2, when exposed to sunlight. After that previtamin D_2 isomerizes to vitamin D_2. [227, 250] It seems that ergosterol helps to protect the organism from ultra-violet (UV) radiation, which can be harmful for the genetic code. From these early forms of life, vitamin D_2 passed to fish and from there, through the food chain to more evolved organisms, preserving most of its character. Of the two known forms of vitamin D for most of the mammals, including humans, the most active form of vitamin D is vitamin D_3, which differs from vitamin D_2 in the side chain of the sterol.

The deficiency of vitamin D leads to rickets, a common disease afflicting children during the nineteenth and the beginning of the twentyteeth centuries. The first studies on the subject pointed out the importance of taking cod-liver oil to prevent rickets [251] but it was in the 1920s that scientists realized that sunlight was essential for the production of vitamin D_3 by the body, [252, 253] and that it promotes calcium deposition in the bones. [254] Vitamin D_3 is produced from the 7-dehydrocholesterol, an sterol that is present in the skin of most higher animals, so vitamin D_3 is not really a vitamin, i.e., it is a substance that the body can manufacture and, therefore, its intake is not essential in the diet.

For many years both forms of vitamin D were a puzzle to scientist until their structures were determine in the 1930s. It is understandable that vitamin D was misidentified as a true vitamin before the resolution of its structure, since it is the sunlight exposure and not the compound, the one that is essential for the body. [255–257] The production of the two forms of vitamin D follows the same mechanism, i.e., the sterol or provitamin D, which is already present in the organism, is transformed in previtamin D (Pre) by the action of UV radiation, which in turn thermally isomerizes to vitamin D (Vit), the thermodynamically most stable form of the two of them (see Scheme 8.1).

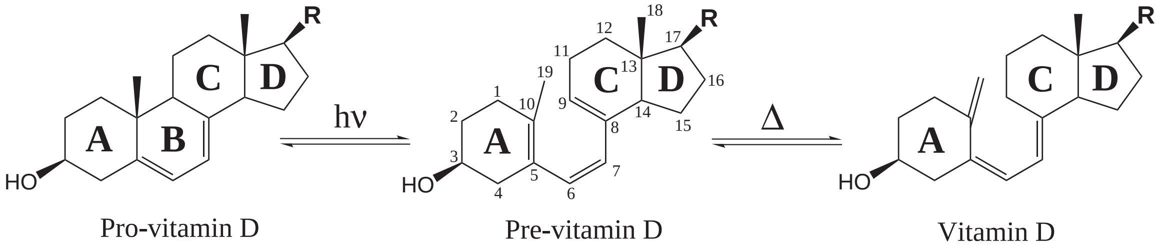

Scheme 8.1: Formation of Previtamin D_3 from pro-vitamin D_3

The action of the light not only affects the first step of the reaction, but also the thermal isomerization to Vit, because some side reactions are possible, i.e. the closure of the B ring leading to lumisterol or the rotation about the C_6–C_7 double bond (from Z to E) producing tachysterol. The production of these side products is reversible and it is possible due to the conformational flexibility of Pre. [258, 259] The thermal isomerization of Vit occurs by a [1,7]-sigmatropic hydrogen shift when the C_5–C_6 and C_7–C_8 single bonds have s-cis conformations (cZc). From the experimental point of view it is not known which is the most stable form of Pre [260], although the theoretical calculations predict that the s-trans,s-cis conformer (tZc) as the one with the lowest energy. [261, 262] The conformational analysis is complicated further by the flexibility of the A and C rings.

Nowadays it is well-known that the thermal isomerization is an intramolecular [1,7]-sigmatopic hydrogen shift [263] with antarafacial stereochemistry. [264, 265] However, there are many cZc conformations because of the A and C cyclohexene rings, each of them with two possibilities for antarafacial hydrogen exchange, i.e. the cis-10,6,8-triene can twist in a right-handed sense, i.e., the dihedral angle about the bond C_5–C_6 is positive following the rules of Klyne and Prelog [266] (the A ring is below the C ring), so we call this configuration antarafacial(+), or it can be antarafacial(-), that is, the triene twistes in a left-handed sense (the dihedral angle about the bond C_5–C_6 is negative), as shown in Scheme 8.2.

Sheves *et al.* [230] using ^{2}H NMR and mass spectrometry techniques obtained that the hydrogen shift prefers a right-handed disposition by a ratio of 2:1. Those authors also reported a kinetic isotope effect (KIE) for the isomerization in isooctane of about 45 at 80 °C. A more reliable value of the KIE was measured by Okamura *et al.* [236] using a pentadeuterio derivative

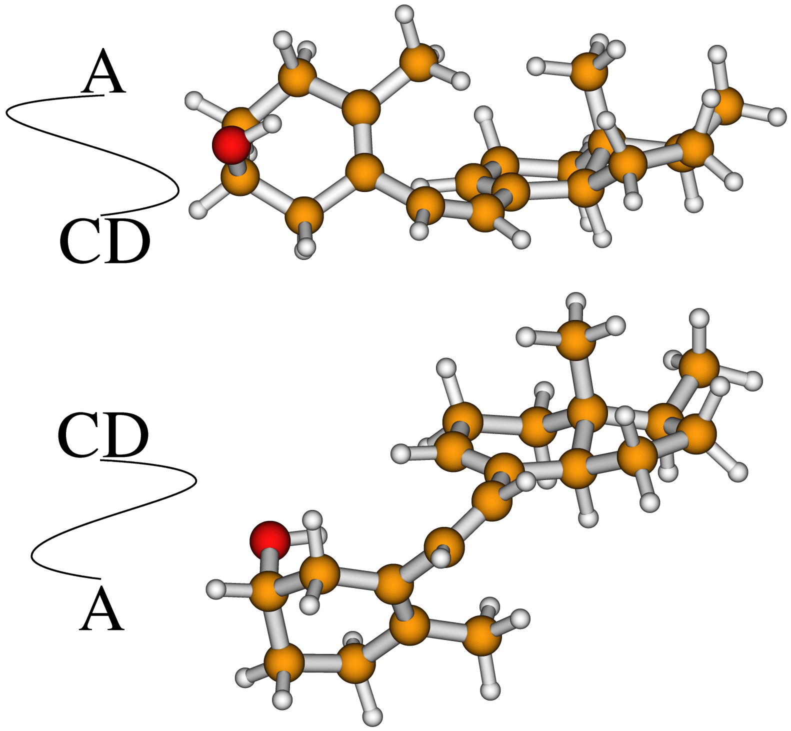

Scheme 8.2: Antarafacial(-)(the A ring if above the C ring) and antarafacial(+) (the A ring is below the C ring configurations of Pre.

of Pre in n-hexane, and at the same temperature of reaction obtained a KIE of 6.2. This value is very similar to 6.5, which is the KIE obtained by Baldwin and Reddy [233] for the [1,7] sigmatropic shift of the 7-methylocta-1,3(Z),5(Z)-triene (hereafter, we would refer to this triene simply as Tri) at 75 °C in 2-methylpentane (see Scheme 8.3). This compound has the same structure of single and double bonds as the Pre for the occurrence of the [1,7]-hydrogen shift, so it was thought that it would be a good model to study the isomerization reaction. In fact, not only the KIEs are very similar, the absolute value of the thermal rate constants for the [1,7]-hydrogen shift are also relatively close in value; thus at 75 °C the reported values are $2.1 \times 10^{-4}\ \mathrm{s}^{-1}$ and $3.3 \times 10^{-4}\ \mathrm{s}^{-1}$ for Tri and for Pre, respectively.

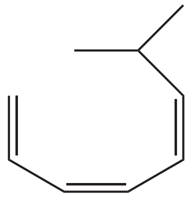

Scheme 8.3: Structure of the 7-methylocta-1,3(Z),5(Z)-triene

The [1,7]-hydrogen shift is a hydrogen transfer reaction, so quantum mechanical tunneling can be of importance. [59] The magnitude of the KIE gives an indication of the importance of this quantum effect. In this context theoretical calculations are of great help because the KIE can be splitted in several contributions. For hydrogen transfer reactions with large barriers, conventional transition state theory [26] (TST) calculations give us a good hint of the importance of tunneling. TST ignores those effects, but we can evaluate the 'quasiclassical' contributions to the KIE, i.e. the rotational and vibrational contributions. It is called 'quasiclassical' KIE because all the $3N-7$ ($3N-6$ if the molecule is linear, where N is the number of atoms) molecular vibrations perpendicular to the reaction coordinate are treated quantum mechanically, so quantum effects due to both the discretization of the vibrational energy and to the zero-point energy are included. TST calculations carried out at 60 °C on a compound similar to Tri, i.e., the 1,3(Z),5(Z)-triene led to a KIE of 3.9. [235] The experimental KIE for Tri at this temperature is 7.0, which is almost double the calculated quasiclassical KIE. Although both trienes are slightly different, most of the large discrepancy between the experimental and theoretical values can be ascribed to tunneling.

Variational transition state theory with multidimensional tunneling corrections [16, 17, 29, 63–65, 67–70, 82, 132, 133] (VTST/MT) can take into account the contribution that is missing in the quasiclassical KIE, i.e., quantum effects due to the reaction coordinate. [It should be noticed that VTST/MT also includes deviations from the TST due to classical recrossing of trajectories, but in this case the large barrier height implies that those contributions to the KIE would be the unity (no recrossing for any of the isotopes) or very close to unity.] Quantum effects are included through a multiplicative transmission coefficient [51, 61, 72–74, 128] to the calculated TST rate constant. A very successful and practical approach is to evaluate this transmission coefficient semiclassically, so the calculated KIE is called 'semiclassical' KIE. The semiclassical KIE calculated in this way can be readily compared to the experimental KIE and it has proved to be a powerful tool for getting insight into reaction mechanisms of complex systems. Four years ago we carried out VTST/MT calculations on Tri, [267] the calculated quasiclassical KIE at 60 °C was 3.7 (a very close value to that obtained for the 1,3(Z),5(Z)-triene), whereas the semiclassical KIE was 5.5. The latter is in much better agreement with the experimental value, so there is strong evidence that tunneling plays an important role in [1,7]-hydrogen shift reactions.

The similarities between Pre and Tri in both the KIEs and the thermal rate constants of [1,7]-hydrogen shifts make it reasonable to assume that this triene could be a good model for the study of the isomerization reaction in the Pre. However, we note that this apparent agreement may hide important differences because both the KIEs and the thermal rate constants are cumulative properties, which may be due to the contribution of one or of several reacting structures. In the triene there are several equilibrium conformations, but only one has the right structure to react, whereas in Pre we may expect to have many reactive configurations due to the flexibility of the rings. In other words, should we expect a strong influence of the A and C rings in the isomerization reaction? How is this flexibility going to affect the thermal rate constants and the tunneling effect? How is the environment going to affect the reactive configurations of Pre?

The objective of this work is to analyze in detail, from a theoretical point of view, the dynamics of the isomerization reaction of Pre to give an answer to the above questions. The rings bring complexity to the problem and, therefore, their incorporation is crucial for the understanding of the isomerization reaction. This is a difficult task due to the large size of the molecule, especially if the goal is to obtain accurate thermal rate constants and, thus, accurate KIEs. It can be achieved by interfacing electronic structure calculations and VTST/MT. The latter has proved to be a powerful tool for getting insight into reaction mechanisms of complex systems, and the present work is pioneer in the use of this approach to study the isomerization reaction in the Pre. To take into account the effect of the environment, we make a comparison of the gas-phase calculations with those obtained in n-hexane. The latter calculations also allow us to make a direct comparison with experiment and to extrapolate our results to less isotropic environments as it could be the isomerization reaction in the human skin.

8.2. Calculation method

All stationary points geometries (equilibrium configurations and transition state structures) were optimized at the MPWB1K density functional method [144] with the 6-31+G(d,p) basis set. [145] This level of theory was already used in the study of the [1,7]-hydrogen shift in Tri with very good results. [267]

The lateral chain (R in Scheme 8.1) distinguishes between the two forms of Pre (i.e. D_2 and D_3). It plays a major role in the transformation of Vit into a hormone, but at this stage of the process the functionality of the lateral chain is irrelevant. Therefore, to reduce computational time we have changed the lateral chain by a methyl group, although we still preserve the names Pre and Vit to refer to these modified compounds.

All the VTST/MT calculations were performed using canonical variational transition state theory (CVT), [66] and quantum effects were incorporated by the small-curvature tunneling (SCT) approach, [19, 86–88] so hereafter, we refer to this methodology with the abbreviation CVT/SCT. To obtain the CVT/SCT thermal rate constants we need information along the minimum energy path (MEP), which is the union of the paths of steepest descent in isoinertial coordinates from the transition state to the reactants and to the products. [73, 76, 84] The signed distance along this path is labeled as s, being $s = 0$ the location of the transition state. For each of the optimized transition state structures, that is, for each of the reaction paths, the MEP was followed in mass-scaled Cartesian coordinates (a type of isoinertial coordinates in which the mass-weighted Cartesian coordinates are divided by the square root of an arbitrary scaling mass μ). The CVT/SCT thermal rate constants at temperatures between 25 and 95 °C were obtained in two steps: (i) the MEP was followed by the Page-McIver algorithm [210] using a stepsize of 0.01 a_0 and a scaling mass $\mu = 1$, and Hessians were calculated each 9 steps in the interval $[-0.63\ a_0,\ 1.53\ a_0]$ for each of the reactive channels, and for both the root and the pentadeuterated compounds; (ii) the gradient and Hessian calculations carried out in step (i) were used as input in the interpolation by mapping scheme. [268] This procedure allows the calculation of converged CVT/SCT thermal rate constants using a small number of gradient and Hessian calculations. All the calculated normal-mode frequencies were scaled by a factor of 0.964. [241]

The CVT/SCT thermal rate constants are given by:

$$k^{\mathrm{CVT/SCT}}(T) = \kappa^{\mathrm{SCT}}(T)\Gamma^{\mathrm{CVT}}(T)k^{\mathrm{TST}}(T) \tag{8.1}$$

where $k^{\mathrm{TST}}(T)$ is the thermal rate constant calculated by TST, i.e.,

$$k^{\mathrm{TST}}(T) = \frac{\sigma}{\beta h}\exp\left\{-\beta[G^{\ddagger,0}(T) - G^{\mathrm{R},0}(T)]\right\} = \frac{\sigma}{\beta h}\exp\left\{-\beta\Delta G^{\ddagger,0}(T)\right\} \tag{8.2}$$

where $\beta = 1/k_BT$, being k_B the Boltzmann constant and T the temperature; h is the Planck constant; σ is the symmetry number for reaction, [31, 78] which in this case is always the unity; $G^{\ddagger,0}(T)$ is the standard-state free energy at the transition state; $G^{\mathrm{R},0}(T)$ is the standard-state free energy of reactants, and the difference in free energy between the two structures is the free energy of activation $\Delta G^{\ddagger,0}$; $\kappa^{\mathrm{SCT}}(T)$ is the tunneling transmission coefficient that takes into account quantum effects due to the reaction coordinate and it is evaluated over the ground-state vibrationally adiabatic potential, which is the sum of the classical potential plus the zero-point energy at each point along the MEP; $\Gamma^{\mathrm{CVT}}(T)$ is a factor given by:

$$\Gamma^{\mathrm{CVT}}(T) = \kappa^{\mathrm{CVT/CAG}} \exp\left\{-\beta[G^{\mathrm{CVT},0}(T) - G^{\ddagger,0}(T)]\right\} \tag{8.3}$$

where $\kappa^{\mathrm{CVT/CAG}}$ is a factor that corrects for the different thresholds which may have the CVT thermal rate constant and the tunneling transmission coefficient [128]. The exponent corrects the TST expression by taking into account recrossing effects, i.e., the bottleneck for reaction is variationally searched and given by the point along the MEP for which the free energy has a maximum, i.e., $G^{\mathrm{CVT},0}(T)$. This value may not coincide with the top of the classical barrier height, in which case $\Gamma^{\mathrm{CVT}}(T)$ would be smaller than unity. For the system studied here $\Gamma^{\mathrm{CVT}}(T)$ is very close to unity in all cases (deviations from unity are smaller than 3%). We note that:

$$G^{\mathrm{X},0}(T) = V(\mathbf{R}_{\mathrm{X}}) + G^{\mathrm{X}}_{\mathrm{RV}}(T) \tag{8.4}$$

where X = R (in Pre structures), ‡ (in TS structures), P (in Vit structures) or CVT; $V(\mathbf{R}_{\mathrm{X}})$ is the potential energy at the geometry $\mathbf{R}_{\mathrm{X}}$ and $G^{\mathrm{X}}_{\mathrm{RV}}(T)$ is the internal free energy of the molecule.

The experimental measurements on the isomerization reaction of Pre were carried out in n-hexane, [236] and in order to take into account the effect of the solvent, we have used the separable equilibrium solvation (SES) approximation. [269]. Specifically, we have performed SM5.43R continuum solvation model [270] single-point calculations on the gas-phase MPWB1K/6-31+G(d,p) geometries at the MPW1K/6-31+G(d,p) level, [271] i.e., at the SM5.43R/MPW1K/6-31+G(d,p)//MPWB1K/6-31+G(d,p) level. Therefore, all gas-phase energies, including those along the MEP were corrected by the interpolated single-point energies (ISPE) algorithm [272] to take into account the solvation of Pre. This procedure allowed us to calculate CVT/SCT thermal rate constants in solution. Hereafter, we denote as CVT/SCT(g) and CVT/SCT(s) the thermal rate constants calculated in gas-phase and in n-hexane, respectively. It should be noticed that in solution Eq. (8.4) is given by:

$$G^{\mathrm{X},0}(T) = V(\mathbf{R}_{\mathrm{X}}) + G^{\mathrm{X}}_{\mathrm{RV}}(T) + \Delta G^{\mathrm{X},0}_{\mathrm{S}}(T) \tag{8.5}$$

where $\Delta G^{\mathrm{X}}_{\mathrm{S}}(T)$ is the standard-state free energy of solvation at the gas-phase geometry $\mathbf{R}_{\mathrm{X}}$.

Finally we carried out SM5.43R/MPW1K/6-31+G(d,p)//MPWB1K/6-31+G(d,p) calculations in n-hexane for Tri, so we could directly compare the [1,7] hydrogen shift in Pre and in Tri in this solvent.

All the electronic structure calculations were performed with *Gaussian03*, [212] the thermal rate constants were calculated with version 9.7 of the POLYRATE program. [213] The GAUSSRATE9.7 [214] program made the linkage between the two packages. Free energies of solvation with the SM5.43R model were computed by a modified version of *Gaussian03* called Minnesota Gaussian Solvation Model (MN-GSM) version 2009. [273]

8.3. Results and discussion

There are several aspect of the thermal isomerization reaction of Pre that need careful consideration, so we have divided the Section in several parts. In the first place we discuss aspects related to the search and characterization of the conformers of both Pre and Vit. With this information at hand it is straightforward to calculate the equilibrium constants. In the second place we discuss some aspects related to the rings configurations at the transition state structures, since the rings have a major influence on the energetics of the process, and therefore on the contribution of those transition states to the total thermal rate constants. Finally we perform the dynamics calculations and obtain thermal rate constants and KIEs for the isomerization reaction in both gas phase and n-hexane. The results are also compared with those obtained for the [1,7] hydrogen shift reaction in Tri. We analyze some important aspects of the statics and the dynamics of the isomerization reaction of Pre, and give some qualitative hints of how the process may occur in human skin and in other anisotropic environments.

8.3.1. Conformations of Pre and Vit

We have carried out an exhaustive conformational study of all the relevant equilibrium configurations for the isomerization reaction. In the case of Pre, a complete conformational analysis involves to take into account both the torsions about the C_5–C_6 and C_7–C_8 single bonds and the flexibility of the A and C rings.

For a given configuration of the rings we use the notation given by Dauben and Funhoff [261] in which the dihedral angles about the C_5–C_6 and C_7–C_8 single bonds can be in s-cis or s-trans dispositions, so they are labeled as (±)c for dihedral angles between 0° and ± 90°, and (±)t for dihedral angles between ± 91° and ± 180°. The sign of the torsional angle is assigned following the rules of Klyne and Prelog. [266] In Pre the C_6–C_7 double bond is always in *Z* configuration and the dihedral angle about the C_7–C_8 can only be (±)c due to steric impediments. For each of the configurations of the rings (with one exception described later on) we have found five conformations, of which the (+)c*Z*(+)c and the (-)c*Z*(-)c are the equilibrium conformations for the antarafacial(+) and for the antarafacial(-) [1,7]-hydrogen shifts, respectively. In the case of Vit the C_5–C_6 and C_7–C_8 double bonds are in *Z* and *E* configurations, respectively, whereas the C_6-C_7 single bond is labelled as (±)c or (±)t as in the Pre single bonds.

The A and C rings in Pre are partially substituted cyclohexenes. In free cyclohexene the two stable configurations are half-chair and twist-boat and the conversion between two half-chair configurations occurs in three stages: [274] (i) from half-chair to twist-boat with a substantial barrier height of about 5.5 kcal/mol; (ii) from twist-boat to twist-boat through a C_S boat configuration and with an almost barrierless process; (iii) from twist-boat to half-chair with the same release in energy that was needed in step (i). In the Pre the situation is different because the substituents break the symmetry. The hydroxyl group in the 3-position is bonded to an asymmetric carbon with *S* configuration, and it can be in pseudoaxial or in pseudoequatorial positions, and the interconversion between different structures is shown in Scheme 8.4. This shows that for the A ring there are four possible configurations, which together with the two configurations of the C ring make a total of eight different configurations.

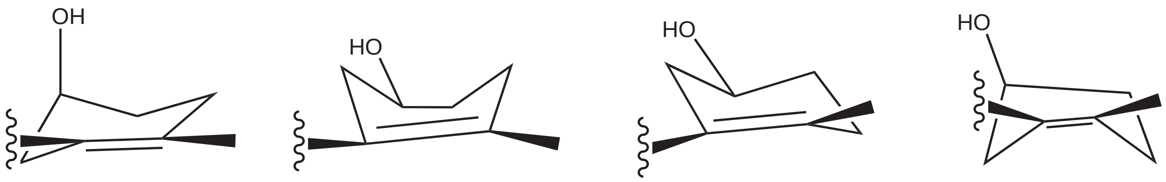

Scheme 8.4: The four different conformations of the A ring

In total there are sixteen reacting conformations because there are eight conformations for the antarafacial(+) attack, and other eight conformations for the antarafacial(-) attack. Taking into account the position of the OH group there four $\text{Pre}_{a(+)}$ [antarafacial(+) with the OH in pseudoaxial (a)], four $\text{Pre}_{e(+)}$ [antarafacial(+) with the OH in pseudoequatorial (e)], four $\text{Pre}_{a(-)}$ [antarafacial(-) with the OH in pseudoaxial (a)], and four $\text{Pre}_{e(-)}$ [antarafacial(-) with the OH in pseudoequatorial (e)]. Therefore, the previous eight first configurations correspond to (+)c*Z*(+)c conformations, whereas the eight last ones correspond to (-)c*Z*(-)c conformations. For instance, as shown in Scheme 8.5, a reacting conformation, which is antarafacial(+), with the OH in pseudoaxial configuration, with a half-chair (HC) conformation for the A ring and with a twist-boat (TB) conformation for the C ring, is denoted as Pre_a(HC,TB)(+)cZ(+)c or shortly as $\text{Pre}_{a(+)}$(HC,TB).

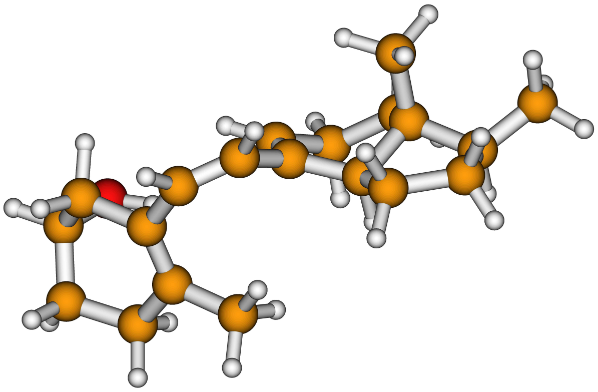

Scheme 8.5: The conformation Pre_a(HC,TC)(+)cZ(+)c.

To uniquely describe a non-reacting conformation, the information on the C_5–C_6 and C_7–C_8 single bonds should be always specified. Thus, for instance, a conformation in which the OH is in a pseudoaxial configuration, with a half-chair (HC) conformation for the A and C rings, with a dihedral angle about the C_5-C_6 bond of 120°, and with a dihedral angle about the C_7–C_8 bond of $-60°$, is denoted as the Pre_a(HC,HC)(+)tZ(-)c conformation. If there are more than one conformation with these characteristics, then the first one is denoted as Pre_a(HC,HC)(+)tZ(-)c(1), the second as Pre_a(HC,HC)(+)tZ(-)c(2), etc. The combination of five conformations due to the C_5–C_6 and C_7–C_8 single bonds with the eight configurations of the rings makes a total of 40 conformations, although we could only locate 35, because none of the five equilibrium conformations of Pre_a(HB,HC) was obtained.

Table 8.1 lists all the conformers of Pre(HC,HC), and among them are the most stable conformers of the reactants. A complete account of the equilibrium conformations of Pre and some of Vit is given in the Appendix B. From the energetics point of view the Pre_a(HC,HC)(+)tZ(-)c conformer is the global minimum among all the conformations of Pre, so we use it as the reference of energy. The cZc configurations of Pre do not lead to the most stable configurations of Vit, since it is well known that ZtE conformations of Vit are more stable than ZcE ones. [275, 276] Those ZtE conformations of Vit were also calculated, and listed in Table 8.1, since they are needed for the evaluation of the thermodynamic equilibrium constants. It should be noticed that in Vit the sign of the antarafacial attack is given by the sign of the torsion about the C_6–C_7 single bond.

Table 8.1: Some energetic (in kcal/mol) and geometric (in degrees) parameters of the lowest conformers of Pre and Vit. The differences in the classical energy (ΔE), and in the free energies (at $T = 37°\mathrm{C}$) in gas phase (ΔG_g) and in n-hexane (ΔG_s) are relative to the Pre$_{\mathrm{a}}$(HC,HC)(+)tZ(-)c conformer

Conformer	ΔE	$\phi_1{}^a$	$\phi_2{}^b$	$\phi_3{}^c$	ΔG^0_g	ΔG^0_s
Pre$_{\mathrm{a}}$(HC,HC)(+)cZ(+)c	1.50	58.8	1.9	45.4	0.72	0.63
Pre$_{\mathrm{a}}$(HC,HC)(+)cZ(-)c	3.25	73.3	-0.5	-11.7	2.83	2.50
Pre$_{\mathrm{a}}$(HC,HC)(+)tZ(-)c	0.00	121.9	-7.2	-44.5	0.00	0.00
Pre$_{\mathrm{a}}$(HC,HC)(-)tZ(+)c	1.43	-151.3	10.3	43.4	0.19	-0.05
Pre$_{\mathrm{a}}$(HC,HC)(-)cZ(-)c	1.48	-55.8	-2.4	-26.2	1.86	2.07
Vit$_{\mathrm{a}}$(T,CH)Z(-)cE	5.91	-2.1	-57.0	0.4	6.70	7.15
Vit$_{\mathrm{a}}$(CH,CH)Z(+)cE	1.83	-0.2	54.2	-0.5	2.32	2.74
Vit$_{\mathrm{a}}$(CH,CH)Z(-)tE	-1.99	1.4	-173.8	1.7	-1.78	-1.60
Pre$_{\mathrm{e}}$(HC,HC)(+)cZ(+)c	1.73	53.2	2.3	44.7	1.80	1.77
Pre$_{\mathrm{e}}$(HC,HC)(+)cZ(-)c	3.52	90.0	-2.1	-37.2	2.36	2.06
Pre$_{\mathrm{e}}$(HC,HC)(+)tZ(-)c	2.06	152.7	-10.2	-42.1	0.67	0.48
Pre$_{\mathrm{e}}$(HC,HC)(-)tZ(+)c	1.72	-127.8	6.9	35.0	0.08	-0.17
Pre$_{\mathrm{e}}$(HC,HC)(-)cZ(-)c	2.87	-59.1	-0.4	-20.0	2.54	2.47
Vit$_{\mathrm{e}}$(CH,CH)Z(-)cE	2.57	-2.8	-58.1	0.7	3.07	3.61
Vit$_{\mathrm{e}}$(T,CH)Z(+)cE	7.83	1.3	53.6	-0.9	7.16	7.65
Vit$_{\mathrm{e}}$(CH,CH)Z(+)tE	-0.94	-2.6	172.7	-3.5	-1.35	-1.33

[a] $\phi_1 = \phi(C_{10} - C_5 - C_6 - C_7)$; [b] $\phi_2 = \phi(C_5 - C_6 - C_7 - C_8)$; [c] $\phi_3 = \phi(C_6 - C_7 - C_8 - C_9)$.

Table 8.2 lists the energetics of the stationary points for each of the sixteen reaction paths. Figure 8.1 relates the configurations of the A and C rings in Pre with those in Vit. For the A and C rings twist-boat conformations in Pre always lead to twisted (T) conformations in Vit, whereas half-chair conformations of the C ring in Pre always lead to chair conformations (CH) in Vit. However, the four half-chair conformations of the A ring in Pre lead to two chair conformations and to two twisted conformations in Vit, due to the characteristics of the reaction (this issue is explained in the Subsection dealing with the transition state structures). The electronic structure calculations carried out at the HF/3-21G level on the 1,2-dimethylencyclohexane [277] show that after the chair configurations the twisted configurations are the next most favorable configurations with a difference in energy with respect to the chair conformations of 4.3 kcal/mol.

In general the relative stability of the equilibrium conformations are a consequence of the differences in energy between the half-chair and twist-boat conformations in Pre and between the chair and twisted conformations in Vit. Thus the Pre(HC,HC) and Vit(CH,CH) configurations are roughly about 8 to 12 kcal/mol more stable than Pre(TB,TB) and Vit(T,T) configurations and about 4 to 6 kcal/mol than the Pre(HC,TB), Pre(TB,HC), Vit(T,CH) and Vit(CH,T) configurations.

Table 8.2: Relative values with respect to the Pre_a(HC,HC)(+)tZ(-)c conformer of classical energies (ΔE), classical energies including zero-point energy ($\Delta E(ZPE)$), standard-state free energies at 37°C in gas phase (ΔG_g^X) and in n-hexane (ΔG_s^X); X = R (in Pre), ‡ (in TS), and P (in Vit). All values are in kcal/mol

Reaction	Conformer	ΔE	$\Delta E(ZPE)$	$\Delta G_g^\text{X}(T = 37°\text{C})$	$\Delta G_s^\text{X}(T = 37°\text{C})$
R1	$\text{Pre}_{\text{a}(+)}$(HC,HC)	1.50	1.44	0.72	0.63
	$\text{TS}_{\text{a}(+)}$(HC,HC)	27.97	25.42	26.38	26.46
	$\text{Vit}_{\text{a}(+)}$(CH,CH)	1.83	2.24	2.32	2.74
R2	$\text{Pre}_{\text{a}(-)}$(HC,HC)	1.48	1.83	1.86	2.07
	$\text{TS}_{\text{a}(-)}$(HC,HC)	29.61	27.32	28.25	28.38
	$\text{Vit}_{\text{a}(-)}$(T,CH)	5.91	6.38	6.70	7.15
R3	$\text{Pre}_{\text{a}(+)}$(HC,TB)	6.02	6.16	5.25	5.26
	$\text{TS}_{\text{a}(+)}$(HC,TB)	31.32	28.79	29.63	29.70
	$\text{Vit}_{\text{a}(+)}$(CH,T)	7.32	7.09	6.43	6.88
R4	$\text{Pre}_{\text{a}(-)}$(HC,TB)	5.61	6.07	5.90	6.04
	$\text{TS}_{\text{a}(-)}$(HC,TB)	29.63	27.30	28.36	28.46
	$\text{Vit}_{\text{a}(-)}$(T,T)	9.76	10.65	10.98	11.18
R5	$\text{Pre}_{\text{e}(+)}$(HC,HC)	1.73	1.92	1.80	1.77
	$\text{TS}_{\text{e}(+)}$(HC,HC)	28.35	25.48	26.31	26.21
	$\text{Vit}_{\text{e}(+)}$(T,CH)	7.83	7.70	7.16	7.65
R6	$\text{Pre}_{\text{e}(-)}$(HC,HC)	2.87	2.93	2.54	2.47
	$\text{TS}_{\text{e}(-)}$(HC,HC)	30.28	27.60	28.39	28.31
	$\text{Vit}_{\text{e}(-)}$(CH,CH)	2.57	2.81	3.07	3.61
R7	$\text{Pre}_{\text{e}(+)}$(HC,TB)	6.85	6.83	6.30	6.15
	$\text{TS}_{\text{e}(+)}$(HC,TB)	31.60	29.07	29.89	29.77
	$\text{Vit}_{\text{e}(+)}$(T,T)	13.41	13.21	12.01	12.43
R8	$\text{Pre}_{\text{e}(-)}$(HC,TB)	6.99	7.10	6.56	6.48
	$\text{TS}_{\text{e}(-)}$(HC,TB)	30.47	28.07	29.09	28.98
	$\text{Vit}_{\text{e}(-)}$(CH,T)	6.20	6.67	6.76	7.17
R9	$\text{Pre}_{\text{e}(+)}$(TB,HC)	6.64	6.37	5.14	5.20
	$\text{TS}_{\text{e}(+)}$(TB,HC)	29.60	27.15	28.05	28.11
	$\text{Vit}_{\text{e}(+)}$(T,CH)	7.22	7.59	7.29	7.71
R10	$\text{Pre}_{\text{e}(-)}$(TB,HC)	7.54	7.33	6.22	6.27
	$\text{TS}_{\text{e}(-)}$(TB,HC)	31.73	29.41	30.38	30.52
	$\text{Vit}_{\text{e}(-)}$(T,CH)	7.27	7.85	7.92	8.49
R11	$\text{Pre}_{\text{e}(+)}$(TB,TB)	11.42	10.52	7.73	7.92
	$\text{TS}_{\text{e}(+)}$(TB,TB)	33.10	30.39	30.85	30.89
	$\text{Vit}_{\text{e}(+)}$(T,T)	12.40	12.37	11.57	11.97
R12	$\text{Pre}_{\text{e}(-)}$(TB,TB)	11.61	11.72	10.68	10.68
	$\text{TS}_{\text{e}(-)}$(TB,TB)	32.02	29.32	29.98	30.09
	$\text{Vit}_{\text{e}(-)}$(T,T)	10.42	10.61	9.98	10.52
R13	$\text{Pre}_{\text{a}(+)}$(TB,HC)	–	–	–	–
	$\text{TS}_{\text{a}(+)}$(TB,HC)	28.60	26.22	27.22	27.30
	$\text{Vit}_{\text{a}(+)}$(T,CH)	5.77	5.85	1.02	1.25
R14	$\text{Pre}_{\text{a}(-)}$(TB,HC)	–	–	–	–
	$\text{TS}_{\text{a}(-)}$(TB,HC)	29.46	27.10	28.02	28.20
	$\text{Vit}_{\text{a}(-)}$(T,CH)	5.55	6.23	6.40	6.65
R15	$\text{Pre}_{\text{a}(+)}$(TB,TB)	11.02	11.12	10.05	9.76
	$\text{TS}_{\text{a}(+)}$(TB,TB)	31.99	29.26	29.79	29.81
	$\text{Vit}_{\text{a}(+)}$(T,T)	10.59	10.86	10.51	11.11
R16	$\text{Pre}_{\text{a}(-)}$(TB,TB)	10.01	10.03	8.93	9.08
	$\text{TS}_{\text{a}(-)}$(TB,TB)	29.72	27.03	28.00	28.17
	$\text{Vit}_{\text{a}(-)}$(T,T)	8.79	9.45	9.29	9.59

Figure 8.1: Correspondence between the initial (Pre) and final (Vit) configurations of the A and C rings for each of the reactive paths.

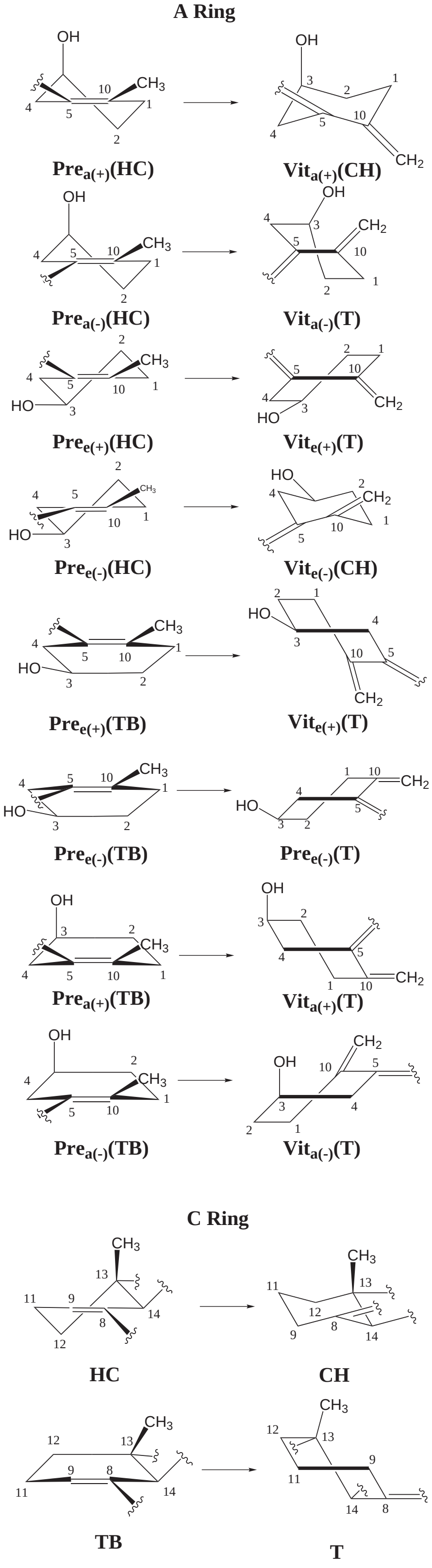

In the $\text{Vit}_\text{a}(-)$ conformations there is an stabilizing interaction between the hydroxyl group and the π orbitals of the C_{10}-C_{19} double bond, which is not present in the rest of conformers (See Scheme 8.6). Thus, the $\text{Vit}_{\text{a}(-)}$(T,T) conformer of reaction R16 is 1.67 kcal/mol more stable than the $\text{Vit}_{\text{e}(-)}$(T,T) conformer of reaction R12. This interaction is also reflected in the value of the OH stretching frequency, which decreases by 25 cm^{-1} for the former conformer.

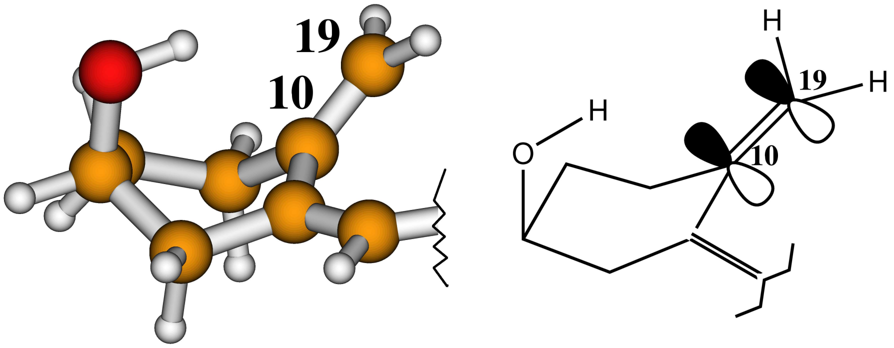

Scheme 8.6: Conformation of the A ring in Vit showing the interaction between the hydroxyl group and the π orbitals of the C_{10}–C_{19} double bond.

8.3.2. Thermodynamics equilibrium constants

The thermodynamics equilibrium constants using n-hexane as solvent can be easily calculated from the standard-state free energies of the conformers of Pre and Vit. We define the coefficient N_R that takes into account the relative free energies of all conformations of Pre, n_Pre, with respect to the global minimum, independently if those conformations are reactive or not, i.e.,

$$N_\text{R} = \sum_{j=1}^{n_\text{Pre}} \exp\left[-\beta \Delta G_j^{\text{R},0}(T)\right] \tag{8.6}$$

being $\Delta G_j^{\text{R},0}(T)$ the difference in free energy between a given conformer j of Pre and the free energy of the global minimum of Pre. Similarly,

$$N_\text{P} = \sum_{k=1}^{n_\text{Vit}} \exp\left[-\beta \Delta G_k^{\text{P},0}(T)\right] \tag{8.7}$$

being $\Delta G_k^{\text{P},0}(T)$ the difference in free energy between a given conformer k of Vit and the free energy of the global minimum of Vit; n_Vit is the number of conformations of Vit.

The equilibrium constants at every temperature for the isomerization reaction are simply:

$$K_\text{eq}(T) = \frac{N_\text{P}}{N_\text{R}} \exp\left[-\beta \Delta G^{\text{RP},0}(T)\right] \tag{8.8}$$

where $\Delta G^{\text{RP},0}$ is the standard-state free energy difference between the global minima of Vit and Pre. The equilibrium constants in n-hexane are obtained when the free energies of Eqs. (8.6), (8.7), and (8.8) also include the free energies of solvation.

Table 8.3: Calculated (in both gas phase $K_{\mathrm{eq},g}$ and in n-hexane $K_{\mathrm{eq},s}$), and experimental, K_{exp}, equilibrium constants for the root species, Pre(d_0), and for the pentadeuterated compound, Pre(d_5)

Molecule	T (°C)	$K_{\mathrm{eq},g}$	$K_{\mathrm{eq},s}$	$K_{\mathrm{exp}}{}^a$
Pre(d_0)	37.0	7.14	4.48	6.14^b, 6.22^c
	60.0	5.42	3.49	4.12^b
	60.1	5.42	3.49	5.37 ± 0.41
	69.35	4.89	3.19	4.53 ± 0.35
	74.35	4.64	3.04	4.17 ± 0.32
	79.9	4.38	2.88	3.82 ± 0.28
	85.5	4.13	2.74	3.51 ± 0.25
Pre(d_5)	60.5	6.12	3.98	5.42 ± 0.17
	69.7	5.54	3.64	4.66 ± 0.19
	74.1	5.29	3.49	4.36 ± 0.23
	80.4	4.96	3.29	3.99 ± 0.25
	85.5	4.72	3.15	3.72 ± 0.28

[a] From Ref. [236] if not indicated otherwise.[b] From Ref. [278]. [c] From Ref. [279].

Table 8.3 lists the calculated and experimental [236] equilibrium constants for the isomerization of the root species [Pre(d_0)] and of the pentadeuterio derivative [Pre(d_5)] that has been isotopically substituted in the 9,14,19,19,19-positions. The experimental equilibrium constants have been measured in n-hexane [236, 278] and the comparison with the calculated values in the same solvent show that the stability of the Vit conformers is underestimated, although the calculations correctly predict the exoergicity of the isomerization reaction. The sums of Eqs. (8.6) and (8.7) run over all possible conformers, but the equilibrium constants are completely determined by the Pre(HC,HC) conformers and by the two Vit(HC,HC)ZtE conformers listed in Table 8.1. The differences between the calculated gas-phase and n-hexane solvent equilibrium constants show that there is a high sensibility of the isomerization reaction to the environment.

The above calculations and the conformational study of the equilibrium configurations of both Pre and Vit may be useful to qualitative described the magnitude of the equilibrium constants obtained by Holick and coworkers [278, 279] in different anisotropic media. Those authors observed that at 37 °C the equilibrium constant varies from 1.76 in $\beta-$cyclodextrins to 11.44 in human skin. The large value of the equilibrium constant in human skin is similar to that obtained in DPPC liposomes. [280] Holick and coworkers [278] pointed out that in the lipids there would be interactions that stabilize more the cZc conformers than the tZc conformers. These interaction would be a result of the amphipathic (with both hydrophilic and hydrophobic parts) nature of both phospholipids and Pre. The OH group of Pre would form a hydrogen bond with the hydrophilic part of the lipid and the hydrophobic part of Pre would interact with the acyl chain of the lipid. However, to our understanding it is difficult to find a reason why these interactions should favor the cZc conformers over the tZc ones, and why this additional stabilization of the cZc form, if present, should increase the equilibrium constant. An easier explanation would be that the most stable conformers of Vit (see Table 8.1) would be stabilized further by these amphipathic interactions. When the isomerization reaction takes place in the presence of $\beta-$cyclodextrins the equilibrium constant is near the unity. Cyclodextrins are a family of compounds made up of sugar molecules bound together in a ring, and in the case of $\beta-$cyclodextrins the diameter of the cavity is about 6.2 Å. The isomerization reaction takes place inside of a cavity formed by the complexation of two $\beta-$cyclodextrins molecules. This cavity may not be large enough to allow rotations about the C_5–C_6 (in the case of Pre) or the C_6–C_7 (in the case of Vit) single bonds. The disappearance of the tZc conformers of Pre and of the ZtE conformers of Vit would decrease the value of the equilibrium constant substantially. We note that the equilibrium constant is a thermodynamics parameter that depends exclusively on the stability of the initial and final states and, therefore, it does not provide information about the kinetics of the process.

All these results show that the environment plays a very important role in the relative stabilities of the equilibrium structures of Pre and Vit, and that from the thermodynamics point of view the formation of Vit is not favored by solvation in nonpolar organic solvents as n-hexane.

8.3.3. Transition state structures

We use the same notation for the transition states as for Pre, although the conformation of the rings would be intermediate between Pre and Vit. The differences in energy due to conformational changes are smaller in the transition state structures than in the equilibrium configurations and they are mainly related to the disposition of the C ring. The antarafacial(+) attack is favored by the HC conformation of Pre, whereas the antarafacial(-) is favored by the TB conformation of Pre, being of great importance in the stability of the transition states the final configuration of the C ring in Vit. Figure 8.1 shows that the HC conformation of Pre leads to CH conformation in Vit when the C_{13} carbon atom is above of the plane formed by the C_8, C_{11}, C_{12}, and C_{14} carbon atoms, and the C_9 carbon atom (the acceptor atom in the hydrogen transfer) is below that plane. The antarafacial(+) attack in which the A ring is below the C and D rings favours the formation of the chair in Vit, whereas the antarafacial(-) attack puts some stress on the C ring because the transfer forces the acceptor to move above the C and D rings. Thus the dihedral angles about the C_8–C_9 and C_9–C_{11} bonds have values of $-19°$ and $-23°$, respectively, in the case of $\mathrm{TS}_{\mathrm{a}(+)}$(HC,HC), but they are closer to planarity in the $\mathrm{TS}_{\mathrm{a}(-)}$(HC,HC) transition state, with values of 5° and $-3°$, respectively (see Scheme 8.7).

If the C ring conformation in Vit is twisted, the C_8 and C_{12} are the lateral carbon atoms and the C_9 and C_{13} are apical atoms pointing above the plane formed by the two lateral atoms and the point at half-distance between the C_9–C_{11} bond. As a consequence, the antarafacial(-) attack requires a smaller distorsion of the C ring than the antarafacial(+) attack, favoring the transition states with the A ring above the C and D rings (see Scheme 8.8). In this context, the hydrogen shift reaction in Pre is different to that in Tri, because for the latter the two antarafacial attacks are equivalent and the two resulting transition states are enantiomers.

The interaction between the OH and the π orbitals of the forming C_{10}–C_{19} double bond is also present in some of the transition state structures, i.e., in the $\mathrm{TS}_{\mathrm{a}}(-)$ configurations. Thus, when both the C and D rings are removed, the optimization of the $\mathrm{TS}_{\mathrm{a}(-)}$(HC) and $\mathrm{TS}_{\mathrm{a}(+)}$(HC) structures with single-point calculations carried out with the SM5.43R model shows that the former structure is more stable than the latter by 0.60 kcal/mol. In the case of the $\mathrm{TS}_{\mathrm{a}(-)}$(TB) conformers the difference regarding to the $\mathrm{TS}_{\mathrm{a}(+)}$(TB) conformers increases to 1.06 kcal/mol.

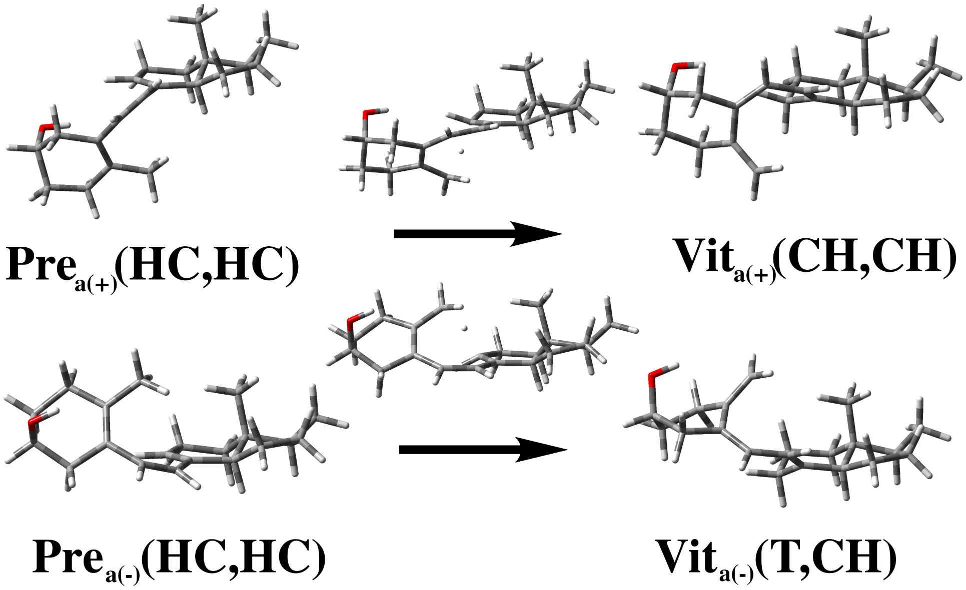

Scheme 8.7: Structural change of the C ring in half-chair configuration depending of the attack antarafacial(+) or antarafacial(-).

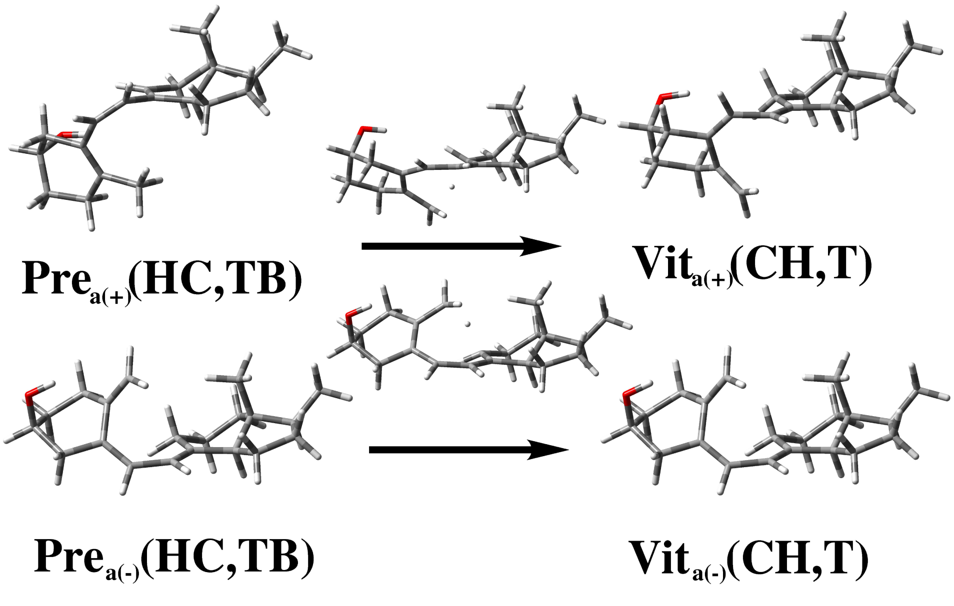

Scheme 8.8: Same as Scheme 8.7 but for the twist-boat conformation of the C Ring of Pre.

8.3.4. Thermal rate constants

The calculation of the thermal rate constants was carried out at several temperatures in the interval between 25°C to 95°C, but here we limit the analysis of the thermal rate constants to mainly two temperatures: $T = 37°\mathrm{C}$ (the normal body temperature), and $T = 60°\mathrm{C}$, one of the temperatures at which there are experimental results of thermal rate constants for the hydrogen shift reaction of both Tri and Pre. The results at other temperatures can be found in the Appendix B.

The total CVT/SCT thermal rate constant for the isomerization reaction can be obtained as a weighted sum the individual constants:

$$k^{\mathrm{CVT/SCT}}(T) = \sum_{i=1}^{n_{\mathrm{R}}} W_i(T) k_i^{\mathrm{CVT/SCT}}(T) \tag{8.9}$$

Hereafter the subscript $i = 1, \ldots, n_{\mathrm{R}}$ would always refer to the ith reaction listed in Table 8.2. The sum of Eq. (8.9) runs over all the $n_{\mathrm{R}} = 16$ reactive paths, with each of the individual thermal rate constants $k_i^{\mathrm{CVT/SCT}}(T)$ given by Eq. (8.1), i.e.,

$$k_i^{\mathrm{CVT/SCT}}(T) = \kappa_i^{\mathrm{SCT}}(T)\Gamma_i^{\mathrm{CVT}}(T) k_i^{\mathrm{TST}}(T) \tag{8.10}$$

The weighting factor $W_i(T)$ is the statistical probability at a given temperature T for the reaction occurring through path i and it is given by,

$$W_i(T) = \frac{\exp\left[-\beta \Delta G_i^{\mathrm{R},0}(T)\right]}{N_{\mathrm{R}}} \tag{8.11}$$

being $\Delta G_i^{\mathrm{R},0}(T)$ the difference in free energy between the reactant of reaction i and the free energy of the global minimum of Pre. The coefficient N_{R} is given by Eq. (8.6).

The contribution in percentage of each of the reaction paths to the total thermal rate constants can be calculated as:

$$\% k_i^{\mathrm{Y}}(T) = \frac{k_i^{\mathrm{W,Y}}(T)}{k^{\mathrm{Y}}(T)} \times 100 \tag{8.12}$$

where $\mathrm{Y} = \mathrm{TST} \;\text{ or }\; \mathrm{CVT/SCT}$, and

$$k_i^{\mathrm{W,Y}}(T) = W_i(T)\; k_i^{\mathrm{Y}}(T) \tag{8.13}$$

We note that the calculated thermal rate constants in n-hexane were readily obtained from the gas-phase ones, because we assume that the variational and quantum effects are the same in n-hexane and in the gas phase. We expect this approximation to work well because the differences in the free energies of activation between gas-phase and solution are quite modest (always smaller than 1 kcal/mol). Specifically, we use the gas-phase information along the reaction path but correcting the free energy of activation with an additional term which is the free energy of solvation (i.e., we use the values of $\Delta G_s^{\ddagger}(T)$ instead of $\Delta G_g^{\ddagger}(T)$ of Table 8.2).

Figure 8.2 plots the contribution in percentage of each of the reaction paths at 37 °C and Table 8.4 lists the total thermal rate constants for the isomerization reaction. The incorporation of the solvent has the effect of lowering the total CVT/SCT thermal rate constants by 30%. It also has an important effect on reactions R1 and R5, because the solvent favors reaction R5 over

Figure 8.2: Histogram plotting the contributions of each of the individual reaction paths (Y=TST or CVT/SCT) to the total total rate constant in both gas-phase and n-hexane solution at $T = 37°C$.

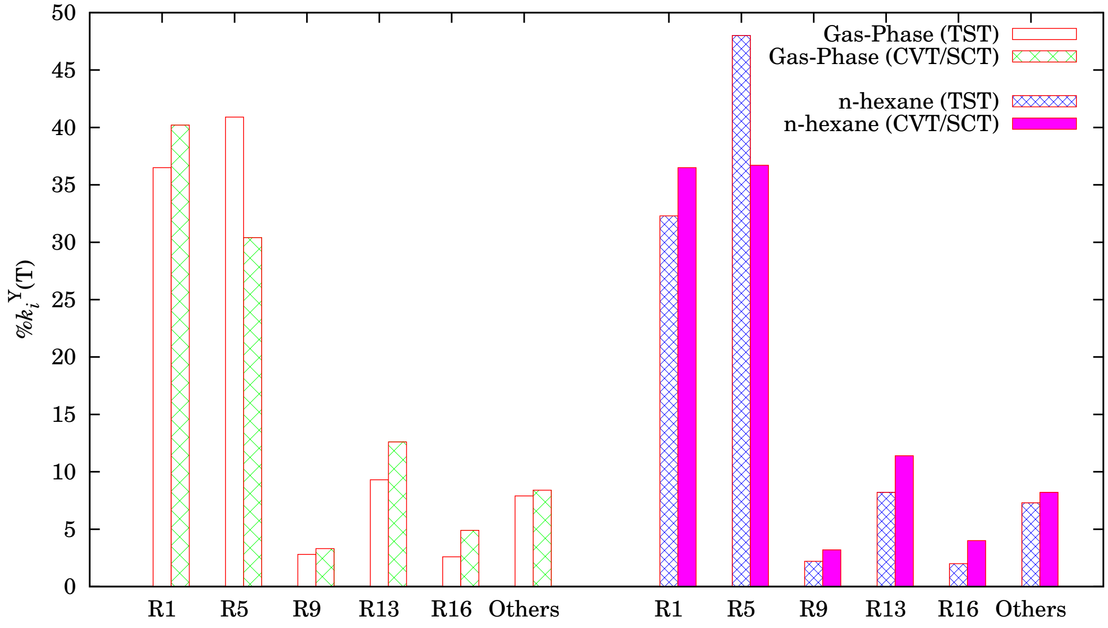

R1. These two reactions are the ones with the lowest classical barriers, so it is understandable that they contribute the most since the two transition states are reached from two of the most stable conformations of the A and C rings, and the antarafacial(+) attack favors the transfer. The TST thermal rate constant is larger for R5 than for R1 but tunneling is more important for R1 so the contribution of both reactions to the total CVT/SCT rate constant is practically the same in n-hexane. As shown in Figure 8.3 the total CVT/SCT thermal rate constants are in quite good agreement with the experimental data from Ref. [236].

At 37 °C the SCT transmission coefficient for R1 is 12.0, whereas for R5 is only 8.06 (see Figure 8.4). The reason for this disparity in the transmission coefficients can be traced to the difference in stability between the chair and twisted conformations of Vit. The $\mathrm{Vit}_{e(+)}$(T,CH) conformer of R5 is 5 kcal/mol less stable than the $\mathrm{Vit}_{a(+)}$(CH,CH) conformer of R1 and, therefore, the MEP for R5 is wider than that for R1. This can be confirmed by evaluating the zero-curvature tunneling transmission coefficients [73] (ZCT), which are calculated considering that the tunneling trajectory of the particle follows the MEP. The ZCT transmission coefficients are 4.49 and 3.39 for R1 and R5, respectively, confirming a narrower MEP for R1. We note that the ZCT transmission coefficients are discussed here for illustrative purposes only, since it is well-known that they underestimate quantum effects. [81, 197]

If we were to consider only these two channels the transmission coefficient would be 10.1, but when all the 16 channels for reaction are included it has a value of 10.8. The two values are not very different, but the total contribution of those additional channels to the CVT/SCT thermal rate constant increases to 27% (7% due to tunneling plus 20% from the TST rate constants). This percentage is not negligible and it shows that is important to seek for transition states coming from highly energetic (low populated) reactive conformers. For instance, the

Figure 8.3: Arrhenius plot that compares experimental and CVT/SCT thermal rate constants in n-hexane for both Pre(d_0) and Pre(d_5).

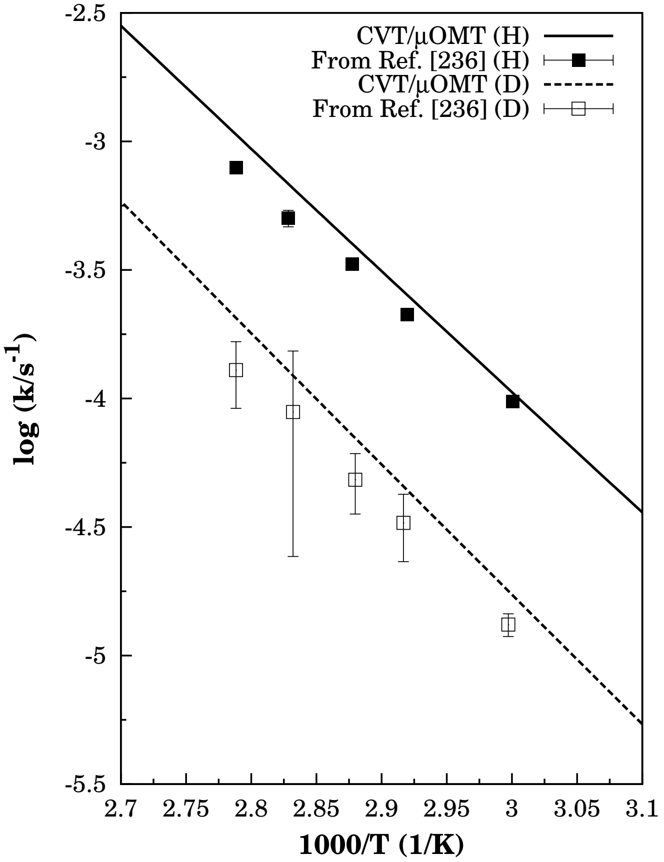

Table 8.4: Calculated and experimental thermal rate constants (in s^{-1}) for the [1,7] hydrogen shifts in Pre an in Tri. The deuterated derivatives have been isotopically substituted in the 9,14,19,19,19-positions in Pre, and in the 7-position in Tri

	Pre (T = 37°C)		Pre (T = 60°C)		Tri (T = 60°C)	
	H	D	H	D	H	D
Rate constant			Gas phase			
k^{TST}	1.18×10^{-6}	3.46×10^{-7}	1.87×10^{-5}	5.91×10^{-6}	1.02×10^{-5}	2.60×10^{-6}
k^{CVT}	1.18×10^{-6}	3.42×10^{-7}	1.85×10^{-5}	5.84×10^{-6}	1.00×10^{-5}	2.60×10^{-6}
$k^{\mathrm{CVT/SCT}}$	1.27×10^{-5}	1.67×10^{-6}	1.39×10^{-4}	2.21×10^{-5}	4.80×10^{-5}	8.72×10^{-6}
			Solution			
k^{TST}	9.09×10^{-7}	2.67×10^{-7}	1.44×10^{-5}	4.59×10^{-6}	1.10×10^{-5}	2.80×10^{-6}
k^{CVT}	9.00×10^{-7}	2.64×10^{-7}	1.42×10^{-5}	4.54×10^{-6}	1.08×10^{-5}	2.80×10^{-6}
$k^{\mathrm{CVT/SCT}}$	1.05×10^{-5}	1.27×10^{-6}	1.04×10^{-4}	1.69×10^{-5}	5.17×10^{-5}	9.37×10^{-6}
k_{exp}	$6.8\times10^{-6,a}$	—	$9.72(\pm 0.03)\times10^{-5,b}$ $6.76\times10^{-5,a}$	$1.32(\pm 0.034)\times10^{-5,b}$	$5.6\times10^{-5,c}$	$8.0\times10^{-6,c}$

[a] From Ref. [278]. From Ref. [236]. From Ref. [233]

Figure 8.4: Histogram plotting the SCT transmission coefficients of all the reactive channels at $T = 37°C$.

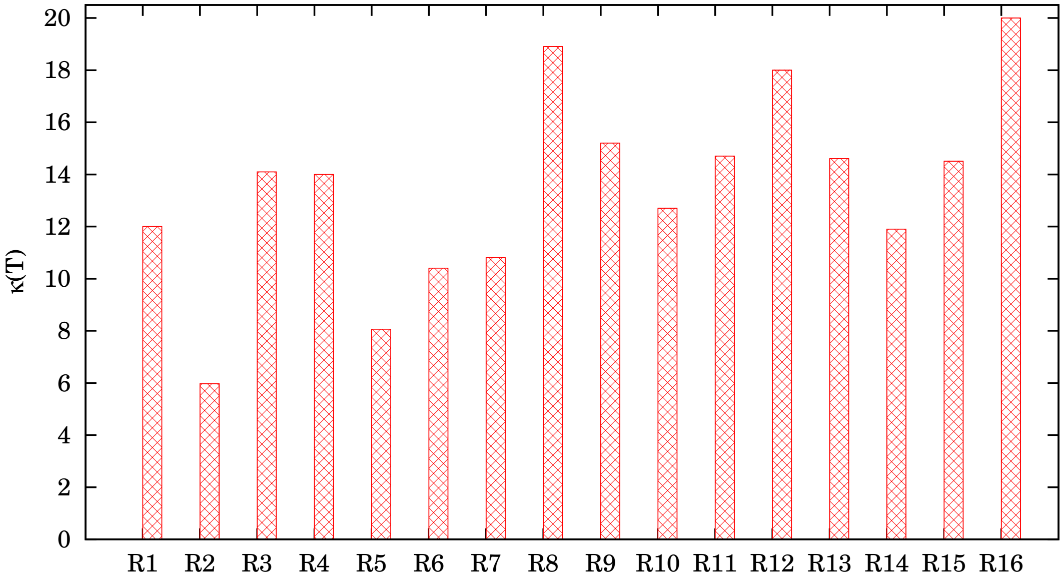

contribution of the $\text{Pre}_{a(-)}$(TB,TB) conformer to the total population of reactants is negligible, but this reactive channel contributes 4% to the total rate constant.

A comparison between Figure 8.4 and Table 8.2 shows that the transition states with a favorable conformation of the C ring, so the [1,7] hydrogen shift is aided (i.e., the antarafacial(+) attack for the HC conformation of the C ring, and the antarafacial(-) for the TB conformation of the C ring) have larger transmission coefficients, besides of having larger TST thermal rate constants. In n-hexane the antarafacial(+) attack contributes about 90%. This value is in agreement with experimental measurements of Sheves *et al.* [230] that showed that the antarafacial(+) attack is preferred, although our percentage is somewhat larger than the 67% predicted by those authors. Tian *et al.* [278] pointed out that a possible reason for the isomerization to be more than 10 times faster in the human skin than in n-hexane is, that within the amphipathic environment of the phospholipids, there would be a larger participation of the antarafacial(-) attack. We agree that this may be the case because anisotropic microenvironments as the skin may accommodate better some of the conformers of Pre and their corresponding transition states than isotropic environments (as n-hexane). Pre itself has some anisotropy with a hydrophilic hydroxyl group in the A ring when the rest of the molecule is hydrophobic, and if this additional stabilization favors some of the antarafacial(-) transition states the thermal rate constants would increase in value.

Further stabilization of those highly energetic antarafacial(-) reactants with the C ring in twisted-boat form would not modify the contribution of reactants to the final rate constants, since that is dominated by the half-chair conformations, which are 5 or more kcal/mol more stable than the twisted-boat conformations. However, it may involve a substantial increase of the contribution of the transition states. For instance, an additional stabilization of these reactants and transition states with respect to the antarafacial(+) stationary points by about 1.7 kcal/mol would increase the thermal rate constants by roughly a factor of 3. This is not the only possibility for increasing the thermal rate constants, since it may also happen that, in this environment, the most stable conformations of Pre would be less stabilized than the transition states. This may also happen in $\beta-$cyclodextrins, which catalyze the isomerization reaction becoming almost 5 times faster than in human skin at 37 °C. In this case the disappearance of the tZc conformers of Pre and the ZtE conformers of Vit due to steric hindrance would aid even more the reaction. This would lead to lower values of the equilibrium constants than in human skin, but to higher thermal rate constants, because in $\beta-$cyclodextrins the lowest conformations of Pre would be cZc, which are higher in energy than the tZc ones, so the barrier heights for reaction would decrease.

From the quassiclassical point of view, the [1,7] hydrogen shift reaction in n-hexane at 60 °C is 23% faster in Pre than in Tri, but this value increases to 50% when tunneling is included. The tunneling contribution is smaller in Tri than in Pre as a result of a wider MEP for the former compound. This difference can be illustrated as indicated earlier by looking at the magnitude of the ZCT transmission coefficients, which are 2.42 and 4.23 for Tri and Pre, respectively. It is also illustrative to note that for both Tri and Pre the energies that contribute the most to tunneling are very close to the top of the vibrationally adiabatic ground-state barrier, and in that region we expect the widthness of the MEP to be controlled by the normal mode with imaginary frequency at the transition state. Its magnitude accounts for the curvature at the top of the barrier, and in this case have values of $1315i$ cm^{-1} and $1420i$ cm^{-1} for the transition state of Tri and for $\mathrm{TS}_{\mathrm{a}(+)}$(HC,HC) of Pre, respectively.

Another important difference between Pre and Tri is that for the latter the two possible antarafacial attacks lead always to transition states that are enantiomers and, therefore, each of them contributes 50%. In Pre this percentage may fluctuate depending on the environment. Tri is a hydrophobic isotropic molecule and, therefore, the incorporation of a nonpolar isotropic organic solvent favors slightly the [1,7] hydrogen shift with respect to gas phase, although even in this case, the total thermal rate constants of the process are larger for the Pre system. On the other hand, we expect Tri to be much less efficient than Pre in anisotropic media, as for instance the human skin, since the latter would be able to interact with both the hydrophobic and hydrophilic parts of the lipids due to its amphipathic character.

8.3.5. Kinetic isotope effects

The evaluation of KIEs by theoretical methods allow the independent analysis of the quasiclassical and tunneling contributions to the final result. We use the notation

$$\eta(T) = \frac{k_{\mathrm{H}}^{\mathrm{CVT/SCT}}(T)}{k_{\mathrm{D}}^{\mathrm{CVT/SCT}}(T)} \tag{8.14}$$

where $\eta(T)$ is the total KIE and $k_{\mathrm{H}}^{\mathrm{CVT/SCT}}(T)$ and $k_{\mathrm{D}}^{\mathrm{CVT/SCT}}(T)$ are the isomerization thermal rate constants for the hydrogen and pentadeuterio compounds, respectively. The pentadeuterio derivative has been isotopically substituted in the 9,14,19,19,19-positions and, therefore, the total value of the KIE is a mixture of primary and secondary contributions, although the secondary KIE will be very close to unity. The total KIE is factorized into their quasiclassical, $\eta_{\mathrm{qc}}(T)$, and tunneling, $\eta_{\mathrm{tun}}(T)$, contribution are given by

$$\eta(T) = \eta_{\mathrm{tun}}(T)\eta_{\mathrm{qc}}(T) \tag{8.15}$$

where

$$\eta_{\text{tun}}(T) = \frac{\kappa_{\text{H}}^{\text{SCT}}(T)}{\kappa_{\text{D}}^{\text{SCT}}(T)} \tag{8.16}$$

and $\eta_{\text{qc}}(T)$ is given by

$$\eta_{\text{qc}}(T) = \eta_{\text{var}}(T)\eta^{\text{TST}}(T) \tag{8.17}$$

where $\eta_{\text{var}}(T)$ and $\eta^{\text{TST}}(T)$ are the variational and TST contributions to the KIE, respectively. The variational contribution is very close to unity (within a 1%), and therefore the quasiclassical contribution is that of the TST.

It is also interesting to analyze the contribution in percentage $\%\eta_i(T)$ of each of the individual reaction paths to the total KIE. It is given by:

$$\%\eta_i(T) = \frac{\%k_{i,\text{D}}}{\eta(T)} \times \eta_{i,\text{qc}}(T)\eta_{i,\text{tun}}(T) \tag{8.18}$$

where $\%k_{i,\text{D}}$ is the percentage contribution of each reaction path to the total thermal rate constant of the pentadeuterated compound, and $\eta_{i,\text{qc}}(T)$ and $\eta_{i,\text{tun}}(T)$ are the quasiclassical and tunneling contributions to the KIE of reaction path i, respectively. The contributions are divided in the same fashion as those for the total KIE. The derivation of Eq. (8.18) is given in the Appendix B.

The KIEs of each of the reaction paths (in n-hexane) with their contribution to the total KIE are plotted in Figure 8.5 at 37 °C. The gas-phase KIEs (not plotted) are quite similar to those in n-hexane but slightly larger, i.e. 7.62 versus 7.39. Even when the tunneling transmission coefficients in n-hexane are considered to be the same as in the gas phase the KIE decreases because the contribution of reaction R5, which has a low KIE due to tunneling, is higher in n-hexane than in gas-phase. A comparison between Figure 8.4 and Figure 8.5 shows that transmission coefficients and the KIEs change in the same fashion, because the quasiclassical contribution to the individual KIEs varies much more uniformly (from 3.01 for R2 to 3.57 for R16) than the tunneling contribution (from 1.53 for R2 to 3.44 for R16). As indicated in the percentages of Figure 8.5 the two reaction paths that contribute the most to the final KIE are R1 and R5 and the individual KIES are 7.50 and 6.17, respectively. The total KIE (7.18) is somewhat larger than the average of these two values (6.84) due to the contribution of the other reaction paths (mainly R13 and R16), that have larger tunneling contributions to the KIE than these two reaction paths. In general, environments like n-hexane, that stabilize reaction path R5, would lead to lower KIEs than environments that preferentially stabilize R1, R13 or R16. From these data we point out that a good low-limit for the total KIE for the isomerization reaction is the individual KIE of reaction R5.

The comparison between the KIEs for the [1,7] hydrogen shifts in Pre and Tri are interesting because there are experimental data for both systems at 60 °C in organic solvents. In the case of Pre the solvent was n-hexane and in the case of Tri the solvent was 2-methylpentane. Both solvents are very similar, so we use this value of the experimental KIE of Tri as if it were obtained in n-hexane. The experimental KIEs are 7.4 and 7.0 for Pre and Tri, respectively, whereas the theoretical calculations in n-hexane are 6.15 and 5.52, respectively. Both theoretical KIEs are underestimated by about a 20% when compared to the experimental values and it is probable that the discrepancy is due to the same source of error for both systems. Despite both systems have quite similar KIEs, the partial contributions to the total KIE are quite different. Thus, the quasiclassical and tunneling contributions are 3.14 and 1.96 in Pre and 3.93 and 1.40 in

Figure 8.5: Histogram plotting the quasiclassical, η_{qc}, and quantum, η_{qc}, contributions of each of the isomerization reaction paths of Pre to the total KIE at $T = 37°\mathrm{C}$. The contribution in percentage, $\%\eta_i$, of each of the paths to the final KIE is indicated next to the bars. The resulting quasiclassical, quantum and total KIEs are plotted in the last three rows.

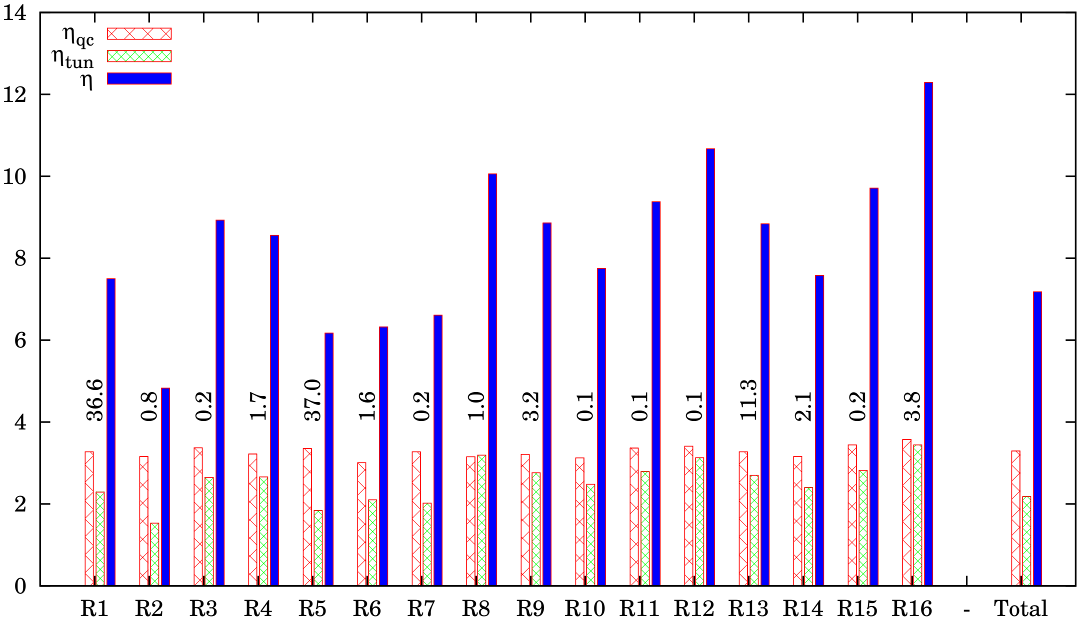

Tri, respectively, and therefore the quasiclassical contribution is larger in Tri, but the tunneling contribution is larger in Pre. In this case, the quasiclassical contribution to the KIE would be mainly due to vibration, so this contribution would be more important when the difference between the free energies of activation for the root and isotopically substituted species is large. As to the tunneling contribution to the KIE, it was expected to be larger for Pre than for Tri, because $\eta_{\mathrm{tun}}(T)$ increases when the tunneling transmission coefficients are larger.

Finally, we note that the R8, R12 and R16 reaction paths have large KIEs due to the tunneling contribution. Therefore, if in human skin the thermal rate constants are larger than in n-hexane due to an increase in the contribution of the antarafacial(-) attack, an experiment including measurements of the isotopically substituted Pre would display larger KIEs than those measured in n-hexane.

8.4. Concluding remarks

We have carried out an exhaustive variational transition state theory theoretical study using the CVT/SCT approach on the [1,7] hydrogen shift reaction (or isomerization reaction) of Pre in both gas-phase and n-hexane environments. The conformational analysis of the equilibrium structures led to a total of 35 conformers of Pre and to 24 conformers of Vit. Those structures were used to obtain the equilibrium constants, and we have obtained that the reaction is exoergic, in good agreement with experimental findings. From the energetics point of view, the configuration of the A and C rings is more relevant for the equilibrium structures than for the saddle points. In particular, due to the characteristics of the [1,7] hydrogen shift, the C ring regulates the antarafacial attack in the transition state structures. Thus, the antarafacial(+) attack is preferred when the C ring has half-chair configuration, whereas the antarafacial(-) attack is preferred when the C ring has twisted-boat configuration. In both gas-phase and n-hexane environments the reaction occurs about 90% through antarafacial(+) attack.

The great flexibility of the A and C rings led to sixteen reaction paths for isomerization and, although the contribution of the two of reaction paths obtained from the most stable configurations of Pre to the thermal rate constants and to the KIEs is substantial (about 70% at 37 °C), the contributions from some of the other reaction paths are relatively important and cannot be neglected. Besides, the contribution of these less important reaction paths increases the tunneling contribution as well as the KIE. The narrow energy window in which the transition states were located makes the hydrogen shift reaction quite sensitive to the environment, and we suggest that a further stabilization of some of the transition states may be the reason for the isomerization reaction to be faster in human skin (anisotropic environment) than in n-hexane (isotropic environment). In fact, both equilibrium and thermal rate constants reduce their value in the presence of n-hexane with respect to the gas-phase values. The comparison between Pre and Tri shows that, although the trienic system is identical for both systems, their dynamics is quite different. Tunneling is more important in Pre than in Tri and for the former, in both gas phase and n-hexane environments, there is preference for the antarafacial(+) attack; a preference that cannot exist in Tri.

Chapter 9

Conclusions

This Dissertation highlights that VTST/MT is a powerful tool for studying the dynamics of proton transfer reactions. In the present work, it has been successfully improved and applied to the study of different chemical reactions.

It describes how to calculate rotational symmetry numbers for various molecular configurations and how to apply them within the context of the transition state theory. Several examples have been included for calculating symmetry numbers for reaction rate constants that are both intuitive and nonintuitive. For most reactions, the overall symmetry number is given by the ratio of the reactant and transition state rotational symmetry numbers. Many of the typical problems that arise when using symmetry numbers have been highlighted. Even complicated scenarios are treated systematically by properly calculating rotational symmetry numbers and differentiating between distinguishable and indistinguishable reaction paths.

The least-action tunneling (LAT) approach for computing the transmission coefficient has been extended to polyatomic reactions. The new method is more complete than the simpler microcanonically optimized multidimensional tunneling (μOMT) approximation, and in the tests presented, the LAT method is slightly more accurate. The detailed analysis of kinetic isotope effects (KIE) of six hydrogen/deuterium/tritium abstraction reactions shows that the least-action transmission coefficient should be used instead of the more inexpensive, but probably less accurate, small-curvature transmission coefficient.

Two algorithms have been presented for efficient direct dynamics evaluation of the LAT transmission coefficients for polyatomic reactions: the interpolated least-action tunneling method based on one-dimensional interpolation algorithm (ILAT1D), and the double interpolated least-action tunneling algorithm (DILAT). The former employs one-dimensional interpolations of the effective potential along nonadiabatic portions of the tunneling paths, and the latter also makes use of those interpolations besides of the interpolations of the values of the action integrals at different tunneling energies. The ILAT1D algorithm is 5 to 10 times faster than the full calculation and the DILAT algorithm can be from 3 to 5 times faster than the ILAT1D algorithm, depending on the characteristics of the nonadiabatic region, but with an error of less than 5%.

High-level MC3BB direct-dynamics CVT/μOMT calculations in the temperatures interval 300-2500 K have been performed for the two competing hydrogen abstraction reactions R1 and R2 from methanol by atomic hydrogen. The results show that, with other factors being equal, multidimensional tunneling models provide both more reliable absolute thermal rate constants and kinetic isotope effects. It turns out that at high temperatures the anharmonicity of the torsional mode about the C–O bond plays an important role, because it leads to thermal rate constants that deviate substantially from those obtained by the harmonic oscillator approximation. On the other hand, these calculations and previous theoretical works clearly indicate that the activation energy for the overall hydrogen abstraction process increases substantially with temperature. Therefore, equations that include this dependency should be used (in detriment of the Arrhenius equation) for further studies involving these type of reactions. Reaction R1 dominates at all temperatures in the interval 300-2500 K, contributing 100% at room temperature and about 75% at $T = 2500$ K, so the branching ratio R1/R2 changes with temperature.

The dynamics of the [1,7] sigmatropic hydrogen shift in 7-methylocta-1,3(Z),5(Z)-triene, considered as a model system of previtamin D_3, has been studied by high-level direct-dynamics CVT/μOMT calculations at the MPWB1K/DIDZ level. All the conformations of 7-methylocta-1,3(Z),5(Z)-triene have being included in the theoretical treatment. The calculated thermal rate constants, the activation energies and primary KIEs are in reasonable agreement with the experimental data when quantum tunneling is taken into account. The CVT/μOMT calculations also indicate that it is important to consider the coupling between the reaction coordinate and the transverse modes to obtain KIEs comparable to the experimental values.

In this Dissertation it has been carried out an exhaustive variational transition state theory theoretical dynamics study of the [1,7] hydrogen shift reaction (or isomerization reaction) of previtamin D_3, in both gas-phase and n-hexane environments. The conformational analysis of the equilibrium structures led to a total of 35 conformers of previtamin D_3 and to 24 conformers of vitamin D_3. Those structures were used to obtain the equilibrium constants, and it has been found that the reaction is exoergic, in good agreement with experimental findings. From the energetics point of view, the configuration of the A and C rings is more relevant for the equilibrium structures than for the saddle points. In particular, due to the characteristics of the [1,7] hydrogen shift, the C ring regulates the antarafacial attack in the transition state structures. Thus, the antarafacial(+) attack is preferred when the C ring has half-chair configuration, whereas the antarafacial(-) attack is preferred when the C ring has twisted-boat configuration. In both gas-phase and n-hexane environments the reaction occurs about 90% through antarafacial(+) attack.

The great flexibility of the A and C rings led to sixteen reaction paths for isomerization and, although the contribution two of the reaction paths obtained from the most stable configurations of previtamin D_3 to the thermal rate constants and to the KIEs is substantial (about 70% at 37 °C), the contributions from some of the other reaction paths are relatively important and cannot be neglected. Besides, the contribution of these less important reaction paths increases the tunneling contribution as well as the KIE. The narrow energy window in which the transition states were located makes the hydrogen shift reaction quite sensitive to the environment, and it has been suggested that a further stabilization of some of the transition states could be the reason for the isomerization reaction to be faster in human skin (anisotropic environment) than in n-hexane (isotropic environment). In fact, both equilibrium and thermal rate constants reduce their value in the presence of n-hexane with respect to the gas-phase values. The comparison between previtamin D_3 and the 7-methylocta-1,3(Z),5(Z)-triene shows that, although the trienic system is identical for both systems, their dynamics is quite different. Tunneling is more important for previtamin D_3 than for the 7-methylocta-1,3(Z),5(Z)-triene. For the former compound, in both gas phase and n-hexane environments, there is a preference for the antarafacial(+) attack; a preference that cannot exist in the 7-methylocta-1,3(Z),5(Z)-triene.

Appendix A

Supporting information for Chapter 4

The ILAT1D algorithm has been tested against full-LAT calculations for the following reactions:

$$\mathrm{O} + \mathrm{HCl} \longrightarrow \mathrm{OH} + \mathrm{Cl} \tag{R1}$$

$$\mathrm{Cl} + \mathrm{HBr} \longrightarrow \mathrm{ClH} + \mathrm{Br} \tag{R2}$$

$$\mathrm{O} + \mathrm{CH_4} \longrightarrow \mathrm{OH} + \mathrm{CH_3} \tag{R3}$$

$$\mathrm{Cl} + \mathrm{CH_4} \longrightarrow \mathrm{ClH} + \mathrm{CH_3} \tag{R4}$$

$$\mathrm{OH} + \mathrm{CH_4} \longrightarrow \mathrm{H_2O} + \mathrm{CH_3} \tag{R5}$$

Table A.1: Number of single-point calculations (NSP) in the nonadiabatic region needed for the evaluation of the transmission coefficients by the full-LAT (taken as reference) and ILAT1D methods for reactions R1 to R5. The latter are given as function of N_S. $\bar{N}_\mathrm{II}$ is the number (on average) of single point calculations carried out in the nonadiabatic region for each tunneling path. The total number of points along each tunneling path is $N = 180$.

			N_S				
Reaction	$\bar{N}_\mathrm{II}$	reference	5	7	9	11	13
R1	42	36585	4336	6050	7740	9410	11043
R2	40	42838	5263	7331	9391	11431	13449
R3	63	153042	12075	16873	21647	26395	31121
R4	57	128089	11085	15450	19791	24101	28378
R5	31	27282	4071	5605	7115	8587	10026

Table A.2: Transmission coefficients, κ, evaluated at T = 200, 300 and 400 K by the full-LAT (taken as reference) and ILAT1D methods for reactions R1 to R5. The latter are given as function of N_{S}.

		N_{S}				
Reaction	reference	5	7	9	11	13
T = 200 K						
R1	56.02	56.08	56.08	56.07	56.03	56.07
R2	3.12	3.12	3.12	3.12	3.12	3.12
R3	117.4	118.6	119.0	118.9	117.7	118.8
R4	10.20	10.33	10.19	10.18	10.16	10.20
R5	16.44	16.46	16.45	16.45	16.44	16.45
T = 300 K						
R1	4.23	4.23	4.23	4.23	4.23	4.23
R2	1.62	1.62	1.62	1.62	1.62	1.62
R3	7.68	7.61	7.64	7.68	7.62	7.71
R4	3.66	3.69	3.66	3.66	3.65	3.66
R5	3.36	3.36	3.36	3.36	3.36	3.36
T = 400 K						
R1	2.11	2.11	2.11	2.11	2.11	2.11
R2	1.31	1.31	1.31	1.31	1.31	1.31
R3	3.02	2.99	2.99	3.00	2.99	3.02
R4	2.28	2.29	2.28	2.28	2.28	2.28
R5	1.96	1.96	1.96	1.96	1.96	1.96

The next figure plots the MUPEs in the calculation of the transmission coefficients by the ILAT1D algorithm for reactions R1 to R5 as a function of N_{S} in the temperatures interval 200–400 K with calculations of the transmission coefficients every 25 K.

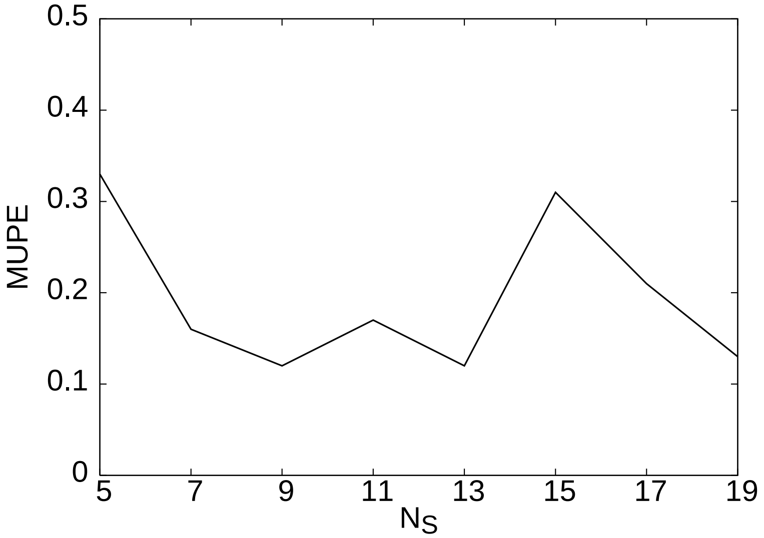

Appendix B

Supporting information for Chapter 8

B.1. Derivation of Equation (8.18)

The total KIE is given by:

$$\eta(T) = \frac{k_{\mathrm{H}}^{\mathrm{CVT/SCT}}(T)}{k_{\mathrm{D}}^{\mathrm{CVT/SCT}}(T)} = \frac{1}{k_{\mathrm{D}}^{\mathrm{CVT/SCT}}(T)} \sum_i W_i^{\mathrm{H}}(T) k_{i,\mathrm{H}}^{\mathrm{CVT/SCT}}(T) \tag{B.1}$$

The substitution of Eqs. (8.10) and Eq. (8.11) into Eq. (B.1) leads to:

$$\eta(T) = \frac{1}{k_{\mathrm{D}}^{\mathrm{CVT/SCT}}(T)} \sum_i \frac{\exp\left[-\beta \Delta G_{i,\mathrm{H}}^{\mathrm{R},0}(T)\right]}{N_{\mathrm{R}}^{\mathrm{H}}} \kappa_{i,\mathrm{H}}^{\mathrm{SCT}}(T) \Gamma_{i,\mathrm{H}}^{\mathrm{CVT}}(T) k_{i,\mathrm{H}}^{\mathrm{TST}}(T) \tag{B.2}$$

It should be noticed that

$$k_{i,\mathrm{H}}^{\mathrm{TST}}(T) = \frac{1}{\beta h} \exp\left\{-\beta \Delta G_{i,\mathrm{H}}^{\ddagger,0,*}(T)\right\} \tag{B.3}$$

and that

$$k_{i,\mathrm{H}}^{\mathrm{W,TST}}(T) = W_i^{\mathrm{H}}(T) k_{i,\mathrm{H}}^{\mathrm{TST}}(T) \tag{B.4}$$

where $\Delta G_{i,\mathrm{H}}^{\ddagger,0,*}(T)$ is the difference between the standard-state free energy at the transition state and that of the reactant of reaction path i, taking as reference the latter. Taking as reference the global minimum of the classical potential the standard-state free energy of activation is given by

$$\Delta G_{i,\mathrm{H}}^{\ddagger,0}(T) = \Delta G_{i,\mathrm{H}}^{\ddagger,0,*}(T) + \Delta G_{i,\mathrm{H}}^{\mathrm{R},0}(T) \tag{B.5}$$

Eq. (B.2) can be written as

$$\eta(T) = \frac{1}{k_{\mathrm{D}}^{\mathrm{CVT/SCT}}(T)} \sum_i \frac{1}{N_{\mathrm{R}}^{\mathrm{H}}} \kappa_{i,\mathrm{H}}^{\mathrm{SCT}}(T) \Gamma_{i,\mathrm{H}}^{\mathrm{CVT}}(T) k_{i,\mathrm{H}}^{\mathrm{W,TST}}(T) \tag{B.6}$$

Multiplying and dividing each term of the sum of Eq. (B.6) by $k_{i,\mathrm{D}}^{\mathrm{W,CVT/SCT}}(T) = W_i^{\mathrm{D}}(T) k_{i,\mathrm{D}}^{\mathrm{CVT/SCT}}(T)$ the following expression is obtained:

$$\eta(T) = \sum_i \frac{W_i^{\mathrm{D}}(T) k_{i,\mathrm{D}}^{\mathrm{CVT/SCT}}(T)}{k_{\mathrm{D}}^{\mathrm{CVT/SCT}}(T)} \frac{\kappa_{i,\mathrm{H}}^{\mathrm{SCT}}(T)}{\kappa_{i,\mathrm{D}}^{\mathrm{SCT}}(T)} \frac{\Gamma_{i,\mathrm{H}}^{\mathrm{CVT}}(T)}{\Gamma_{i,\mathrm{D}}^{\mathrm{CVT}}(T)} \frac{k_{i,\mathrm{H}}^{\mathrm{TST}}(T)}{k_{i,\mathrm{D}}^{\mathrm{TST}}(T)} \tag{B.7}$$

Now each of the contributions can be easily separated:

$$\eta_i^{\mathrm{W,TST}}(T) = \frac{k_{i,\mathrm{H}}^{\mathrm{W,TST}}(T)}{k_{i,\mathrm{D}}^{\mathrm{W,TST}}(T)} = \frac{N_{\mathrm{R}}^{\mathrm{D}}}{N_{\mathrm{R}}^{\mathrm{H}}} \exp\left\{-\beta[\Delta G_{i,\mathrm{H}}^{\ddagger,0}(T) - \Delta G_{i,\mathrm{D}}^{\ddagger,0}(T)]\right\} \tag{B.8}$$

$$\eta_{i,\mathrm{var}}(T) = \frac{\Gamma_{i,\mathrm{H}}^{\mathrm{CVT}}(T)}{\Gamma_{i,\mathrm{D}}^{\mathrm{CVT}}(T)} \tag{B.9}$$

$$\eta_{i,\mathrm{tun}}(T) = \frac{\kappa_{i,\mathrm{H}}^{\mathrm{SCT}}(T)}{\kappa_{i,\mathrm{D}}^{\mathrm{SCT}}(T)}, \tag{B.10}$$

and

$$P_{i,\mathrm{D}}^{\mathrm{CVT/SCT}}(T) = \frac{k_{i,\mathrm{D}}^{\mathrm{W,CVT/SCT}}(T)}{k_{\mathrm{D}}^{\mathrm{CVT/SCT}}(T)} \tag{B.11}$$

The quasiclassical contribution is

$$\eta_{i,\mathrm{qc}}(T) = \eta_i^{\mathrm{TST}}(T)\eta_{i,\mathrm{var}}^{\mathrm{CVT}}(T) \tag{B.12}$$

The total KIE can be expressed as:

$$\eta(T) = \sum_i P_{i,\mathrm{D}}^{\mathrm{CVT/SCT}}(T)\eta_{i,\mathrm{qc}}(T)\eta_{i,\mathrm{tun}}(T) \tag{B.13}$$

The contribution in percentage of each reaction path is given by Eq. (8.18) and it can be readily obtained by multiplying Eq. (B.13) by 100 and dividing it by $\eta(T)$, i.e.

$$\%\eta_i(T) = \frac{\%k_{i,\mathrm{D}}^{\mathrm{CVT/SCT}}(T)}{\eta(T)} \times \eta_{i,\mathrm{qc}}(T)\eta_{i,\mathrm{tun}}(T) \tag{B.14}$$

where

$$\%k_{i,\mathrm{D}}^{\mathrm{CVT/SCT}}(T) = P_{i,\mathrm{D}}^{\mathrm{CVT/SCT}}(T) \times 100 \tag{B.15}$$

B.2. Tables

Table B.1: Calculated properties (energies in kcal/mol and dihedral angles in degrees) of the stationary points for the isomerization reaction in gas-phase. The differences in the classical energy (ΔE), classical energy plus the zero-point energy (ΔE(ZPE)), and in the free energies ($\Delta G^o_{310\ \mathrm{K}}$.$\Delta G^o_{333\ \mathrm{K}}$) are relative to the Pre$_\mathrm{a}$(HC,HC)(+)tZ(-)c conformer. The difference in the classical energy ΔE(TS) is relative to the TS$_\mathrm{a}$(HC,HC)(+)cZ(+)c; $\omega^\ddagger$ (in cm^{-1} is the imaginary frequency at the transition state

Structure	Structure	ΔE	ΔE(ZPE)	ΔE(TS)	$\omega^\ddagger$	Φ_1	Φ_2	Φ_3	$\Delta G^o_{310\ \mathrm{K}}$	$\Delta G^o_{333\ \mathrm{K}}$
Pre$_{\mathrm{a}(+)}$(HC,HC)	Pre$_\mathrm{a}$(HC,HC)(+)cZ(+)c	3.25	3.42			73.3	-0.5	-11.7	2.83	2.78
	Pre$_\mathrm{a}$(HC,HC)(+)cZ(-)c	0.00	0.00			121.9	-7.2	-46.5	0.00	0.00
	Pre$_\mathrm{a}$(HC,HC)(+)tZ(-)c	1.43	1.39			-151.3	10.3	43.4	0.19	0.09
	Pre$_\mathrm{a}$(HC,HC)(-)tZ(+)c	5.01			21i	-147.4	4.1			
Pre$_{\mathrm{a}(-)}$(HC,HC)	Pre$_\mathrm{a}$(HC,HC)(-)cZ(-)c	1.48	1.83			-55.8	-2.4	-26.2	1.86	1.87
TS$_{\mathrm{a}(-)}$(HC,HC)	TS$_\mathrm{a}$(HC,HC)(-)cZ(-)c	29.61	27.32	1.64	1348i	-24.3	-20.5	-1.9	28.25	28.37
TS$_{\mathrm{a}(+)}$(HC,HC)	TS$_\mathrm{a}$(HC,HC)(+)cZ(+)c	27.97	25.42	0.00	1420i	21.6	22.2	3.7	26.38	26.50
Vit$_{\mathrm{a}(-)}$(T,CH)	Vit$_\mathrm{a}$(T,CH)Z(-)cE	5.91	6.38			-2.1	-57.0	0.4	6.70	6.74
Vit$_{\mathrm{a}(+)}$(CH,CH)	Vit$_\mathrm{a}$(CH,CH)Z(+)cE	1.83	2.24			-0.2	54.2	-0.5	2.32	2.34
	Vit$_\mathrm{a}$(CH,CH)Z(-)tE	-1.99	-1.21			1.4	-173.8	1.7	-1.78	-1.80
Pre$_{\mathrm{a}(+)}$(HC,TB)	Pre$_\mathrm{a}$(HC,TB)(+)cZ(+)c	6.02	6.16			59.5	2.1	50.7	5.25	5.18
	Pre$_\mathrm{a}$(HC,TB)(+)cZ(-)c	5.59	4.97			97.9	-5.1	-35.9	3.66	3.54
	Pre$_\mathrm{a}$(HC,TB)(+)tZ(-)c	5.77	6.06			130.5	-8.3	-22.4	5.38	5.33
	Pre$_\mathrm{a}$(HC,TB)(-)tZ(+)c	6.04	5.90			-152.8	10.7	43.5	3.67	3.48
Pre$_{\mathrm{a}(-)}$(HC,TB)	Pre$_\mathrm{a}$(HC,TB)(-)cZ(-)c	5.61	6.07			-61.0	-2.4	-7.5	5.90	5.89
TS$_{\mathrm{a}(-)}$(HC,TB)	TS$_\mathrm{a}$(HC,TB)(-)cZ(-)c	29.63	27.30	1.67	1426i	-26.6	-18.7	-0.9	28.36	28.49
TS$_{\mathrm{a}(+)}$(HC,TB)	TS$_\mathrm{a}$(HC,TB)(+)cZ(+)c	31.32	28.79	3.35	1421i	23.7	19.1	2.7	29.63	29.74
Vit$_{\mathrm{a}(-)}$(T,T)	Vit$_\mathrm{a}$(T,T)Z(-)cE	9.76	10.65			-4.9	-48.9	2.9	10.98	11.03
Vit$_{\mathrm{a}(+)}$(CH,T)	Vit$_\mathrm{a}$(CH,T)Z(+)cE	7.32	7.09			-0.2	68.0	-1.0	6.43	6.38
	Vit$_\mathrm{a}$(CH,T)Z(-)tE	1.70	2.34			1.0	-175.9	2.1	1.76	1.73

$\Phi_1 = \mathrm{C}_{10} - \mathrm{C}_5 - \mathrm{C}_6 - \mathrm{C}_7$, $\Phi_2 = \mathrm{C}_5 - \mathrm{C}_6 - \mathrm{C}_7 - \mathrm{C}_8$, $\Phi_3 = \mathrm{C}_6 - \mathrm{C}_7 - \mathrm{C}_8 - \mathrm{C}_9$.

Table B.1: (cont.)

Structure	Structure	ΔE	ΔE(ZPE)	ΔE(TS)	$\omega^{\ddagger}$	Φ_1	Φ_2	Φ_3	$\Delta G^o_{310\ \mathrm{K}}$	$\Delta G^o_{333\ \mathrm{K}}$
$\mathrm{Pre}_{\mathrm{e}(+)}$(HC,HC)	$\mathrm{Pre}_{\mathrm{e}}$(HC,HC)(+)cZ(+)c	1.73	1.92			53.2	2.3	44.7	1.80	1.79
	$\mathrm{Pre}_{\mathrm{e}}$(HC,HC)(+)cZ(-)c	3.52	3.33			90.0	-2.1	-37.2	2.36	2.27
	$\mathrm{Pre}_{\mathrm{e}}$(HC,HC)(+)tZ(-)c	2.06	1.84			152.7	-10.2	-42.1	0.67	0.56
	$\mathrm{Pre}_{\mathrm{e}}$(HC,HC)(-)tZ(+)c	1.72	1.32			-127.8	6.9	35.0	0.08	-0.03
$\mathrm{Pre}_{\mathrm{e}(-)}$(HC,HC)	$\mathrm{Pre}_{\mathrm{e}}$(HC,HC)(-)cZ(-)c	2.87	2.93			-59.1	-0.4	-20.0	2.54	2.51
$\mathrm{TS}_{\mathrm{e}(-)}$(HC,HC)	TS_{e}(HC,HC)(-)cZ(-)c	30.28	27.60	2.32	1373i	-23.2	-21.4	-1.9	28.39	28.48
$\mathrm{TS}_{\mathrm{e}(+)}$(HC,HC)	TS_{e}(HC,HC)(+)cZ(+)c	28.35	25.48	0.38	1401i	23.7	21.1	3.0	26.31	26.41
$\mathrm{Vit}_{\mathrm{e}(-)}$(CH,CH)	$\mathrm{Vit}_{\mathrm{e}}$(CH,CH)Z(-)cE	2.57	2.81			-2.8	-58.1	0.7	3.07	3.10
$\mathrm{Vit}_{\mathrm{e}(+)}$(T,CH)	$\mathrm{Vit}_{\mathrm{e}}$(T,CH)Z(+)cE	7.83	7.70			1.3	53.6	-0.9	7.16	7.12
	$\mathrm{Vit}_{\mathrm{e}}$(HC,CH)Z(-)tE	-0.94	-0.56			-2.6	172.7	-3.5	-1.35	-1.41
$\mathrm{Pre}_{\mathrm{e}(+)}$(HC,TB)	$\mathrm{Pre}_{\mathrm{e}}$(HC,TB)(+)cZ(+)c	6.85	6.83			59.4	1.8	10.5	6.30	6.25
	$\mathrm{Pre}_{\mathrm{e}}$(HC,TB)(+)cZ(-)c	7.37	7.11			81.8	-1.2	-28.4	6.39	6.32
	$\mathrm{Pre}_{\mathrm{e}}$(HC,TB)(+)tZ(-)c	6.79	5.90			133.0	-8.8	-27.3	4.89	4.75
	$\mathrm{Pre}_{\mathrm{e}}$(HC,TB)(-)tZ(+)c	6.17	6.32			-129.6	7.2	33.6	4.26	4.11
$\mathrm{Pre}_{\mathrm{e}(-)}$(HC,TB)	$\mathrm{Pre}_{\mathrm{e}}$(HC,TB)(-)cZ(-)c	6.99	7.10			-60.6	-3.1	-12.7	6.56	6.51
$\mathrm{TS}_{\mathrm{e}(-)}$(HC,TB)	TS_{e}(HC,TB)(-)cZ(-)c	30.47	28.07	2.50	1444i	-24.8	-19.7	-1.1	29.09	6.78
$\mathrm{TS}_{\mathrm{e}(+)}$(HC,TB)	TS_{e}(HC,TB)(+)cZ(+)c	31.60	29.07	3.63	1435i	24.6	18.9	2.9	29.89	11.90
$\mathrm{Vit}_{\mathrm{e}(-)}$(CH,T)	$\mathrm{Vit}_{\mathrm{e}}$(CH,T)Z(-)cE	6.20	6.67			-4.3	-51.8	2.5	6.76	29.21
$\mathrm{Vit}_{\mathrm{e}(+)}$(T,T)	$\mathrm{Vit}_{\mathrm{e}}$(T,T)Z(+)cE	13.41	13.21			0.4	65.7	-1.0	12.01	30.00
	$\mathrm{Vit}_{\mathrm{e}}$(T,T)Z(-)tE	2.67	2.93			-2.6	172.7	-2.2	2.14	2.08

Table B.1: (cont.)

Structure	Structure	ΔE	ΔE(ZPE)	ΔE(TS)	$\omega^{\ddagger}$	Φ_1	Φ_2	Φ_3	$\Delta G^{o}_{310\ \mathrm{K}}$	$\Delta G^{o}_{333\ \mathrm{K}}$
Pre$_{e(+)}$(TB,HC)	Pre$_{e}$(TB,HC)(+)cZ(+)c	6.64	6.37			51.4	3.9	43.4	5.14	5.03
	Pre$_{e}$(TB,HC)(+)cZ(-)c	6.64	6.14			127.7	-4.2	-41.2	4.38	4.23
	Pre$_{e}$(TB,HC)(+)tZ(-)c	5.74	5.12			145.7	-9.2	-39.6	2.91	2.71
	Pre$_{e}$(TB,HC)(-)tZ(+)c	9.79	9.86			-163.0	1.5	-85.9	9.41	9.36
Pre$_{e(-)}$(TB,HC)	Pre$_{e}$(TB,HC)(-)cZ(-)c	7.54	7.33			-51.1	-3.9	-24.9	6.22	6.12
TS $_{e(-)}$(TB,HC)	TS$_{e}$(TB,HC)(-)cZ(-)c	31.73	29.41	3.77	1423i	-21.5	-22.9	-2.8	30.38	30.50
TS$_{e(+)}$(TB,HC)	TS$_{e}$(TB,HC)(+)cZ(+)c	29.60	27.15	1.63	1459i	21.9	22.7	4.3	28.05	28.16
Vit$_{e(-)}$(T,CH)	Vit$_{e}$(T,CH)Z(-)cE	7.27	7.85			-2.8	-58.5	2.5	7.92	7.95
Vit$_{e(+)}$(T,CH)	Vit$_{e}$(T,CH)Z(+)cE	7.22	7.59			5.2	52.7	-2.3	7.29	7.28
	Vit$_{e}$(T,CH)Z(-)tE	3.41	3.38			7.2	-169.1	3.6	2.10	1.99
Pre$_{e(+)}$(TB,HB)	Pre$_{e}$(TB,TB)(+)cZ(+)c	11.42	10.52			50.9	3.9	46.7	7.73	7.49
	Pre$_{e}$(TB,TB)(+)cZ(-)c	13.06	12.27			83.8	-0.4	-34.1	9.69	9.46
	Pre$_{e}$(TB,TB)(+)tZ(-)c	10.82	10.20			143.9	-10.2	-25.9	7.72	7.50
	Pre$_{e}$(TB,TB)(-)tZ(+)c	10.05	9.77			-144.6	8.5	38.6	8.43	8.30
Pre$_{e(-)}$(TB,HB)	Pre$_{e}$(TB,TB)(-)cZ(-)c	11.61	11.72			-52.8	-6.1	-12.5	10.68	10.59
TS$_{e(-)}$(TB,HB)	TS$_{e}$(TB,TB)(-)cZ(-)c	32.02	29.32	4.05	1448i	-22.6	-21.4	-2.3	29.98	30.07
TS$_{e(+)}$(TB,HB)	TS$_{e}$(TB,TB)(+)cZ(+)c	33.10	30.39	5.13	1434i	23.6	20.1	3.6	30.85	30.92
Vit$_{e(-)}$(T,T)	Vit$_{e}$(T,T)Z(-)cE	10.42	10.61			-6.4	-55.1	3.9	9.98	9.94
Vit$_{e(+)}$(T,T)	Vit$_{e}$(T,T)Z(+)cE	12.40	12.37			3.9	63.1	-2.2	11.57	11.50
	Vit$_{e}$(T,T)Z(-)tE	7.09	7.10			6.6	-169.7	3.4	5.80	5.69

Table B.1: (cont.)

Structure	Structure	ΔE	ΔE(ZPE)	ΔE(TS)	$\omega^{\ddagger}$	Φ_1	Φ_2	Φ_3	$\Delta G^o_{310\text{ K}}$	$\Delta G^o_{333\text{ K}}$
Pre$_{\text{a}(+)}$(HB,HC)	Pre$_\text{a}$(TB,HC)(+)cZ(+)c									
	Pre$_\text{a}$(TB,HC)(+)cZ(-)c									
	Pre$_\text{a}$(TB,HC)(+)tZ(-)c									
	Pre$_\text{a}$(TB,HC)(-)tZ(+)c									
Pre$_{\text{a}(-)}$(HB,HC)	Pre$_\text{a}$(TB,HC)(-)cZ(-)c									
TS$_{\text{a}(-)}$(HB,HC)	TS$_\text{a}$(TB,HC)(-)cZ(-)c	29.46	27.10	1.49	$1429i$	-22.9	-21.9	-2.8	28.02	28.13
TS$_{\text{a}(+)}$(HB,HC)	TS$_\text{a}$(TB,HC)(+)cZ(+)c	28.60	26.22	0.63	$1438i$	19.9	23.1	4.3	27.22	27.35
Vit$_{\text{a}(-)}$(T,CH)	Vit$_\text{a}$(T,CH)Z(-)cE	5.55	6.23			-6.6	-55.7	2.2	6.40	6.44
Vit$_{\text{a}(+)}$(T,CH)	Vit$_\text{a}$(T,CH)Z(+)cE	5.77	5.85			1.9	55.5	-2.9	1.02	0.96
	Vit$_\text{a}$(T,CH)Z(-)tE	1.83	2.31			4.1	-168.8	3.3	5.38	5.32
Pre$_{\text{a}(+)}$(TB,TB)	Pre$_\text{a}$(TB,TB)(+)cZ(-)c	11.02	11.12			51.9	4.4	11.7	10.05	9.97
	Pre$_\text{a}$(TB,TB)(+)cZ(+)c	9.89	10.08			76.6	1.0	-27.7	9.62	9.59
	Pre$_\text{a}$(TB,TB)(+)tZ(-)c	10.57	10.49			165.1	-10.2	-32.8	9.21	9.10
	Pre$_\text{a}$(TB,TB)(-)tZ(+)c	8.66	8.41			-149.6	9.3	41.2	6.63	6.47
Pre$_{\text{a}(-)}$(TB,TB)	Pre$_\text{a}$(TB,TB)(-)cZ(-)c	10.01	10.03			-52.9	-6.3	-11.3	8.93	8.85
TS$_{\text{a}(-)}$(TB,TB)	TS$_\text{a}$(TB,TB)(-)cZ(-)c	11.89			$64i$	-56.8	-4.5	-1.8	28.00	28.12
TS$_{\text{a}(+)}$(TB,TB)	TS$_\text{a}$(TB,TB)(+)cZ(+)c	29.72	27.03	1.75	$1492i$	-24.7	-20.1	4.2	29.79	29.88
Vit$_{\text{a}(-)}$(T,T)	Vit$_\text{a}$(T,T)Z(-)cE	31.99	29.26	4.03	$1429i$	20.8	21.1	4.4	9.29	9.30
Vit$_{\text{a}(+)}$(T,T)	Vit$_\text{a}$(T,T)Z(+)cE	8.79	9.45			-9.9	-50.0	-2.6	10.51	10.49
	Vit$_\text{a}$(T,T)Z(-)tE	5.54	5.77			3.7	-169.5	4.44	4.44	4.34

Table B.2: Total rate constants of the isomerization reaction of Pre(d_0) and Pre(d_5) in gas-phase

T(K)	$k_{\text{tot}}^{\text{TST}}(T)$	$k_{\text{tot}}^{\text{VTST}}(T)$	$k_{\text{tot}}^{\mu\text{OMT}}(T)$	$k^{\text{exp}}(T)$
H				
298.00	2.34(-07)	2.32(-07)	3.18(-06)	
298.15	2.39(-07)	2.37(-07)	3.24(-06)	
300.00	3.09(-07)	3.06(-07)	4.02(-06)	
309.65	1.11(-06)	1.10(-06)	1.21(-05)	
310.15	1.19(-06)	1.18(-06)	1.27(-05)	
333.25	1.87(-05)	1.85(-05)	1.39(-04)	0.972(-04)±0.03
333.65	1.96(-05)	1.93(-05)	1.45(-04)	
342.50	5.08(-05)	5.02(-05)	3.34(-04)	2.12(-04)±0.08
342.85	5.27(-05)	5.21(-05)	3.45(-04)	
347.25	8.31(-05)	8.21(-05)	5.15(-04)	
347.50	8.52(-05)	8.42(-05)	5.27(-04)	3.34(-04)±0.17
348.20	9.15(-05)	9.04(-05)	5.61(-04)	
353.05	1.49(-04)	1.47(-04)	8.62(-04)	
353.55	1.56(-04)	1.54(-04)	9.00(-04)	5.02(-04)±0.37
351.50	1.28(-04)	1.26(-04)	7.52(-04)	
353.10	1.50(-04)	1.48(-04)	8.65(-04)	
358.65	2.56(-04)	2.53(-04)	1.40(-03)	7.91(-04)±0.33
368.20	6.24(-04)	6.16(-04)	3.08(-03)	
388.20	3.49(-03)	3.44(-03)	1.44(-02)	
400.00	8.88(-03)	8.75(-03)	3.33(-02)	
5D				
298.00	6.49(-08)	6.43(-08)	3.72(-07)	
298.15	6.63(-08)	6.57(-08)	3.79(-07)	
300.00	8.63(-08)	8.55(-08)	4.80(-07)	
309.65	3.23(-07)	3.20(-07)	1.58(-06)	
310.15	3.46(-07)	3.42(-07)	1.67(-06)	
333.25	5.91(-06)	5.84(-06)	2.21(-05)	
333.65	6.18(-06)	6.12(-06)	2.31(-05)	0.132(-04)±0.0134
342.50	1.65(-05)	1.63(-05)	5.68(-05)	
342.85	1.72(-05)	1.70(-05)	5.88(-05)	0.328(-04)±0.096
347.25	2.74(-05)	2.71(-05)	9.06(-05)	0.483(-04)±0.128
347.50	2.82(-05)	2.78(-05)	9.28(-05)	
348.20	3.03(-05)	3.00(-05)	9.93(-05)	
353.05	5.00(-05)	4.94(-05)	1.58(-04)	
353.55	5.26(-05)	5.20(-05)	1.65(-04)	
351.50	4.27(-05)	4.22(-05)	1.36(-04)	
353.10	5.03(-05)	4.97(-05)	1.58(-04)	0.886(-04)±0.643
358.65	8.76(-05)	8.66(-05)	2.65(-04)	1.29(-04)±0.374
368.20	2.19(-04)	2.17(-04)	6.19(-04)	
388.20	1.29(-03)	1.28(-03)	3.23(-03)	
400.00	3.38(-03)	3.34(-03)	7.96(-03)	

Table B.3: Calculated $\eta(T)$ and experimental $\eta_{\mathrm{exp}}(T)$ KIEs for the isomerization reaction of Pre in gas-phase

T(K)	$\eta(T)$	$\eta_{\mathrm{exp}}(T)$
298.00	8.55	
298.15	8.53	
300.00	8.38	
309.65	7.66	
310.15	7.62	
333.25	6.29	7.36
333.65	6.27	
342.50	5.88	6.46
342.85	5.87	
347.25	5.69	
347.50	5.68	6.92
348.20	5.65	
353.05	5.47	
353.55	5.45	5.67
351.50	5.53	
353.10	5.47	
358.65	5.27	6.13
368.20	4.97	
388.20	4.45	
400.00	4.19	

Table B.4: Equilibrium constants for isomerization reaction of Pre(d_0) in gas-phase

T(K)	$K_{\mathrm{eq}}(T)$	Exp.
298.00	8.38	
298.15	8.36	
300.00	8.15	
309.65	7.19	
310.15	7.14	
333.25	5.42	5.37
333.65	5.39	
342.50	4.89	4.53
342.85	4.87	
347.25	4.65	
347.50	4.64	4.17
348.20	4.60	
353.05	4.38	
353.55	4.35	3.82
351.50	4.45	3.51
353.10	4.37	
358.65	4.13	
368.20	3.77	
388.20	3.14	
400.00	2.84	

Table B.5: Equilibrium constants for isomerization reaction of Pre(d_5) in gas-phase

T(K)	$K_{\mathrm{eq}}(T)$	Exp.
298.00	9.47	
298.15	9.45	
300.00	9.22	
309.65	8.13	
310.15	8.08	
333.25	6.15	5.42
333.65	6.12	
342.50	5.56	4.66
342.85	5.54	
347.25	5.29	
347.50	5.28	4.36
348.20	5.24	
353.05	4.99	
353.55	4.96	3.99
351.50	5.07	3.72
353.10	4.98	
358.65	4.72	
368.20	4.31	
388.20	3.61	
400.00	3.27	

Table B.6: Calculated properties (energies in kcal/mol and dihedral angles in degrees) of the stationary points for the isomerization reaction in n-hexane. The differences in the classical energy (ΔE), classical energy plus the zero-point energy (ΔE(ZPE)), and in the free energies ($\Delta G^o_{310\text{ K}}.\Delta G^o_{333\text{ K}}$) are relative to the Pre_a(HC,HC)(+)tZ(-)c conformer. The difference in the classical energy ΔE(TS) is relative to the TS_a(HC,HC)(+)cZ(+)c; $\omega^\ddagger$ (in cm^{-1} is the imaginary frequency at the transition state

Structure	Structure	ΔE	ΔE(ZPE)	ΔE(TS)	$\omega^\ddagger$	Φ_1	Φ_2	Φ_3	$\Delta G^o_{310\text{ K}}$	$\Delta G^o_{333\text{ K}}$
$\text{Pre}_{\text{a}(+)}$(HC,HC)	Pre_a(HC,HC)(+)cZ(+)c	1.26	1.19			58.8	1.9	45.4	0.63	0.58
	Pre_a(HC,HC)(+)cZ(-)c	2.92	3.09			73.3	-0.5	-11.7	2.50	2.45
	Pre_a(HC,HC)(+)tZ(-)c	0.00	0.00			121.9	-7.2	-46.5	0.00	0.00
	Pre_a(HC,HC)(-)tZ(+)c	1.19	1.14			-151.3	10.3	43.4	-0.05	-0.15
$\text{Pre}_{\text{a}(-)}$(HC,HC)	Pre_a(HC,HC)(-)cZ(-)c	1.70	2.04			-55.8	-2.4	-26.2	2.07	2.08
$\text{TS}_{\text{a}(-)}$(HC,HC)	TS_a(HC,HC)(-)cZ(-)c	29.73	27.44	1.69	1348i	-24.3	-20.5	-1.9	28.38	28.50
$\text{TS}_{\text{a}(+)}$(HC,HC)	TS_a(HC,HC)(+)cZ(+)c	28.04	25.50	0.00	1420i	21.6	22.2	3.7	26.46	26.57
$\text{Vit}_{\text{a}(-)}$(T,CH)	Vit_a(T,CH)Z(-)cE	6.37	6.83			-2.1	-57.0	0.4	7.15	7.20
$\text{Vit}_{\text{a}(+)}$(CH,CH)	Vit_a(CH,CH)Z(+)cE	2.26	2.66			-0.2	54.2	-0.5	2.74	2.77
	Vit_a(CH,CH)Z(-)tE	-1.81	-1.03			1.4	-173.8	1.7	-1.60	-1.62
$\text{Pre}_{\text{a}(+)}$(HC,TB)	Pre_a(HC,TB)(+)cZ(+)c	6.04	6.18			59.5	2.1	50.7	5.26	5.19
	Pre_a(HC,TB)(+)cZ(-)c	5.34	4.72			97.9	-5.1	-35.9	3.41	3.29
	Pre_a(HC,TB)(+)tZ(-)c	5.61	5.90			130.5	-8.3	-22.4	5.22	5.17
	Pre_a(HC,TB)(-)tZ(+)c	5.81	5.67			-152.8	10.7	43.5	3.44	3.25
$\text{Pre}_{\text{a}(-)}$(HC,TB)	Pre_a(HC,TB)(-)cZ(-)c	5.75	6.21			-61.0	-2.4	-7.5	6.04	6.03
$\text{TS}_{\text{a}(-)}$(HC,TB)	TS_a(HC,TB)(-)cZ(-)c	29.73	27.40	1.69	1426i	-26.6	-18.7	-0.9	28.46	28.59
$\text{TS}_{\text{a}(+)}$(HC,TB)	TS_a(HC,TB)(+)cZ(+)c	31.39	28.85	3.34	1421i	23.7	19.1	2.7	29.70	29.80
$\text{Vit}_{\text{a}(-)}$(T,T)	Vit_a(T,T)Z(-)cE	9.96	10.86			-4.9	-48.9	2.9	11.18	11.23
$\text{Vit}_{\text{a}(+)}$(CH,T)	Vit_a(CH,T)Z(+)cE	7.77	7.54			-0.2	68.0	-1.0	6.88	6.83
	Vit_a(CH,T)Z(-)tE	1.84	2.47			1.0	-175.9	2.1	1.89	1.86

$\Phi_1 = \text{C}_{10} - \text{C}_5 - \text{C}_6 - \text{C}_7$, $\Phi_2 = \text{C}_5 - \text{C}_6 - \text{C}_7 - \text{C}_8$, $\Phi_3 = \text{C}_6 - \text{C}_7 - \text{C}_8 - \text{C}_9$.

Table B.6: (cont.)

Structure	Structure	ΔE	ΔE(ZPE)	ΔE(TS)	$\omega^{\ddagger}$	Φ_1	Φ_2	Φ_3	$\Delta G^o_{310\ \mathrm{K}}$	$\Delta G^o_{333\ \mathrm{K}}$
Pre$_{\mathrm{e}(+)}$(HC,HC)	Pre$_{\mathrm{e}}$(HC,HC)(+)cZ(+)c	1.70	1.90			53.2	2.3	44.7	1.77	1.76
	Pre$_{\mathrm{e}}$(HC,HC)(+)cZ(-)c	3.23	3.03			90.0	-2.1	-37.2	2.06	1.97
	Pre$_{\mathrm{e}}$(HC,HC)(+)tZ(-)c	1.87	1.65			152.7	-10.2	-42.1	0.48	0.37
	Pre$_{\mathrm{e}}$(HC,HC)(-)tZ(+)c	1.46	1.07			-127.8	6.9	35.0	-0.17	-0.29
Pre$_{\mathrm{e}(-)}$(HC,HC)	Pre$_{\mathrm{e}}$(HC,HC)(-)cZ(-)c	2.80	2.86			-59.1	-0.4	-20.0	2.47	2.44
TS$_{\mathrm{e}(-)}$(HC,HC)	TS$_{\mathrm{e}}$(HC,HC)(-)cZ(-)c	30.21	27.52	2.17	1373i	-23.2	-21.4	-1.9	28.31	28.40
TS$_{\mathrm{e}(+)}$(HC,HC)	TS$_{\mathrm{e}}$(HC,HC)(+)cZ(+)c	28.84	25.98	0.80	1401i	23.7	21.1	3.0	26.21	26.31
Vit$_{\mathrm{e}(-)}$(CH,CH)	Vit$_{\mathrm{e}}$(CH,CH)Z(-)cE	3.11	3.35			-2.8	-58.1	0.7	3.61	3.64
Vit$_{\mathrm{e}(+)}$(T,CH)	Vit$_{\mathrm{e}}$(T,CH)Z(+)cE	8.32	8.19			1.3	53.6	-0.9	7.65	7.61
	Vit$_{\mathrm{e}}$(HC,CH)Z(-)tE	-0.92	-0.54			-2.6	173.9	-3.5	-1.33	-1.39
Pre$_{\mathrm{e}(+)}$(HC,TB)	Pre$_{\mathrm{e}}$(HC,TB)(+)cZ(+)c	6.70	6.68			59.4	1.8	10.5	6.15	6.10
	Pre$_{\mathrm{e}}$(HC,TB)(+)cZ(-)c	7.21	6.95			81.8	-1.2	-28.4	6.23	6.15
	Pre$_{\mathrm{e}}$(HC,TB)(+)tZ(-)c	5.96	5.69			133.0	-8.8	-27.3	4.75	4.61
	Pre$_{\mathrm{e}}$(HC,TB)(-)tZ(+)c	6.65	6.18			-129.6	7.2	33.6	4.05	3.90
Pre$_{\mathrm{e}(-)}$(HC,TB)	Pre$_{\mathrm{e}}$(HC,TB)(-)cZ(-)c	6.91	7.02			-60.6	-3.1	-12.7	6.48	6.43
TS$_{\mathrm{e}(-)}$(HC,TB)	TS$_{\mathrm{e}}$(HC,TB)(-)cZ(-)c	30.36	27.97	2.32	1444i	-24.8	-19.7	-1.1	28.98	7.19
TS$_{\mathrm{e}(+)}$(HC,TB)	TS$_{\mathrm{e}}$(HC,TB)(+)cZ(+)c	31.48	28.94	3.43	1435i	24.6	18.9	2.9	29.77	12.33
Vit$_{\mathrm{e}(-)}$(CH,T)	Vit$_{\mathrm{e}}$(CH,T)Z(-)cE	6.61	7.08			-4.3	-51.8	2.5	7.17	29.10
Vit$_{\mathrm{e}(+)}$(T,T)	Vit$_{\mathrm{e}}$(T,T)Z(+)cE	13.83	13.64			0.4	65.7	-1.0	12.43	29.87
	Vit$_{\mathrm{e}}$(T,T)Z(-)tE	2.66	2.92			-2.6	172.7	-2.2	2.13	2.07

Table B.6: (cont.)

Structure	Structure	ΔE	ΔE(ZPE)	ΔE(TS)	$\omega^{\ddagger}$	Φ_1	Φ_2	Φ_3	$\Delta G^{o}_{310\ \mathrm{K}}$	$\Delta G^{o}_{333\ \mathrm{K}}$
$\mathrm{Pre}_{\mathrm{e}(+)}$(TB,HC)	$\mathrm{Pre}_{\mathrm{e}}$(TB,HC)(+)cZ(+)c	6.70	6.43			51.4	3.9	43.4	5.20	5.09
	$\mathrm{Pre}_{\mathrm{e}}$(TB,HC)(+)cZ(-)c	6.65	6.15			127.7	-4.2	-41.2	4.39	4.24
	$\mathrm{Pre}_{\mathrm{e}}$(TB,HC)(+)tZ(-)c	5.58	4.96			145.7	-9.2	-39.6	2.75	2.55
	$\mathrm{Pre}_{\mathrm{e}}$(TB,HC)(-)tZ(+)c	9.67	9.74			-163.0	1.5	-85.9	9.29	9.24
$\mathrm{Pre}_{\mathrm{e}(-)}$(TB,HC)	$\mathrm{Pre}_{\mathrm{e}}$(TB,HC)(-)cZ(-)c	7.59	7.38			-51.1	-3.9	-24.9	6.27	6.18
TS $_{\mathrm{e}(-)}$(TB,HC)	TS_{e}(TB,HC)(-)cZ(-)c	31.88	29.55	3.83	1423i	-21.5	-22.9	-2.8	30.52	30.64
$\mathrm{TS}_{\mathrm{e}(+)}$(TB,HC)	TS_{e}(TB,HC)(+)cZ(+)c	29.66	27.21	1.62	1459i	21.9	22.7	4.3	28.11	28.22
$\mathrm{Vit}_{\mathrm{e}(-)}$(T,CH)	$\mathrm{Vit}_{\mathrm{e}}$(T,CH)Z(-)cE	7.83	8.41			-2.8	-58.5	2.5	8.49	8.51
$\mathrm{Vit}_{\mathrm{e}(+)}$(T,CH)	$\mathrm{Vit}_{\mathrm{e}}$(T,CH)Z(+)cE	7.64	8.01			5.2	52.7	-2.3	7.71	7.69
	$\mathrm{Vit}_{\mathrm{e}}$(T,CH)Z(-)tE	3.38	3.35			7.2	-169.1	3.6	2.07	1.97
$\mathrm{Pre}_{\mathrm{e}(+)}$(TB,HB)	$\mathrm{Pre}_{\mathrm{e}}$(TB,TB)(+)cZ(+)c	11.60	10.71			50.9	3.9	46.7	7.92	7.67
	$\mathrm{Pre}_{\mathrm{e}}$(TB,TB)(+)cZ(-)c	12.92	12.12			83.8	-0.4	-34.1	9.54	9.31
	$\mathrm{Pre}_{\mathrm{e}}$(TB,TB)(+)tZ(-)c	10.61	9.99			143.9	-10.2	-25.9	7.51	7.29
	$\mathrm{Pre}_{\mathrm{e}}$(TB,TB)(-)tZ(+)c	10.05	9.76			-144.6	8.5	38.6	8.42	8.29
$\mathrm{Pre}_{\mathrm{e}(-)}$(TB,HB)	$\mathrm{Pre}_{\mathrm{e}}$(TB,TB)(-)cZ(-)c	11.62	11.73			-52.8	-6.1	-12.5	10.68	10.60
$\mathrm{TS}_{\mathrm{e}(-)}$(TB,HB)	TS_{e}(TB,TB)(-)cZ(-)c	32.13	29.43	4.08	1448i	-22.6	-21.4	-2.3	30.09	30.18
$\mathrm{TS}_{\mathrm{e}(+)}$(TB,HB)	TS_{e}(TB,TB)(+)cZ(+)c	33.14	30.44	5.10	1434i	23.6	20.1	3.6	30.89	30.96
$\mathrm{Vit}_{\mathrm{e}(-)}$(T,T)	$\mathrm{Vit}_{\mathrm{e}}$(T,T)Z(-)cE	10.96	11.15			-6.4	-55.1	3.9	10.52	10.48
$\mathrm{Vit}_{\mathrm{e}(+)}$(T,T)	$\mathrm{Vit}_{\mathrm{e}}$(T,T)Z(+)cE	12.80	12.77			3.9	63.1	-2.2	11.97	11.91
	$\mathrm{Vit}_{\mathrm{e}}$(T,T)Z(-)tE	7.06	7.07			6.6	-169.7	3.4	5.77	5.66

Table B.6: (cont.)

Structure	Structure	ΔE	ΔE(ZPE)	ΔE(TS)	$\omega^{\ddagger}$	Φ_1	Φ_2	Φ_3	$\Delta G^{o}_{310\ \mathrm{K}}$	$\Delta G^{o}_{333\ \mathrm{K}}$
Pre$_{\mathrm{a}(+)}$(HB,HC)	Pre$_{\mathrm{a}}$(TB,HC)(+)cZ(+)c									
	Pre$_{\mathrm{a}}$(TB,HC)(+)cZ(-)c									
	Pre$_{\mathrm{a}}$(TB,HC)(+)tZ(-)c									
	Pre$_{\mathrm{a}}$(TB,HC)(-)tZ(+)c									
Pre$_{\mathrm{a}(-)}$(HB,HC)	Pre$_{\mathrm{a}}$(TB,HC)(-)cZ(-)c									
TS$_{\mathrm{a}(-)}$(HB,HC)	TS$_{\mathrm{a}}$(TB,HC)(-)cZ(-)c	29.64	27.29	1.60	1429i	-22.9	-21.9	-2.8	28.20	28.32
TS$_{\mathrm{a}(+)}$(HB,HC)	TS$_{\mathrm{a}}$(TB,HC)(+)cZ(+)c	28.68	26.30	0.63	1438i	19.9	23.1	4.3	27.30	27.43
Vit$_{\mathrm{a}(-)}$(T,CH)	Vit$_{\mathrm{a}}$(T,CH)Z(-)cE	5.80	6.48			-6.6	-55.7	2.2	6.65	6.69
Vit$_{\mathrm{a}(+)}$(T,CH)	Vit$_{\mathrm{a}}$(T,CH)Z(+)cE	6.38	6.45			1.9	55.5	-2.9	1.25	1.19
	Vit$_{\mathrm{a}}$(T,CH)Z(-)tE	2.07	2.55			4.1	-168.8	3.3	5.98	5.93
Pre$_{\mathrm{a}(+)}$(TB,TB)	Pre$_{\mathrm{a}}$(TB,TB)(+)cZ(-)c	10.73	10.83			51.9	4.4	11.7	9.76	9.68
	Pre$_{\mathrm{a}}$(TB,TB)(+)cZ(+)c	9.33	9.51			76.6	1.0	-27.7	9.06	9.02
	Pre$_{\mathrm{a}}$(TB,TB)(+)tZ(-)c	10.57	10.49			165.1	-10.2	-32.8	9.22	9.10
	Pre$_{\mathrm{a}}$(TB,TB)(-)tZ(+)c	8.27	8.01			-149.6	9.3	41.2	6.23	6.07
Pre$_{\mathrm{a}(-)}$(TB,TB)	Pre$_{\mathrm{a}}$(TB,TB)(-)cZ(-)c	10.16	10.18			-52.9	-6.3	-11.3	9.08	9.00
TS$_{\mathrm{a}(-)}$(TB,TB)	TS$_{\mathrm{a}}$(TB,TB)(-)cZ(-)c	29.89	27.20	1.85	1492i	-24.7	-20.1	-1.8	28.17	28.29
TS$_{\mathrm{a}(+)}$(TB,TB)	TS$_{\mathrm{a}}$(TB,TB)(+)cZ(+)c	32.00	29.27	3.96	1429i	20.8	21.1	4.2	29.81	29.89
Vit$_{\mathrm{a}(-)}$(T,T)	Vit$_{\mathrm{a}}$(T,T)Z(-)cE	9.08	9.74			-9.9	-50.0	4.4	9.59	9.60
Vit$_{\mathrm{a}(+)}$(T,T)	Vit$_{\mathrm{a}}$(T,T)Z(+)cE	11.19	11.47			0.9	69.2	-2.6	11.11	11.10
	Vit$_{\mathrm{a}}$(T,T)Z(-)tE	5.76	6.00			3.7	-169.5	3.4	4.66	4.56

Table B.7: Total rate constants of the isomerization reaction of Pre(d_0) and Pre(d_5) in n-hexane

T(K)	$k_{\text{tot}}^{\text{TST}}(T)$	$k_{\text{tot}}^{\text{VTST}}(T)$	$k_{\text{tot}}^{\mu\text{OMT}}(T)$	$k^{\text{exp}}(T)$
			H	
298.00	1.79(-07)	1.77(-07)	2.34(-06)	
298.15	1.83(-07)	1.81(-07)	2.38(-06)	
300.00	2.36(-07)	2.33(-07)	2.96(-06)	
309.65	8.52(-07)	8.44(-07)	8.93(-06)	
310.15	9.09(-07)	9.00(-07)	9.44(-06)	
333.25	1.44(-05)	1.42(-05)	1.04(-04)	0.972(-04)±0.03
333.65	1.50(-05)	1.49(-05)	1.09(-04)	
342.50	3.92(-05)	3.87(-05)	2.52(-04)	2.12(-04)±0.08
342.85	4.06(-05)	4.02(-05)	2.60(-04)	
347.25	6.42(-05)	6.34(-05)	3.90(-04)	
347.50	6.58(-05)	6.50(-05)	3.99(-04)	3.34(-04)±0.17
348.20	7.07(-05)	6.99(-05)	4.25(-04)	
353.05	1.15(-04)	1.14(-04)	6.54(-04)	
353.55	1.21(-04)	1.19(-04)	6.83(-04)	5.02(-04)±0.37
351.50	9.86(-05)	9.74(-05)	5.70(-04)	
353.10	1.16(-04)	1.14(-04)	6.57(-04)	
358.65	1.99(-04)	1.96(-04)	1.06(-03)	7.91(-04)±0.33
368.20	4.85(-04)	4.79(-04)	2.35(-03)	
388.20	2.73(-03)	2.69(-03)	1.11(-02)	
400.00	6.97(-03)	6.87(-03)	2.59(-02)	
			5D	
298.00	5.01(-08)	4.97(-08)	2.83(-07)	
298.15	5.12(-08)	5.08(-08)	2.88(-07)	
300.00	6.67(-08)	6.60(-08)	3.65(-07)	
309.65	2.50(-07)	2.48(-07)	1.20(-06)	
310.15	2.67(-07)	2.65(-07)	1.28(-06)	
333.25	4.59(-06)	4.54(-06)	1.70(-05)	
333.65	4.80(-06)	4.75(-06)	1.78(-05)	0.132(-04)±0.0134
342.50	1.29(-05)	1.27(-05)	4.39(-05)	
342.85	1.34(-05)	1.32(-05)	4.55(-05)	0.328(-04)±0.096
347.25	2.14(-05)	2.11(-05)	7.01(-05)	0.483(-04)±0.128
347.50	2.20(-05)	2.17(-05)	7.18(-05)	
348.20	2.36(-05)	2.34(-05)	7.69(-05)	
353.05	3.90(-05)	3.86(-05)	1.22(-04)	
353.55	4.11(-05)	4.06(-05)	1.28(-04)	
351.50	3.33(-05)	3.29(-05)	1.06(-04)	
353.10	3.92(-05)	3.88(-05)	1.23(-04)	0.886(-04)±0.643
358.65	6.85(-05)	6.77(-05)	2.06(-04)	1.29(-04)±0.374
368.20	1.72(-04)	1.70(-04)	4.83(-04)	
388.20	1.02(-03)	1.01(-03)	2.54(-03)	
400.00	2.68(-03)	2.64(-03)	6.28(-03)	

Table B.8: Calculated $\eta(T)$ and experimental $\eta_{\mathrm{exp}}(T)$ KIEs for the isomerization reaction of Pre in n-hexane

T(K)	$\eta(T)$	$\eta_{\mathrm{exp}}(T)$
298.00	8.26	
298.15	8.24	
300.00	8.10	
309.65	7.42	
310.15	7.39	
333.25	6.13	7.36
333.65	6.12	
342.50	5.74	6.46
342.85	5.73	
347.25	5.56	
347.50	5.55	6.92
348.20	5.52	
353.05	5.35	5.67
353.55	5.33	
351.50	5.40	
353.10	5.35	6.13
358.65	5.16	
368.20	4.88	
388.20	4.37	
400.00	4.12	

Table B.9: Equilibrium constants for isomerization reaction of Pre(d_0) in n-hexane

T(K)	$K_{\mathrm{eq}}(T)$	Exp.
298.00	5.18	
298.15	5.17	
300.00	5.05	
309.65	4.51	
310.15	4.48	
333.25	3.49	5.37
333.65	3.48	
342.50	3.19	4.53
342.85	3.18	
347.25	3.04	
347.50	3.04	4.17
348.20	3.02	
353.05	2.88	
353.55	2.87	3.82
351.50	2.92	3.51
353.10	2.88	
358.65	2.74	
368.20	2.52	
388.20	2.14	
400.00	1.96	

Table B.10: Equilibrium constants for isomerization reaction of Pre(d_5) in n-hexane

T(K)	$K_{\mathrm{eq}}(T)$	Exp.
298.00	5.92	
298.15	5.91	
300.00	5.78	
309.65	5.15	
310.15	5.13	
333.25	4.00	5.42
333.65	3.98	
342.50	3.65	4.66
342.85	3.64	
347.25	3.49	
347.50	3.48	4.36
348.20	3.46	
353.05	3.31	
353.55	3.29	3.99
351.50	3.36	3.72
353.10	3.31	
358.65	3.15	
368.20	2.90	
388.20	2.47	
400.00	2.27	

Bibliography

[1] F. Louis, C. A. Gonzalez, R. E. Huie, and M. J. Kurylo, "An *ab-initio* study of the kinetics of the reactions of halomethanes with the hydroxyl radical. 2. A comparison between theoretical and experimental values of the kinetic parameters for 12 partially halogenated methanes", *J. Phys. Chem. A* **104**(38), p. 8773 (2000).

[2] N. L. Haworth, G. B. Bacskay, and J. C. Mackie, "The role of phosphorus dioxide in the H+ OH recombination reaction: *Ab-initio* quantum chemical computation of thermochemical and rate parameters", *J. Phys. Chem. A* **106**(8), p. 1533 (2002).

[3] K. Hiraoka, A. Wada, H. Kitagawa, M. Kamo, H. Unagiike, T. Ueno, T. Sugimoto, T. Enoura, N. Sogoshi, and S. Okazaki, "The reactions of H and D atoms with thin films of formaldehyde and methanol at cryogenic temperatures", *Astrophys. J.* **620**(1), p. 542 (2005).

[4] M. J. Knapp and J. P. Klinman, "Environmentally coupled hydrogen tunneling", *Eur. J. Biochem.* **269**(13), p. 3113 (2002).

[5] J. P. Klinman, "Linking protein structure and dynamics to catalysis: the role of hydrogen tunnelling", *Phil. Trans. R. Soc. B* **361**(1472), p. 1323 (2006).

[6] G. Chowdhury, V. Junnotula, J. S. Daniels, M. M. Greenberg, and K. S. Gates, "DNA strand damage product analysis provides evidence that the tumor cell-specific cytotoxin tirapazamine produces hydroxyl radical and acts as a surrogate for O_2", *J. Med. Chem* **15**(11), p. 1247 (1972).

[7] P. Navasumrit, T. H. Ward, N. J. F. Dodd, and P. J. O'Connor, "Ethanol-induced free radicals and hepatic DNA strand breaks are prevented in vivo by antioxidants: effects of acute and chronic ethanol exposure", *Carcinogenesis* **21**(1), p. 93 (2000).

[8] M.D. Le Page and B.R. James, "Nickel bromide as a hydrogen transfer catalyst", *Chemical Communications* **2000**(17), p. 1647 (2000).

[9] B. P. Roberts, "Polarity-reversal catalysis of hydrogen-atom abstraction reactions: concepts and applications in organic chemistry", *Chem. Soc. Rev.* **28**(1), p. 25 (1999).

[10] P. W. May, "CVD diamond: a new technology for the future?", *Endeavour* **19**(3), p. 101 (1995).

[11] B. Temelso, C. D. Sherrill, R. C. Merkle, and R. A. Freitas Jr., "High-level *ab initio* studies of hydrogen abstraction from prototype hydrocarbon systems", *J. Phys. Chem. A* **110**(38), p. 11160 (2006).

[12] H.D. Meyer, U. Manthe, and LS Cederbaum, "The multi-configurational time-dependent Hartree approach", *Chemical Physics Letters* **165**(1), p. 73 (1990).

[13] F. Huarte-Larrañaga and U. Manthe, "Thermal rate constants for polyatomic reactions: first principles quantum theory", *Z. Phys. Chem.* **221**(2), p. 171 (2007).

[14] M. Kryvohuz, "Semiclassical instanton approach to calculation of reaction rate constants in multidimensional chemical systems", *J. Chem. Phys.* **134**(7), p. 114103 (2011).

[15] W. H. Miller, "Semiclassical limit of quantum mechanical transition state theory for nonseparable systems", *J. Chem. Phys.* **62**(5), p. 1899 (1975).

[16] D. G. Truhlar, A. D. Isaacson, and B. C. Garrett, *Theory of chemical reaction dynamics* volume 4 , p. 65, CRC Boca Raton, FL (1985).

[17] A. Fernández-Ramos, A. Ellingson, B. C. Garrett, and D. G. Truhlar, *Variational transition state theory with multidimensional tunneling* volume 23 , p. 125, Wiley Online Library (2007).

[18] R. A. Marcus and M. E. Coltrin, "A new tunnneling path for reactions such as $H+H_2 \rightarrow H_2+H$", *J. Chem. Phys.* **67**(6), p. 2609 (1977).

[19] R. T. Skodje, D. G. Truhlar, and B. C. Garrett, "A general small-curvature approximation for transition-state-theory transmission coefficients", *J. Phys. Chem.* **85**(21), p. 3019 (1981).

[20] B. C. Garrett, T. Joseph, T. N. Truong, and D. G. Truhlar, "Application of the large-curvature tunneling approximation to polyatomic molecules: abstraction of H or D by methyl radical", *Chem. Phys.* **136**(2), p. 271 (1989).

[21] A. Fernández-Ramos and D. G. Truhlar, "Improved algorithm for corner-cutting tunneling calculations", *J. Chem. Phys.* **114**(4), p. 1491 (2001).

[22] A. Fernández-Ramos, D. G. Truhlar, J. C. Corchado, and J. Espinosa-Garcia, "Interpolated algorithm for large-curvature tunneling calculations of transmission coefficients for variational transition state theory calculations of reaction rates", *J. Phys. Chem. A* **106**(19), p. 4957 (2002).

[23] A. Fernández-Ramos and D. G. Truhlar, "A new algorithm for efficient direct dynamics calculations of large-curvature tunneling and its application to radical reactions with 9-15 atoms", *J. Chem. Theory Comput* **1**(6), p. 1063 (2005).

[24] Y.-P. Liu, D.-h. Lu, A. González-Lafont, D. G. Truhlar, and B. C. Garrett, "Direct dynamics calculation of the kinetic isotope effect for an organic hydrogen-transfer reaction, including corner-cutting tunneling in 21 dimensions", *J. Am. Chem. Soc.* **115**(17), p. 7806 (1993).

[25] B. C. Garrett and D. G. Truhlar, "A least-action variational method for calculating multidimensional tunneling probabilities for chemical reactions", *J. Chem. Phys.* **79**(10), p. 4931 (1983).

[26] H. Eyring, “The activated complex in chemical reactions”, *J. Chem. Phys.* **3**(2), p. 107 (1935).

[27] M. G. Evans and M. Polanyi, “Kinetic effects of pressure”, *Trans. Faraday Soc.* **31**, p. 875 (1935).

[28] D. G. Truhlar, A. D. Isaacson, and B. C. Garrett, “Generalized transition state theory”, *Theory of chemical reaction dynamics* **4**, p. 65 (1985).

[29] D. G. Truhlar, B. C. Garrett, and S. J. Klippenstein, “Current status of transition-state theory”, *J. Phys. Chem.* **100**(31), p. 12771 (1996).

[30] B. C. Garrett and D. G. Truhlar, “Encyclopedia of computational chemistry”, volume 5 , p. 3094. (1998).

[31] E. Pollak and P. Pechukas, “Symmetry numbers, not statistical factors, should be used in absolute rate theory and in Broensted relations”, *J. Am. Chem. Soc* **100**(10), p. 2984 (1978).

[32] D. R. Coulson, “Statistical factors in reaction rate theories”, *J. Am. Chem. Soc.* **100**(10), p. 2992 (1978).

[33] G. Herzberg and M. Structure, *Spectra of diatomic molecules 1*, Van Nostrand D (ed), Princeton, NJ (1950).

[34] D. A. McQuarrie, *Statistical Mechanics*, CA: University Science Books, Sausalito (2000).

[35] E. B. Wilson Jr, “The statistical weights of the rotational levels of polyatomic molecules, including methane, ammonia, benzene, cyclopropane and ethylene”, *J. Chem. Phys.* **3**(5), p. 276 (1935).

[36] P. R Bunker and P. Jensen, *Molecular Symmetry and Spectroscopy*, (1998).

[37] A. Chakraborty, D. G. Truhlar, J. M. Bowman, and S. Carter, “Calculation of converged rovibrational energies and partition function for methane using vibrational–rotational configuration interaction”, *J. Chem. Phys.* **121**(5), p. 2071 (2004).

[38] D. G. Truhlar, “Interpretation of ortho–para hydrogen conversion”, *J. Chem. Phys.* **65**(3), p. 1008 (1976).

[39] D. M. Dennison, “A note on the specific heat of the hydrogen molecule”, *P. Roy. Soc. Lond. A. Mat.* **115**(771), p. 483 (1927).

[40] G. C. Schatz and A. Kuppermann, “Quantum mechanical reactive scattering for three-dimensional atom plus diatom systems. II. Accurate cross sections for H+H_2”, *J. Chem. Phys.* **65**(11), p. 4668 (1976).

[41] D. G. Truhlar and J. Abdallah Jr, “New methods for calculating scattering cross sections for rearrangement collisions”, *Phys. Rev. A* **9**(1), p. 297 (1974).

[42] Y.-Y. Chuang, M. L. Radhakrishnan, P. L. Fast, C. J. Cramer, and D. G. Truhlar, “Direct dynamics for free radical kinetics in solution: Solvent effect on the rate constant for the reaction of methanol with atomic hydrogen”, *J. Phys. Chem. A* **103**(25), p. 4893 (1999).

[43] W. P. Hu, I. Rossi, J. C. Corchado, and D. G. Truhlar, "Molecular modeling of combustion kinetics. The abstraction of primary and secondary hydrogens by hydroxyl radical", *J. Phys. Chem. A* **101**(37), p. 6911 (1997).

[44] D. G. Truhlar, "A simple approximation for the vibrational partition function of a hindered internal rotation", *J. Comput. Chem.* **12**(2), p. 266 (1991).

[45] Y.-Y. Chuang and D. G. Truhlar, "Statistical thermodynamics of bond torsional modes", *J. Chem. Phys.* **112**(3), p. 1221 (2000).

[46] Y.-Y. Chuang and D. G. Truhlar, "Erratum: "Statistical thermodynamics of bond torsional modes (vol 112, pg 1221, 2000)", *J. Chem. Phys.* **121**(14), p. 7036(E) (2004).

[47] `http://www.en.wikipedia.org/wiki/Tartaric_acid`.

[48] `http://www.en.wikipedia.org/wiki/Diastereomer`.

[49] G. Gamow, "Quantum theory of atomic nucleus", *Z. Phys.* **51**, p. 204 (1928).

[50] C. Eckart, "The penetration of a potential barrier by electrons", *Phys. Rev.* **35**(11), p. 1303 (1930).

[51] H. S. Johnston, *Gas Phase Reaction Rate Theory*, Ronald Press New York (1966).

[52] E. Wigner, "On the penetration of potential barriers in chemical reactions", *Z. Phys. Chem. B* **19**, p. 203 (1932).

[53] R. P. Bell, "The Application of Quantum Mechanics to Chemical Kinetics", *Proc. Roy. Soc. A* **139**(838), p. 466 (1933).

[54] B. C. Garrett and D. G. Truhlar, "Generalized transition state theory calculations for the reactions D+H and H+D using an accurate potential energy surface: Explanation of the kinetic isotope effect", *J. Chem. Phys.* **72**(6), p. 3460 (1980).

[55] B. C. Garrett, D. G. Truhlar, J. M. Bowman, A. F. Wagner, D. Robie, S. Arepalli, N. Presser, and R. J. Gordon, "*Ab initio* predictions and experimental confirmation of large tunneling contributions to rate constants and kinetic isotope effects for hydrogen atom transfer reactions", *J. Am. Chem. Soc.* **108**(12), p. 3515 (1986).

[56] C. Alhambra, M. L. Sánchez, J. C. Corchado, J. Gao, and D. G. Truhlar, "Quantum mechanical tunneling in methylamine dehydrogenase)", *Chem. Phys. Lett.* **355**(3-4), p. 388 (2002).

[57] Z. D. Nagel and J. P. Klinman, "Tunneling and dynamics in enzymatic hydride transfer", *Chem. Rev.* **106**(8), p. 3095 (2006).

[58] A. Kohen and H. H. Limbach, editors, *Isotope effects in Chemistry and Biology*, CRC, Boca Raton, FL (2006).

[59] J. T. Hynes, R. L. Schowen, J. P. Klinman, and H. H. Limbach, editors, *Hydrogen-transfer reactions*, Wiley-VCH Weinheim (2007).

[60] D. G. Truhlar, J. Gao, M. Garcia-Viloca, C. Alhambra, J. Corchado, M. L. Sánchez, and T. D. Poulsen, "Ensemble-averaged variational transition state theory with optimized multidimensional tunneling for enzyme kinetics and other condensed-phase reactions", *Int. J. Quantum Chem.* **100**(6), p. 1136 (2004).

[61] J. Pu, J. Gao, and D. G. Truhlar, "Multidimensional tunneling, recrossing, and the transmission coefficient for enzymatic reactions", *Chem. Rev.* **106**(8), p. 3140 (2006).

[62] M Jordan and R. Gilbert, "Classical trajectory studies of the reaction CH_4+ H → CH_3+ H_2", *J. Chem. Phys.* **102**(14), p. 5669 (1995).

[63] E. Wigner, "Calculation of the rate of elementary association reactions", *J. Chem. Phys.* **5**(9), p. 720 (1937).

[64] J. Horiuti, "On the statistical mechanical treatment of the absolute rate of chemical reaction", *Bull. Chem. Soc. Jpn.* **13**(1), p. 210 (1938).

[65] J. C. Keck, "Variational theory of reaction rates", *Adv. Chem. Phys.* **13**, p. 85 (1967).

[66] B. C. Garrett and D. G. Truhlar, "Criterion of minimum state density in the transition state theory of bimolecular reactions", *J. Chem. Phys.* **70**(4), p. 1593 (1979).

[67] B. C. Garrett and D. G. Truhlar, "Variational transition-state theory", *Acc. Chem. Res.* **13**(4), p. 440 (1980).

[68] P. Pechukas, "Transition state theory", *Annu. Rev. Phys. Chem.* **32**(1), p. 159 (1981).

[69] D. G. Truhlar, W. L. Hase, and J. T. Hynes, "Current status of transition-state theory", *J. Phys. Chem.* **87**(15), p. 2664 (1983).

[70] D. G. Truhlar and B. C. Garrett, "Variational transition state theory", *Annu. Rev. Phys. Chem.* **35**(1), p. 159 (1984).

[71] S. C. Tucker and D. G. Truhlar, "Dynamical formulation of transition state theory: variational transition states and semiclassical tunneling", *NATO ASI Ser. C* **13**, p. 291 (1989).

[72] J. O. Hirschfelder and E. Wigner, "Some quantum-mechanical considerations in the theory of reactions involving an activation energy", *J. Chem. Phys.* **7**(8), p. 616 (1939).

[73] D. G. Truhlar and A. Kupperman, "Exact tunneling calculations", *J. Am. Chem. Soc.* **93**(8), p. 1840 (1971).

[74] A. Kuppermann, "An exact quantum mechanical transition state theory. 1. An overview", *J. Phys. Chem.* **83**(1), p. 171 (1979).

[75] B. C. Garrett, D. G. Truhlar, R. S. Grev, and A. W. Magnuson, "Improved treatment of threshold contributions in variational transition-state theory", *J. Chem. Phys.* **84**(13), p. 1730 (1980).

[76] K. Fukui, S. Kato, and H. Fujimoto, "Constituent analysis of the potential gradient along a reaction coordinate. Method and an application to methane + tritium reaction", *J. Am. Chem. Soc.* **97**(1), p. 1 (1975).

[77] B. C. Garrett and D. G. Truhlar, "Generalized transition state theory. Classical mechanical theory and applications to collinear reactions of hydrogen molecules", *J. Phys. Chem.* **83**(8), p. 1052 (1979).

[78] A. Fernández-Ramos, B. A. Ellingson, R. Meana-Pañeda, J. M. C. Marques, and D. G. Truhlar, "Symmetry numbers and chemical reaction rates", *Theor. Chem. Acc.* **118**(4), p. 813 (2007).

[79] B. A. Ellingson, B. J. Lynch, S. L. Mielke, and D. G. Truhlar, "Statistical thermodynamics of bond torsional modes: Tests of separable, almost-separable, and improved Pitzer–Gwinn approximations", *J. Chem. Phys.* **125**(8), p. 84305 (2006).

[80] Y. K. Sturdy and D. C. Clary, "Torsional anharmonicity in transition state calculations", *Phys. Chem. Chem. Phys.* **9**(19), p. 2397 (2007).

[81] D. G. Truhlar and A. Kuppermann, "Exact and approximate quantum mechanical reaction probabilities and rate constants for the collinear H+H reaction", *J. Chem. Phys.* **56**(5), p. 2232 (1972).

[82] T. C. Allison and D. G. Truhlar, *Modern Methods for Multidimensional Dynamics Computations in Chemistry* , p. 618, World Scientific Singapore (1998).

[83] R. E. Wyatt, "Quantum Mechanics of the H+H Reaction: Investigation of Vibrational Adiabatic Models", *J. Chem. Phys.* **51**(8), p. 3489 (1969).

[84] R. A. Marcus, "On the analytical mechanics of chemical reactions. Quantum mechanics of linear collisions", *J. Chem. Phys.* **45**(12), p. 4493 (1966).

[85] B. C. Garrett and D. G. Truhlar, "Reliable *ab-initio* calculation of a chemical reaction rate and a kinetic isotope effect: H+ H_2 and ^{2}H+ $^2H_22$", *Proc. Nat. Acad. Sci. USA* **76**(10), p. 4755 (1979).

[86] R. T. Skodje, D. G. Truhlar, and B. C. Garrett, "Vibrationally adiabatic models for reactive tunneling", *J. Chem. Phys.* **77**(12), p. 5955 (1982).

[87] D.-h. Lu, T. N. Truong, V. S. Melissas, G. C. Lynch, Y.-P. Liu, B. C. Garrett, R. Steckler, A. D. Isaacson, S. N. Rai, G. C. Hancock, J. G. Lauderdale, T. Joseph, and D. G. Truhlar, "Polyrate 4: A new version of a computer program for the calculation of chemical reaction rates for polyatomics", *Comput. Phys. Commun.* **71**(3), p. 235 (1992).

[88] Y.-P. Liu, G. C. Lynch, T. N. Truong, D.-h. Lu, and D. G. Truhlar, "Molecular modeling of the kinetic isotope effect for the [1,5]-sigmatropic rearrangement of cis-1,3-pentadiene", *J. Am. Chem. Soc.* **115**(6), p. 2408 (1993).

[89] V. K. Babamov and R. A. Marcus, "Dynamics of hydrogen atom and proton transfer reactions. Symmetric case", *J. Chem. Phys.* **74**(3), p. 1790 (1981).

[90] B. C. Garrett, D. G. Truhlar, A. F. Wagner, and T. H. Dunning Jr, "Variational transition state theory and tunneling for a heavy–light–heavy reaction using an *ab-initio* potential energy surface. ^{37}Cl+H(D)^{35}Cl → H(D)^{37}Cl + ^{35}Cl ", *J. Chem. Phys.* **78**(7), p. 4400 (1983).

[91] B. C. Garrett, N. Abusalbi, D. J. Kouri, and D. G. Truhlar, "Test of variational transition state theory and the least-action approximation for multidimensional tunneling probabilities against accurate quantal rate constants for a collinear reaction involving tunneling into an excited state", *J. Chem. Phys.* **83**(5), p. 2252 (1985).

[92] T. N. Truong, D.-h. Lu, G. C. Lynch, Y.-P. Liu, V. S. Melissas, J. J. P. Stewart, R. Steckler, B. C. Garrett, A. D. Isaacson, A. González-Lafont, S. N. Rai, G. C. Hancock, T. Joseph, and D. G. Truhlar, "MORATE: a program for direct dynamics calculations of chemical reaction rates by semiempirical molecular orbital theory", *Comput. Phys. Commun.* **75**(1-2), p. 143 (1993).

[93] W. H. Miller, B. A. Ruf, and Y. T. Chang, "A diabatic reaction path hamiltonian", *J. Chem. Phys.* **89**(10), p. 6298 (1988).

[94] B. A. Ruf and W. H. Miller, "A new (cartesian) reaction-path model for dynamics in polyatomic systems, with application to H-atom transfer in malonaldehyde", *J. Chem. Soc., Faraday Trans. 2* **84**(9), p. 1523 (1988).

[95] N. Makri and W. H. Miller, "A semiclassical tunneling model for use in classical trajectory simulations", *J. Chem. Phys.* **91**(7), p. 4026 (1989).

[96] M. M. Kreevoy, D. Ostovic, D. G. Truhlar, and B. C. Garrett, "Phenomenological manifestations of large-curvature tunneling in hydride transfer reactions", *J. Phys. Chem.* **90**(16), p. 3766 (1986).

[97] G. C. Lynch, D. G. Truhlar, and B. C. Garrett, "Test of the accuracy of small-curvature and minimum-energy reference paths for parametrizing the search for least-action tunneling paths:(H, D)+ H'Br→ (H,D)Br+ H' ", *J. Chem. Phys.* **90**(6), p. 3102 (1989).

[98] T. Taketsugu and K. Hirao, "A least-action variational method for determining tunneling paths in multidimensional system", *J. Chem. Phys.* **107**(24), p. 10506 (1997).

[99] C. S. Tautermann, A. F. Voegele, Loerting T., and K. R. Liedl, "The optimal tunneling path for proton transfer in malonaldehyde", *J. Chem. Phys.* **117**(5), p. 1962 (2002).

[100] C. S. Tautermann, A. F. Voegele, Loerting T., and K. R. Liedl, "An accurate semiclassical method to predict ground-state tunneling splittings", *J. Chem. Phys.* **117**(5), p. 1967 (2002).

[101] C. S. Tautermann, A. F. Voegele, and K. R. Liedl, "The ground-state tunneling splitting of various carboxylic acid dimers", *J. Chem. Phys.* **120**(2), p. 631 (2004).

[102] J. Zheng, S. Zhang, B. J. Lynch, J. C. Corchado, Y.-Y. Chuang, P. L. Fast, W.-P. Hu, Y.-P. Liu, G. C. Lynch, K. A. Nguyen, C. F. Jackels, A. Fernández Ramos, B. A. Ellingson, V. S. Melissas, J. Villa, I. Rossi, E. L. Coitiño, J. Pu, T. V. Albu, R. Steckler, B. C. Garrett, A. D. Isaacson, and D. G. Truhlar, "POLYRATE−version 2008, University of Minnesota, Minneapolis, (2009)".

[103] J. M. Bowman, D. Wang, X. Huang, F. Huarte-Larrañaga, and U Manthe, "The importance of an accurate CH_4 vibrational partition function in full dimensionality calculations of the H+ $CH_4 \rightarrow H_2+CH_3$ reaction ", *J. Chem. Phys.* **114**(21), p. 9683 (2001).

[104] F. Huarte-Larrañaga and U Manthe, "Vibrational excitation in the transition state: The $CH_4 + H \rightarrow CH_3 + H_2$ reaction rate constant in an extended temperature interval", *J. Chem. Phys.* **116**(7), p. 2863 (2002).

[105] J. C. Pu, J. Corchado and D. G. Truhlar, "Test of variational transition state theory with multidimensional tunneling contributions against an accurate full-dimensional rate constant calculation for a six-atom system", *J. Chem. Phys.* **115**(13), p. 6266 (2001).

[106] J. Pu and D. G. Truhlar, "Validation of variational transition state theory with multidimensional tunneling contributions against accurate quantum mechanical dynamics for $H+ CH_4 \rightarrow H_2+ CH_3$ in an extended temperature interval", *J. Chem. Phys.* **117**(4), p. 1479 (2002).

[107] J. A. Sansón, M. L. Sánchez, and J.C. Corchado, "Importance of anharmonicity, recrossing effects, and quantum mechanical tunneling in transition state theory with semiclassical tunneling. A test case: the H_2 + Cl hydrogen abstraction reaction ", *J. Phys. Chem. A* **110**(2), p. 589 (2005).

[108] S. Coleman, "Fate of the false vacuum: Semiclassical theory", *Phys. Rev. D* **15**(10), p. 2929 (1977).

[109] V.A. Benderskii, D. E. Makarov, and C. A. Wight, "Chemical dynamics at low temperatures", *Adv. Chem. Phys.* **88**, p. 1 (1994).

[110] Y. Zhao, T. Yamamoto, and W. H. Miller, "Path integral calculation of thermal rate constants within the quantum instanton approximation: Application to the $H + CH_4 \longrightarrow H_2 + CH_3$ hydrogen abstraction reaction in full Cartesian space", *J. Chem. Phys.* **120**(7), p. 3100 (2004).

[111] A. Fernández-Ramos, Z. Smedarchina, W. Siebrand, M. Z. Zgierski, and M. A. Rios, "Direct-Dynamics Approaches to Proton Tunneling Rate Constants. A Comparative Test for Molecular Inversions and an Application to 7-Azaindole Tautomerization", *J. Am. Chem. Soc.* **121**(26), p. 6280 (1999).

[112] T. Yamamoto, "Quantum statistical theory of the rate of exchange chemical reactions in the gas phase", *J. Chem. Phys.* **33**(1), p. 281 (1960).

[113] A. Kuppermann and E. F. Greene, "Chemical reaction cross sections and rate constants", *J. Chem. Educ.* **45**(6), p. 361 (1968).

[114] D. E. Manolopoulos and D. C. Clary, "Quantum calculations on reactive collisions", *Annu. Rep. Prog. Chem., Sect. C* **86**, p. 95 (1989).

[115] T. J. Park and J. C. Light, "Accurate qunatum thermal rate constants for the three-dimensional $H+H_2$ reaction", *J. Chem. Phys.* **91**(2), p. 974 (1989).

[116] D. G. Truhlar, D. W. Schwenke, and D. J. Kouri, "Quantum dynamics of chemical reactions by converged algebraic variational calculations", *J. Phys. Chem.* **94**(19), p. 7346 (1990).

[117] S. K. Gray, E. M. Goldfield, G. C. Schatz, and G. G. Balint-Kurti, "Helicity decoupled quantum dynamics and capture model cross sections and rate constants for $O(^1D)+H_2 \rightarrow OH+H$ ", *Phys. Chem. Chem. Phys.* **1**(6), p. 1141 (1999).

[118] S. L. Mielke, G. C. Lynch, D. G. Truhlar, and D. W. Schwenke, "*Ab-initio* chemical kinetics: Converged quantal reaction rate constants for the $D + H_2$ system", *J. Phys. Chem.* **98**(33), p. 8000 (1994).

[119] S. J. Mielke, D. W. Schwenke, B. C. Garrett, D. G. Truhlar, J. V. Michael, M.-C. Su, and Sutherland J. W., "$H+H_2$ thermal reaction: a convergence of theory and experiment", *Phys. Rev. Lett* **91**(6), p. 63201 (2003).

[120] N. Balucani, D. Skouteris, G. Capozza, E. Segoloni, P. Casavecchia, M. H. Alexander, G. Capecchi, and H.-J. Werner, "The dynamics of the prototype abstraction reaction $Cl(^2P_{3/2,1/2}) + H_2$: A comparison of crossed molecular beam experiments with exact quantum scattering calculations on coupled *ab-initio* potential energy surfaces", *Phys. Chem. Chem. Phys.* **6**(21), p. 5007 (2004).

[121] C. S. Ceotto, S. Yang, and W. H. Miller, "Quantum reaction rate from higher derivatives of the thermal flux-flux autocorrelation function at time zero", *J. Chem. Phys.* **122**(4), p. 044109 (2005).

[122] A. Chakraborty and D. G. Truhlar, "Quantum mechanical reaction rate constants by vibrational configuration interaction: The $OH + H_2 \longrightarrow H_2O + H$ reaction as a function of temperature", *Proc. Nat. Acad. Sci. USA* **102**(19), p. 6744 (2005).

[123] G. Nyman, R. van Harrevelt, and U. Manthe, "Thermochemistry and accurate quantum reaction rate calculations for $H_2/HD/D_2 + CH_3$", *J. Phys. Chem. A* **111**(41), p. 10331 (2007).

[124] G. Wentzel, "Eine verallgemeinerung der quantenbedingungen für die zwecke der wellenmechanik", *Z. Phys.* **38**(6), p. 518 (1926).

[125] H. A. Kramers, "Wave mechanics and half-integral quantisation", *Z. Phys.* **39**(10/11), p. 828 (1960).

[126] L. Brillouin, "The ondulatory mechanics of Schrodinger; A general method of resolution by successive approximations", *Comptes Rendus* **24**, p. 183 (1926).

[127] E. C. Kemble, *The Fundamental Principles of Quantum Mechanics with Elementary Applications*, Dover Publications New York (1937).

[128] B. C. Garrett, D. G. Truhlar, R. S. Grev, and A. W. Magnuson, "Improved treatment of threshold contributions in variational transition-state theory", *J. Phys. Chem.* **84**(13), p. 1730 (1980).

[129] C. S. Tautermann, A. F. Voegele, T. Loerting, and K. R. Liedl, "The optimal tunneling path for the proton transfer in malonaldehyde", *J. Chem. Phys.* **117**(5), p. 1962 (2002).

[130] T. Yamamoto and W. H. Miller, "Semiclassical calculation of thermal rate constants in full Cartesian space: The benchmark reaction $D + H_2 \rightarrow DH + H$", *J. Chem. Phys.* **118**(5), p. 2135 (2003).

[131] R. Meana-Pañeda, D. G. Truhlar, and A Fernández-Ramos, "Least-action transmission coefficient for polyatomic reactions", *J. Chem. Theory Comput.* **6**(1), p. 6 (2010).

[132] B. C. Garrett and D. G. Truhlar, *Theory and applications of computational chemistry: The first forty years* , p. 67, CRC Boca Raton, FL (2005).

[133] D. G. Truhlar and B. C. Garrett, *Hydrogen-Transfer Reactions, Vol. 2* , p. 833, Wiley-VCH Weinheim, Germany (2007).

[134] A. Fernández-Ramos, Z. Smedarchina, and J. Rodríguez-Otero, "Double proton transfer in the complex of acetic acid with methanol: theory versus experiment", *J. Chem. Phys.* **114**(4), p. 1567 (2001).

[135] D. G. Truhlar, F. B. Brown, R. Steckler, and A. D. Isaacson, *The Theory of Chemical Reaction Dynamics* , p. 285, D. Reidel Dordrecht, The Netherlands (1986).

[136] D. G. Truhlar and M. S. Gordon, "From force fields to dynamics: classical and quantal paths", *Science* **249**(4968), p. 491 (1990).

[137] A. González-Lafont, T. N. Truong, and D. G. Truhlar, "Direct dynamics calculations with NDDO (neglect of diatomic differential overlap) molecular orbital theory with specific reaction parameters", *J. Phys. Chem.* **95**(12), p. 4618 (1991).

[138] K. Allemann and N. S. Scrutton, editors, RSC Publishing Cambridge, UK (2009).

[139] R. J. Renka and A. K. Cline, "A triangle-based C^1 interpolation method", *Rocky Mountain J. Math.* **14**(1), p. 223 (1984).

[140] R. J. Renka, "Interpolatory tension splines with automatic selection of tension factors", *SIAM J. Sci. Stat. Comput.* **8**(3), p. 393 (1987).

[141] R. J. Renka, "Algorithm 716. TSPACK: Tension spline curve-fitting package", *ACM Trans. Math. Software* **19**(1), p. 81 (1993).

[142] W. H. Press, S. A. Teukolsky, W. T. Vetterling, and B. P. Flannery, Cambridge University Press Cambridge, UK (2007).

[143] T. N. Truong, D.-h. Lu, G. C. Lynch, Y.-P. Liu, V. S. Melissas, J. J. P. Stewart, R. Steckler, B. C. Garrett, A. D. Isaacson, A. González-Lafont, S. N. Rai, G. C. Hancock, T. Joseph, and D. G. Truhlar, "MORATE: A Program for Direct Dynamics Calculations of Chemical Reaction Rates by Semiempirical Molecular Orbital Theory", *Comput. Phys. Commun.* **75**, p. 143 (1993).

[144] Y. Zhao and D. G. Truhlar, "Hybrid meta density functional theory methods for thermochemistry, Thermochemical kinetics, and noncovalent interactions: The MPW1B95 and MPWB1K models and comparative assessments for hydrogen bonding and van der Waals interactions", *J. Phys. Chem A* **108**(33), p. 6908 (2004).

[145] W. J. Hehre, R. Ditchfield, and J. A. Pople, "Self—consistent molecular orbital methods. XII. Further extensions of Gaussian—type basis sets for use in molecular orbital studies of organic molecules", *J. Chem. Phys* **56**(5), p. 2257 (1972).

[146] T. E. Sharp and H. S. Johnston, "Hydrogen-deuterium kinetic isotope effect, an experimental and theoretical study over a wide range of temperature", *J. Chem. Phys.* **37**(7), p. 1541 (1962).

[147] H. Carmichael and H. S. Johnston, "Correlation of activation energies and bond energies in CF_3 reactions", *J. Chem. Phys.* **41**(7), p. 1975 (1964).

[148] R. A. Marcus, "Summarizing lecture: factors influencing enzymatic H-transfers, analysis of nuclear tunnelling isotope effects and thermodynamic versus specific effects", *Phil. Trans. R. Soc. Lond. B* **361**(1472), p. 1445 (2006).

[149] K. Y. Wong, J. P. Richard, and J. Gao, "Theoretical analysis of kinetic isotope effects on proton transfer reactions between substituted alpha-methoxystyrenes and substituted acetic acids", *J. Am. Chem. Soc.* **131**(39), p. 13963 (2009).

[150] Z. Smedarchina, Willem Siebrand, A. Fernández-Ramos, and Q. Cui, "Kinetic isotope effects for concerted multiple proton transfer: a direct dynamics study of an active-site model of carbonic anhidrase II", *J. Am. Chem. Soc.* **125**(1), p. 243 (2003).

[151] C. S. Tautermann, M. J. Loferer, A. F. Voegele, and K. R. Liedl, "Double hydrogen tunneling revisited: The breakdown of experimental tunneling criteria", *J. Chem. Phys.* **120**(24), p. 11650 (2004).

[152] Z. Smedarchina and W. Siebrand, "Generalized Swain–Schaad relations including tunneling and temperature dependence", *Chem. Phys. Lett.* **410**(4-6), p. 370 (2005).

[153] Y. Zhang and H. Lin, "Quantum tunneling in testosterone 6β-hydroxylation by cytochrome P450: Reaction dynamics calculations employing multiconfiguration molecular-mechanical potential energy surfaces", *J. Phys. Chem. A* **113**(43), p. 11501 (2009).

[154] A. Dybala-Defratyka, P. Paneth, R. Banerjee, and D. G. Truhlar, "Coupling of hydrogenic tunneling to active-site motion in the hydrogen radical transfer catalyzed by a coenzyme B_{12}-dependent mutase", *Proc. Nat. Acad. Sci. USA* **104**(26), p. 10774 (2007).

[155] Y. Kim, "Direct Dynamics Calculation for the Double Proton Transfer in Formic Acid Dimer", *J. Am. Chem. Soc.* **118**(6), p. 1522 (1996).

[156] Y. Kim, "Dynamics and kinetic isotope effect for the double proton transfer in formamidine monohydrated complex using direct semiempirical dynamics calculation", *J. Phys. Chem. A* **102**(18), p. 3025 (1998).

[157] T. Loerting, K. R. Liedl, and B. M. Rode, "Large curvature tunneling effects reveal concerted hydrogen exchange rates in cyclic hydrogen fluoride clusters comparable to carboxylic acid dimers", *J. Am. Chem. Soc.* **120**(2), p. 404 (1998).

[158] P. S. Zuev, R. S. Sheridan, T. V. Albu, D. G. Truhlar, D. A. Hrovat, and W. T. Borden, "Carbon tunneling from a single quantum state", *Science* **299**(5608), p. 867 (2003).

[159] A. Datta, D. A. Hrovat, and W. T. Borden, "Calculations predict rapid tunneling by carbon from the vibrational ground state in the ring opening of cyclopropylcarbinyl radical at cryogenic temperatures", *J. Am. Chem. Soc.* **130**(21), p. 6684 (2008).

[160] Y. Kim, A. V. Marenich, J. Zheng, K. H. Kim, M. Kołodziejska-Huben, M. Rostkowski, P. Paneth, and D. G. Truhlar, "Mechanistic analysis of the base-catalyzed HF elimination from 4-fluoro-4-(4-nitrophenyl) butane-2-one based on liquid-phase kinetic isotope effects calculated by dynamics modeling with multidimensional tunneling", *J. Chem. Theory Comput.* **5**(1), p. 59 (2008).

[161] I. Tejero, N. González-Garcia, A. González-Lafont, and J. M. Lluch, "Tunneling in green tea: understanding the antioxidant activity of catechol-containing compounds. A variational transition-state theory study", *J. Am. Chem. Soc.* **129**(18), p. 5846 (2007).

[162] L. Masgrau, K. E. Ranaghan, N. S. Scrutton, A. J. Mulholland, and M. J. Sutcliffe, "Tunneling and classical paths for proton transfer in an enzyme reaction dominated by tunneling: Oxidation of tryptamine by aromatic amine dehydrogenase", *J. Phys. Chem. B* **111**(11), p. 3032 (2007).

[163] D. N. Peles and J. D. Thoburn, "Multidimensional Tunneling in the [1, 5] Shift in (Z)-1, 3-Pentadiene: How Useful Are Swain- Schaad Exponents at Detecting Tunneling?", *J. Org. Chem.* **73**(8), p. 3135 (2008).

[164] A. Wu, E. A. Mader, A. Datta, D. A. Hrovat, W. T. Borden, and J. M. Mayer, "Nitroxyl radical plus hydroxylamine pseudo self-exchange reactions: Tunneling in hydrogen atom transfer", *J. Am. Chem. Soc.* **131**(33), p. 11985 (2009).

[165] C. K. Westbrook and F. L. Dryer, "Comprehensive mechanism for methanol oxidation", *Combust. Sci. Technol.* **20**(3), p. 125 (1979).

[166] J. Dove and J. Warnatz, "Calculation of burning velocity and flame structure in methanol–air mixtures", *Ber. Bunsenges. Phys. Chem.* **87**(11), p. 1040 (1983).

[167] J. Warnatz, *Combustion Chemistry* , p. 197, Springer-Verlag New York (1984).

[168] T. S. Norton and F. L. Dryer, "Toward a comprehensive mechanism for methanol pyrolysis", *Int. J. Chem. Kin.* **22**(3), p. 219 (1990).

[169] H. H. Grotheer, S. Kelm, H. S. T. Driver, R. J. Hutcheon, R. D. Lockett, and G. N. Robertson, "Elementary reactions in the methanol oxidation system. 1. Establishment of the mechanism and modeling of laminar burning velocities", *Ber. Bunsenges. Phys. Chem* **96**(10), p. 1360 (1992).

[170] B. Yang and K. Seshadri, "The asymptotic structure of methanol-air diffusion flames", *Combust. Sci. and Technol.* **97**(1), p. 193 (1994).

[171] T. J. Held and F. L. Dryer, "", *Symp. (Int.) Combust.* **25**, p. 901 (1994).

[172] T. J. Held and F. L. Dryer, "A comprehensive mechanism for methanol oxidation", *Int. J. Chem. Kin.* **30**(11), p. 805 (1998).

[173] K. Seshadri, "Multistep asymptotic analyses of flame structures", *Symp. (Int.) Combust.* **26**(1), p. 831 (1996).

[174] S. C. Li and F. A. Williams, "Experimental and numerical studies of two-stage methanol flames", *Symp. (Int.) Combust.* **26**(1), p. 1017 (1996).

[175] J. Li, Z. Zhao, A. Kazakov, M. Chaos, F.L. Dryer, and J. J. Scire Jr., “A comprehensive kinetic mechanism for CO, CH_2O, and CH_3OH combustion”, *Int. J. Chem. Kin.* **39**(3), p. 109 (2007).

[176] P. S. Veloo, Y. L. Wang, F. N. Egolfopoulos, and C. K. Westbrook, “A comparative experimental and computational study of methanol, ethanol, and n-butanol flames”, *Combust. Flame* **157**(10), p. 1989 (2010).

[177] R. T. Skodje, A. S. Tomlin, S. J. Klippenstein, L. B. Harding, and M. J. Davis, “Theoretical validation of chemiscal kinetic mechanisms: combustion of methanol”, *J. Phys. Chem. A* **114**(32), p. 8286 (2010).

[178] J. Vandooren and P. J. Van Tiggelen, “Experimental investigation of methanol oxidation in flames: Mechanisms and rate constants of elementary steps”, *Symp. (Int.) Combust.* **18**(1), p. 473 (1981).

[179] K. Spindler and H. G. Wagner, “Zum thermischen unimolekularen Zerfall von Methanol”, *Ber. Bunsenges. Phys. Chem.* **86**(6), p. 2 (1982).

[180] P. H. Cribb, J. E. Dove, and S. Yamazaki, “A kinetic study of the pyrolysis of methanol using shock tube and computer simulation techniques”, *Combust. Flame* **88**(2), p. 169 (1992).

[181] D. Aronowitz, D. W. Naegeli, and I. Glassman, “Kinetics of the pyrolysis of methanol”, *J. Phys. Chem.* **81**(25), p. 2555 (1977).

[182] K. Hoyermann, R. Sievert, and H. G. Wagner, “Mechanism of the reaction of H atoms with methanol”, *Ber. Bunsenges. Phys. Chem* **85**(2), p. 149 (1981).

[183] G. Lendvay, T. Bérces, and F. Márta, “An *ab initio* study of the three-channel reaction between methanol and hydrogen atoms: BAC-MP4 and Gaussian-2 calculations”, *J. Phys. Chem. A* **101**(8), p. 1588 (1997).

[184] W. K. Aders and H. G. Wagner, “Die reaktion von wasserstoffatomen mit methanol”, *Z. Phys. Chem* **74**, p. 224 (1971).

[185] J. F. Meagher, P. Kim, J. H. Lee, and R. B. Timmons, “Kinetic isotope effects in the reactions of hydrogen and deuterium atoms with dimethyl ether and methanol”, *J. Phys. Chem.* **78**(26), p. 2650 (1974).

[186] W. Tsang, “Chemical kinetic data base for combustion chemistry. Part 2. Methanol”, *J. Phys. Chem. Ref. Data* **16**(3), p. 471 (1987).

[187] D. L. Baulch, C. T. Bowman, C. J. Cobos, R. A. Cox, Th. Just, J. A. Kerr, M. J. Pilling, D. Stocker, J. Troe, W. Tsang, R. W. Walker, and J. Warnatz, “Evaluated kinetic data for combustion modeling: Supplement ii”, *J. Phys. Chem. Ref. Data* **34**(3), p. 757 (2005).

[188] P. Blowers, L. Ford, and R. Masel, “*Ab initio* calculations of the reactions of hydrogen with methanol: a comparison of the role of bond distorsion and Pauli repulsions on the intrinsic barriers for chemical reactions”, *J. Phys. Chem. A* **102**(46), p. 9267 (1998).

[189] T. Zhu, J. Li, D. A. Liotard, C. J. Cramer, and D. G. Truhlar, "Analytical energy gradients of a self-consistent reaction-field solvation model based on CM2 atomic charges", *J. Chem. Phys.* **110**(12), p. 5503 (1999).

[190] J. T. Jodkowski, M. T. Rayez, J. C. Rayez, T. Bérces, and S. Dobé, "Theoretical study of the kinetics of the hydrogen abstraction from methanol. 3. Reaction of methanol with hydrogen atom, methyl and hydroxyl radicals", *J. Phys. Chem. A* **103**(19), p. 3750 (1999).

[191] B. Kerkeni and D. C. Clary, "*Ab initio* rate constants from hyperspherical quantum scattering: Application to $H + C_2H_6$ and $H + CH_3OH$", *J. Chem. Phys.* **121**(14), p. 6809 (2004).

[192] B. Kerkeni and D. C. Clary, "Kinetic isotope effects in the reactions of D atoms with CH_4, C_2H_6, and CH_3OH: Quantum synamics calculations", *J. Phys. Chem. A* **108**(41), p. 8966 (2004).

[193] J. Pu and D. G. Truhlar, "Benchmark calculations of reaction energies, barrier heights, and transition-state geometries for hydrogen abstraction from methanol by a hydrogen atom", *J. Phys. Chem. A* **109**(5), p. 773 (2005).

[194] E. F. V. Carvalho, A. N. Barauna, F. B. C. Machado, and O. Roberto-Neto, "DFT study for the reactions of H atoms with CH_3OH and C_2H_5OH", *Int. J. Quantum Chem.* **108**(13), p. 2476 (2008).

[195] E. F. V. Carvalho, A. N. Barauna, F. B. C. Machado, and O. Roberto-Neto, "Theoretical calculations of energetics, structures, and rate constants for the $H + CH_3OH$ hydrogen abstraction reactions", *Chem. Phys. Lett.* **463**(1-3), p. 33 (2008).

[196] A. González-Lafont, T. N. Truong, and D. G. Truhlar, "Interpolated variational transition-state theory: practical methods for estimating variational transition-state properties and tunneling contributions to chemical reaction rates from electronic structure calculations ", *J. Chem. Phys.* **95**(12), p. 8875 (1991).

[197] A. Fernández-Ramos, J. Rodríguez-Otero, and M. A. Rios, "High level and dual level direct dynamics in the intramolecular proton transfer of hydrogenoxalate anion. Influence of tunneling and isotopic effect", *J. Phys. Chem. A* **102**(17), p. 2954 (1998).

[198] J. M. L. Martin and G. De Oliveira, "Towards standard methods for benchmark quality *ab initio* thermochemistry—W1 and W2 theory", *J. Chem. Phys.* **111**(5), p. 1843 (1999).

[199] A. D. Boese and J. M. L. Martin, "Development of density functionals for thermochemical kinetics", *J. Chem. Phys.* **121**(8), p. 3405 (2004).

[200] Y. Zhao, B. J. Lynch, and D. G. Truhlar, "Doubly hybrid meta DFT: New multi-coefficient correlation and density functional methods for thermochemistry and thermochemical kinetics", *J. Phys. Chem. A* **108**(21), p. 4786 (2004).

[201] J. Berkowitz, G. B. Ellison, and D. Gutman, "Three methods to measure RH bond energies", *J. Phys. Chem.* **98**(11), p. 2744. Enthalpies of formation of the hydroxymethyl,

methoxy and hydrogen atom radicals were taken from Table X. The Enthalpy of formation of methanol (–45.44 ± 0.14 kcal/mol) was obtained from the NIST website. (1994).

[202] Y. Kim, "Scaling all correlation energy in perturbation theory calculations of bond energies and barrier heights", *J. Am. Chem. Soc.* **108**(18), p. 5412 (1986).

[203] A. D. Becke, "Density-functional exchange-energy approximation with correct asymptotic behavior", *Phys. Rev. A* **38**(6), p. 3098 (1988).

[204] A. D. Becke, "Density-functional thermochemistry. IV. A new dynamical correlation functional and implications for exact-exchange mixing", *J. Chem. Phys.* **104**(3), p. 1040 (1996).

[205] Y. Zhao, B. J. Lynch, and D. G. Truhlar, "Development and assessment of a new hybrid density functional model for thermochemical kinetics", *J. Phys. Chem A* **108**(14), p. 2715 (2004).

[206] B. J. Lynch, Y. Zhao, and D.G. Truhlar, "Effectiveness of diffuse basis functions for calculating relative energies by density functional theory", *J. Phys. Chem. A* **107**(9), p. 1384 (2003).

[207] K. Fukui, "The path of chemical reactions-the IRC approach", *Acc. Chem. Research* **14**(12), p. 363 (1981).

[208] M. A. Eliason and J. O. Hirschfelder, "General collision theory treatment for the rate of bimolecular, gas-phase reactions", *J. Chem. Phys.* **30**(6), p. 1426 (1956).

[209] C. Steel and J. K. Laidler, "High frequency factors in unimolecular reactions", *J. Chem. Phys.* **34**(5), p. 1827 (1961).

[210] M. Page and J. W. McIver Jr, "On evaluating the reaction path Hamiltonian", *J. Chem. Phys.* **88**(2), p. 922 (1988).

[211] Y.-Y. Chuang and D. G. Truhlar, "Reaction-path dynamics in redundant internal coordiantes", *J. Phys. Chem. A* **102**(25), p. 242 (1998).

[212] M. J. Frisch, G. W. Trucks, H. B. Schlegel, G. E. Scuseria, M. A. Robb, J. R. Cheeseman, J. A. Montgomery Jr., T. Vreven, K. N. Kudin, J. C. Burant, J. M. Millam, S. S. Iyengar, J. Tomasi, V. Barone, B. Mennucci, M. Cossi, G. Scalmani, N. Rega, G. A. Petersson, H. Nakatsuji, M. Hada, M. Ehara, K. Toyota, R. Fukuda, J. Hasegawa, M. Ishida, T. Nakajima, Y. Honda, O. Kitao, H. Nakai, M. Klene, X. Li, J. E. Knox, H. P. Hratchian, J. B. Cross, C. Adamo, J. Jaramillo, R. Gomperts, R. E. Stratmann, O. Yazyev, A. J. Austin, R. Cammi, C. Pomelli, J. W. Ochterski, P. Y. Ayala, K. Morokuma, G. A. Voth, P. Salvador, J. J. Dannenberg, V. G. Zakrzewski, S. Dapprich, A. D. Daniels, M. C. Strain, O. Farkas, D. K. Malick, A. D. Rabuck, K. Raghavachari, J. B. Foresman, J. V. Ortiz, Q. Cui, A. G. Baboul, S. Clifford, J. Cioslowski, B. B. Stefanov, G. Liu, A. Liashenko, P. Piskorz, I. Komaromi, R. L. Martin, D. J. Fox, T. Keith, M. A. Al-Laham, C. Y. Peng, A. Nanayakkara, M. Challacombe, P. M. W. Gill, B. Johnson, W. Chen, M. W. Wong, C. Gonzalez, and J. A. Pople, "Gaussian03, Gaussian, Inc., Pittsburgh PA, (2003)".

[213] J. C. Corchado, Y.-Y. Chuang, P. L. Fast, W.-P. Hu, Y.-P. Liu, G. C. Lynch, K. A. Nguyen, C. F. Jackels, A. Fernández Ramos, B. A. Ellingson, B. J. Lynch, J. Zheng, V. S. Melissas, J. Villa, I. Rossi, E. L. Coitiño, J. Pu, T. V. Albu, R. Steckler, B. C. Garrett, A. D. Isaacson, and D. G. Truhlar, "POLYRATE−version 9.7, University of Minnesota, Minneapolis, (2007)".

[214] J. C. Corchado, Y.-Y. Chuang, E. L. Coitiño, Ellingson, J. Zheng, and D. G. Truhlar, "GAUSSRATE−version 9.7, University of Minnesota, Minneapolis, (2007)".

[215] D Lovy, WinDig version 2.5 is a free data digitizer for Windows. http://www.unige.ch/sciences/chifi/cpb/windig.html.

[216] K. S. Pitzer, "Energy levels and thermodynamic functions for molecules with internal rotation: II. Unsymmetrical tops attached to a rigid frame", *J. Chem. Phys.* **14**(4), p. 239 (1946).

[217] W. H. Gardiner Jr, "Temperature dependence of bimolecular reaction rates", *Acc. Chem. Res.* **10**, p. 326 (1977).

[218] N. C. Blais, D. G. Truhlar, and B. G. Garrett, "Dynamical calculation of the temperature dependence of the activation energy for a chemical reaction from 444 to 2400 K", *J. Chem. Phys.* **85**(9), p. 1094 (1981).

[219] N. C. Blais, D. G. Truhlar, and B. C. Garrett, "Temperature dependence of the activation energy: D+H", *J. Chem. Phys.* **76**(5), p. 2768 (1982).

[220] B. C. Garrett, D. G. Truhlar, J. M. Bowman, A. F. Wagner, D. Robie, S. Arepalli, N. Presser, and R. J. Gordon, "*Ab initio* predictions and experimental confirmation of large tunneling contributions to rate constants and kinetic isotope effects for hydrogen atom transfer reactions", *J. Am. Chem. Soc.* **108**(12), p. 3515 (1986).

[221] R. C. Tolman, "Statistical mechanics applied to chemical kinetics", *J. Am. Chem. Soc.* **42**(12), p. 2506 (1920).

[222] R. C. Tolman, Claredon Press Oxford, UK (1938).

[223] D. G. Truhlar, "Interpretation of the Activation Energy", *J. Chem. Ed.* **55**(5), p. 309 (1978).

[224] D. G. Truhlar and A. Kohen, "Convex arrhenius plots and their interpretation", *Proc. Nat. Acad. Sci. USA* **98**(3), p. 848 (2001).

[225] L. Masgrau, A. González-Lafont, and J. M. Lluch, "The curvature of the Arrhenius plots predicted by conventional canonical transition-state theory in the absence of tunneling", *Theor. Chem. Acc.* **110**(5), p. 352 (2003).

[226] J. Zheng and D. G. Truhlar, "Kinetics of hydrogen-transfer isomerizations of butoxyl radicals", *Phys. Chem. Chem. Phys.* **12**(28), p. 7782 (2010).

[227] M. F. Holick, "Vitamin D: A millenium perspective", *J. Cell. Biochem.* **88**(2), p. 296 (2003).

[228] X. Q. Tian and M. F. Holick, “A liposomal model that mimics the cutaneous production of vitamin D_3”, *J. Biol. Chem.* **274**(7), p. 4174 (1999).

[229] O. Dmitrenko, R. D. Bach, R. R. Sicinski, and W. Reischl, “Computational insight into the effect of C (19) substituents on [1, 7]-hydrogen shift in previtamin D”, *Theoretical Chemistry Accounts: Theory, Computation, and Modeling (Theoretica Chimica Acta)* **109**(4), p. 170 (2003).

[230] M. Sheves, E. Berman, Y. Mazur, and Z. V. I. Zaretskii, “Use of ^{2}H NMR and mass spectrometry for the investigation of the vitamin D_3-Previtamin D_3 equilibrium”, *J. Am. Chem. Soc.* **101**(7), p. 1882 (1979).

[231] C. Alhambra, J. C. Corchado, M. L. Sánchez, J. Gao, and D. G. Truhlar, “Quantum dynamics of hydride transfer in enzyme catalysis”, *J. Am. Chem. Soc* **122**(34), p. 8197 (2000).

[232] J. E. Baldwin and V. P. Reddy, “Kinetics and deuterium kinetic isotope effects for the thermal [1, 7] sigmatropic rearrangements of cis,cis-1,3,5-octatriene”, *J. Am. Chem. Soc.* **109**(26), p. 8051 (1987).

[233] J. E. Baldwin and P. Reddy, “Primary deuterium kinetic isotope effects for the thermal [1,7] sigmatropic rearrangement of 7-methylocta-1,3(Z),5(Z)-triene”, *J. Am. Chem. Soc.* **110**(24), p. 8223 (1988).

[234] F. Jensen, “A theoretical study of the allene effect in [1,n] sigmatropic hydrogen shifts”, *J. Am. Chem. Soc.* **117**(28), p. 7487 (1995).

[235] B. A. Hess Jr., “Computational support for tunneling in thermal [1,7]-hydrogen shift reactions”, *J. Org. Chem.* **66**(17), p. 5897 (2001).

[236] W. H. Okamura, H. Y. Elnagar, M. Ruther, and S. Dobreff, “Thermal [1,7]-sigmatropic shift of previtamin D_3 to vitamin D_3: Synthesis and study of the pentadeuterio derivatives”, *J. Org. Chem.* **58**(3), p. 600 (1993).

[237] Y. Zhao and D. G. Truhlar, “Hybrid meta density functional theory methods for thermochemistry, thermochemical kinetics, and noncovalent interactions: The MPW1B95 and MPWB1K models and comparative assessments for hydrogen bonding and van der Waals interactions”, *J. Phys. Chem. A* **108**(33), p. 6908 (2004).

[238] J. P. Perdew, *Unified theory of exchange and correlation beyond the local density approximation* volume 91 , p. 110, (1991).

[239] C. F. Jackels, Z. Gu, and D. G. Truhlar, “Reaction-path potential and vibrational frequencies in terms of curvilinear internal coordinates”, *J. Chem. Phys.* **102**(8), p. 3188 (1995).

[240] G. A. Natanson, B. C. Garrett, T. N. Truong, T. Joseph, and D. G. Truhlar, “The definition of reaction coordinates for reaction-path dynamics”, *J. Chem. Phys.* **94**(12), p. 7875 (1991).

[241] I. M. Alecu, J. Zheng, Y. Zhao, and D. G. Truhlar, "Computational thermochemistry: Scale factor databases and scale Factors for vibrational frequencies obtained from electronic model chemistries", *J. Chem. Theory Comput.* **6**(9), p. 2872 (2010).

[242] Bruce C. Garrett and D. G. Truhlar, "Generalized transition state theory. classical mechanical theory and applications to collinear reactions of hydrogen molecules", *J. Phys. Chem.* **83**(8), p. 1052 (1979).

[243] B. C. Garrett and D. G. Truhlar, "Correction generalized transition state theory. Classical mechanical theory and applications to collinear reactions of hydrogen molecules", *J. Phys. Chem.* **83**(23), p. 3058 (1979).

[244] D.-h. Lu, T. N. Truong, V. S. Melissas, G. C. Lynch, Y. P. Liu, B. C. Garrett, R. Steckler, A. D. Isaacson, S.N. Rai, G. C. Hancock, J. G. Lauderdale, T. Joseph, and D. G. Truhlar, "POLYRATE 4: A new version of a computer program for the calculation of chemical reaction rates for polyatomics", *Computer Physics Communications* **71**(3), p. 235 (1992).

[245] D. K. Bondi, J. N. L. Connor, B. C. Garrett, and D. G. Truhlar, "Test of variational transition state theory with a large-curvature tunneling approximation against accurate quantal reaction probabilities and rate coefficients for three collinear reactions with large reaction-path curvature: Cl + HCl, Cl + DCl, and Cl + MuCl", *J. Chem. Phys.* **78**(10), p. 5891 (1983).

[246] D. L. Thompson, *Modern methods for multidimensional dynamics computations in chemistry*, World Scientific Pub Co Inc (1998).

[247] G. H. Peslherbe and W. L. Hase, "A comparison of classical trajectory and statistical unimolecular rate theory calculations of Al decomposition", *J. Chem. Phys.* **101**(10), p. 8535 (1994).

[248] L. Vereecken and J. Peeters, "The 1,5-H-shift in 1-butoxy: A case study in the rigorous implementation of transition state theory for a multirotamer system", *J. Chem. Phys.* **119**(10), p. 5159 (2003).

[249] Y. Kim, D. G. Truhlar, and M. M. Kreevoy, "An experimentally based family of potential energy surfaces for hydride transfer between NAD^+ analogs", *J. Am. Chem. Soc.* **113**(21), p. 7837 (1991).

[250] M. F. Holick, *Vetebrate Endocrinology: Fundamentals and Biomedical Implications* , p. 7, Academic Press Orlando, FL (1989).

[251] E. Mellanby and M. D. Cantag, "Experimental investigation on rickets", *Lancet* **196**, p. 407 (1919).

[252] A. F. Hess, "The prevention and cure of rickets by sunlight", *Am. J. Public Health* **12**(2), p. 104 (1922).

[253] H. Goldblatt and K. N. Soames, "A study of rats on a normal diet irradiated daily by the mercury vapor quartz lamp or kept in darkness", *Biochem. J.* **17**(2), p. 294 (1923).

[254] E. V. McCollum, N. Simmonds, J. E. Becker, and P. G. Shipley, "Studies on experimental rickets. XXI. An experimental demostration of the existence of a vitamin that promotes calcium deposition", *J. Biol. Chem.* **53**, p. 293 (1922).

[255] L. Rosenfeld, "Vitamine–vitamin. The early years of discovery", *Clin. Chem.* **43**(4), p. 680 (1997).

[256] M. F. Holick, T. C. Chen, Z. Lu, and E. Sauter, "Vitamin D and skin physiology: A D-lightful story", *J. Bone Miner. Res.* **22**(S2), p. V28 (2007).

[257] H. F. Deluca, *Vitamin D* volume 1 , p. 3, Elsevier, Inc. Amsterdam, The Netherlands (2005).

[258] H. J. C. Jacobs and E. Havinga, *Photochemistry of vitamin D and its isomers and of simple trienes* , p. 305–373, John Wiley & Sons, Inc. (2007).

[259] M. F. Holick, *Vitamin D* volume 1 , p. 37, Elsevier, Inc. Amsterdam, The Netherlands (2005).

[260] W. G. Dauben and D. J. H. Funhoff, "NMR spectroscopic investigation of previtamin D_3: Total assignment of chemical shifts and conformational studies", *J. Org. Chem.* **53**(22), p. 5376 (1988).

[261] W. G. Dauben and D. J. H. Funhoff, "Theoretical evaluation of the conformation of previtamin D_3", *J. Org. Chem.* **53**(21), p. 5370 (1988).

[262] O. Dmitrenko, J. H. Frederick, and W. Reischl, "Previtamin D conformations and the wavelength-dependent photoconversions of previtamin D", *J. Photoch. Photobio. A* **139**(2-3), p. 125 (2001).

[263] J. L. M. A. Schlatmann, J. Pot, and E. Havinga, "Studies on vitamin D and related compounds. XVIII. An investigation into the interconversion of precalciferol and calciferol and of analogous compounds", *Recl. Trav. Chim. Pays-Bas.* **83**(11), p. 1173 (1964).

[264] C. A. Hoeger and W. H. Okamura, "On the antarafacial stereochemistry of the thermal [1,7]-sigmatropic hydrogen shift", *J. Am. Chem. Soc.* **107**(1), p. 268 (1985).

[265] C. A. Hoeger, A. D. Johnston, and W. H. Okamura, "Thermal [1,7]-sigmatropic hydrogen shifts: Stereochemistry kinetics, isotope effects and π-facial selectivity", *J. Am. Chem. Soc.* **109**(15), p. 4690 (1987).

[266] W. Klyne and V. Prelog, "Description of steric relationships across single bonds", *Experientia* **16**, p. 521 (1960).

[267] S. H. Mousavipour, A. Fernández-Ramos, R. Meana-Pañeda, E. Martínez-Núñez, S. Vázquez, and M. A. Ríos, "Direct-dynamics VTST study of the [1,7] hydrogen shift in 7-methylocta-1,3(Z),5(Z)-triene. A model systm for the hydrogen transfer reaction in previtamin D_3", *J. Phys. Chem. A* **111**(4), p. 719 (2007).

[268] J. C. Corchado, E. L. Coitiño, Y.-Y. Chuang, P. L. Fast, and D. G. Truhlar, "Interpolated variational transition-state theory by mapping", *J. Phys. Chem. A* **102**(14), p. 2424 (1998).

[269] Y.-Y. Chuang, C. J. Cramer, and D. G. Truhlar, “The interface of electronic structure and dynamics for reactions in solution”, *Int. J. Quantum Chem.* **70**(4-5), p. 887 (1998).

[270] J. D. Thompson, C. J. Cramer, and D. G. Truhlar, “New universal solvation model and comparison of the accuracy of the SM5.42R, SM5.43R, C-PCM, D-PCM, and IEF-PCM continuum solvation models for aqueous and organic solvation free energies and for vapor pressures”, *J. Phys. Chem. A* **108**(31), p. 6532 (2004).

[271] B. J. Lynch, P. L. Fast, M. Harris, and D. G. Truhlar, “Adiabatic connection for kinetics”, *J. Phys. Chem A* **104**(21), p. 4811 (2000).

[272] Y.-Y. Chuang, J. C. Corchado, and D. G. Truhlar, “Mapped interpolation scheme for single-point energy corrections in reaction rate calculations and a critical evaluation of the dual-level reaction path dynamics methods”, *J. Phys. Chem. A* **103**(8), p. 1140 (1999).

[273] A. V. Marenich, C. P. Kelly, J. D. Thompson, G. D. Hawkins, C. C. Chambers, D. J. Giesen, P. Winget, C. J. Cramer, and D. G. Truhlar, “Minnesota Solvation Database–version 2009, University of Minnesota, Minneapolis (2009)”.

[274] S. V. Shishkina, O. V. Shishkin, and J. Leszczynski, “Three-stage character of ring inversion in cyclohexene”, *Chem. Phys. Lett.* **354**(5-6), p. 428 (2002).

[275] E. Martínez-Núñez, S. A. Vázquez, and R. A. Mosquera, “Conformational analysis of model compounds of vitamin D by theoretical calculations”, *J. Comput. Chem.* **18**(13), p. 1647 (1997).

[276] E. Martínez-Núñez, E. Cabaleiro-lago, A. Fernández-Ramos, J. M. Hermida-Ramón, and A. Peña Gallego, “A DFT study of a model compound of vitamin D”, *J. Mol. Struct. (THEOCHEM)* **492**(1-3), p. 143 (1999).

[277] H.-J. Hofmann and R. Cimiraglia, “Conformation dynamics of 1,2-dimetylenecyclohexane: A model for ring-A mobility in vitamins D”, *J. Org. Chem.* **55**(7), p. 2151 (1990).

[278] X. Q. Tian, T. C. Chen, L. Y. Matsuoka, J. Wortsman, and M. F. Holick, “Kinetic and thermodynamic studies of the conversion of previtamin D_3 to vitamin D_3 in human skin”, *J. Biol. Chem.* **268**(20), p. 14888 (1993).

[279] X. Q. Tian and M. F. Holick, “Catalyzed themal isomerization between previtamin D_3 and vitamin D_3 via β-cyclodestrin complexation”, *J. Biol. Chem.* **270**(15), p. 8706 (1995).

[280] X. Q. Tian and M. F. Holick, “A liposomal model that mimics the cutaneous production of vitamin D_3”, *J. Biol. Chem.* **274**(7), p. 4174 (1999).